Measurement of the $K^+ \to \pi^+ \nu \bar{\nu}$ Branching Ratio

Tetsuro Sekiguchi

Department of Physics, University of Tokyo
and
High Energy Accelerator Research Organization (KEK),
Institute for Nuclear and Particle Studies (INPS)

December, 2004

Abstract

The BNL-E949 experiment [1] was a successor to BNL-E787, and was aimed to measure the branching ratio of the $K^+ \to \pi^+\nu\bar{\nu}$ decay in the momentum region $211 \leq P \leq 229$ MeV/c. After detector upgrades were made, data equivalent to 1.77×10^{12} K^+ decays at rest were collected in a 2002 physics run. The data were analyzed via a blind analysis with a technique called the "Bifurcation Method". The signal region was enlarged compared to that in E787 with increased confidence in the likelihood analysis. An enlargement of the signal region increased the acceptance by 30%. The total background level in the signal region was 0.30 ± 0.02 events. An examination of the signal region yielded one candidate event near the upper kinematic limit for the $K^+ \to \pi^+\nu\bar{\nu}$ decay. Based on this candidate event, an upper limit for the branching ratio $\mathcal{B}(K^+ \to \pi^+\nu\bar{\nu}) < 8.76 \times 10^{-10}$ (90% CL) was obtained, which was consistent with the results from E787. Combining the E787 and E949 results, the branching ratio was determined to be $(1.47^{+1.60}_{-0.93}) \times 10^{-10}$ (68% CL interval) based on the three observed events. The limits on the Cabibbo-Kobayashi-Maskawa matrix element, V_{td}, were set to be $0.0024 < |V_{td}| < 0.0322$ with the measured $K^+ \to \pi^+\nu\bar{\nu}$ branching ratio.

This report is based on a dissertation that was submitted to the graduate school of the University of Tokyo.

[1] This research was supported by the Japan-U.S. Cooperative Research Program in High Energy Physics and the Grant-in-Aid for Scientific Research on Priority Areas "Origin of Mass".

Contents

Chapter 1

Introduction

The Standard Model (SM) in particle physics has accounted for almost all particles, and their processes that we have observed. It consists of two gauge theories: one is "Quantum Chromodynamics" (QCD), which accounts for the strong interaction, and the other is "Glashow-Weinberg-Salam" (GWS) theory, which accounts for the weak and electromagnetic interactions and their unification. In the context of the SM, the masses of all particles, except for the photon and gluon, arise from spontaneous symmetry breaking that occurs due to the existence of a scaler particle, called the Higgs boson.

CP violation was discovered in the middle of the 1960's. Reasonable explanations for the mechanism of CP violation have been explored for years. The "Kobayashi-Maskawa" (KM) theory naturally and reasonably explains CP violation by introducing a 3×3 unitary matrix, called the "Cabibbo-Kobayashi-Maskawa" (CKM) matrix. Many experiments are currently being undertaken to determine the CKM matrix elements.

For many years physics beyond the SM, or new physics (NP), has been searched for. There are two approaches: one is a direct search of new particles in a very high-energy region; the other is the observation of any possible discrepancy between measured and predicted quantities in electroweak processes. The search for the decay $K^+ \to \pi^+\nu\bar{\nu}$ is an attempt to utilize the latter of two approaches.

1.1 Weak Interaction and CP Violation

The weak interaction operates on all quarks and leptons through the mediators W^+, W^- and Z^0 bosons. There are charged and neutral current processes in the weak interaction. In the charged-current processes one quark can transform into another quark with a different flavor (e.g., u$\to$d), and one lepton can transform into another lepton with a different charge (e.g., e$^-$ $\to \nu_e$). Particle "flavors" are conserved in the strong and electromagnetic interactions (e.g., $q\bar{q} \to q'\bar{q}'$ or $e^+e^- \to \mu^+\mu^-$). In the neutral-current processes, however, a quark cannot transform into another quark with the same charge and a different flavor (e.g., s$\to$d). These are called flavor changing neutral current (FCNC) processes, and are forbidden at a tree level.

Historically, Cabibbo introduced the angle θ_C to explain quark mixing in the weak interaction [1] and Glashow, Iliopoulos and Miani proposed a fourth quark (charm quark) to explain the absence of the FCNC processes (GIM mechanism [2]). The weak eigenstates,

d' and s', not the mass eigenstates, d and s, participate in the weak interaction. Their relation is written as

$$\begin{pmatrix} d' \\ s' \end{pmatrix} = \begin{pmatrix} \cos\theta_C & \sin\theta_C \\ -\sin\theta_C & \cos\theta_C \end{pmatrix} \begin{pmatrix} d \\ s \end{pmatrix}, \tag{1.1}$$

where θ_C is called the Cabibbo angle. A neutral current, J^0, is expressed by the following description (in omitting the γ-matrices):

$$\begin{aligned} J^0 &= \bar{u}u + \bar{c}c + \bar{d}'d' + \bar{s}'s' \\ &= \bar{u}u + \bar{c}c + (\bar{d}d + \bar{s}s)\cos^2\theta_C + (\bar{d}d + \bar{s}s)\sin^2\theta_C \quad &: \text{(flavor conserving term)} \\ &\quad +(\bar{d}s + \bar{s}d - \bar{d}s - \bar{s}d)\sin\theta_C\cos\theta_C &: \text{(flavor changing term)} \\ &= \bar{u}u + \bar{c}c + \bar{d}d + \bar{s}s. \end{aligned} \tag{1.2}$$

The term that accounts for the FCNC processes vanishes, and therefore the absence of the FCNC processes at a tree level is explained by this description. GIM cancellation can also work at 1-loop diagrams, where the initial-to-final quark transitions are effectively the FCNC processes, if the quarks in the intermediate state (e.g., the u and c quarks in the $K^0 - \bar{K}^0$ mixing) have the same mass. Since the quark masses depend on the quark flavors, this cancellation is not perfect, and thus the FCNC processes are allowed as "rare decays" at higher orders.

Kobayashi and Maskawa extended the concept of this quark mixing up to the third generation, and explained CP violation by introducing an imaginary phase into a quark mixing matrix [3]. The weak eigenstates d', s', b' are connected to their mass eigenstates d, s, b by a 3×3 unitary matrix V,

$$\begin{pmatrix} d' \\ s' \\ b' \end{pmatrix} = V \begin{pmatrix} d \\ s \\ b \end{pmatrix} = \begin{pmatrix} V_{ud} & V_{us} & V_{ub} \\ V_{cd} & V_{cs} & V_{cb} \\ V_{td} & V_{ts} & V_{tb} \end{pmatrix} \begin{pmatrix} d \\ s \\ b \end{pmatrix}. \tag{1.3}$$

This matrix is known as the Cabibbo-Kobayashi-Maskawa (CKM) matrix. The unitary matrix has four independent parameters, which in the leading order of the Wolfenstein parameterization [4] are A, λ, ρ and η. In terms of these parameters, the CKM matrix can be written as

$$\begin{pmatrix} V_{ud} & V_{us} & V_{ub} \\ V_{cd} & V_{cs} & V_{cb} \\ V_{td} & V_{ts} & V_{tb} \end{pmatrix} \simeq \begin{pmatrix} 1-\lambda^2/2 & \lambda & A\lambda^3(\rho - i\eta) \\ -\lambda & 1-\lambda^2/2 & A\lambda^2 \\ A\lambda^3(1-\rho-i\eta) & -A\lambda^2 & 1 \end{pmatrix}. \tag{1.4}$$

The CKM matrix elements are written in powers of $\lambda = \sin\theta_c = 0.22$. CP invariance of the Lagrangian for weak interactions is violated when the CKM matrix is a complex one. The parameter η describes CP violation in the SM, since a non-zero value of the parameter η breaks the CP invariance for weak interactions. Experimentally allowed ranges of the magnitude of the CKM matrix elements are

$$\begin{pmatrix} |V_{ud}| & |V_{us}| & |V_{ub}| \\ |V_{cd}| & |V_{cs}| & |V_{cb}| \\ |V_{td}| & |V_{ts}| & |V_{tb}| \end{pmatrix} \simeq \begin{pmatrix} [0.9739, 0.9751] & [0.221, 0.227] & [0.0029, 0.0045] \\ [0.221, 0.227] & [0.9730, 0.9744] & [0.039, 0.044] \\ [0.0048, 0.014] & [0.037, 0.043] & [0.9990, 0.9992] \end{pmatrix} \tag{1.5}$$

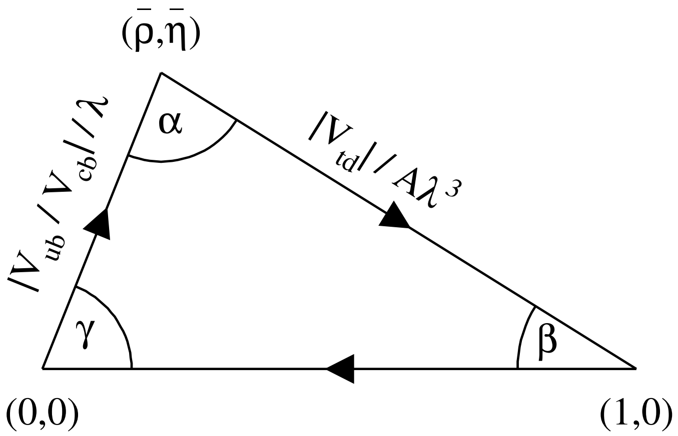

Figure 1.1: Unitarity triangles in the $\rho - \eta$ plane. Two sides of the triangle can be expressed by the CKM matrix elements $|V_{td}|/A\lambda^3$ and $|V_{ub}/V_{cb}|/\lambda$, respectively, where A and λ are parameters in the Wolfenstein parameterization.

in the 90% confidence level intervals [5].

The CKM matrix elements (particularly those involving couplings to the top quark) can be determined "indirectly" from flavor-changing second-order weak processes that involve the up-type quarks in an internal loop (e.g., $K^+ \to \pi^+\nu\bar{\nu}$). It is assumed that the dominant contribution to the processes comes from the t quark loop. The agreement or disagreement between the measured and predicted quantities can put constraints on new physics.

All of the direct and indirect information concerning the CKM matrix elements can be summarized in terms of "unitarity triangles". The unitarity of this matrix can be expressed in terms of six unitarity conditions, which can be represented graphically in the form of triangles, all of which must have the same area. The area of these triangles is equal to one half of the Jarlskog invariant, J_{CP} [6]. Applying the unitarity property $V^\dagger V = 1$ to the CKM matrix in (1.4) implies

$$V_{ub}^* V_{ud} + V_{cb}^* V_{cd} + V_{tb}^* V_{td} \simeq V_{ub}^* - \lambda V_{cb}^* + V_{td} = 0, \tag{1.6}$$

where the approximations $V_{ud} \simeq V_{tb}^* \simeq 1$ and $V_{cd} \simeq -\lambda$ have been made. This equation can be represented graphically, as shown in Figure 1.1, where we have divided all of the sides by λV_{cb}^*. The apex of the triangle is given by two well-known Wolfenstein parameters, $\bar{\rho}$ and $\bar{\eta}$, where $\bar{\rho} = \rho(1 - \lambda^2/2)$ and $\bar{\eta} = \eta(1 - \lambda^2/2)$. Their information currently comes from several measurements of B meson decays, as well as a measurement of the indirect CP violation parameter from $K^0 - \bar{K}^0$ mixing, ϵ_K. It is desirable to over-constrain each of the unitarity relations and to measure the J_{CP} in as many independent ways as possible, because any disagreement among the independent measurements would indicate the presence of new physics beyond the SM.

CP violation is essential to explain the matter-antimatter asymmetry of the universe. The parameters for CP violation in the SM are not sufficient to explain the observed matter-antimatter asymmetry. There must be some other sources of CP violation in nature in order to completely explain the matter-antimatter asymmetry. Powerful tests of our understanding of CP violation and quark mixing will come from comparisons of

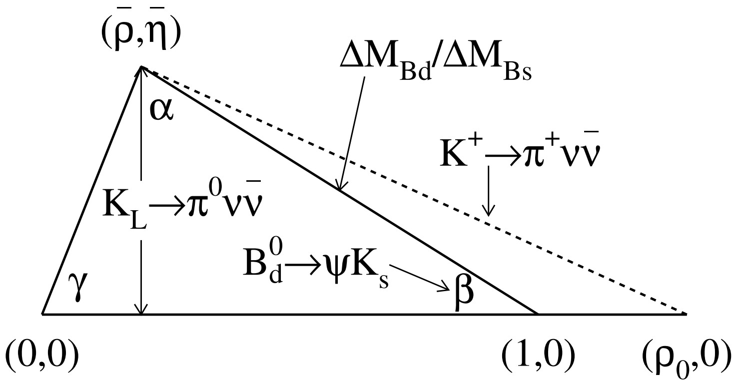

Figure 1.2: Unitarity triangle determined by B and K decays. The ρ and η can be determined by two ways: angle β from the CP violation asymmetry in the decay $B_d^0 \to J/\psi K_s^0$, and the length of the side from $\Delta M_{B_s}/\Delta M_{B_d}$ in $B^0 - \bar{B}^0$ mixing; the height of the triangle from $\mathcal{B}(K_L^0 \to \pi^0\nu\bar{\nu})$ and the radius of a circle centered at $(\rho_0, 0)$ from $\mathcal{B}(K^+ \to \pi^+\nu\bar{\nu})$.

the results from B meson and kaon decays with small theoretical ambiguities. In other words, since the CKM phase should be the only source of CP violation within the SM, precise measurements of all the CKM matrix elements are crucial. The determination of ρ and η independently from B and K decays, as shown in Figure 1.2, can be examined in two ways, as follows:

- A comparison of angle β from the ratio $\mathcal{B}(K_L^0 \to \pi^0\nu\bar{\nu})/\mathcal{B}(K^+ \to \pi^+\nu\bar{\nu})$ and from CP violation asymmetry ($\mathcal{A}_{CP}$) in the decay $B_d^0 \to J/\psi K_s^0$.
- A comparison of the magnitude $|V_{td}|$ from $K^+ \to \pi^+\nu\bar{\nu}$ and from the mixing frequencies of B_s and B_d mesons, expressed in terms of the ratio of the mass differences, $\Delta M_{B_s}/\Delta M_{B_d}$.

The motivation to search for $K^+ \to \pi^+\nu\bar{\nu}$ stems from a desire to measure the small, imprecisely-determined CKM matrix element $|V_{td}|$. Another goal is to search for non-SM physics. These will be discussed in the following sections.

1.2 The Rare Decay $K^+ \to \pi^+\nu\bar{\nu}$

The decay $K^+ \to \pi^+\nu\bar{\nu}$ is a FCNC process that is prohibited in the first order (see Figure 1.3). However, this decay is allowed in the second order, and is described by a "Box" diagram and two "Z-penguin" diagrams, as shown in Figure 1.4. The weak amplitude for this process is represented as

$$\mathcal{M} \sim \sum_{i=u,c,t} V_{is}^* V_{id} \frac{\gamma^\mu q_\mu + m_i}{q^2 - m_i^2}, \tag{1.7}$$

where the V_{ij}'s are the CKM matrix elements, the γ^μ's are the Dirac matrices, the q_μ is the momentum transfer, and the m_i's are quark masses. $\mathcal{M}$ vanishes if all of the quark masses, m_i, are equal, because of the unitarity of the CKM matrix. However, the

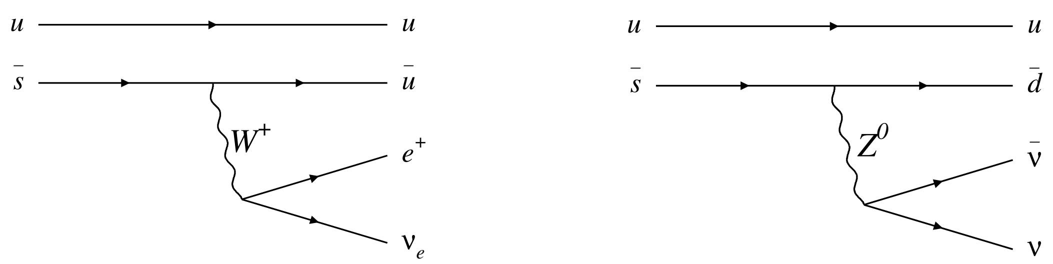

Figure 1.3: Feynman diagram for the weak decay $K^+ \to \pi^0 e^+ \nu_e$, which is allowed in the SM (left). Feynman diagram for the $K^+ \to \pi^+ \nu \bar{\nu}$ decay in a tree level, which is not allowed (right).

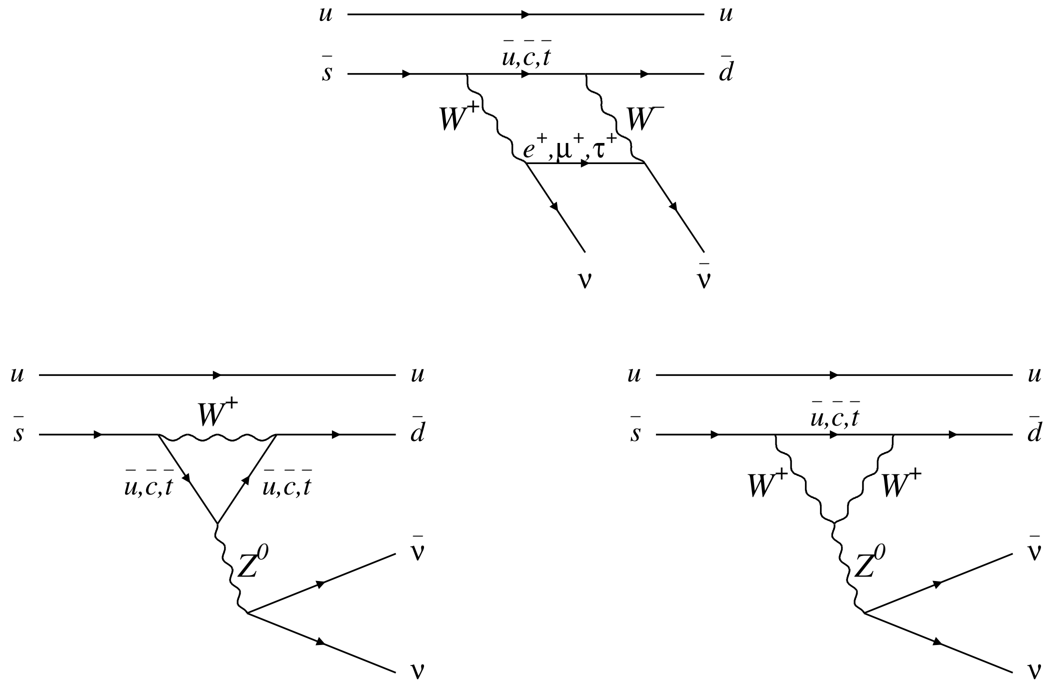

Figure 1.4: Second-order weak processes that contribute to the $K^+ \to \pi^+ \nu \bar{\nu}$ branching ratio: the "Box" diagram (upper) and two "Z-penguin" diagrams (bottom).

breaking of flavor symmetry, which results in the different quark masses, allows this decay to proceed at a very small rate. Since the top quark violates the quark mass equality at a maximum, its contribution to the $K^+ \to \pi^+\nu\bar{\nu}$ branching ratio is the largest. This decay is sensitive to the weak coupling of top to down quarks, given by the CKM matrix element, V_{td}.

The branching ratio for $K^+ \to \pi^+\nu\bar{\nu}$ is calculated by following the convention in [7]. The effective Hamiltonian can be written in the SM as

$$\mathcal{H}^{SM}_{eff} = \frac{G_F}{\sqrt{2}}\frac{\alpha}{2\pi\sin^2\Theta_W}\sum_{l=e,\mu,\tau}(V^*_{cs}V_{cd}X^l_{\mathrm{NL}} + V^*_{ts}V_{td}X(x_t))(\bar{s}d)_{V-A}(\bar{\nu}_l\nu_l)_{V-A}, \tag{1.8}$$

where

$$X(x_t) \equiv X_0(x_t) + \frac{\alpha_s(m_t)}{4\pi}X_1(x_t) = \eta_X \cdot X_0(x_t) \tag{1.9}$$

and

$$X_0(x_t) \equiv C_0(x_t) - 4B_0(x_t), \quad \eta_X = 0.995. \tag{1.10}$$

$B_0(x_j)$ and $C_0(x_j)$ in (1.10) are functions of $x_j \equiv m_j^2/M_W^2$, and were derived for the first time by Inami and Lim in 1981 [8]. The coefficient X^l_{NL} and the function $X(x_t)$ are the charm and top quark contributions, including QCD corrections at the next-leading-order (NLO) level [9, 10, 11].

The theoretical uncertainty in the dominant top contribution is very small, and is essentially determined by the experimental error on the top quark mass, m_t. With the top quark mass in the minimal subtraction ($\overline{MS}$) scheme $m_t = (168.1 \pm 4.1)$ GeV,

$$X(x_t) = 1.529 \pm 0.042 \tag{1.11}$$

is obtained. The $\overline{MS}$ top quark mass is taken from [7].

The largest theoretical uncertainty in estimating $\mathcal{B}(K^+ \to \pi^+\nu\bar{\nu})$ originates from the charm contribution. The perturbative charm contribution is described in terms of the parameter

$$P_c(X) \equiv \frac{1}{\lambda^4}[\frac{2}{3}X^e_{\mathrm{NL}} + \frac{1}{3}X^\tau_{\mathrm{NL}}] = 0.39 \pm 0.07, \tag{1.12}$$

where $\lambda = \sin\theta_c$. The numerical error on the right-hand side of (1.12) is obtained by varying the charm mass, m_c, the scale factor, $\mu_c = \mathcal{O}(m_c)$ and the coupling constant, $\alpha_s(M_Z^2)$, by certain amounts.

With these definitions the branching ratio for $K^+ \to \pi^+\nu\bar{\nu}$ can be written as

$$\mathcal{B}(K^+ \to \pi^+\nu\bar{\nu}) = \kappa_+ \cdot \left[\left(\frac{\mathrm{Im}\lambda_t}{\lambda^5}X(x_t)\right)^2 + \left(\frac{\mathrm{Re}\lambda_c}{\lambda}P_c(X) + \frac{\mathrm{Re}\lambda_t}{\lambda^5}X(x_t)\right)^2\right], \tag{1.13}$$

where

$$\kappa_+ \equiv r_+\frac{3\alpha^2\mathcal{B}(K^+ \to \pi^0e^+\nu)}{2\pi^2\sin^4\Theta_W}\lambda^8 = (4.84 \pm 0.06) \times 10^{-11}\left[\frac{\lambda}{0.224}\right]^8 \tag{1.14}$$

and the λ_j's ($\equiv V^*_{js}V_{jd}$) are from the CKM matrix elements. The r_+ ($= 0.901$) represents isospin breaking corrections in relating $K^+ \to \pi^+\nu\bar{\nu}$ to the well-measured leading decay $K^+ \to \pi^0e^+\nu$ [12]. In obtaining the numerical value in (1.14), we used [13]

$$\sin^2\Theta_W = 0.231, \qquad \alpha = \frac{1}{127.9}, \qquad \mathcal{B}(K^+ \to \pi^0e^+\nu) = (4.87 \pm 0.06) \times 10^{-2}. \tag{1.15}$$

$\lambda = \lvert V_{us}\rvert = 0.2240 \pm 0.0036$
$\bar{\rho} = 0.187 \pm 0.059$
$\bar{\eta} = 0.354 \pm 0.027$
$\lvert V_{cb}\rvert = (41.5 \pm 0.8) \times 10^{-3}$
$\lvert V_{ub}/V_{cb}\rvert = 0.092 \pm 0.014$
$\lvert V_{td}\rvert = (8.24 \pm 0.54) \times 10^{-3}$
$\mathrm{A} = \lvert V_{cb}\rvert/\lambda^2 = 0.827 \pm 0.016$
$\sin 2\beta = 0.732 \pm 0.049$
$m_t = 168.1 \pm 4.1$ GeV
$X(x_t) = 1.529 \pm 0.042$
$P_c(X) = 0.389 \pm 0.073$
$\rho_0 = 1 + \lambda^4 P_c(X)/\lvert V_{cb}\rvert^2 X(x_t) = 1 + P_c(X)/A^2 X(x_t) = 1.373 \pm 0.068$
$\xi = f_{B_s}\sqrt{B_s}/f_{B_d}\sqrt{B_d} = 1.24 \pm 0.08$

Table 1.1: Parameters that are used in the SM prediction of the $\mathcal{B}(K^+ \to \pi^+\nu\bar{\nu})$.

Employing the improved Wolfenstein decomposition of the CKM matrix [14], expression (1.13) describes in the $\bar{\rho} - \bar{\eta}$ plane an ellipse with a small eccentricity, namely

$$(\sigma\bar{\eta})^2 + (\bar{\rho} - \bar{\rho}_0)^2 = \frac{\sigma\mathcal{B}(K^+ \to \pi^+\nu\bar{\nu})}{\bar{\kappa}_+ \lvert V_{cb}\rvert^4 X^2(x_t)}, \tag{1.16}$$

where

$$\bar{\rho}_0 \equiv 1 + \frac{\lambda^4 P_c(X)}{\lvert V_{cb}\rvert^2 X(x_t)}, \qquad \sigma \equiv \left(1 - \frac{\lambda^2}{2}\right)^{-2}, \qquad \overline{\kappa}_+ \equiv \frac{\kappa_+}{\lambda^8} = (7.64 \pm 0.09) \times 10^{-6}. \tag{1.17}$$

Using (1.13) and varying m_t, $\lvert V_{cb}\rvert$, $P_c(X)$ and $\lvert V_{td}\rvert$, which is constrained by $\lvert V_{ub}/V_{cb}\rvert$ and the $B^0 - \bar{B}^0$ mixing in the $\bar{\rho} - \bar{\eta}$ plane, the branching ratio of $K^+ \to \pi^+\nu\bar{\nu}$ is predicted to be

$$\mathcal{B}(K^+ \to \pi^+\nu\bar{\nu}) = (0.78 \pm 0.12) \times 10^{-10} \tag{1.18}$$

within the SM [7]. Here, the parameters used are summarized in Table 1.1. It should be noted that, for an uncertainty of 15% in (1.18), the theoretical uncertainty is ~7% at present, mainly due to the charm quark contribution.

The measurement of $\mathcal{B}(K^+ \to \pi^+\nu\bar{\nu})$ is regarded to be one of the cleanest ways to extract $\lvert V_{td}\rvert$ for the following reasons:

- Long-distance contributions to the branching ratio are negligible (at most 10^{-13}) [15].
- The uncertainty from the hadronic matrix element has been removed by using $\mathcal{B}(K^+ \to \pi^0 e^+\nu)$.
- The remaining theoretical uncertainties (7%) are relatively small and reliable as compared with the errors in other K and B decays.

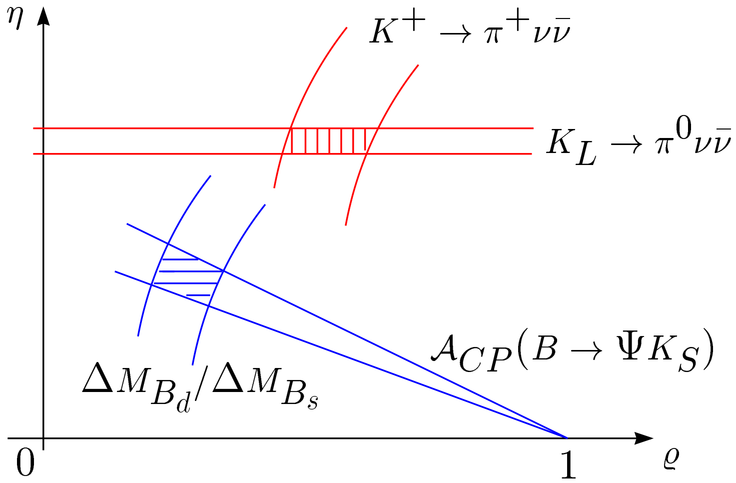

Figure 1.5: Schematic determination of the unitarity triangle vertex (ρ,η) from the B system (horizontally hatched) and from the $K \to \pi\nu\bar{\nu}$ (vertically hatched). Both determinations can be performed with small theoretical uncertainties; any discrepancy between them would indicate new physics, as illustrated in this hypothetical example [17].

The theoretical uncertainty will be reduced if we obtain better knowledge about the QCD corrections to the charm contribution at the next-to-next-leading-order (NNLO) level. A precise measurement of $\Delta M_{B_d}/\Delta M_{B_s}$ in $B^0 - \bar{B}^0$ mixing would also narrow down the SM prediction, once $B_s^0 - \bar{B}_s^0$ mixing has been observed [16]. A precise measurement of the $K^+ \to \pi^+\nu\bar{\nu}$ branching ratio is therefore a stringent test of the SM and also a probe for new physics.

1.3 Physics beyond the Standard Model

Since the theoretical uncertainty included in the $K^+ \to \pi^+\nu\bar{\nu}$ branching ratio is small, a precise measurement of the branching ratio can investigate whether there are non-SM effects in this decay mode or not. A possible discrepancy between the measured branching ratio and the SM prediction would indicate the existence of new physics beyond the SM.

What should be performed in testing the SM is to determine ρ and η independently from the K and B decays, as shown in Figure 1.5. The information that is currently being used to constrain the unitarity triangle is obtained only from the charged current processes (i.e. tree-level amplitudes) and the $\Delta F = 2$ $(F = S, B)$ loop-induced processes. For example, determinations of ρ and η can be obtained from the $B_d^0 - \bar{B}_d^0$ mixing and the CP violating asymmetry in $B_d^0 \to J/\psi K_s^0$, both of which are mediated by $\Delta B = 2$ loop-induced processes. On the contrary, $K^+ \to \pi^+\nu\bar{\nu}$ and $K_L^0 \to \pi^0\nu\bar{\nu}$ are mediated via the $\Delta S = 1$ FCNC transition. New physics may therefore be seen in a discrepancy between K and B decays [17].

Several SM extensions to new physics would affect the $K^+ \to \pi^+\nu\bar{\nu}$ branching ratio. In the "Minimal Flavor Violation" (MFV) model, where the origin of CP violation and quark mixing comes from the CKM matrix, as in the SM, and process-independent universal master functions, which are real and which in the SM reduce to the Inami-Lim functions, are considered, the $K^+ \to \pi^+\nu\bar{\nu}$ branching ratio is allowed to be as large as 1.9×10^{-10} [18]. In the "Enhanced Z^0 Penguin" model [19], where a new imaginary phase is introduced, the $K^+ \to \pi^+\nu\bar{\nu}$ branching ratio is expected to be almost the same as the SM prediction; however, the $K_L^0 \to \pi^0\nu\bar{\nu}$ branching ratio is predicted to be $(3.1 \pm 0.1) \times 10^{-10}$, which is 10-times larger than the SM prediction, and is close to the Grossman-Nir limit, $\mathcal{B}(K_L^0 \to \pi^0\nu\bar{\nu})/\mathcal{B}(K^+ \to \pi^+\nu\bar{\nu}) < 4.4$ [20]. Another interesting prediction derived from this model is that the value of $\sin 2\beta$ obtained from $K \to \pi\nu\bar{\nu}$ is not equal to that obtained from $B_d^0 \to J/\psi K_s^0$.

An analysis of $K^+ \to \pi^+\nu\bar{\nu}$ can also be used to search for the decay $K^+ \to \pi^+X^0$, where X^0 is a weakly-interacting massless Nambu-Goldstone boson led by family symmetry breaking (called "familon"). The branching ratio of this decay gives the information on the energy scale at which the family symmetry is spontaneously broken [21]. The current 90% CL upper limit obtained from the BNL-E787 is 0.59×10^{-10} [22, 23].

1.4 History of the Search for $K^+ \to \pi^+\nu\bar{\nu}$

An experimental search for the rare decay $K^+ \to \pi^+\nu\bar{\nu}$ has been made for more than thirty years. Figure 1.6 summarizes the history of the search. The experiments at the Bevatron in Lawrence Berkeley Laboratory (by J.H. Klems *et al* [24] and by G.D. Cable *et al* [25]) and the experiment at KEK (by Y. Asano *et al* [26]) examined stopped K^+ decays. In these experiments, π^+'s and μ^+'s from K^+ decays were detected with tracking chambers and scintillation counters in a half volume of the detectors without magnetic fields. The range of a charged particle was measured in scintillation counters along with the track extrapolated from the chambers. The π^+ identification was performed by finding the $\pi^+ \to \mu^+ \to e^+$ decay sequence. In the other half volume, large gamma detectors were located to detect extra photon activities, mainly from $K^+ \to \pi^+\pi^0$. The E787 experiment at Brookhaven National Laboratory (BNL) followed these experiments with a cylindrically symmetric spectrometer [27]. The BNL-E787 phase I (1988-1991) lowered the upper limit of the branching ratio to 2.4×10^{-9} at the 90% confidence level (CL) [28].

After several upgrades were made, BNL-E787 restarted to search for $K^+ \to \pi^+\nu\bar{\nu}$ (phase II, 1995-1998), and observed the first $K^+ \to \pi^+\nu\bar{\nu}$ candidate event from their 1995 data [22]. BNL-E787 observed another $K^+ \to \pi^+\nu\bar{\nu}$ candidate event from the 1998 data, and the branching ratio was measured to be $(1.57^{+1.75}_{-0.82}) \times 10^{-10}$ at the 68% CL interval based on two events observed in the π^+ momentum region $211 < P < 229$ MeV/c [23]. This branching ratio was consistent with the SM prediction $(0.78 \pm 0.12) \times 10^{-10}$, although the central value was twice the SM prediction.

The consistency between the measured branching ratio and the SM prediction should be confirmed with better precision. The BNL-E949 experiment aims to increase the statistics of the $K^+ \to \pi^+\nu\bar{\nu}$ events and test the SM with better precision, and also to search for new physics.

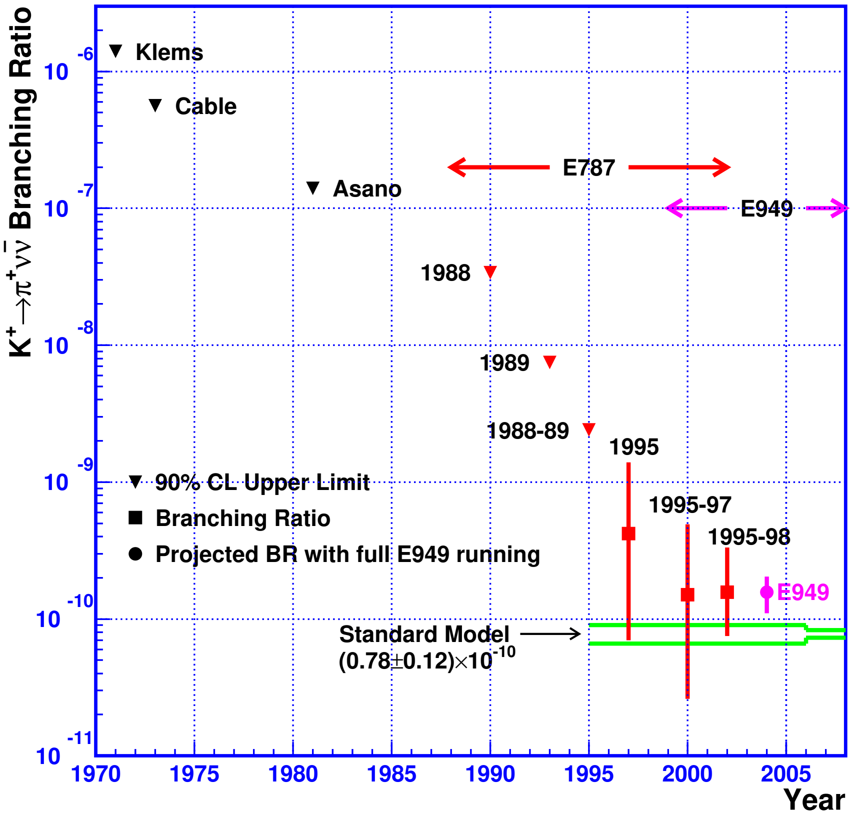

Figure 1.6: History of the search for $K^+ \to \pi^+\nu\bar{\nu}$. The vertical and horizontal axes show the $K^+ \to \pi^+\nu\bar{\nu}$ branching ratio and the publication year, respectively. The triangles represent the upper limit for the branching ratio at the 90% confidence level. The boxes represent the central value of the measured branching ratio. The dot represents an expected branching ratio with the full E949 running period, assuming that the central value of the branching ratio is 1.57×10^{-10}. The error bars show the 68% CL intervals. The SM prediction is expected to be narrowed down in the near future once $B_s - \bar{B}_s$ mixing has been observed [16].

Chapter 2

Experiment BNL-E949

2.1 Experimental Overview

The experimental signature of the $K^+ \to \pi^+\nu\bar{\nu}$ decay is a single π^+ track and no other particle from a K^+ decay, because two neutrinos in the final state cannot be detected in the apparatus. Figure 2.1 shows the momentum spectra of charged particles in K^+ decays in the rest frame. $K^+ \to \pi^+\nu\bar{\nu}$ is a three-body decay and has a momentum < 227 MeV/c.

Since, in the SM, the branching ratio of $K^+ \to \pi^+\nu\bar{\nu}$ is expected to be at 10^{-10}, all other kaon decay modes could be sources of background. The two-body decays $K^+ \to \pi^+\pi^0$ ($K_{\pi2}$) and $K^+ \to \mu^+\nu_\mu$ ($K_{\mu2}$) have large branching ratios (0.212 for $K_{\pi2}$ and 0.635 for $K_{\mu2}$). These decays are main sources of background when two photons from π^0 are missed in $K_{\pi2}$ or μ^+ is misidentified as π^+ in $K_{\mu2}$. In addition, a pion beam that scatters in the kaon stopping target and enters the fiducial region of the detector is also a major source of background when π^+ is misidentified as K^+ in the beam instrumentation. In order to distinguish $K^+ \to \pi^+\nu\bar{\nu}$ signal events from these background events, the experimental setup should satisfy the following requirements:

- The beam intensity should be as high as possible, since the decay rate is extremely rare.
- Pion contamination in the kaon beam should be reduced to be as low as possible to minimize events with the scattered pion beam (Pion Scattering events).
- In order to suppress the $K_{\pi2}$ and $K_{\mu2}$ backgrounds, the signal region is selected to be in the momentum region $211 \le P \le 229$ MeV/c, because $K_{\pi2}$ and $K_{\mu2}$ are two-body decays and have monochromatic momenta of 205 and 236 MeV/c, respectively. Contributions of the other kaon decay modes to this region are small. The kinematics of charged particles from K^+ decay should be precisely measured.
- Any particles other than π^+ from K^+ decay should be detected in the detector. Events with photon activities coincident with the π^+ should be vetoed, which helps to suppress the $K_{\pi2}$ background.

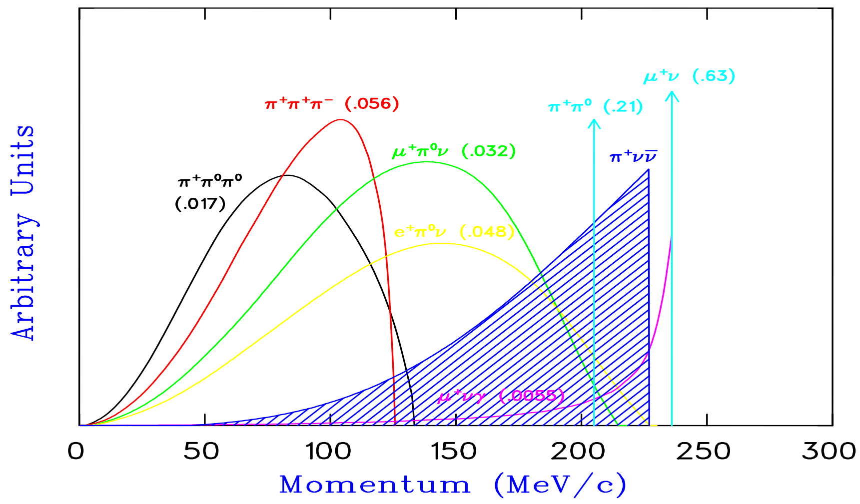

Figure 2.1: Momentum spectra (in MeV/c) of charged particles from K^+ decays in the rest frame. The values in the parentheses represent the branching ratios for their decay modes. The hatched spectrum shows the π^+ momentum in the $K^+ \to \pi^+\nu\bar{\nu}$ decay assuming the $V - A$ interaction.

- The charged particle should be identified as π^+, which is achieved by observing the $\pi^+ \to \mu^+ \to e^+$ decay sequence. This helps to suppress the $K_{\mu 2}$ background.

The BNL-E949 experiment [29] is a successor to the experiment BNL-E787, whose data taking was completed in 1998. The beam and apparatus are similar to those of E787, but several upgrades have been made:

Beam

- The proton intensity increased by a factor of two compared to E787, which resulted in a twice higher kaon intensity than that in E787.

Detector

- A new lead/scintillator sandwich sampling calorimeter was installed to the barrel region; a 2.3 radiation length was added. Also installed were photon detectors that cover small solid angles near the beam line.
- One third of the plastic scintillators in the π^+ range counters were replaced, which enabled us to achieve greater outputs of light.
- A gain monitor system, operated by blue LED flashers, was installed. The gain fluctuations of a phototube could be tracked down spill by spill, or even within a spill. This resulted in more precise energy calibration.
- Electronics for the drift chamber and straw chambers embedded in the range counters were modified to meet the high rates.

- Signals from several beam counters were read out by waveform digitizers. Signal pileup due to the high beam intensity was solved by pulse-shape analysis.

Trigger and DAQ

- The level 0 trigger board was upgraded [30].
- Digital mean-timer modules were used for online photon rejection [30]. This helped to avoid any accidental loss in the trigger.

In the following sections, details concerning the E949 experiment are described. The production of a high-intensity kaon beam is described in the next section; the E949 detector is explained in Section 2.3; the trigger and the Monte Carlo simulation are explained in Sections 2.4 and 2.5; and the data taking during the physics run in 2002 is summarized in Section 2.6.

2.2 High-Intensity Kaon Beam

The K^+ beam is produced by a high-intensity proton beam from the Alternating Gradient Synchrotron (AGS) at BNL. A schematic view of the AGS accelerator complex is shown in Figure 2.2. Protons are accelerated to a momentum of 21.5 GeV/c. 65 trillion protons (Tp) are extracted in a 2.2-second long "spill" once every 5.4 seconds [1] from the AGS. The slow extracted beam (SEB) is transported to the kaon production target for E949. The production target is made of a platinum that extends 6 cm to the beam direction, and is located on a water-cooled copper base. The typical AGS running condition is 45 Tp on the production target per 2.2 second spill at 21.5 GeV/c.

Low Energy Separated Beam line III [31] (LESBIII, shown in Figure 2.3) collects and focuses kaons produced at the production target. The beam emitted toward 0 degree contains about 500 pions and 500 protons for every kaon, and is momentum-selected by a dipole magnet (D1 in Figure 2.3). Two electrostatic separators (Separators 1 and 2 in Figure 2.3) sweep pions and protons out of the beam. The resulting beam is further selected by a second dipole magnet (D2 in Figure 2.3). LESBIII contains a number of focusing quadrupole (Q1-10), sextupole (S1-3), and octupole (O1) magnets and collimating slits, and has a total length of 19.6 m from the production target to the E949 target. Kaons with 710 MeV/c were transported. The angular acceptance of LESBIII is 12 msr and the momentum acceptance is 4.5% FWHM. LESBIII provides the world's highest-intensity kaon beam of 710 MeV/c with a flux of about 5×10^5 K^+'s per Tp on the production target. The $K^+ : \pi^+$ ratio in the beam is about 3:1 [2]. Proton contamination is negligible due to a large deflection of protons by the separators. Under the typical AGS running condition of 45 Tp on the production target per spill, 1.3×10^7 K^+'s emerge from LESBIII.

[1] The original request of E949 for AGS running was beam extraction of 4.1 seconds once every 6.4 seconds. Before the 2001 engineering run started, a motor generator (MG) in AGS was broken and had to be replaced with a backup (old) MG, which resulted in a poor duty factor.

[2] The K/π ratio in E787 was 4:1. This worse K/π ratio was due to a problem with the second separator.

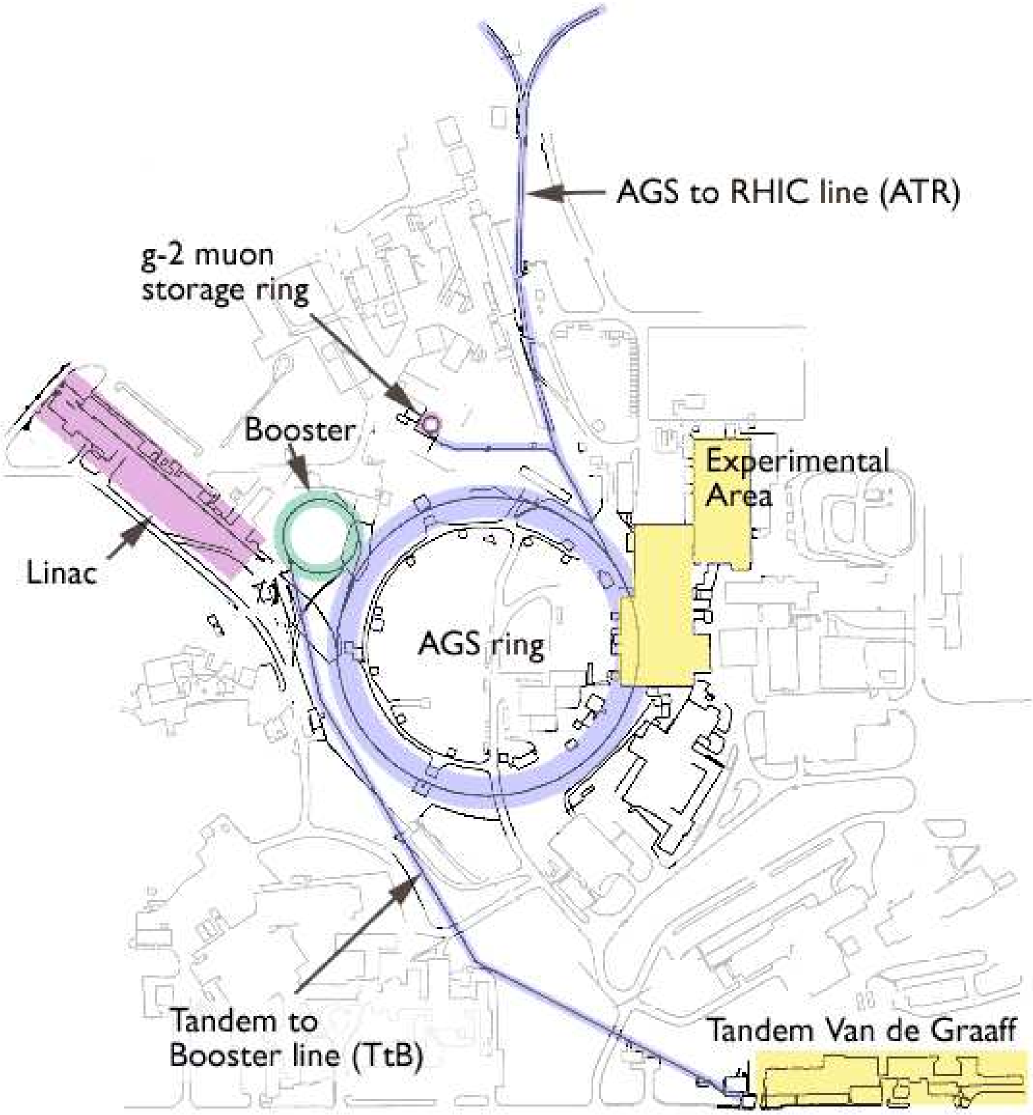

Figure 2.2: Schematic view of the AGS complex, which consists of a 200 MeV LINAC, a booster and a synchrotron. The secondary beam lines are located in the experimental area.

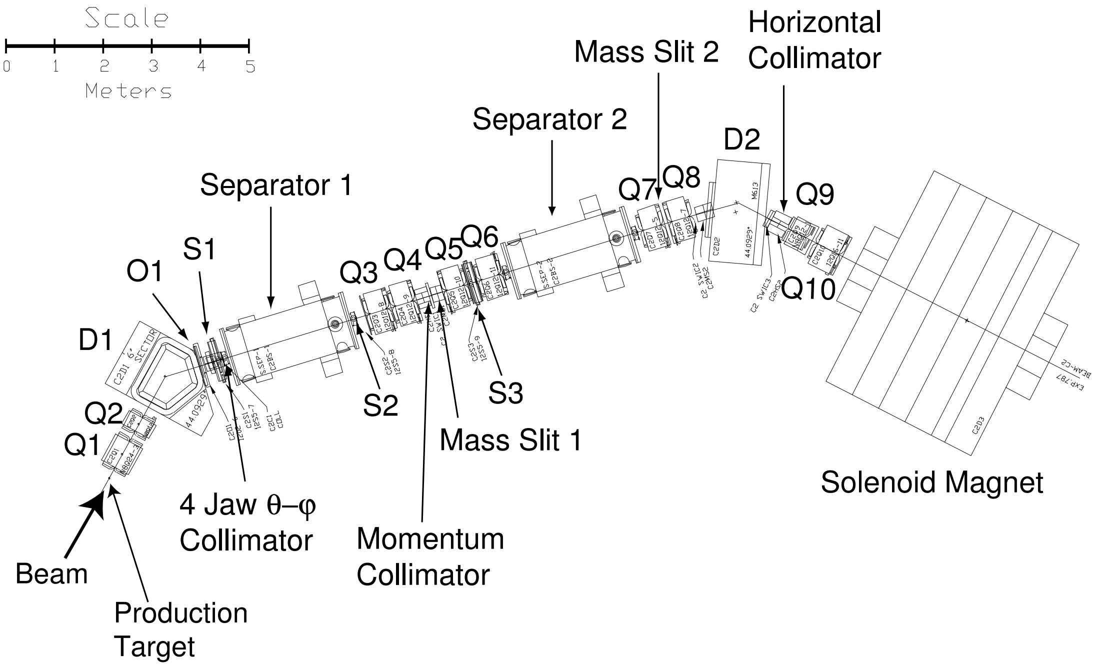

Figure 2.3: Low-energy separated beam line III at BNL.

2.3 The Detector

A side view of the E949 detector is shown in Figure 2.4. The E949 detector consists of beam instrumentation, a target of scintillating fibers, a central drift chamber, a stack of plastic scintillators (Range Stack), and hermetic photon detectors. The whole detector is surrounded by a solenoid magnet with a 1 Tesla magnetic field along the beam line for momentum measurements. The coordinates of the detector are defined such that the origin is at the center of the target; the z-axis is along the beam direction; the x-axis and y-axis are set in the horizontal and vertical directions, respectively.

2.3.1 Beam Instrumentation

Since the beam intensity is very high and the beam contains pions with a ratio of $K^+ : \pi^+ = 3 : 1$, a single kaon entering the target should be identified by the beam instrumentation. It has three roles: kaon identification, slowing down the kaon, and the detection of extra beam particles if they exist at the kaon beam time or the kaon decay time. The beam instrumentation from upstream to downstream consists of a Čerenkov counter, beam wire chambers, degraders and a beam hodoscope.

The kaon beam from LESBIII enters the Čerenkov counter located just downstream of the last quadrupole magnet (Q10) and 2 m upstream of the target. A side view of the Čerenkov counter is shown in Figure 2.5. In E949, the reflection index (n) of the radiator is 1.49, which gives a threshold of Čerenkov radiation $\beta_{\check{C}} = 1/n = 0.671$ and a reflection threshold $\beta_{ref} = \sqrt{\frac{1}{n^2-1}} = 0.905$. Kaons and pions with a momentum of 710 MeV/c have $\beta_{K^+} = 0.821$ and $\beta_{\pi^+} = 0.981$, respectively; the Čerenkov light from kaons

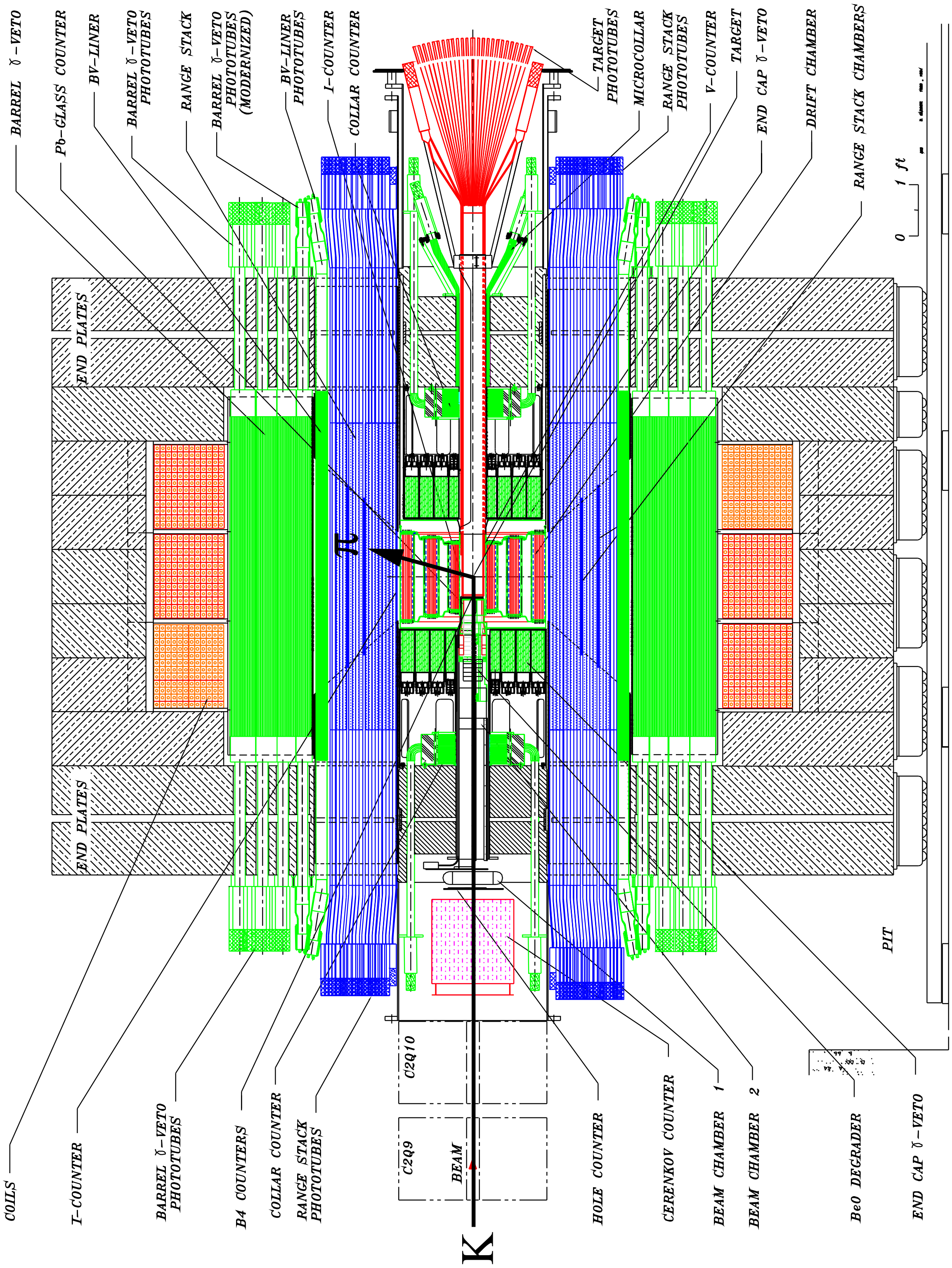

Figure 2.4: Side view of the E949 detector.

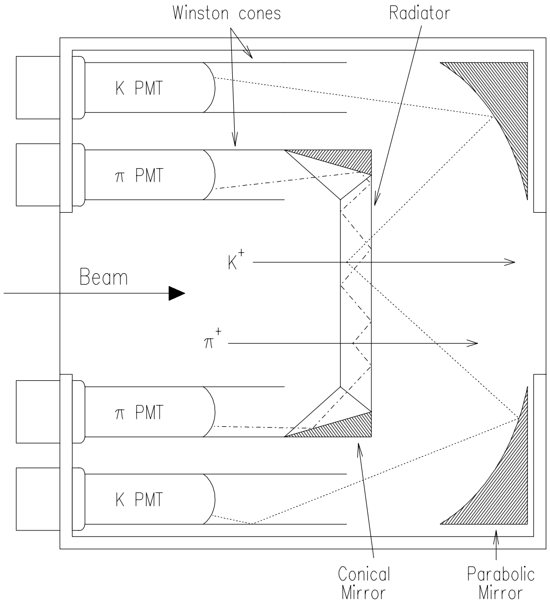

Figure 2.5: Side view of the Čerenkov counter.

and pions is unreflected and reflected at the inner surface of the radiator, respectively. The light from a kaon exits the radiator and is reflected by a parabolic mirror to the outer ring of 14 photomultiplier (PMT) tubes (Kaon Čerenkov Counter), while that from a pion is internally reflected within the radiator and detected in the inner ring of 14 PMTs (Pion Čerenkov Counter). The PMT signals are fed to time-to-digital converters (TDCs) via discriminators as well as to 500 MHz transient digitizers based on gallium-arsenide (GaAs) charge-coupled devices (CCDs) [32]. The pulse-height information in every 2 ns interval is recorded in CCDs to reproduce the time development of the pulses. A charged particle passing through the Čerenkov counter fires a number of PMTs in the Kaon or Pion Čerenkov Counters; PMT hits coincident with each other are called a "cluster". A kaon is identified by requiring that the Kaon Čerenkov Counter has a hit cluster and the Pion Čerenkov Counter has no hit cluster. The average time of the hits in each cluster is compared to the K^+ decay time; any extra particle coincident with the K^+ decay time is rejected, since it is likely that an extra particle, not the initial kaon, may be the origin of the charged track that enters the fiducial region of the detector. Two incoming particles close in time can fire the same PMTs, and a pileup signal may not be found by the TDCs; the pulse shapes recorded in the CCDs can be used to discriminate such pileup signals.

Behind the Čerenkov counter, two beam wire chambers (BWPCs) are located, and allow to monitor the beam profile and to identify multiple incoming particles. Cross-sectional views of the BWPCs are shown in Figure 2.6. The first chamber (BWPC1) consists of 3 planes of sense wires, labeled U, V and X. The direction of the sense wires in the X-plane is vertical and the U- and V-planes are at $\pm 45^{\circ}$ to the vertical plane. The sense wires are made of gold-plated tungsten with 0.012 mm diameter. The BWPC1 has 72, 60 and 60 readout channels for the X-, U- and V-planes, respectively, with a 2.54 mm wire spacing. The spacial resolution is 1.54 mm, and the active area is 178 mm (horizontal) by 50.8 mm (vertical). The cathode foils are 0.025-mm thick aluminized mylar coated

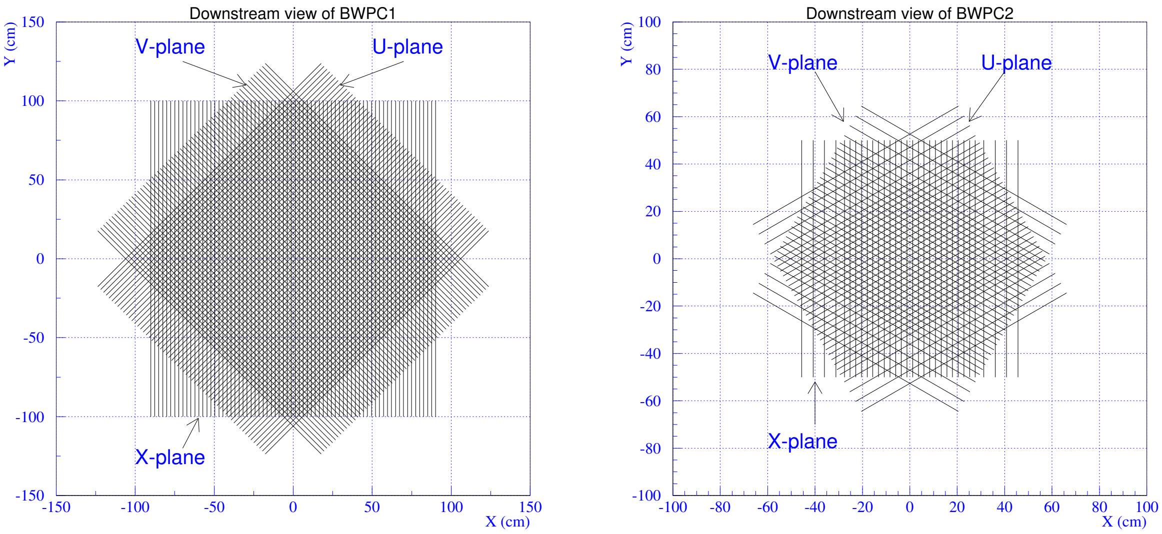

Figure 2.6: Cross-sectional views of the beam wire chambers (BWPCs): the first BWPC (left) and the second BWPC (right).

with carbon. The anode-cathode distance is 3.175 mm, and the total thickness of the BWPC1 is approximately 56 mm. The BWPC1 is filled with a mixture of CF4 (80%) and Isobutane (20%). The second chamber (BWPC2) is located at 90 cm downstream of the BWPC1 and consists of three planes (U, V and X). The direction of the sense wires in the X-plane is vertical, and the U and V sense wires are at $\pm 60^\circ$ to the vertical plane. Each plane has 24 readout channels with a 2.40-mm wire spacing in the central region (57.6 mm) and 8 channels with a 4.80-mm wire-spacing in the peripheral region (19.2 mm on each end). The cathode foils are 0.008-mm single-side aluminized mylar coated with carbon. The anode-cathode distance is 1.5875 mm. The BWPC2 is filled with the same gas as BWPC1.

Downstream of the BWPCs, cylindrical degraders are located for slowing down the kaons so that they come to rest in the target. The degraders have inactive and active parts. The upstream inactive degrader is made of 111.1-mm long beryllium oxide (BeO) and 4.76 mm Lucite. The total thickness is appropriate for stopping kaons with a momentum of 710 MeV/c. BeO, with high density and low atomic number, minimizes multiple scattering. The downstream active degrader (AD) consists of 40 layers of 2 mm thick scintillator disks (in 139 mm diameter) alternating with 2-mm thick copper disks (in 136 mm diameter). The AD is split into 12 azimuthal segments, and the scintillation lights in each segment are sent to a single PMT through 14 wave length shifting (WLS) fibers. The PMT outputs are fed to TDCs and CCDs. The signals from 4 PMTs are multiplexed and fed to a single analog-to-digital converter (ADC). Using this information, the AD has abilities to identify the beam particles and to detect the activities coincident with kaon decays.

After passing through the degraders, just in front of the target, a beam hodoscope (B4 Hodoscope) detects the incoming particle and identifies the particle as a kaon by measuring the energy deposit. An end view of the B4 Hodoscope is shown in Figure 2.7.

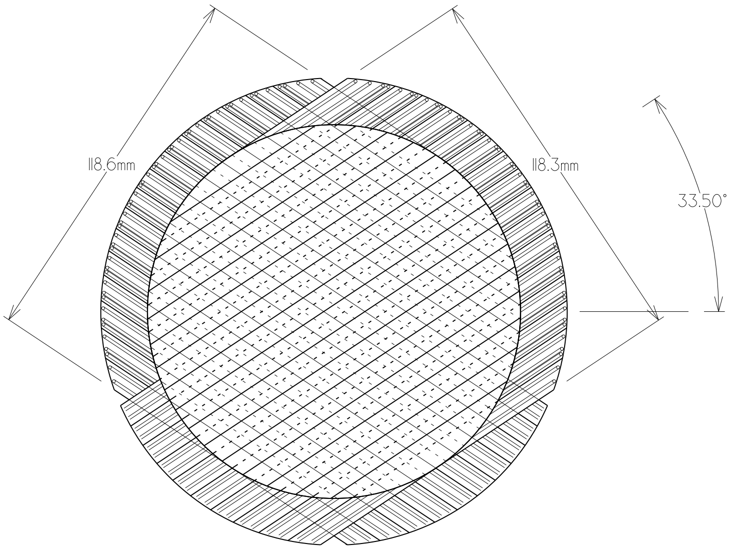

Figure 2.7: End view of the B4 Hodoscope.

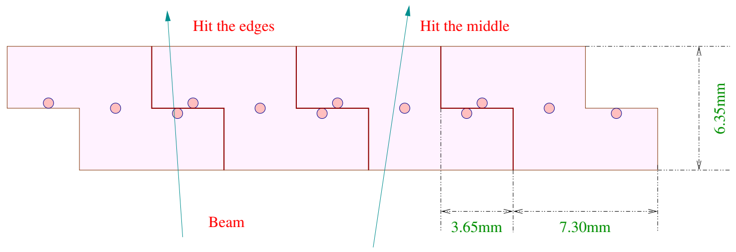

Figure 2.8: Schematic cross section of the B4 Hodoscope.

The B4 Hodoscope consists of two planes (U- and V-plane, 119 mm diameter) to provide position information. Each plane has 12 scintillator fingers. The cross section of the finger has a "Z-shape", as shown in Figure 2.8, which has a 6.35-mm thick middle part and 3.175-mm thick edge parts. This shape makes the B4 Hodoscope to have no inactive region and to improve the spatial resolution. In each finger, 3 WLS fibers are embedded and fed to a single PMT that is read out by TDCs, ADCs and CCDs. A double-pulse fitting is performed to the signals recorded in the CCDs to find a pileup. The time development of the output signals are fitted with single- or double-pulse assumption. If the fitted pulse is more likely to be a double pulse and the time of the second pulse is coincident with the K^+ decay time, the event is rejected.

Kaons with decay-in-flight, nuclear interactions in the degrader materials or scatterings out of beam do not reach the E949 target; 3.9×10^6 kaons enter the E949 target per spill.

2.3.2 Target

Kaons, slowed down by the degraders, enter the scintillating fiber target located in the center of the spectrometer. Kaons lose energy, come to rest, and decay in the target. The target consists of 413 5-mm square and 3.1-m long plastic scintillating fibers that are bundled to form a 12-cm diameter cylinder. A number of smaller fibers (called "edge

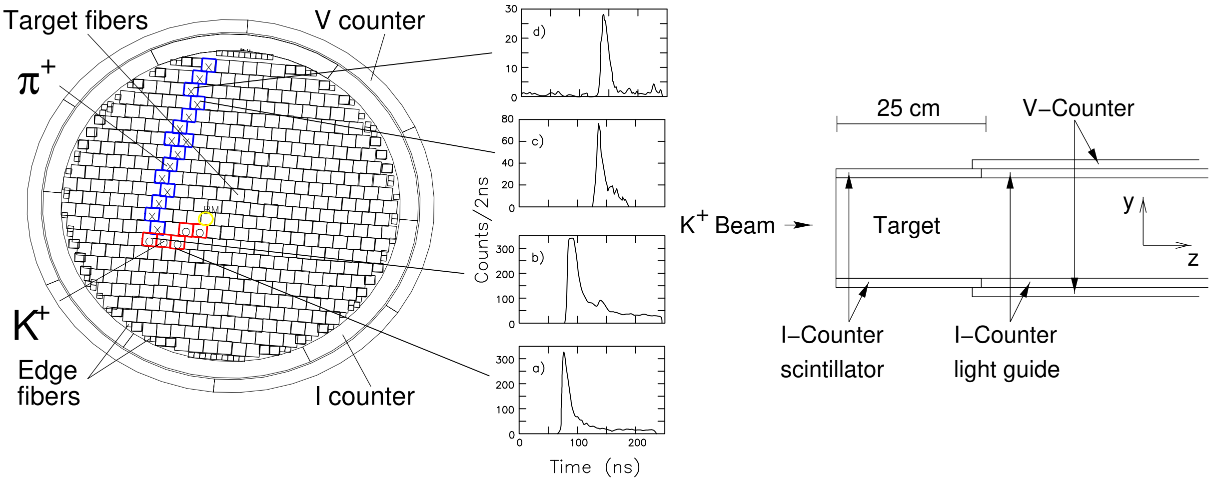

Figure 2.9: End (left) and side (right) views of the target. The CCD pulse-shape information is used to find kaon and pion clusters, as shown in the left figure; the lower two plots, labeled by "a)" and "b)", are CCD pulses for a kaon, and the upper two plots, labeled by "c)" and "d)", are those for a pion. Two layers of 6 plastic scintillators, I-Counter (IC) and V-Counter (VC), surround the target.

fibers") are filled in the gaps near the outer edge of the target. End and side views of the target are shown in Figure 2.9. Each of the 5.0-mm fibers is connected to a PMT, whereas the edge fibers are grouped into 12 and each group of the edge fibers is connected to a single PMT. The PMTs are read out by ADCs, TDCs and CCDs. Kaons, whose velocities are small, typically lose a large amount of energy (few tens MeV) in each fiber, while pions from kaon decays lose about 1 MeV per fiber, since they travel as minimum ionizing particles (MIPs). Pattern recognition is performed to find fibers that belong to a kaon's path or a pion's path. The CCD pulse information is used to find clusters for kaons (kaon fibers) and pions (pion fibers). A double-pulse fitting is performed to find the fiber where a $K^+ \to \pi^+$ decay vertex is located and to estimate the energy loss and range of the pion hidden in the kaon fiber.

The fiducial region of the target is defined by two layers of 6 plastic-scintillating counters that surround the target (see Figure 2.9). The inner scintillators, called I-Counter (IC), tag charged decay products for a trigger before they enter the drift chamber. The IC is 6.4-mm thick at an inner radius of 6.0 cm, and extends 24 cm downstream from the upstream face of the target. Each scintillator is instrumented with a PMT, and is read out by an ADC, a TDC and a 500 MHz transient digitizer based on flash ADC (TD) [33]. The outer scintillators, called the V-Counter (VC), overlap the downstream edge of the IC by 6 mm, and serve to detect particles that decay downstream of the fiducial region of the target. The VC is 5-mm thick and 1.96-m long, and is staggered with respect to the IC. Each scintillator is instrumented with a PMT, which is read out by an ADC and a TDC.

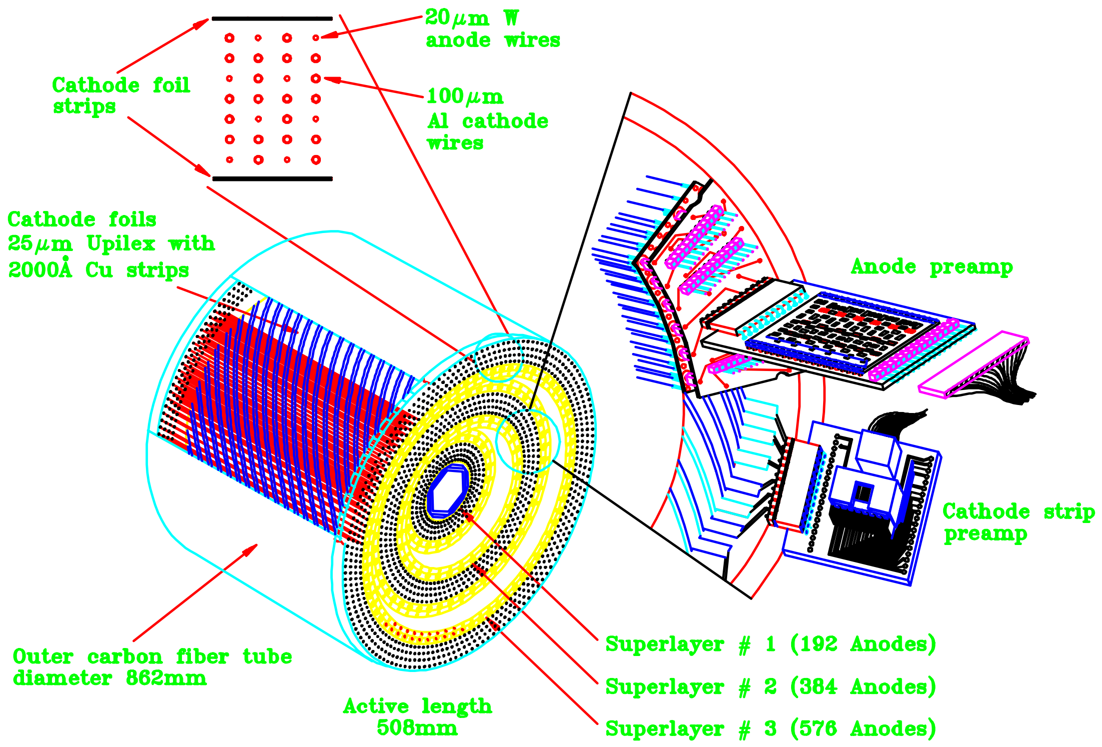

Figure 2.10: Schematic view of the Ultra Thin Chamber.

2.3.3 Drift Chamber

The drift chamber, called "Ultra Thin Chamber" (UTC), is located just outside of the IC. The whole E949 spectrometer is in a 1 Tesla magnetic field. Positively charged particles are bent clockwise in the view from downstream. The primary functions of the UTC are momentum measurements of charged particles and to provide a matching between the tracks in the target and in the Range Stack.

The UTC has a length of 51 cm and inner and outer radii of 7.85 cm and 43.31 cm, respectively. The UTC is composed of 12 layers of drift cells, grouped into 3 superlayers; the inner superlayer has 4 layers of 48 cells, the middle superlayer has 4 layers of 96 cells, and the outer superlayer has 4 layers of 144 cells (shown in Figure 2.10). Each cell is composed of 9 wires stung axially; a single anode wire, made of gold-coated tungsten with 20-μm diameter, is surrounded by 8 cathode wires made of gold-coated aluminum with 100-μm diameter, which are arranged in a "square". Adjacent cells share the cathode wires at the boundaries. The cells in each layer are staggered by one-half cell with respect to the neighboring layers in order to resolve a left-right ambiguity. The superlayers are filled with a mixture of argon (49.6%), ethane (49.6%) and ethanol (0.8%) gases. The cathode wires are grounded, and the anode wires are maintained at 2 kV (gain = 8×10^4, drift velocity = 5 cm/μs). Each anode wire is instrumented with an ADC and a TDC. The drift time to the anode wires provides (x, y) positions for charged tracks.

The inner and outer radii of each superlayer have helical arrays of cathode strips, whose pitch-angle is 45°. The strips, whose width is 7 mm, are made of 1200-Å thick copper coated with 300-Å thick nickel, and mounted on a 25-μm thick Kapton foil. The

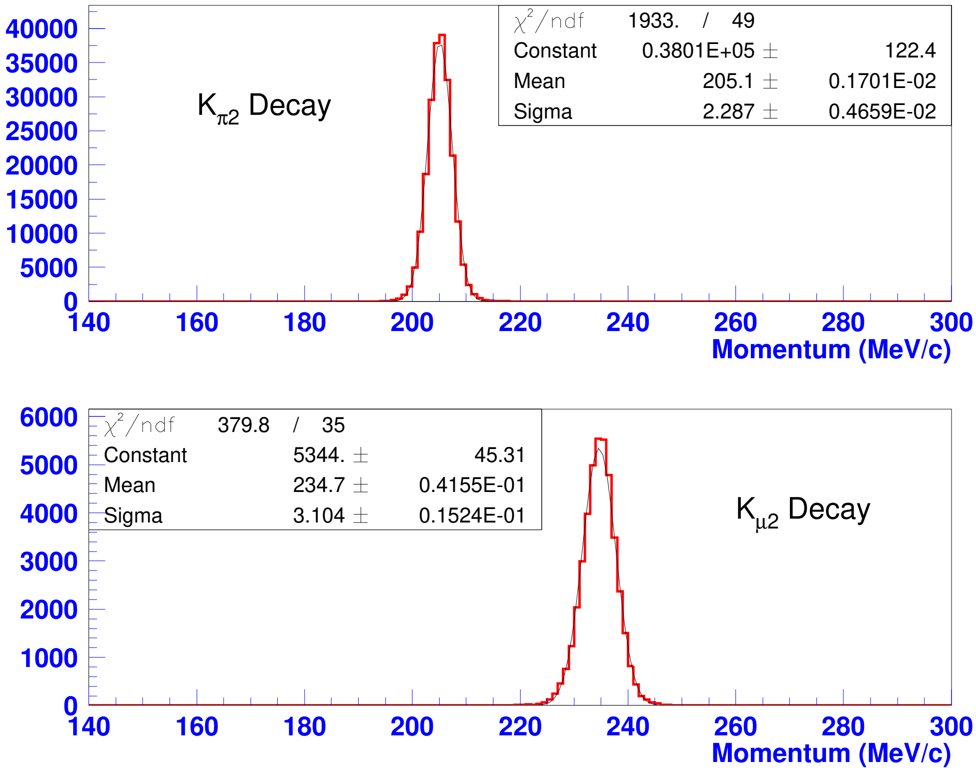

Figure 2.11: Momentum distributions for $K_{\pi2}$ (top) and $K_{\mu2}$ (bottom) decays.

separation between the strips is 1 mm. The cathode foils have 48, 72, 108, 144, 180, and 216 strips from the inner to the outer layers, respectively. The Z position of a charged track is measured from the energy-weighted mean of the cluster of hit strips. The resolution for a z-position measurement is about 1 mm. Each cathode strip is instrumented with an ADC and a TDC.

There are 2 inactive regions filled with nitrogen gas between the 3 superlayers. The differential pressure in the 5 gas volumes supports the cathode foils (excluding the innermost and outermost foils, which are held in place by support tubes). The total mass in the active region of UTC (excluding the inner and outer support tubes and innermost and outermost foils) amounts to 2×10^{-3} radiation lengths. The momentum resolutions ($\Delta P/P$) for the two body decays $K_{\pi2}$ and $K_{\mu2}$ are 1.1% and 1.3%, respectively, as shown in Figure 2.11. More information on the UTC is given in [34].

2.3.4 Range Stack

The primary functions of the Range Stack (RS) are energy and range measurements of charged particles and their identification. The RS is located just outside the UTC at an inner radius of 45.08 cm and an outer radius of 84.67 cm. It consists of 19 layers of plastic scintillators, azimuthally segmented into 24 sectors (see Figure 2.12). Conventionally, the 24 sectors are grouped into 6 (sectors 1-4, 5-8, 9-12, 13-16, 17-20, 21-24); a group of 4 sectors is called a "hextant". The scintillators of layers 2-18 have a thickness of 1.905 cm and a length of 182 cm. The scintillators of layer 19 have a thickness of 1 cm; this

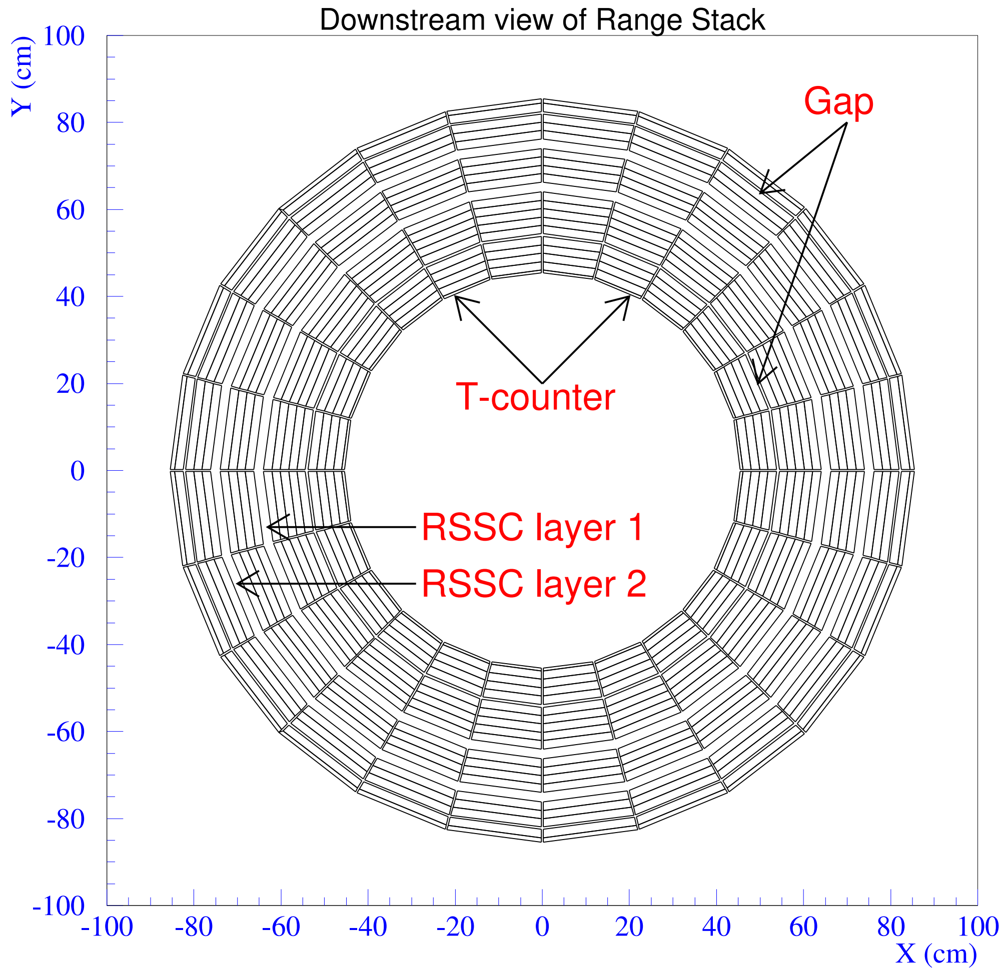

Figure 2.12: End view of the Range Stack. Two layers of the Range Stack Straw Chambers are located after layers 10 and 14.

layer is mainly used to veto charged particles with long range by requiring that they do not reach the layer-19 scintillators. The scintillation light in the layer 2-19 counters is led by light guides to PMTs at both the upstream and downstream ends. The innermost counters, called T-Counters, have a thickness of 6.35 mm and a length of 52 cm. 17 WLS fibers are embedded in each scintillator for read out, and are grouped and fed to a single PMT at each end. The T-Counter signals are used to produce a trigger signal and to define the fiducial region as 2π sr solid angle, which is almost the same as the solid-angle acceptance of UTC. Each PMT of the RS scintillators is read out by an ADC and a TDC. Signals from 4 PMTs at the same end, same hextant and same layer are mixed together and read out by a single Transient Digitizer based on flash ADC (TD). The signals are demultiplexed in offline event reconstruction by using TDC information in order to determine from which counter the signal comes. The ADCs record charges in 100 ns, and the TDCs record the timings of hits in the range of 10 μs. The TDs record pulse-heights of PMT signals in 2 ns intervals (500 MHz sampling) up to 2 μs to provide information on the time development of the pulses. This 500 MHz sampling provides detailed information about the pulse shapes, which enables the separation of two pulses close in time [3] by performing an offline pulse fitting (explained later). The gate width of the TDs is narrower than that of the TDCs in order to reduce the data size. The time of a hit in the RS counters is obtained from the average of the upstream and downstream TDC times, and the z position of the hit is obtained from the time difference. In the case that TDC hit information is missed due to some reasons, the hit information is complemented with corresponding TD information if available.

The π^+'s from the $K^+ \to \pi^+\nu\bar{\nu}$ decay, whose momentum is up to 227 MeV/c, should come to rest in the RS. Pions with 227 MeV/c can propagate into plastic scintillators by roughly 40 cm. The total radial thickness of the RS and target is 45 cm. Almost all of the π^+'s, bent in a 1 Tesla magnetic field, therefore lose their entire kinetic energy and come to rest in the Range Stack. On the other hand, the momenta of μ^+'s from kaon decays at rest are at most 236 MeV/c. Muons with 236 MeV/c (such as μ^+'s from $K_{\mu 2}$ decays) can propagate into plastic scintillators by 54.3 cm. Hence, $K_{\mu 2}$ decays are largely suppressed by requiring that charged tracks come to rest in the RS. However, the μ^+'s from $K^+ \to \mu^+\nu_\mu\gamma$ and $K^+ \to \mu^+\pi^0\nu_\mu$ decays could come to rest in the RS. Besides, a π^+ can decay in flight and the secondary μ^+ may come to rest in the RS. The identification of π^+ in the RS is performed by observing the $\pi^+ \to \mu^+ \to e^+$ decay sequence in the TDs and TDCs of the counter where the π^+ comes to rest (called the stopping counter). Typical TD pulses in and around the stopping counter for a pion track are shown in Figure 2.13. The μ^+ from the $\pi^+ \to \mu^+\nu_\mu$ decay at rest has the kinetic energy of 4 MeV (equivalent range in plastic scintillator is 1 mm) and rarely goes out of the stopping counter. On the contrary, the e^+ from the $\mu^+ \to e^+\nu_e\bar{\nu_\mu}$ decay at rest has a kinetic energy of up to 52 MeV, and the e^+ track loses kinetic energy not only in the stopping counter, but also in the neighboring counters. The $\pi^+ \to \mu^+$ decay at rest, whose lifetime is 26 ns, is detected by using TD information of the stopping counter by performing a double-pulse fitting, while the sequential $\mu^+ \to e^+$ decay, whose lifetime is 2.2 μs, is detected by using TDC information of the stopping counter as well as the neighboring counters by requiring

[3] Separation of two pulses as close as 5 ns is achieved by the TD pulse shape information and double-pulse fitting algorithm.

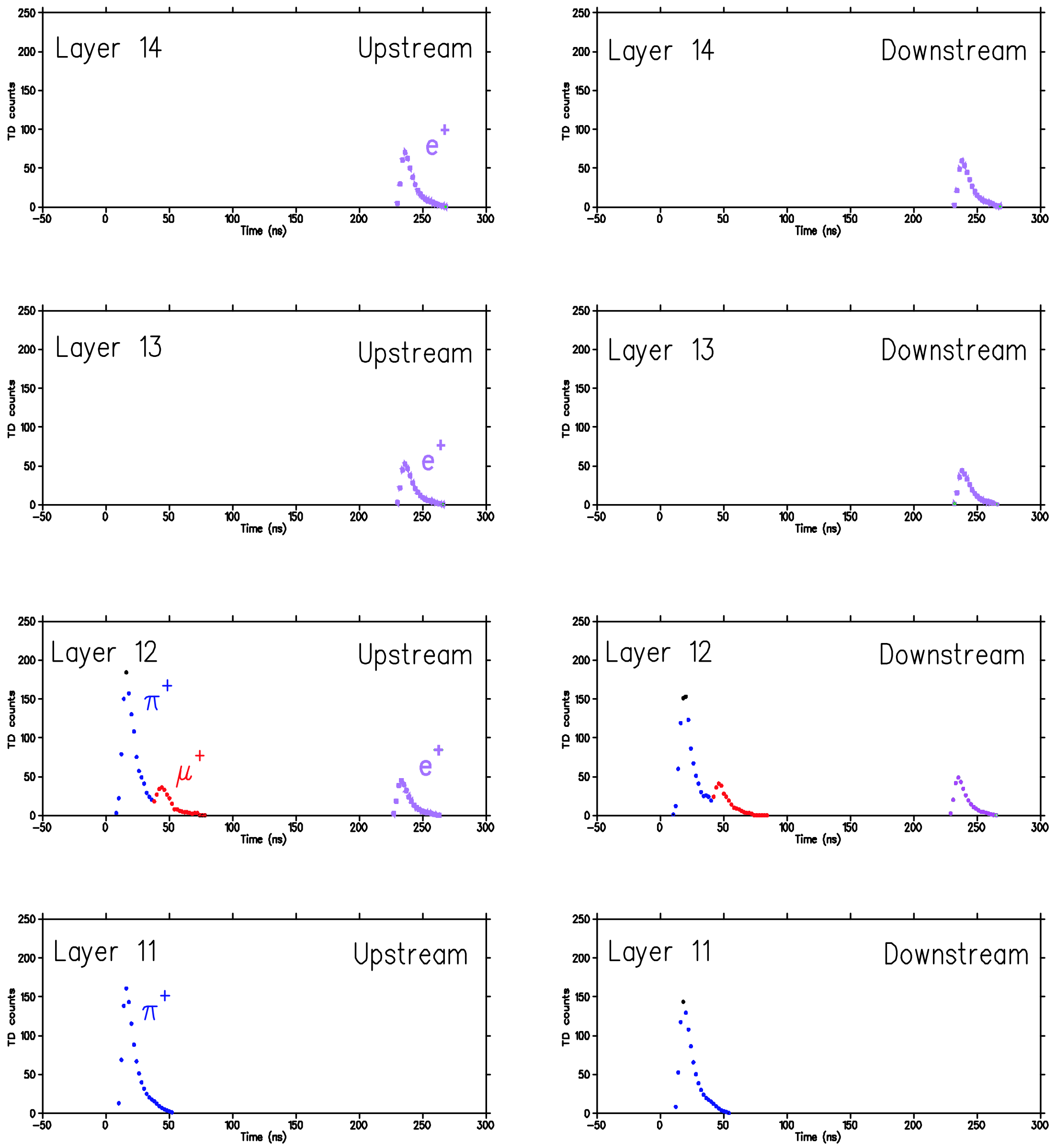

Figure 2.13: Pulses in and around the stopping counter recorded by the TDs of the upstream and downstream ends. The $\pi^+ \to \mu^+ \to e^+$ decay sequence is found in the stopping counter (Layer 12 in this figure). The μ^+ from the $\pi^+ \to \mu^+\nu_\mu$ decay is contained in the stopping counter. The positron from the $\mu^+ \to e^+\nu_e\bar{\nu_\mu}$ decay should also be found in the counters around the stopping counter (Layers 13 and 14 in this figure).

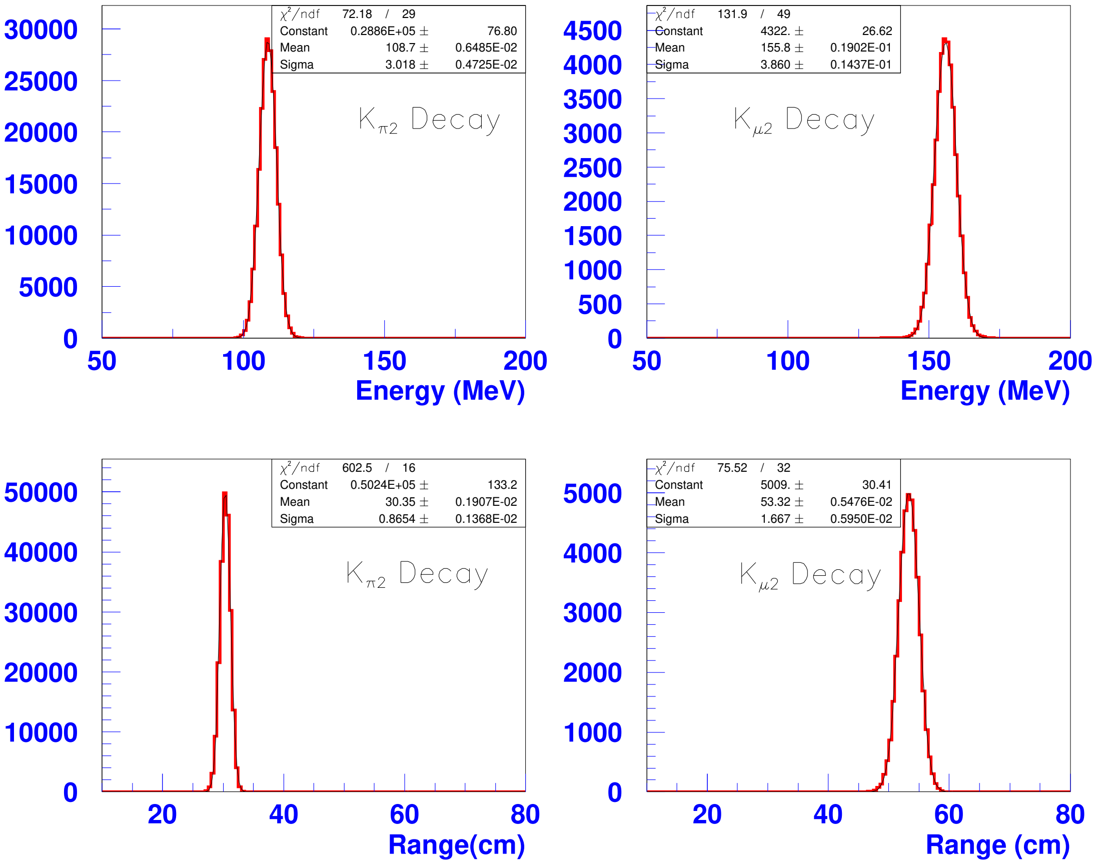

Figure 2.14: Energy (top) and range (bottom) distributions of fully contained $K_{\pi2}$ (left) and $K_{\mu2}$ (right) decays.

that the times of the hits from the e^+ track are consistent with each other.

Range Stack Straw Chambers (RSSCs) are located after layers 10 and 14 in the RS. The inner RSSC consists of two layers of 24 straws per sector, and the outer RSSC consists of two layers of 28 straws per sector. The RSSCs are used to determine the trajectory and the range of a charged particle in the RS. Information on the RSSC is given in [35].

Energy and range measurements of charged tracks, as well as momentum measurement, are crucial to distinguish the π^+'s in the signal region from backgrounds due to $K_{\pi2}$ and $K_{\mu2}$ decays, which have monochromatic momenta of 205 and 236 MeV/c, respectively. Energy resolutions of 2.8% and 2.5% and range resolutions of 2.9% and 3.1% are achieved for fully contained $K_{\pi2}$ and $K_{\mu2}$ decays, respectively (see Figure 2.14).

2.3.5 Photon Detectors

The detection of any activities coincident with the charged track is crucial for suppressing the backgrounds for $K^+ \to \pi^+\nu\bar{\nu}$. Photons from $K_{\pi2}$ and other radiative decays are detected by hermetic photon detectors, which are shown in Figure 2.15. The photon detectors, surrounding the K^+ decay vertex in a 4π solid angle, are located in the barrel, upstream and downstream end caps, and near the beam line. Photon veto is performed

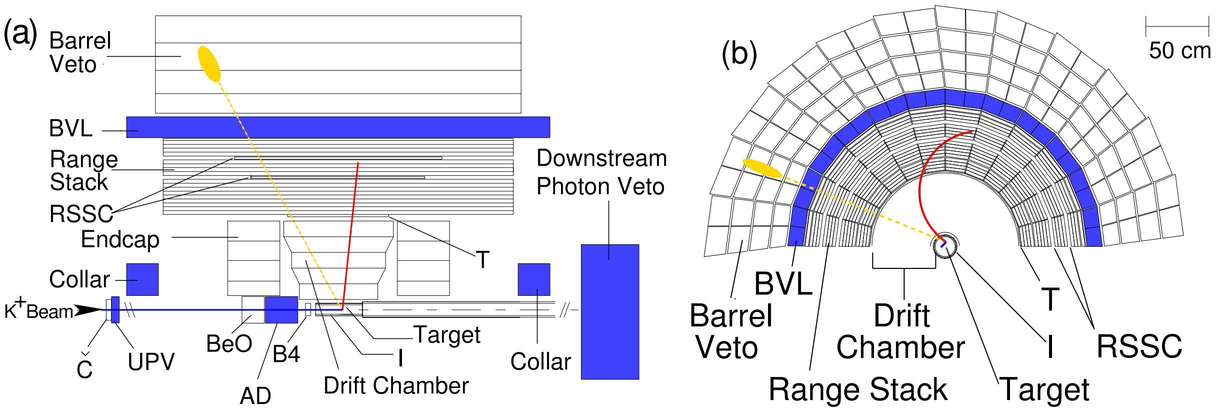

Figure 2.15: Schematic side (left) and end (right) views of the upper half of the E949 detector. Newly installed or upgraded photon detectors for E949 are shaded in this figure.

by the Barrel Veto (BV), the Barrel Veto Liner (BVL), the upstream and downstream End Caps (ECs), the upstream and downstream Collar detectors (CO), the downstream Microcollar detector (MC), as well as the target and Range Stack.

The Barrel Veto, 1.9-m long, is located in the outermost barrel region with an inner radius of 94.5 cm and an outer radius of 145.3 cm. It surrounds two thirds of the 4π sr solid angle. The BV consists of 48 azimuthal sectors; each sector consists of four radial segments. The radial modules consist of 16, 18, 20, 21 layers of 1-mm thick lead and 5-mm thick plastic scintillator from inner to outer modules, respectively. The azimuthal boundaries of each sector are tilted so that photons from the decay vertex should not travel along the inactive inter-sector gaps without losing their energy in the active regions. The BV has the 14.3 radiation lengths in total. Each end of each module is read out by a PMT and the signals are recorded by an ADC and a TDC. The time resolutions of individual BV counters are found to be 1.0 ns. The resolution is limited by the sampling time of the TDCs. The fraction of the photon energy left in scintillators is about 30%.

The Barrel Veto Liner, which is newly installed for the E949, is located just outside the Range Stack and inside the Barrel Veto. The BVL, with the inner radius of 85.2 cm and the outer radius of 93.5 cm, consists of 48 azimuthal sectors; each sector consists of 12 layers of 1-mm thick lead and 5-mm thick plastic scintillators. The BVL has 2.3 radiation lengths in total. The length of the BVL (2.2 m) is larger than that of the BV, so that the BVL adds active material to the region where the radiation length is relatively small. Each end of each module is read out by a PMT and the signals are recorded by an ADC and a TDC. Groups of adjacent sectors in each end are read by the TDs. The time resolutions of the individual BVL counters are found to be 0.5 ns. Their resolution is also limited by the TDC sampling time [4]. The fraction of the photon energy, seen by scintillator, is about 30%.

The End Cap photon detector [36] is located in the 1 Tesla magnetic field and covers

[4]The BVL's TDCs have shorter sampling times.

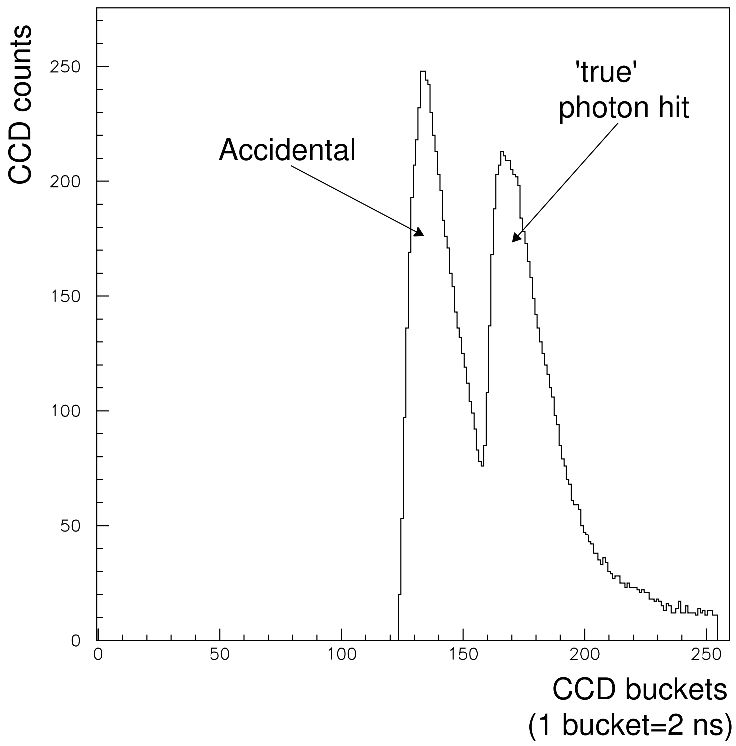

Figure 2.16: Pulses recorded in the End Cap CCD. The first pulse is due to an early accidental hit and the second pulse is due to the photon from $K_{\pi 2}$ decays.

roughly one-third of the 4π sr photon coverage. The End Cap is exposed in a high counting-rate environment near the beam line; beam particles cause many hits that are not coincident with kaon decays. These hits from beam particles may mask photons from $K_{\pi 2}$ decays in the case that an accidental hit arises earlier than the photon hit (see Figure 2.16). The upstream End Cap detector consists of 75 undoped Cesium Iodide (CsI) crystals segmented to the four rings (13, 14, 21 and 27 crystals from the inner to outer rings, respectively), and the downstream End Cap detector consists of 68 crystals in the four rings (11, 13, 19 and 25 from inner to outer rings, respectively). A total of 143 crystals with a pentagonal cross-section are used (Figure 2.17). Each crystal has a length of 25 cm (13.5 radiation lengths) and the whole End Cap detector is designed to minimize photon escape through its radial cracks. Fine-mesh PMTs [37], which maintain high gains in strong magnetic fields, are attached directly to the crystals to achieve efficient light collection (Figure 2.17). Only the fast component of the CsI light output with a decay time of a few tens of nanosecond at a wavelength of 305 mm is selected by ultraviolet (UV) transmitting optical filters. The PMT signals are read out by ADCs, TDCs, and CCDs. The pulses recorded in the CCDs are used to separate two pulses close in time by using a pulse-finding algorithm, which can reduce accidental vetoes and photon inefficiencies.

There are other photon detectors. The Collar, Microcollar, Upstream Photon Veto (UPV), Downstream Photon Veto (DPV), and Ring Veto (RV) are located around the beam line and cover the region with small angles around the beam line. They can detect photons that are emitted toward the beam line and which can not be detected by the BV,

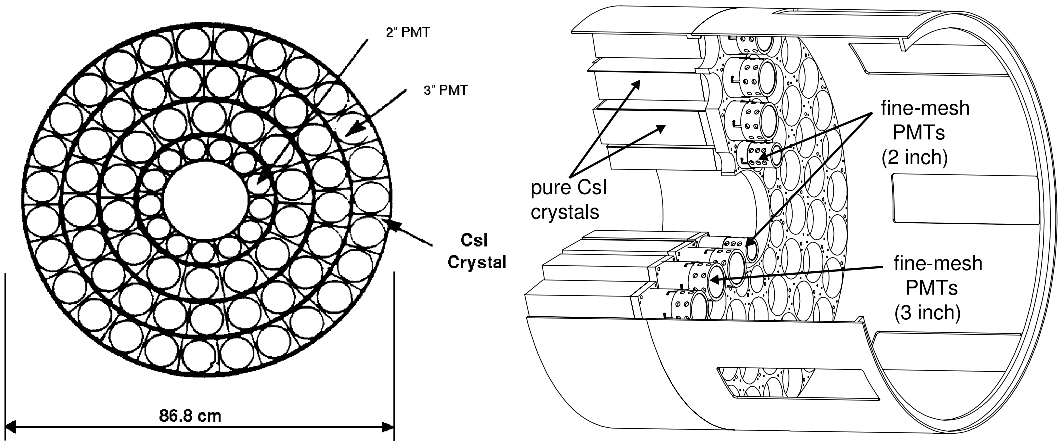

Figure 2.17: End view (left) and back view (right) of the End Cap.

BVL, EC and RS.

2.4 The Trigger

3.9×10^6 kaons enter the E949 target for a 2.2-second long spill once every 5.4 seconds. The information on an incoming kaon and a secondary charged track (and photons) is recorded by ADCs, TDCs, CCDs and TDs of various detector subsystems. The trigger selects signal-like events out of all kaon decays. Digitized information of the selected events, which correspond to 70-80 Kbyte of data per event, is transfered from the electronics hut to the main computer for data taking.

The trigger is composed of a fast level-0 trigger and level-1.1 and -1.2 triggers. The level-0 trigger makes decisions entirely with logic pulses from detectors. The level-0 trigger has a rejection of 10^3 and introduces 38 ns of dead time for every coincident hit in the first two layers of the Range Stack (T•2). The level-1.1 and -1.2 triggers involve partial processing of ADC and TD data, and operate on the lower rate events that pass the level-0 trigger. The level-1.1 trigger has a rejection of 12 after level-0, and introduces 10 to 20 μs of dead time per level-0 trigger. The level-1.2 trigger has a rejection of 2 after level-1.1 and introduces a dead time of up to 100 μs per level-1.1 trigger. The entire trigger for $K^+ \to \pi^+\nu\bar{\nu}$ therefore has a rejection of 24000, and reduces the 2.6×10^6 kaon decays to 100 events per spill.

The trigger for $K^+ \to \pi^+\nu\bar{\nu}$ (referred to as $\pi\nu\bar{\nu}(1)$ trigger) consists of the following requirements:

$$\begin{aligned}\pi\nu\bar{\nu}(1) \quad \equiv \quad & \mathrm{KB}\cdot\mathrm{DC}\cdot\mathrm{T}\bullet 2\cdot\mathrm{IC}\cdot\overline{\mathrm{L0\_zfrf}}\cdot(6_{ct}+7_{ct})\cdot\overline{19_{ct}}\cdot\mathrm{L0\_rr1(1)}\cdot \\ & \overline{\mathrm{BV}+\mathrm{BVL}+\mathrm{EC}}\cdot\mathrm{HEX}\cdot\mathrm{L1.1}\cdot\mathrm{L1.2}, \qquad (2.1)\end{aligned}$$

where

- K^+ Stop Requirements:

- KB : KB requires a coincident hit in the Kaon Čerenkov Counter, the B4 Hodoscope, and the target. This requirement ensures that a kaon enters the target.
- DC : Online delayed coincidence, in which the times in the Kaon Čerenkov Counter and the I-Counter are examined. The IC time is required to be at least 2 ns later than the time in the Kaon Čerenkov Counter. This delayed coincidence requirement ensures that a kaon decays at rest.

- Fiducial Requirements on Charged Tracks:
  - T•2 : A coincidence hit is required in the first two layers (T-Counter and layer 2) of the Range Stack in the same sector. This condition requires that a charged track from a kaon decay enters the Range Stack.
  - IC : At least one hit in the I-Counter is required to be coincident with the T•2 time. This condition requires that a charged track from a kaon decay enters the fiducial region of the detector.
  - $\overline{\text{L0\_zfrf}}$: A charged track is required to stop in the active region of the Range Stack scintillators. Events are rejected if the charged track comes to rest in the support materials for the second RSSC. In such a case, μ^+'s from $K_{\mu 2}$ decays can fake that they come to rest in the Range Stack layer 14.

- Range Requirements on Charged Tracks:
  - $(6_{ct}+7_{ct})$: A charged track must reach the Range Stack layer 6 or 7. The T•2 sector and two sectors clockwise from the T•2 sector are defined as the charged track (ct) sectors. This condition removes short-range tracks (e.g., $K^+ \to \pi^+\pi^0\pi^0$).
  - $\overline{(19_{ct})}$: A charged track is not allowed to reach the Range Stack layer 19. This condition removes μ^+ tracks from $K_{\mu 2}$ decays.
  - L0_rr(1) : Refined range requirement on a charged track. μ^+'s from $K_{\mu 2}$ decays are suppressed by the $\overline{(19_{ct})}$ requirement. However, some of the μ^+'s can still survive the requirement if their polar angle (compared to beam direction) is small and they stop near the edge of the RS scintillators. Events are rejected if the range calculated in the online trigger is too long. The online range in the target is obtained from the number of hit fibers, and the online range in the Range Stack is obtained from the polar angle and the stopping layer of the charged track. The polar angle is measured by the z positions at RS layers 11, 12 and 13, which are obtained from the end-to-end time difference of both-end hits. The online stopping counter is found by the "stopping counter finder" (SCF), which defines the outermost and most clockwise ct counter as the stopping counter.

- Online Photon Veto:
  - $\overline{\text{BV} + \text{BVL} + \text{EC}}$: Online photon veto in the BV, BVL and EC. Any photon hit which is coincident with T•2 and whose energy is above a threshold is

not allowed. Each PMT signal from each end of the BV and BVL counters is discriminated by the threshold corresponding to 5 MeV, and the mean time of the discriminated signals from both ends is given by digital mean-timers [30]. Events are rejected if the output signals of the mean timers are coincident with T•2. Each PMT signal from each End Cap crystal is discriminated by the threshold corresponding to 20 MeV. Events are rejected if the output signals are coincident with T•2.

  - HEX : 24 sectors of the Range Stack are conventionally grouped into 6; a group of 4 sectors is called a "hextant". Only one hextant is allowed to have hits coincident with T•2, or two hextants if they are adjacent. This rejects events with multiple tracks and events with photon activities in the RS.

- Level-1.1 (online $\pi^+ \to \mu^+$ decay requirement):

  - L1.1 : Level-1.1 trigger requires a signature of $\pi^+ \to \mu^+$ decay in the online stopping counter. The pulse height (PH) and the area (PA) of the pulse(s) recorded by the TDs in the stopping counter are compared. The decision is made by a control board with Application Specific Integrated Circuits (ASICs) in each TD board. The ratio of the pulse height to the pulse area, PH/PA, would be smaller for double pulses than for a single pulse. Events are rejected if the PH/PA ratio is large.

- Level-1.2 (requirements for stopping counter finding):

  - L1.2 : Level-1.2 trigger consists of three parts: (1) Events are rejected if coincident hits are detected in a RS counter near the stopping counter. It rejects $K_{\mu 2}$ events that pass Level-1.1 since accidental hits from the outside provide the double-pulse $\pi^+ \to \mu^+$ decay signature in the stopping counter. (2) Events are rejected if one of two adjacent hextant hits is not due to a charged track. This requirement removes those events that pass the HEX requirement because of accidental hits. (3) Events are rejected if the SCF assignments are screwed up (e.g., stopping layer is more than 19, etc).

The $\pi\nu\bar{\nu}(1)$ trigger is for the $K^+ \to \pi^+\nu\bar{\nu}$ decay in the momentum region above the $K_{\pi 2}$ peak. The trigger for the region below the $K_{\pi 2}$ peak is called $\pi\nu\bar{\nu}(2)$; this region is not used in this analysis.

In addition to the $K^+ \to \pi^+\nu\bar{\nu}$ trigger, various "monitor" triggers also collected events for use in data quality assessments, calibrations of detector subsystems, and acceptance and background calculations.

- $K_{\pi 2}(1)$= $\mathrm{KB} \cdot \mathrm{T} \bullet 2 \cdot (6_{ct} + 7_{ct}) \cdot \overline{(19_{ct})}$,
- $K_{\pi 2}(2)$= $\mathrm{KB} \cdot \mathrm{DC} \cdot \mathrm{T} \bullet 2 \cdot \mathrm{IC} \cdot (6_{ct} + 7_{ct}) \cdot \overline{(19_{ct})} \cdot \mathrm{HEX} \cdot \mathrm{L1.1} \cdot \mathrm{L1.2}$,
- $K_{\mu 2}(1)$= $\mathrm{KB} \cdot \mathrm{T} \bullet 2 \cdot (6_{ct} + 7_{ct}) \cdot (17_{ct} + 18_{ct} + 19_{ct})$,
- $\pi_{scatter} = \pi_B \cdot \overline{\mathrm{DC}} \cdot \mathrm{T} \bullet 2 \cdot \mathrm{IC} \cdot (6_{ct} + 7_{ct}) \cdot \overline{\mathrm{BV} + \mathrm{BVL} + \mathrm{EC}} \cdot \mathrm{HEX}$,

where π_B requires that a pion enters the target. Because each monitor trigger is highly prescaled, the number of whole monitor triggers in each spill should be at most 10.

2.5 Monte Carlo Simulation

The detector and the physics processes in it are modeled by a Monte Carlo (MC) simulation program. The MC includes all of the detector elements, except for the beam instrumentation upstream of the target. It generates data, except for the TD and CCD pulse-shape information. The simulation of kaon decays in the E949 detector starts from a "beam file" with the x, y, z positions of kaon decays in the target obtained from an analysis of $K_{\mu 2}$ decays.

Multiple Coulomb scatterings of charged particles with various nuclei in the detector are calculated according to the theory of Moliere [38], with corrections for the spin of the scattered particle and the form factor of the nucleus [39]. Hadronic interactions of positively charged pions in the plastic scintillators are calculated using a combination of data and phenomenological models [40]. Photon and electron interactions are calculated using the EGS4 electromagnetic-shower simulation package [41].

The accuracy and the performance of the MC is verified by comparing the different kinematic variables from data and MC for $K_{\pi 2}$ and $K_{\mu 2}$ decays.

2.6 Summary of 2002 Data Taking

The E949 experiment had the first physics run for 12 weeks from March to June in 2002. The data collected in the run period corresponded to 1.77×10^{12} kaon decays in the target. Figure 2.18 shows the number of accumulated kaon decays as a function of the data-taking days for the various running years of E787 and E949. The E949 run was performed under a high beam-intensity environment. The proton intensity of the AGS increased twice as high as in E787. A comparison of the running conditions for E787 and E949 is tabulated in Table 2.1. A comparison of the total number of kaon decays in the target for E787 and E949 is tabulated in Table 2.2; the total exposure of kaons available for E949 was 30% of E787.

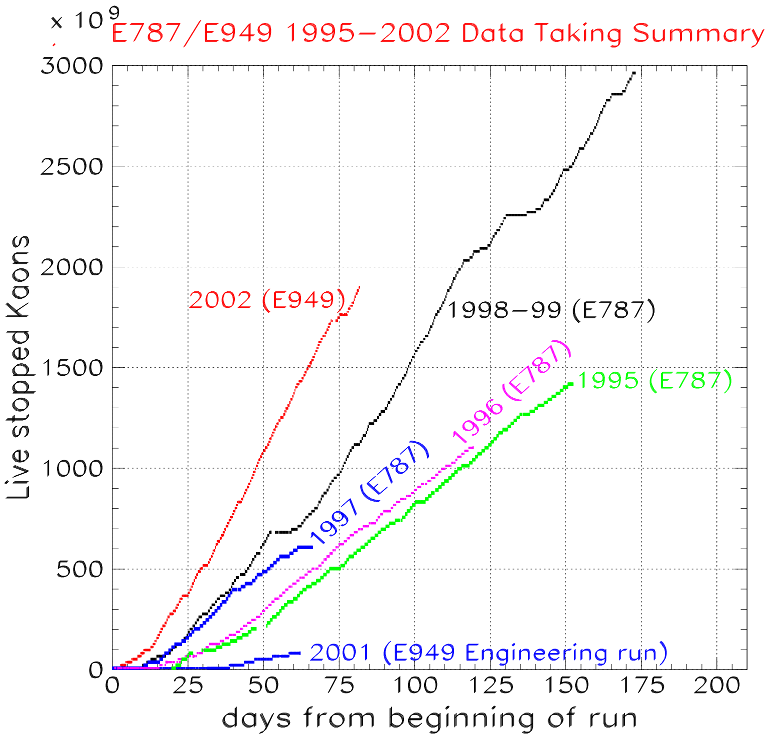

Figure 2.18: Number of kaon decays in the target as a function of the data-taking days for E787 and E949.

	E787 1998	E949 2002
AGS momentum (GeV/c)	24	21.5
AGS intensity (10^{12} protons(Tp)/spill)	25-40	65
Spill length (sec)	2.2	2.2
Beam cycle (sec)	4.2	5.4
Duty factor (%)	52	41
K^+ exposure to the target (10^6/spill)	2.1	3.9

Table 2.1: Running conditions for E787 in 1998 and E949 in 2002.

	E787	E949
Total number of kaon decays in the target	5.94×10^{12}	1.77×10^{12}

Table 2.2: Total number of kaon decays in the target for E787 and E949.

Chapter 3

Analysis

In this chapter, issues concerning offline analysis, particularly the characteristics of the backgrounds that pass the online trigger conditions, the signal selection criteria (cuts) used to suppress them, and the methods used to perform the offline analysis, are described.

3.1 Background Overview

The branching ratio of the $K^+ \to \pi^+\nu\bar{\nu}$ decay is expected to be 10^{-10}. Considering the acceptance factors of the analysis, more than 10^{12} kaons have to decay in the apparatus so that one candidate event can be observed. The backgrounds should be suppressed to be less than one event in order to have confidence that the candidate event really comes from the $K^+ \to \pi^+\nu\bar{\nu}$ decay. Although the trigger suppresses the backgrounds, the data accumulated by the trigger still contain many background events. It is therefore important to investigate the backgrounds that pass the trigger and to understand their characteristics.

Figure 3.1 shows the range in a plastic scintillator (in cm) versus the momentum (in MeV/c) of charged particles for the events that pass the $K_{\pi2}(1)$ trigger. In this figure, there are various sources of background. Events in the $K_{\pi2}$ peak are due to π^+ tracks from $K^+ \to \pi^+\pi^0$ decays with a momentum of 205 MeV/c, an energy of 108 MeV and a range of 30 cm. Events in the $K_{\mu2}$ peak are due to μ^+ tracks from $K^+ \to \mu^+\nu_\mu$ decays with a momentum of 236 MeV/c, an energy of 153 MeV and a range of 55 cm. Both events in the $K_{\pi2}$ range tail and events in the $K_{\mu2}$ range tail ($K_{\mu2}$ Range Tail events) have ranges (and energy) smaller than that expected from these decays, due to elastic (inelastic) scattering in the Range Stack. Events in the muon band (Muon Band events) are due to multi-body decays, such as $K^+ \to \mu^+\nu_\mu\gamma$ (radiative $K_{\mu2}$, or $K_{\mu\nu\gamma}$) and $K^+ \to \mu^+\pi^0\nu_\mu$ ($K_{\mu3}$), π^+ decay in flight in the target, and $K_{\mu2}$ decay with inelastic scattering in the target, such that the range, energy and momentum are all smaller than the $K_{\mu2}$ peak values. The momentum end points of the $K_{\mu\nu\gamma}$ and $K_{\mu3}$ decays are 236 MeV/c and 215 MeV/c, respectively. Events in the pion band are due to pions in the beam that scatter into the Range Stack.

The backgrounds can be categorized into two types: backgrounds that arise from K^+ decays and those from beam particles. The K^+-originated backgrounds can be further categorized into two types based on the particle type: π^+-related and μ^+-related back-

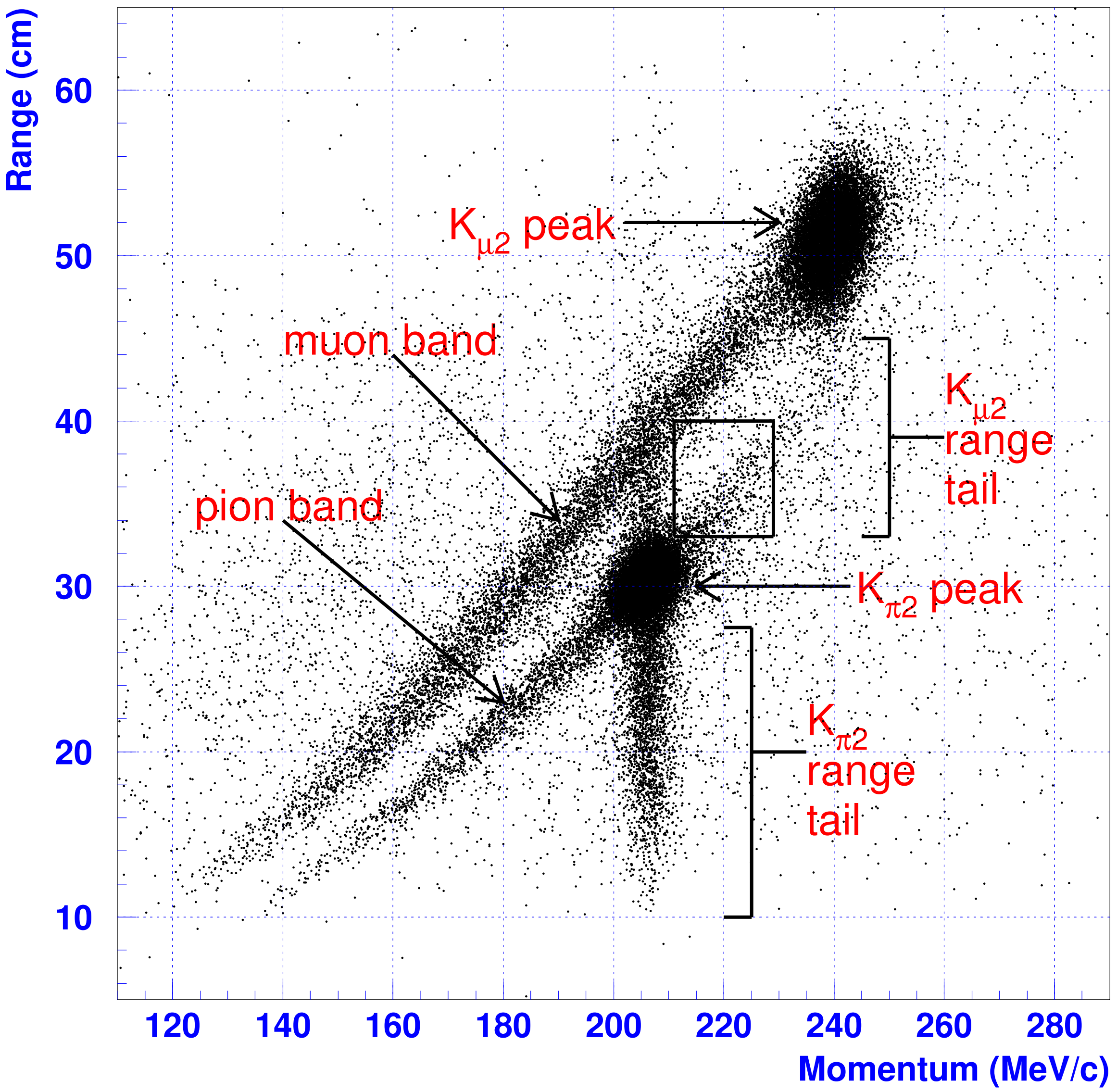

Figure 3.1: Range in a plastic scintillator (in cm, y-axis) and the momentum (in MeV/c, x-axis) of the charged particles for events that pass the $K_{\pi2}(1)$ trigger. The rectangle just above the $K_{\pi2}$ peak shows the signal region for $K^+ \to \pi^+\nu\bar{\nu}$ ($\pi\nu\bar{\nu}(1)$ region).

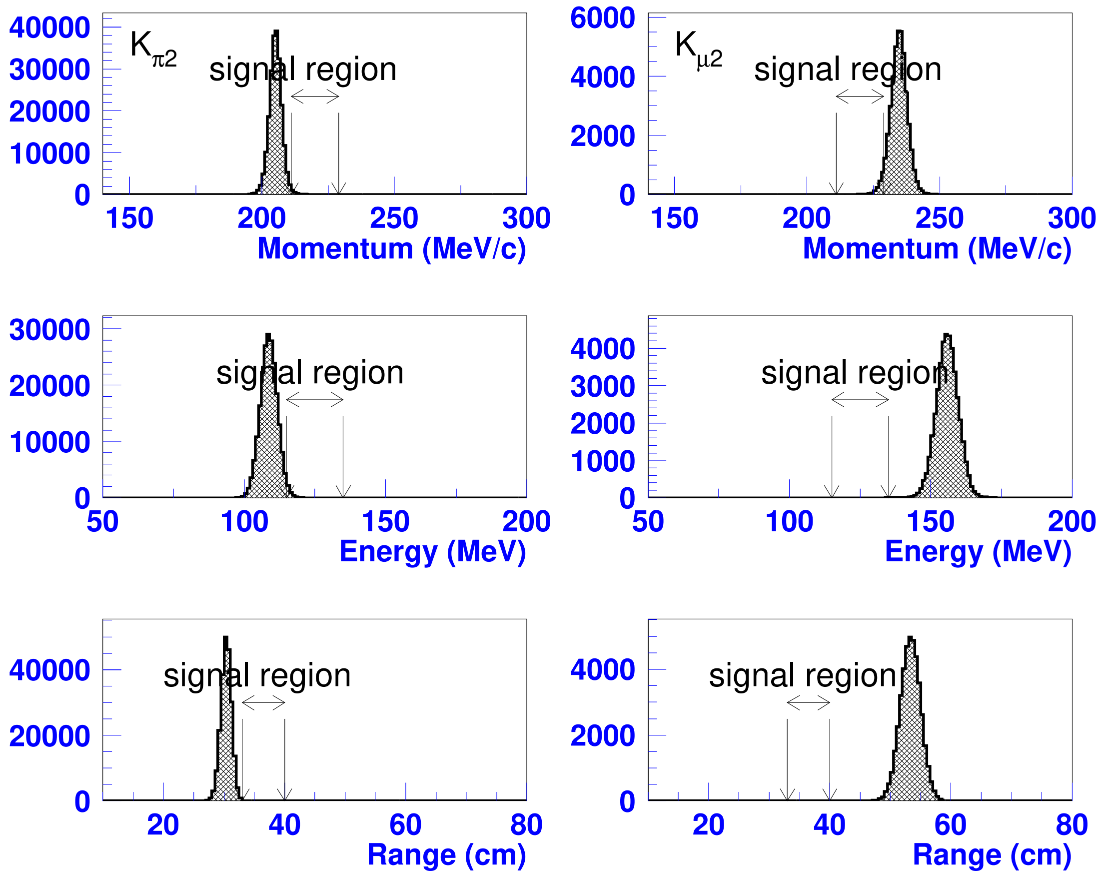

Figure 3.2: Momentum (top), energy (middle) and range (bottom) distributions for the $K_{\pi 2}$ (left column) and $K_{\mu 2}$ (right column) decays. The arrows indicate the boundaries of the signal region.

grounds. As shown in Figure 2.1, the K^+-originated backgrounds from the multi-body decays are suppressed by choosing a momentum region higher than the $K_{\pi 2}$ peak for the signal region. They can also be suppressed by not allowing photon activities, since some of them include π^0's in their decay. The remaining and most contributing backgrounds from K^+ decays are therefore $K_{\pi 2}$ and $K_{\mu 2}$. The momentum, energy and range distributions for the $K_{\pi 2}$ and $K_{\mu 2}$ are shown in Figure 3.2. $K_{\mu\nu\gamma}$ can also be one of main backgrounds because the momentum of the decay could be in the signal region.

The events in the $K_{\pi 2}$ peak can fake the $K^+ \to \pi^+ \nu \bar{\nu}$ if the momentum, energy and range are all mis-measured and two photons from the π^0 in the final state are missed. This background can be removed by setting a lower boundary of the signal region above the $K_{\pi 2}$ peaks. The $K_{\pi 2}$ events are also suppressed by requiring no photon activity in the detector. The energy of photons from $\pi^0 \to \gamma\gamma$ in the $K_{\pi 2}$ decay is evenly distributed in the region $20.2 < E_\gamma < 225.3$ MeV. The $K_{\pi 2}$ events have been removed by an online photon veto in the trigger. The online rejection against $K_{\pi 2}$ events is on the order of 10^4. A further rejection of 10^2 is needed to suppress the $K_{\pi 2}$ background to much less than one event. Offline photon veto is performed by imposing timing windows with respect to the charged track timing and the energy thresholds to the photon hits.

The events in the $K_{\mu 2}$ peak can fake $K^+ \to \pi^+\nu\bar{\nu}$ if the momentum, energy and range are mis-measured and the μ^+ is misidentified as a π^+. This background can be removed by cuts on the kinematic values. The upper bound of the signal region is set at a momentum of 229 MeV/c, an energy of 135 MeV and a range of 40 cm. The upper bound for the momentum is set at about 2σ apart from the $K_{\mu 2}$ peak; those for the energy and range are much away from the peaks. The events in the $K_{\mu 2}$ peak can therefore hardly contribute to the signal region. On the contrary, the $K_{\mu 2}$ Range Tail events have the same momentum as that in the $K_{\mu 2}$ peak, but their energy and range satisfy the signal region. In this case, only a cut on the upper bound of the momentum at 2σ works. Thus, the contribution of the $K_{\mu 2}$ Range Tail events to the signal region is supposed to be larger than the other sources of the background. The Muon Band events, particularly the $K_{\mu\nu\gamma}$ decay, can also encroach on the signal region. These momentum and energy satisfy the signal region, but the range for the μ^+'s is slightly longer than that for the π^+'s at a given value of the momentum (see Figure 3.1). The Muon Band events are thereby removed by requiring a relation between the range and the momentum expected for the π^+ tracks. The details of this cut are described in Section 3.5.2. These μ^+-related backgrounds (referred to as "Muon background") can also be removed by observing the signature of a $\pi^+ \to \mu^+ \to e^+$ decay sequence in and around the stopping counter. However, if the $\mu^+ \to e^+$ decay has an additional accidental hit, the Muon background fakes the $\pi^+ \to \mu^+ \to e^+$ decay sequence. A rejection to the fake $\pi^+ \to \mu^+ \to e^+$ decay sequence is also needed. The details are described in Section 3.5.3.

The non-K^+ decay backgrounds are categorized into three types: Single Beam background, Double Beam background, and charge exchange interaction background (referred to as "CEX" background).

The Single Beam background can be further categorized into two; kaon entering and pion entering cases. If a single kaon entering the apparatus decays in flight (DIF) to π^+ and π^0 ($K_{\pi 2}$ DIF, see the top diagram in Figure 3.3), the kinematic values of the π^+ can shift up to higher due to a Lorentz boost. If the two photons from the $K_{\pi 2}$ DIF are missed, such an event fakes the $K^+ \to \pi^+\nu\bar{\nu}$ signal. The kaon DIF events tend to have earlier decay timings in the target than the stopped kaon decay events. The Single Kaon Beam background is suppressed by imposing a delayed coincidence (DC) to the decay time. If a pion in the beam scatters in the target and then enters the fiducial region of the detector (Pion Scattering events, see the bottom diagram in Figure 3.3), the event fakes the $K^+ \to \pi^+\nu\bar{\nu}$ signal because some of these scattered pions satisfy the kinematics of the signal. The scattered pion leaves the target immediately after entering the target. The Single Pion Beam background is also suppressed by the DC. It is also suppressed by kaon identification in the Čerenkov counter and the B4 Hodoscope.

The Double Beam background can also be categorized into two; kaon-kaon entering and kaon-pion entering cases. In the kaon-kaon entering case, the first kaon enters and stops in the target, and the second kaon entering the target decays in flight to π^+ and the π^+ enters the fiducial region of the detector (see the top diagram in Figure 3.4). The kaon-pion case is the same as the kaon-kaon case, except that the second pion scatters in the target and enters the fiducial region to satisfy the kinematics of the signal (see the bottom diagram in Figure 3.4). For both cases, the Double Beam backgrounds can imitate the $K^+ \to \pi^+\nu\bar{\nu}$ signal, if the decay products from the first kaon are missed and

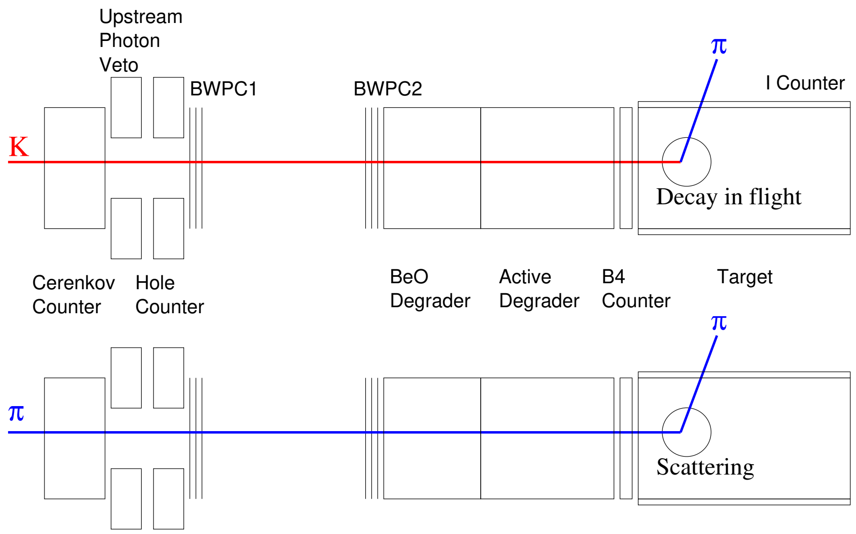

Figure 3.3: Schematic diagrams of the Single Beam background: a Single Kaon Beam background (top) and a Single Pion Beam background (bottom).

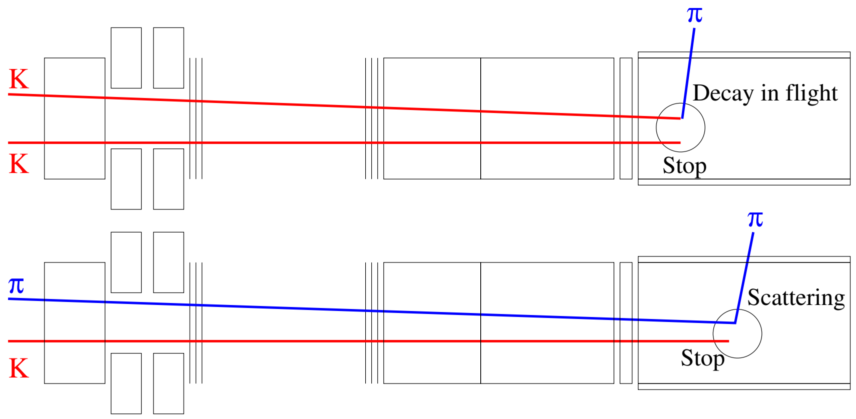

Figure 3.4: Schematic diagrams of the Double Beam background: a $K - K$ Double Beam background (top) and a $K - \pi$ Double Beam background (bottom).

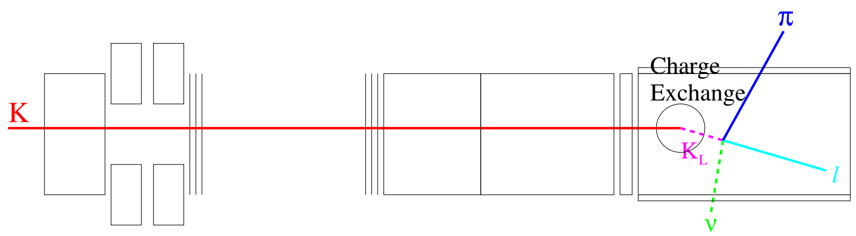

Figure 3.5: Schematic diagram of the charge exchange interaction background.

Background	BR	kinematics	PV	PID	multi-tracks	beam PID	extra beam	DC
$K^+ \to \mu^+ \nu_\mu$	0.64	$\surd$		$\surd$				
$K^+ \to \pi^+ \pi^0$	0.21	$\surd$	$\surd$					
$K^+ \to \mu^+ \nu_\mu \gamma$	0.005	$\surd$	$\surd$	$\surd$				
Single K Beam			$\surd$					$\surd$
Single π Beam						$\surd$		$\surd$
Double $K-K$ Beam			$\surd$		$\surd$		$\surd$	
Double $K-\pi$ Beam					$\surd$	$\surd$	$\surd$	
CEX					$\surd$			$\surd$

Table 3.1: Tools against the main backgrounds: 1) kinematics: Phase Space Cuts (P, E and R), dE/dx cuts, Range-Momentum Consistency cut; 2) PV: Photon Veto Cuts; 3) PID: $\pi^+ \to \mu^+ \to e^+$ Decay Sequence Cuts; 4) multi-tracks: veto the multi-track events; 5) beam PID: the particle identification in the beam instrumentation; 6) extra beam: veto the extra beam particles coincident with the charged track; and 7) DC: Delayed Coincidence Cuts.

the second kaon or pion is not detected in the beam line detectors. These backgrounds can be suppressed by looking for any extra activities that are coincident with the charged track in the beam instrumentation, target, and Range Stack.

The charge exchange (CEX) interaction background can occur as follows: a kaon entering the target interacts with a neutron in the carbon of the scintillators ($K^+ n \to K^0 p$) and the resultant K_L^0 decays to $\pi^+ l^- \bar{\nu}_l$, where $l^- = e^-$ or μ^- (see Figure 3.5). If the π^+ satisfies the signal kinematics and the l^- is missed, the event can imitate the $K^+ \to \pi^+ \nu \bar{\nu}$ signal. The K_L^0 does not deposit energy along the path in the target; the CEX background event has a gap between kaon and pion fibers in the target. It is therefore suppressed by requiring no large gap between the kaon and pion fibers. The CEX background is also suppressed by the DC, since only the K_L^0's that travel a short distance can be allowed by requiring no large gap.

The rejection tools for each background in this experiment are tabulated in Table 3.1.

3.2 Analysis Strategy and Method

In the Standard Model, the predicted branching ratio for $K^+ \to \pi^+ \nu \bar{\nu}$ is at 10^{-10}; the backgrounds should therefore be suppressed to the level of 10^{-11}. This large suppression of the backgrounds makes a reliable estimation of the backgrounds in the signal region difficult, because any measurement involving low statistics could be subject to large statistical fluctuations. Furthermore, the development of signal selection criteria (cuts) using a smaller and smaller number of events could result in a "bias", because cuts that are designed to remove a single event or a small number of events may not work properly on a larger data sample.

To avoid this bias, a "blind" analysis is indispensable. That is, background sources are identified a *priori* and a signal region ($\pi \nu \bar{\nu}(1)$ region) is determined so that the sensitivity is expected to be optimized. The signal region is masked out until the cut development and the background estimation are finalized. Cuts to suppress the backgrounds are developed using events outside the signal region.

The analysis is performed in the following way:

- Real data is used as much as possible, because a Monte Carlo simulation would not necessarily represent pathological events that are contained in the real data due to hardware problems or unexpected biases; these events may slip through the cuts designed by the MC sample and pretend to be $K^+ \to \pi^+ \nu \bar{\nu}$ signals.

- The "Bifurcation Method" is used for the background estimations. The background is estimated by at least two uncorrelated cuts, or groups of cuts; they can be independently inverted to create high-statistic background samples from real data. The details of the Bifurcation Method are explained in Section 4.1.

- For a background study, the real data are divided into two portions: a uniformly-sampled one-third portion of the whole data is used to develop the cuts, and the remaining two-third portion is used to measure the final background levels. This helps to estimate the background levels in a less-biased manner. For signal examination, all of the data are examined.

- The background levels and signal acceptances can be controlled continuously by changing the severities of the cuts used in the Bifurcation Method. The variation of the background levels and acceptances at various cut positions can be used to create functions. Details of the functions are described in Section 3.6.

- Acceptance measurements of the signal selection cuts are made with some monitor trigger data. The $K^+ \to \pi^+ \nu \bar{\nu}$ phase space acceptance and the π^+ stop efficiency [1] are obtained from the Monte Carlo $K^+ \to \pi^+ \nu \bar{\nu}$ sample.

- The branching ratio is calculated by a likelihood analysis.

3.3 Event Reconstruction

The data collected by the trigger are analyzed by a series of offline software programs. Event reconstruction starts from investigations of the trigger bit and of such information as the *online* stopping counter. Then, hit counters of a positively-charged track (track counters) are searched for in the Range Stack. The search starts from finding a (offline) T•2 sector. If there are coincident hits in the first two RS layers in the same sector, it is treated as the T•2 sector. Otherwise, the online T•2 sector is used. The counters that are coincident with the T•2 hit are searched for in the outgoing and clockwise direction, and such counters are treated as track counters. The average time of the track counters is defined as the "track time". The counter in the outermost layer and the most clockwise sector is treated as the *offline* stopping counter.

Track reconstructions in the target and UTC are performed twice. At first, in x-y plane, a circular track is fitted to the UTC hit wires. The fitted track is extrapolated to

[1] This accounts for the rate of π^+ nuclear interactions in the Range Stack and π^+ decay-in-flights.

the target to determine the target fibers that belong to the track (pion fibers) and the kaon decay vertex. Pattern recognition in the target is made to determine the kaon and pion fibers using the UTC track information. Once the pion fibers are found, the UTC fitting is repeated with the information on the pion passage and kaon decay vertex in the target. The pattern recognition is also re-done after the UTC track fitting is finalized. The times of the kaon and the (outgoing) pion are obtained from the average of the kaon and pion fiber times, respectively. The energies of the kaon and the pion in the target are calculated by summing up the energy deposits in the kaon and pion fibers, respectively. The total momentum is obtained by correcting the momentum in the UTC by the target range, the I-Counter range and the amount of dead materials due to the inner wall of the UTC.

In the stopping counter, a pulse fitting is performed to find a $\pi^+ \to \mu^+$ decay signature. Both single-pulse and double-pulse fittings are applied to the TD pulse shape and the fitting algorithm returns the χ^2 of both single-pulse and double-pulse fittings, the energy and time of the second pulse, etc.

The total energy deposit of the track in the RS is obtained by summing up the energy deposits in the track counters and by subtracting the muon energy in the stopping counter calculated in the TD pulse fitting. The range of the track is calculated via a track-fitting method. A track is propagated by losing energy with Bethe-Block equation and by bending in a 1 Tesla magnetic field. A projection of the track onto the x-y plane is fitted to the sector crossing points, the RSSC hit positions and the energy in the stopping counter by changing the incident momentum and the angle at the entrance of the RS until the fitting χ^2 is minimized (see Figure 3.6). The projection of the track onto the r-z plane is assumed to be the same as the extrapolation of the UTC track. In the r-z plane, a matching of the extrapolated track to the measured z positions, obtained from the end-to-end time differences in the individual RSSCs and the RS counters, is examined. The range in the RS is calculated from the path length of the fitted track, and the total range of the track is calculated by adding the target range, the I-Counter range and the range in the dead materials.

Details concerning the event reconstruction are described in Appendix A.

3.4 Data Reduction

Data collected by the $\pi\nu\bar{\nu}(1)$ trigger were stored on 300 magnetic tapes; their total data size was 7 Tera bytes. In order to reduce the data to a reasonable size, two steps of data reductions are made before the background study. In the first step, called "Pass 1", badly reconstructed events and obvious muon and beam background events are removed by several cuts which maintain high acceptance for $K^+ \to \pi^+\nu\bar{\nu}$ events. This "Pass 1" processing reduces the data by a factor of 10. Details of the "Pass 1" cuts are described in Appendix B.1. In the second step, called "Pass 2", some loose versions of the final analysis cuts are applied to the "Pass 1" output data sample. In the "Pass 2" data reduction, some combinations of the "Pass 2" cuts are used to divide the data sample into 3 groups: $K_{\pi 2}$ enhanced, muon enhanced and beam enhanced background samples. The "Pass 2" cuts are tabulated in Table 3.2. The developments of the Bifurcation cuts and the

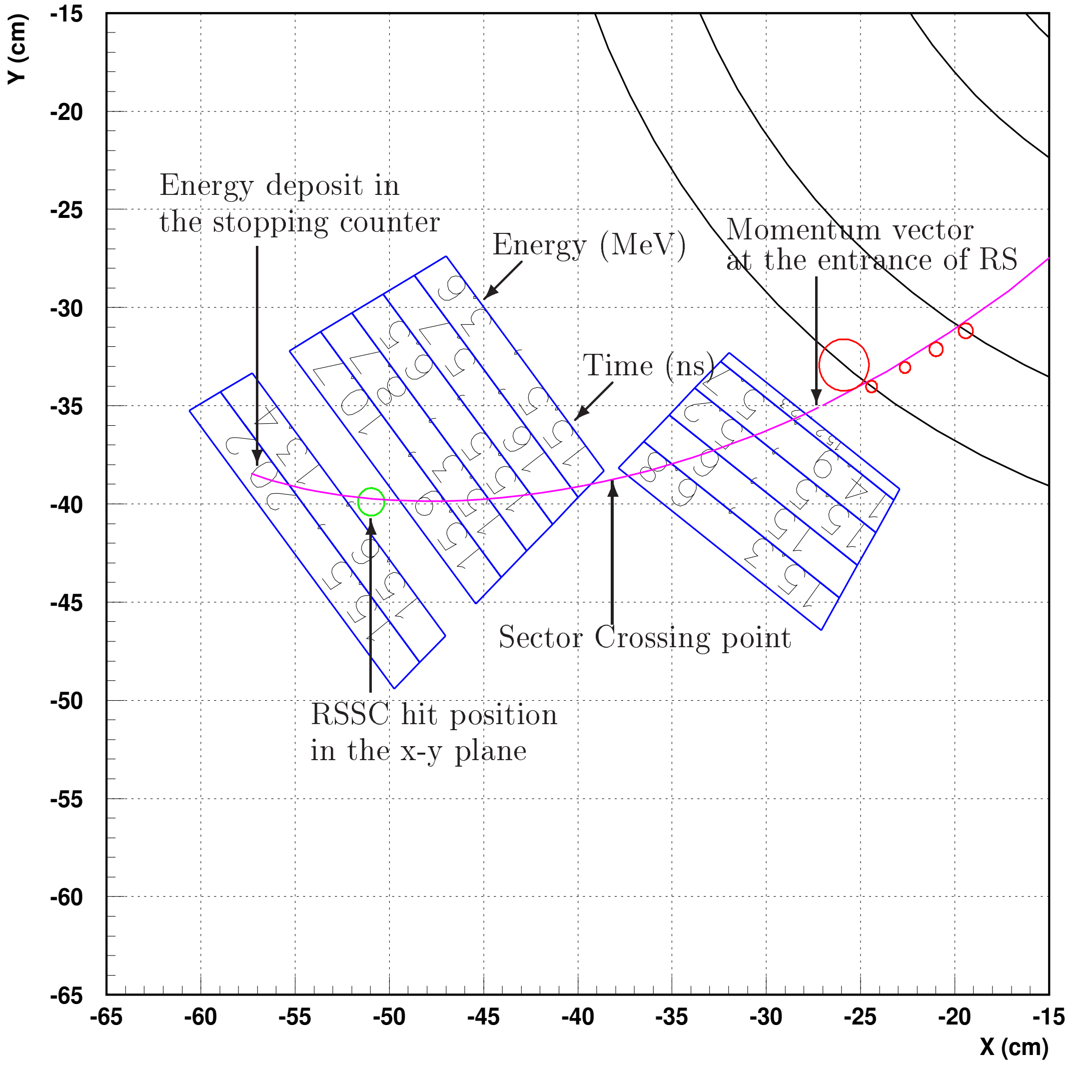

Figure 3.6: Range Stack track fitting in the x-y plane.

Cuts	$K_{\pi 2}$ enhanced	Muon enhanced	Beam enhanced
Target reconstruction cut	$\surd$	$\surd$	$\surd$
Photon veto cut		$\surd$	$\surd$
$\pi^+ \to \mu^+$ double pulse fitting cut	$\surd$		$\surd$
Beam dE/dx & extra beam cut	$\surd$	$\surd$	
Target photon veto		$\surd$	$\surd$
Delayed coincidence cut		$\surd$	
$\pi_{scatter}$ selection cut			$\surd$

Table 3.2: Pass 2 cuts to produce the $K_{\pi 2}$, muon and beam enhanced background samples. The photon veto cut means photon veto in the BV, BVL, EC and RS. The $\pi_{scatter}$ selection cut selects those events with prompt decay timings and with any activities in the target.

background estimations are performed with the Pass 2 output data sample. Details on the "Pass 2" cuts are described in Appendix B.2.

3.5 Signal Selection and Background Suppression

3.5.1 Single Kaon Identification

It is crucial to require that a single kaon enters the target and decays at rest. The former requirement suppresses the Pion Scattering events and the events with extra beam particles that can satisfy the signal kinematics. The latter requirement is very important because the momenta of the $K_{\pi 2}$- and $K_{\mu 2}$-decay products are monochromatic in the kaon rest frame, and one can therefore separate the signal from these backgrounds by selecting the kinematic region that is apart from the monochromatic peaks.

In order to ensure these requirements, several cuts explained in the following paragraphs are prepared.

Delayed Coincidence Cuts

The (offline) Delayed Coincidence Cuts require that a kaon should decay at least 2 ns later than it enters the target. Events are required to satisfy $t_\pi - t_K \geq 2$ ns, where t_K is the target kaon time, which is the average time of the target kaon fibers, and t_π is the target pion time, which is the average time of the target pion fibers. The distribution of $t_\pi - t_K$ is shown in Figure 3.7. The $t_\pi - t_K$ distribution for stopped kaons shows an exponential curve with a kaon lifetime of 12 ns, while that for scattered pions or kaons decaying in flight shows a prompt peak of around 0 ns. Most of these events are removed by the requirement $t_\pi - t_K \geq 2$ ns.

Typically, kaons have 3 or 4 hit fibers with large energy, and pions as decay products have more than 5 hit fibers with a small energy. Kaons sometimes come to rest at the edge of the target or the I-Counter. Since the decay products do not deposit any energy in the target and no pion fiber can be found, the pion time is defined as the time of the I-Counter hit along the UTC track. Another case is that only a few pion fibers are

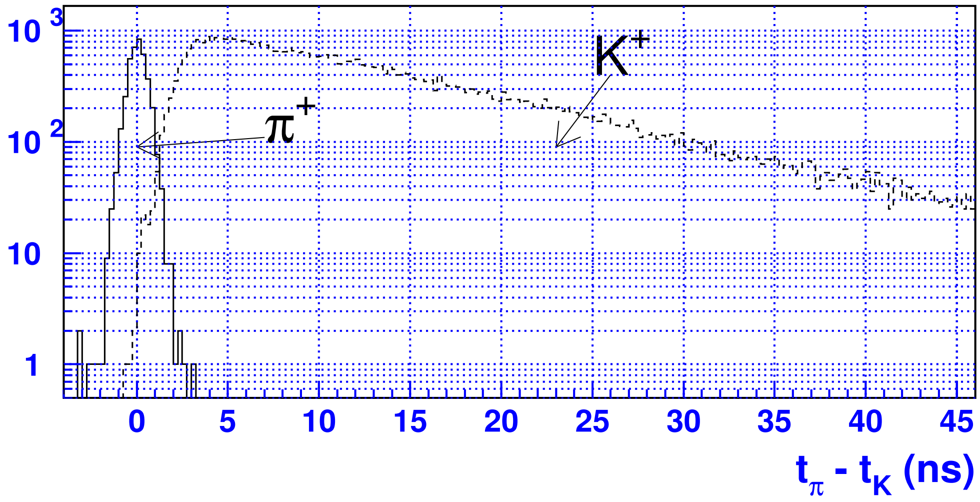

Figure 3.7: Distribution of the time difference, $t_\pi - t_K$, for stopped kaon (dashed) and scattered pion (solid) events. The time difference for kaons is derived from stopped kaon events in the $K_{\mu 2}$ monitor trigger data, and that for scattered pions is from Pion Scattering events in the $\pi\nu\bar{\nu}(1)$ trigger data.

found, since a kaon comes to rest at the target edge. Both are cases in which the pion time has a large uncertainty. In some cases, kaons have a kinetic energy smaller than 50 MeV (typically more than 80 MeV) at the entrance of the target. In other cases, kaons have only a few hit fibers in the target. For both cases, the kaon time also has a large uncertainty. It is therefore possible that events with large uncertainties on the kaon and pion times satisfy the delayed coincidence requirement. The requirement $t_\pi - t_K \geq 2$ ns is tightened depending on the following conditions:

- $t_\pi - t_K \geq 5$ ns if the discrepancy between the target kaon time (t_K) and B4 Hodoscope hit time (t_{B4}) is greater than 1 ns ($|t_K - t_{B4}| > 1$ ns).
- $t_\pi - t_K \geq 6$ ns if the discrepancy between the target pion time (t_π) and the track time (t_{RS}) is greater than 1.5 ns ($|t_\pi - t_{RS}| > 1.5$ ns).
- $t_\pi - t_K \geq 5$ ns if t_π is obtained from the time of an I-Counter hit, not of target pion fiber hits.
- $t_\pi - t_K \geq 4$ ns if the energy deposit of a kaon in the target (E_K) is less than or equal to 50 MeV ($E_K \leq 50$ MeV).
- $t_\pi - t_K \geq 3$ ns if there are less than 4 target pion fibers found.
- $t_\pi - t_K \geq 3$ ns if a beam likelihood value (L_{beam}) is less than 200 ($L_{beam} \leq 200$).
- $t_\pi - t_K \geq 4$ ns if the discrepancy between any of the individual kaon fiber times (t^i_K) and the average kaon time is greater than 2 ns ($|t^i_K - t_K| > 2$ ns).
- $t_\pi - t_K \geq 4$ ns if the discrepancy between any of the individual pion fiber times (t^i_π) and the average pion time is greater than 3.5 ns ($|t^i_\pi - t_\pi| > 3.5$ ns).

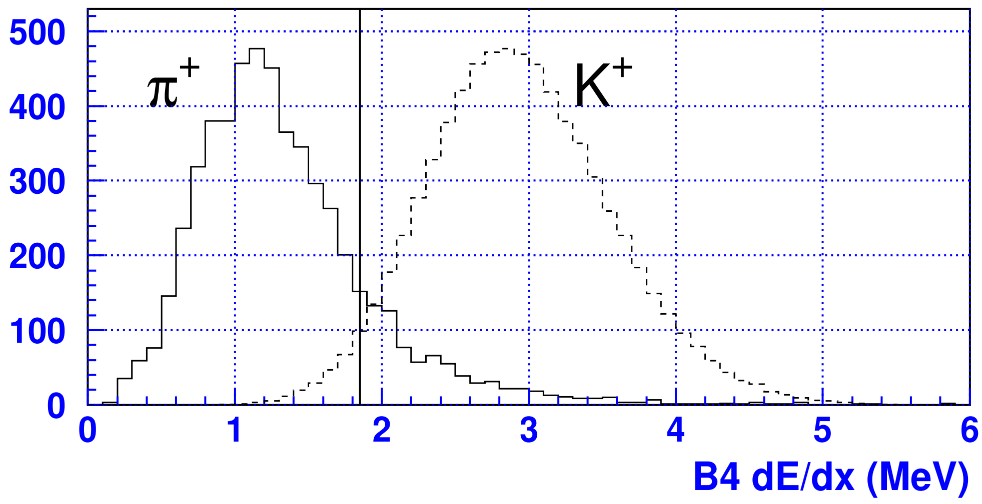

Figure 3.8: dE/dx in the B4 Hodoscope for beam kaons (dashed) and pions (solid). The kaon events are derived from stopped kaon events in the $K_{\mu 2}$ trigger data and the pion events are from Pion Scattering events in the $\pi\nu\bar{\nu}(1)$ trigger data. Events with B4 dE/dx less than 1.85 MeV are rejected.

dE/dx Cut in the B4 Hodoscope

The dE/dx cut in the B4 Hodoscope requires that the energy deposit of an incoming beam particle is consistent with that of the kaons. The velocity of kaons, whose energy loss in the degrader is large, is $\beta \approx 0.57$, while that of pions is $\beta \approx 0.97$ [42]. Kaons (pions) therefore deposit large (small) energies in the B4 Hodoscope. The dE/dx in the B4 Hodoscope is shown in Figure 3.8. Events are required to satisfy the B4 dE/dx greater than or equal to 1.85 MeV. The pion events in the peak of the Landau distribution are removed by this cut.

Cuts on Extra Beam Particles at the Track Time

Any cuts to reject events with multiple beam particles require that the beam detectors should not have hits coincident with the track time. In Double Beam background events, the earlier kaon comes to rest in the target, and the incoming second kaon or pion promptly produces a charged track in the Range Stack. The extra incoming particle therefore has coincident hits in the beam detectors at the track time. Any hits coincident with the track time are searched for in the Kaon and Pion Čerenkov Counters (using CCDs and TDCs), the two BWPCs (using TDCs), and the B4 Hodoscope (using CCDs and TDCs). The time distributions in the beam instrumentation for the Double Beam background are shown in Figures 3.9, 3.10 and 3.11.

There are other cuts for the extra beam particles. In the B4 Hodoscope, a double pulse fitting is performed with the CCD pulse-shape information. For each module in the B4 Hodoscope, the CCD pulse shape is fitted with both single- and double-pulse assumptions. A clustering is performed by looking for second hits in the modules whose pulse shape

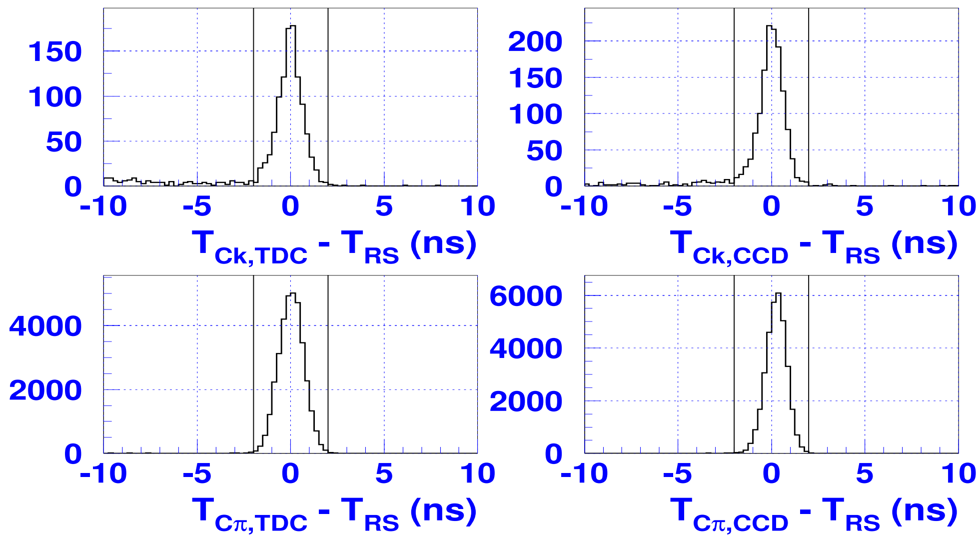

Figure 3.9: Timing of hits in the Kaon (top) and Pion (bottom) Čerenkov Counters with reference to the track time (T_{RS}). The times were derived from TDCs (left) and CCDs (right). The vertical lines at ±2 ns show the cut positions.

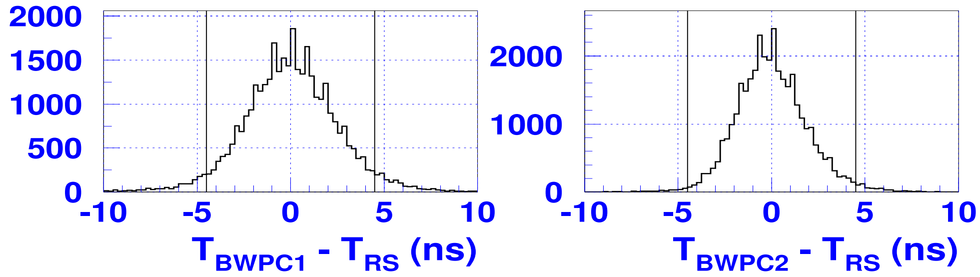

Figure 3.10: Timing of hits in the BWPC1 (left) and BWPC2 (right) with reference to the track time (T_{RS}). The vertical lines at ±4.5 ns show the cut positions.

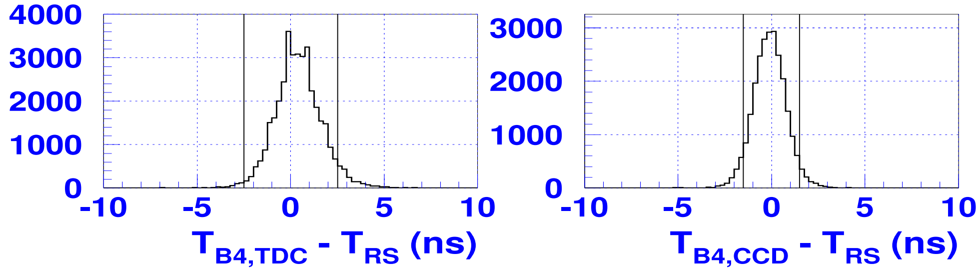

Figure 3.11: Timing of hits in the B4 Hodoscope with reference to the track time (T_{RS}). The times were derived from TDCs (left) and CCDs (right). The vertical lines at ±2.5 ns (left) and ±1.5 ns (right) show the cut positions.

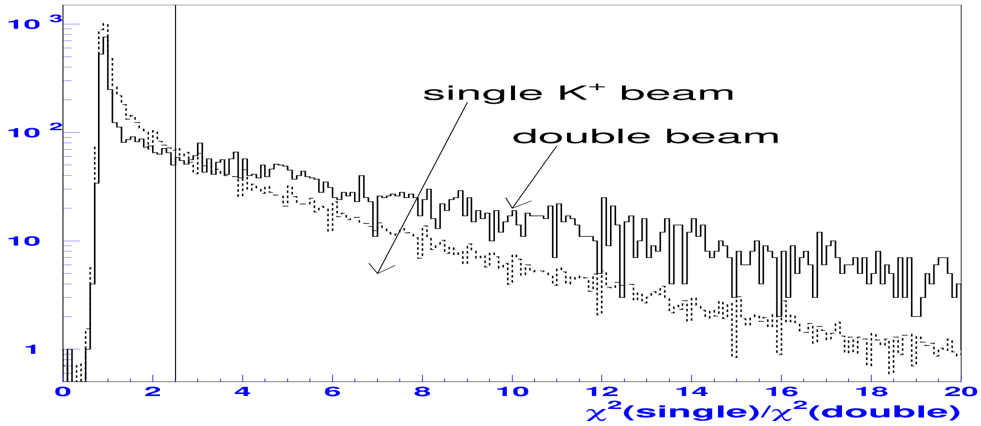

Figure 3.12: Ratio of a single-pulse fit χ^2 to that of a double-pulse fit for single kaon beam events (dashed) and double beam events (solid). Events with χ^2 ratio greater than 2.5 are selected as double-pulse events.

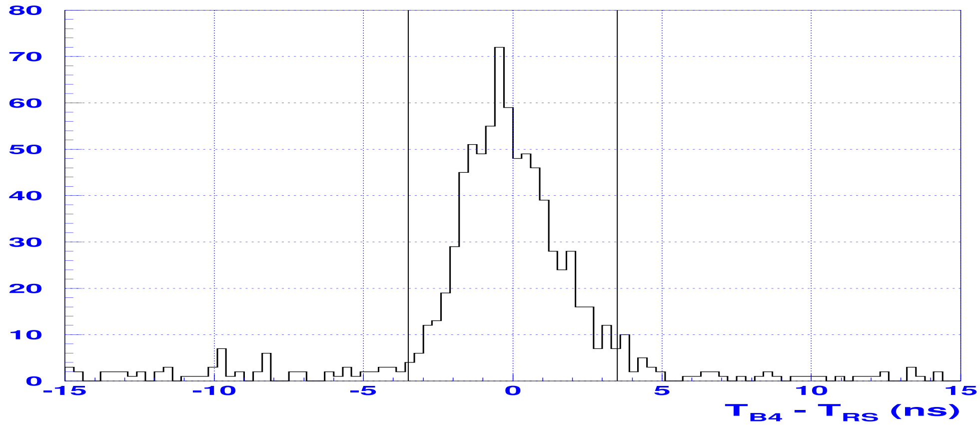

Figure 3.13: Average time of the second pulses from the B4 CCD double-pulse fitting with reference to the track time for the double-pulse events. The vertical lines at ± 3.5 ns show the cut position.

has the signature of double pulses [2]. Events are rejected if the average time of the second hits in the cluster is within ± 3.5 ns of the track time. The χ^2 ratios for single kaon beam and double beam events are shown in Figures 3.12. The average time of the second hits with reference to the track time for the double-pulse events is shown in Figure 3.13.

Beam Likelihood Cut

Kaons, which come to rest in the target, satisfy a relation between the energy deposits in the B4 Hodoscope (B4 dE/dx), the energy deposits in the target (E_K) and the stopping z positions, which are related to the kaon path length (Z_{Kstop}). The stopping z position is derived by extrapolating the UTC track to the decay vertex in the target. The stopping z

[2]The double-pulse signature means that a single-pulse fit χ^2 divided by that of a double-pulse fit is greater than 2.5 and the energy of the fitted second pulse is above a threshold.

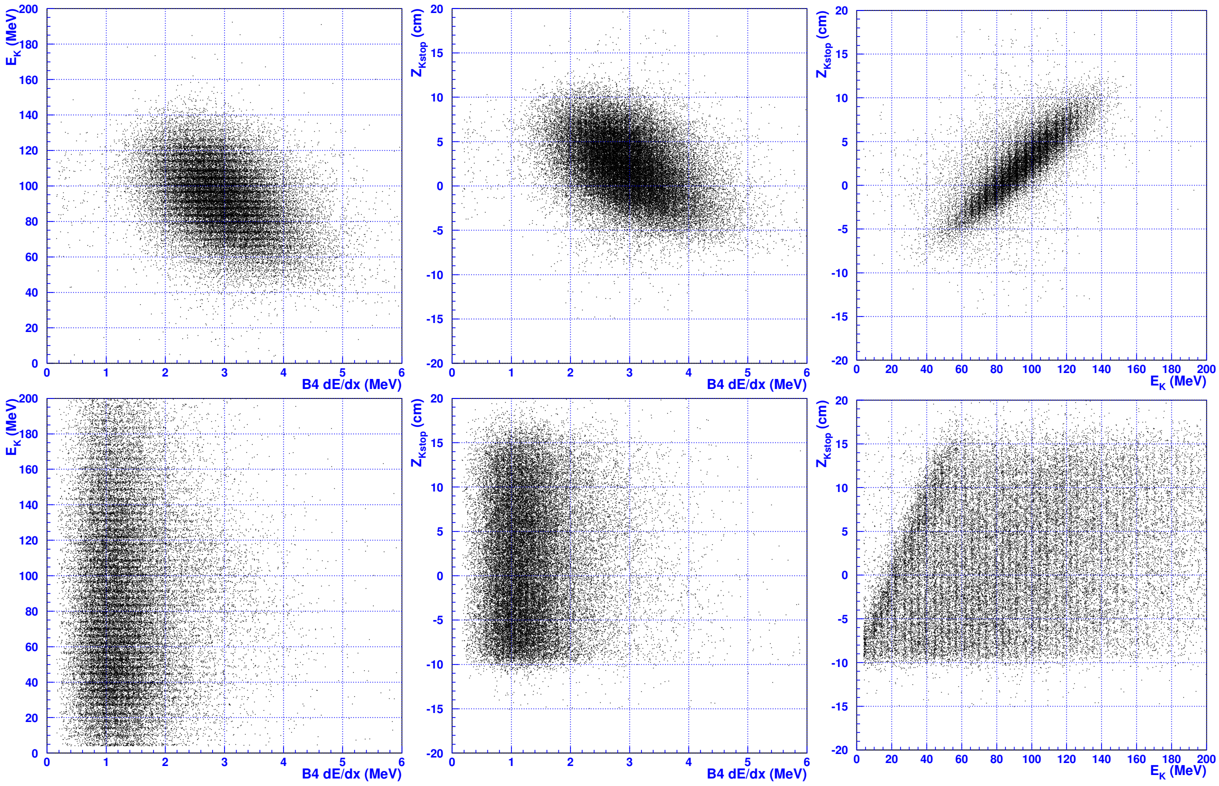

Figure 3.14: Scatter plots of the target kaon energy v.s. energy deposit in the B4 Hodoscope (left column), the stopping z position in the target v.s. energy deposit in the B4 Hodoscope (middle column) and the stopping z position in the target v.s. target kaon energy (right column) for stopped kaons (top raw) and scattered pions (bottom raw). The stopped kaon and scattered pion events were derived from the $K_{\mu 2}$ monitor trigger data and the $\pi\nu\bar{\nu}(1)$ trigger data, respectively.

positions for scattered pions and kaons decaying in flight represent the positions where the scattering and decay-in-flight occur; these pions and kaons do not have such a relation. Figure 3.14 shows scatter plots of the target kaon energy v.s. energy deposit in the B4 Hodoscope (left column), the stopping z position in the target v.s. energy deposit in the B4 Hodoscope (middle column) and the stopping z position in the target v.s. target kaon energy (right column) for stopped kaons (top raw) and scattered pions (bottom raw). A clear relation in the stopped kaon events can be seen in this figure, but in the Pion Scattering events the target energy and stopping z position are evenly spread, although the B4 dE/dx concentrates around 1 MeV. A likelihood is constructed by these three quantities to separate the stopped kaons from the other beam particles. The likelihood values for stopped kaons and scattered pions are shown in Figure 3.15. This cut requires that events should have the likelihood value greater than 2. It also requires that kaons should have an energy greater than 25 MeV and the number of kaon fibers greater than 2 to ensure good stopped kaon events.

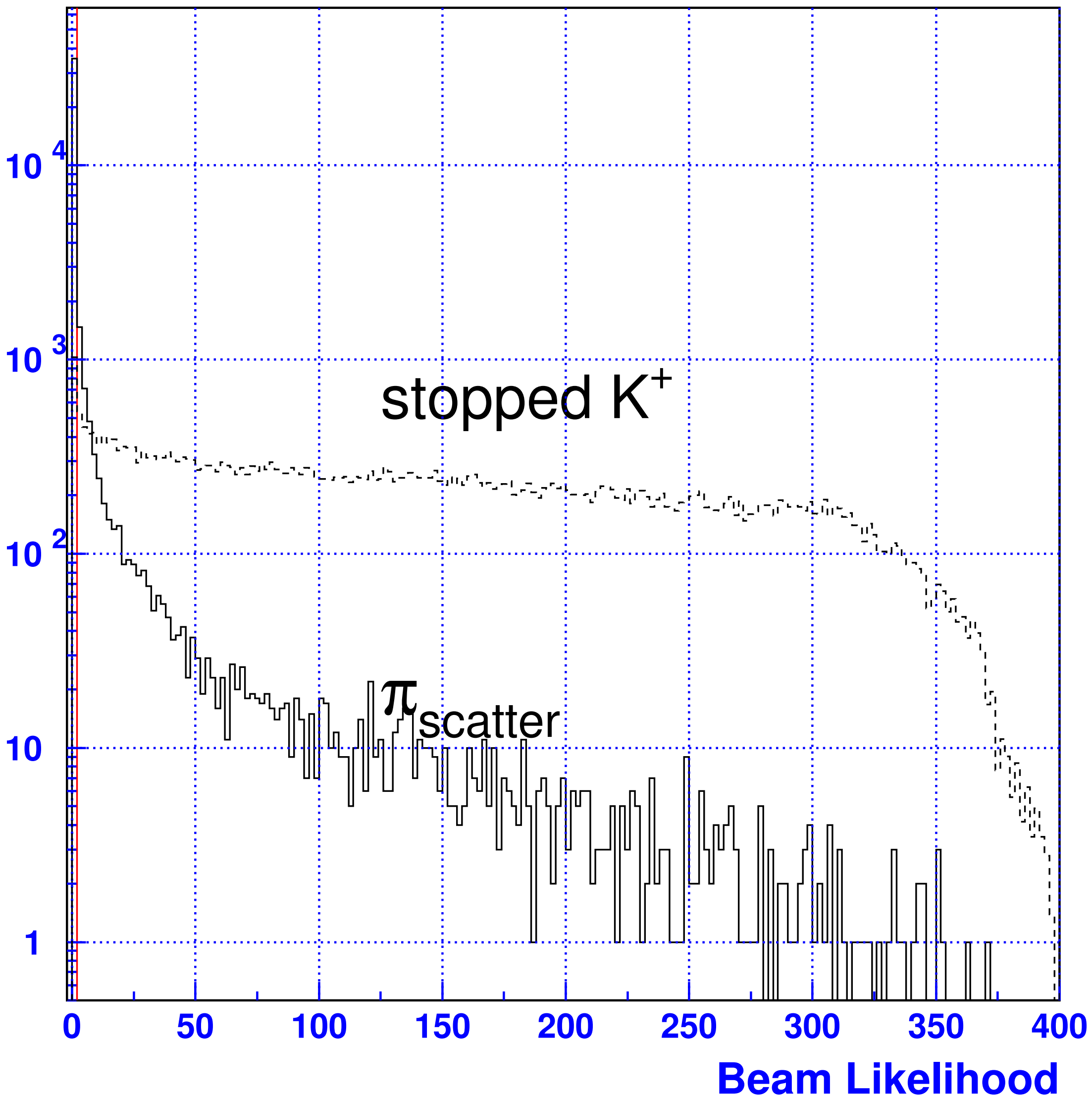

Figure 3.15: Beam likelihood for stopped kaons (dashed) and scattered pions (solid). The vertical line shows the cut position. It is required that the beam likelihood value is greater than 2. The stopped kaon and scattered pion events were derived from the $K_{\mu 2}$ monitor trigger data and the $\pi\nu\bar{\nu}(1)$ trigger data, respectively.

3.5.2 Pion Identification I: Kinematics

Since the signal region is selected to be the region between the $K_{\pi2}$ and $K_{\mu2}$ kinematic peaks in this analysis, the most important thing is a correct measurement of the charged track kinematics and the particle identification. π^+ from $K^+ \to \pi^+\nu\bar{\nu}$ in the signal region is identified by the following requirements:

- Phase Space Cuts,
- dE/dx Cuts in the Range Stack, and
- Range-Momentum Consistency Cut for particle identification.

Phase Space Cuts

The Phase Space Cuts require that the momentum, kinetic energy and range should be in the following regions:

$$\begin{array}{lcl} \text{Momentum} & : & 211 \leq P \leq 229 \text{ MeV/c}, \\ \text{Energy} & : & 115 \leq E \leq 135 \text{ MeV}, \\ \text{Range} & : & 33 \leq R \leq 40 \text{ cm}. \end{array}$$

As shown in Figure 3.2, the upper edges of the signal region are apart from the $K_{\mu2}$ peaks. However, the lower edges are on the tails of the $K_{\pi2}$ kinematics distributions. It has been observed that the measured $K_{\pi2}$ momentum has correlations with the polar angle and the azimuthal angle of the charged track (see Figure 3.16). Because of this correlation, the $K_{\pi2}$ events with small polar angles ($|\cos\theta| \sim 0.5$) tend to contaminate the signal region. In order to avoid this, a correction is made so that the correlation can be removed (see Figure 3.17). Although the correlation on the peak positions is corrected, the sigmas still have a dependence on the polar angle. Therefore, the lower edges of the Phase Space Cuts are tightened according to the following conditions:

$$\begin{aligned} P_{dev} &\equiv \frac{P_{meas} - P_{peak}}{\sigma_P} \geq 2.5, \\ E_{dev} &\equiv \frac{E_{meas} - E_{peak}}{\sigma_E} \geq 2.5, \\ R_{dev} &\equiv \frac{R_{meas} - R_{peak}}{\sigma_R} \geq 2.75, \end{aligned}$$

where P_{meas}, E_{meas}, R_{meas} are the measured values of momentum, energy and range; P_{peak}, E_{peak}, and R_{peak} are the $K_{\pi2}$ kinematic peak positions as functions of the polar and azimuthal angles; and σ_P, σ_E, and σ_R are their resolutions as a function of the polar angle. Because of these tightened cut conditions, the background contamination does not depend on the polar and azimuthal angles.

dE/dx Cuts in the Range Stack

A main purpose of the cuts is to remove events with energy deposits in the RS track counters that are not consistent with those of a π^+ track. There is a case that charged

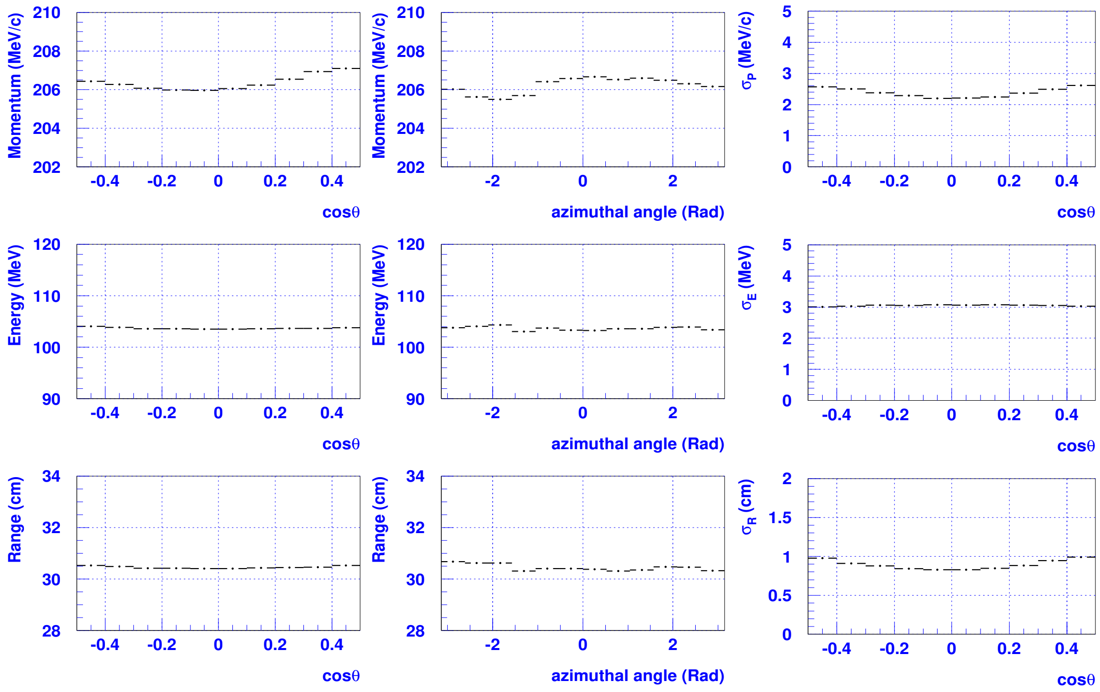

Figure 3.16: $K_{\pi 2}$ peaks and resolutions as functions of the polar (θ) and azimuthal angles. Left column: momentum (top), energy (middle) and range (bottom) peaks v.s. $\cos\theta$. Middle column: momentum (top), energy (middle) and range (bottom) peaks v.s. azimuthal angle. Right column: momentum (top), energy (middle) and range (right) resolutions v.s. $\cos\theta$.

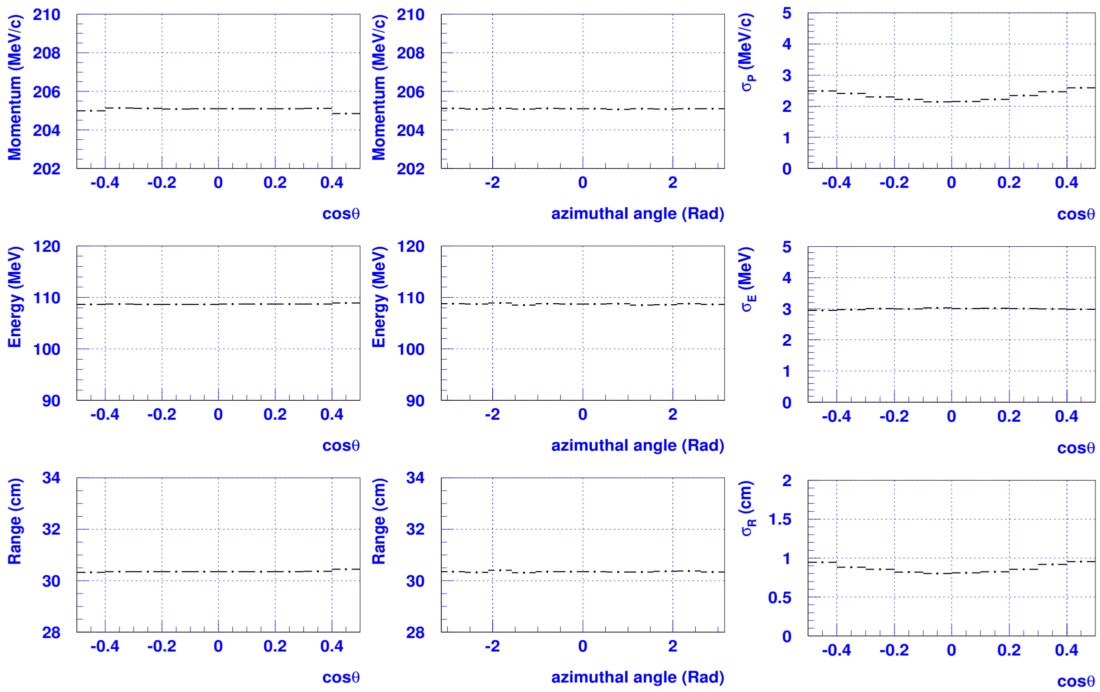

Figure 3.17: $K_{\pi 2}$ peaks and resolutions as functions of the polar and azimuthal angles after a correction.

particles inelastically (or elastically) scatter in the RS scintillators and lose energy of a few tens MeV in the scattering process. If a μ^+ from $K_{\mu 2}$ consumes its kinetic energy in the scattering process, the measured kinetic energy is underestimated and the event can contaminate the signal region. There is another case that a photon or an extra track deposits energy in the track counters and the extra energy is counted by ADCs. If a photon in $K_{\pi 2}$ decay deposits the energy in some of the track counters and another photon is missed, the measured kinetic energy is overestimated and the event can contaminate the signal region. The dE/dx Cuts in the Range Stack can remove these events.

The dE/dx Cuts in the Range Stack (RS dE/dx Cuts) are composed of three cuts:

- Cut on Maximum Energy Deviation:
  The energy deviation in each track counter is investigated.

$$\text{Energy deviation } (\chi_i) \equiv \frac{\log E^i_{exp} - \log E^i_{meas}}{\sigma^i}, \tag{3.1}$$

  where E^i_{exp} and E^i_{meas} are the expected and measured energy deposits in the ith track counter, respectively, and σ^i is the sigma of $\log E^i_{meas}$. The expected energy deposit is calculated from the measured path length in the counter, assuming that the track is a pion. The logarithm is used for both the expected and measured energies to reduce the Landau tail effect. σ^i is calibrated with the Pion Scattering events in the $\pi_{scatter}$ monitor trigger, and the energy dependence on the σ's is taken into account. The distributions of the maximum energy deviation for pion and muon tracks are shown in Figure 3.18. Events are rejected if the absolute value of the maximum deviation is greater than or equal to 4.

- Cut on the Confidence Level in RS Energy Measurements:
  A confidence level is computed with the energy deviations in all of the track counters, except for the T-Counter, the stopping counter and the counter in which a sector crossing occurs. The confidence-level distributions for pion and muon tracks are shown in Figure 3.19. Events are rejected if the confidence level is less than 0.04. In the case that the maximum energy deviation is positive, the cut position on the confidence level is tightened from 0.04 to 0.2. This tightening aims at events with photon overlapping, in which the maximum deviations are small.

- Cut on Likelihood for RS Energy Measurements:
  A likelihood is constructed with the energy differences $\Delta E \equiv \log E^i_{exp} - \log E^i_{meas}$ for layers up to the previous layer of the stopping layer. The distributions of the likelihood value for pion and muon tracks are shown in Figure 3.20. Events are rejected if the likelihood value, $\mathcal{L}_{RS}$, is not in the region $0 < \mathcal{L}_{RS} \leq 10$.

Range-Momentum Consistency Cut

This cut aims to check whether the range of the charged track is consistent with that for pions. Muons typically have a longer range than pions when the momentum is the same. The range deviation in the Range Stack is defined as

$$\chi_{R-P} \equiv \frac{R_{meas} - R_{exp}}{\sigma_R}, \tag{3.2}$$

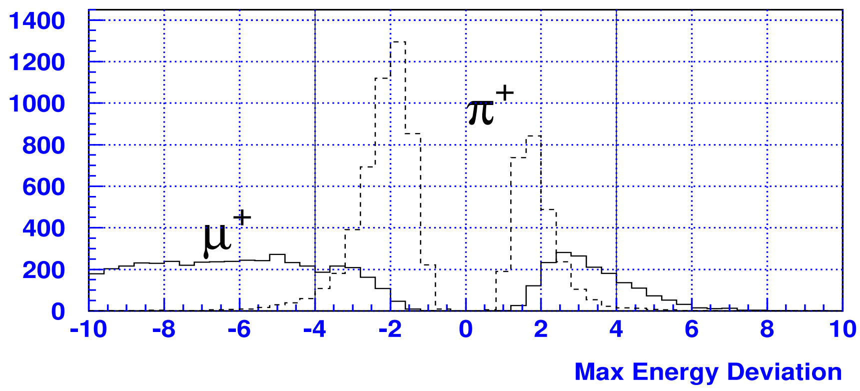

Figure 3.18: Distributions of the maximum energy deviation for pion (dashed) and muon (solid) tracks. The pion and muon events are derived from the $\pi\nu\bar{\nu}(1)$ trigger data. It is required that the maximum energy deviation is between -4 and 4.

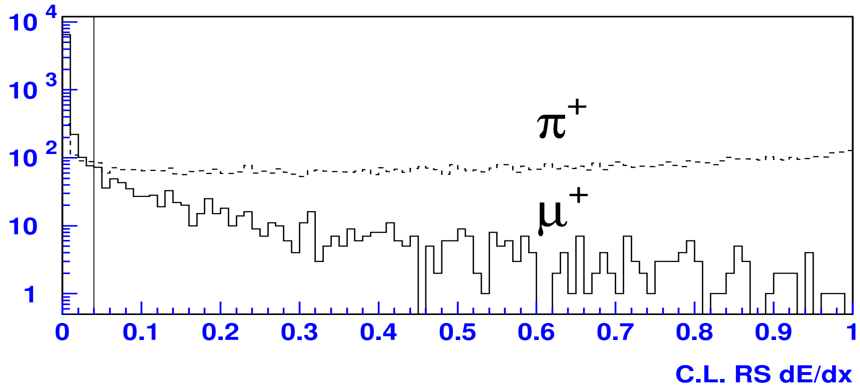

Figure 3.19: Distributions of the confidence level in the RS dE/dx measurement for pion (dashed) and muon (solid) tracks. The pion and muon events are derived from the $\pi\nu\bar{\nu}(1)$ trigger data. Events with a confidence level less than 0.04 are rejected.

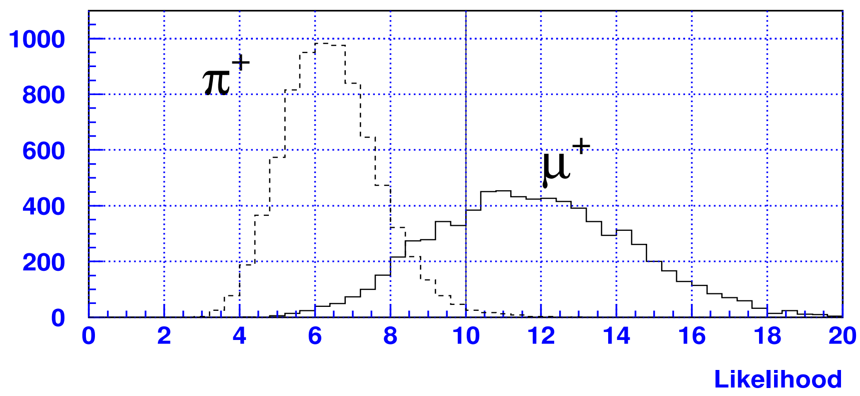

Figure 3.20: Distributions of the likelihood for the RS energy measurement for pion (dashed) and muon (solid) tracks. The pion and muon events are derived from the $\pi\nu\bar{\nu}(1)$ trigger data. It is required that the likelihood value $\mathcal{L}_{RS}$ is $0 < \mathcal{L}_{RS} \leq 10$.

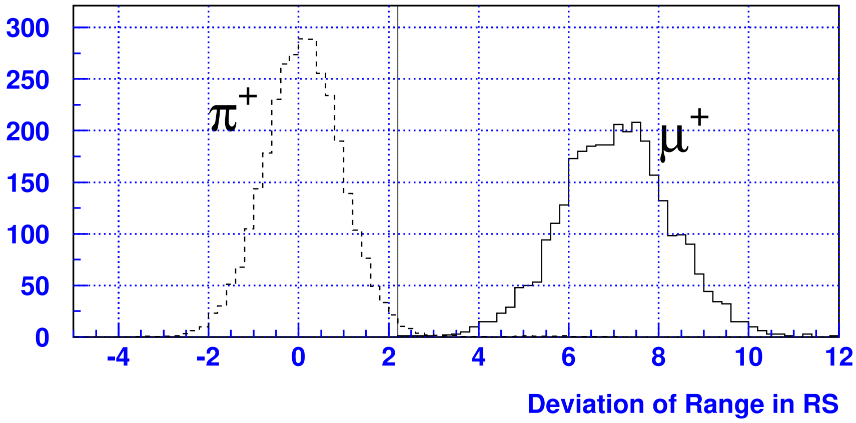

Figure 3.21: Distributions of the range deviation in the RS for pion (dashed) and muon (solid) tracks. The pion and muon events are derived from the $\pi\nu\bar{\nu}(1)$ trigger data. It is required that the range deviation is less than or equal to 2.2.

where R_{meas} is the measured range in the RS, R_{exp} is the expected range in the RS, which is calculated from the momentum measured by the UTC with an assumption that the track is a pion, and σ_R is the sigma of the measured range as a function of the momentum. The distributions of the range deviation for pions and muons are shown in Figure 3.21. Events are rejected if the range deviation is greater than 2.2.

3.5.3 Pion Identification II: $\pi^+ \to \mu^+ \to e^+$ Decay Sequence

Pion identification is also performed by searching for a $\pi^+ \to \mu^+ \to e^+$ decay sequence in the stopping counter. As explained in Section 2.3.4, the signature of the $\pi^+ \to \mu^+ \to e^+$ decay sequence is as follows:

- Three pulses of the $\pi^+ \to \mu^+ \to e^+$ decay sequence are found in the stopping counter.
- The kinetic energy of the μ^+ from $\pi^+ \to \mu^+\nu$ decay is 4.2 MeV. The actual energy measured by TDs is 3.04 MeV, due to a saturation effect in plastic scintillators [43]. The path length of the μ^+ with 4.2 MeV is 1 mm, and the μ^+ should therefore be detected only in the stopping counter.
- The e^+ from $\mu^+ \to e^+\nu\bar{\nu}$ decay has a kinetic energy of $0 < E < 53$ MeV. Most of the e^+'s exit the stopping counter and deposit energy in other RS counters.

When the charged track is a pion, three pulses from the $\pi^+ \to \mu^+ \to e^+$ decay sequence should be observed by the TDs at both ends of the stopping counter. On the contrary, when the charged track is a muon, only two pulses from the $\mu^+ \to e^+$ decay can be observed. A muon fakes a pion when an extra pulse is detected, in addition to the two pulses of $\mu^+ \to e^+$ decay. To eliminate the Muon background, two stages of suppressions are imposed.

In the first stage, $\pi^+ \to \mu^+$ double-pulse fitting is performed. The pulse development in the stopping counter is recorded, in a period of 2 μs, by 500 MHz Transient Digitizers

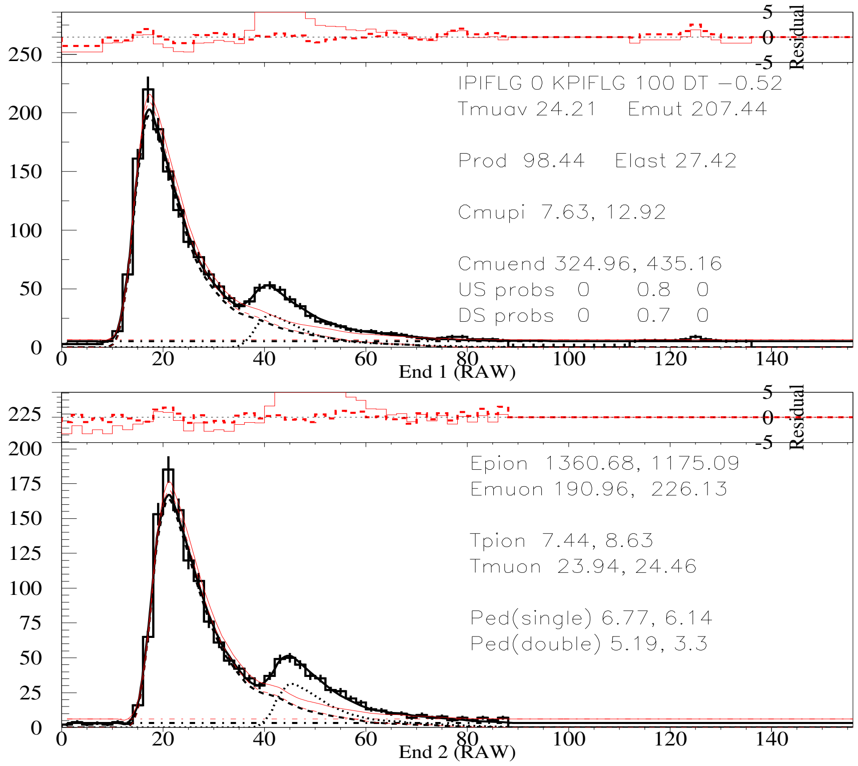

Figure 3.22: Double-pulse fitting of the TD pulse shapes in the stopping counter for a pion event. The upper and lower plots are the TD pulse shapes for the downstream and upstream ends, respectively. The horizontal axis represents the time in ns and the vertical axis represents the pulse height in TD counts. The histogram shows the pulse shape recorded by the TDs. The black and red solid lines show the double-pulse and single-pulse fits, respectively. The dashed lines show the shapes of the first and second pulses from the fitting. The values on the plots are explained in Appendix A.1.

based on flash ADCs (TDs). In event reconstruction, the pulse shapes in the time range of 100 ns are fitted with both single-pulse and double-pulse assumptions (sometimes a triple-pulse assumption if more than two pulses are found), as shown in Figure 3.22. The first two pulses of the $\pi^+ \to \mu^+$ decay can be observed by requiring that the double-pulse fitting qualities are better than those from the single-pulse fitting. Events with muon tracks that have only a single pulse in $0 \sim 100$ ns have been removed by the $\pi^+ \to \mu^+$ Double-Pulse Fitting Cut.

In the second stage, a further suppression is made to the muon events that pass the Double-Pulse Fitting Cut. There are four cases that the two-pulse $\mu^+ \to e^+$ decay fakes the three-pulse $\pi^+ \to \mu^+ \to e^+$ decay sequence.

- Pion time accidental [3]: An accidental activity makes the first pulse, and the second and third pulses are the two pulses of the $\mu^+ \to e^+$ decay (see the top figure in Figure 3.23).

[3] Times of the first, second and third pulses are referred to as the pion, muon and positron times, respectively

Cut	Pion time accidental	Early muon decay	Muon time accidental	Tail Fluctuation
π^+ Time Consistency Cut	$\surd$			
$\mu^+ \to e^+$ Decay Requirement		$\surd$		
Cut on Muon Time Accidental			$\surd$	
Cut on Muon Time Accidental in the Track Counters			$\surd$	
Neural Net $\pi^+ \to \mu^+$ Decay Cut			$\surd$	$\surd$

Table 3.3: List of the $\pi^+ \to \mu^+ \to e^+$ Decay Sequence Cuts and the targeting backgrounds.

- Early muon decay: The two-pulse $\mu^+ \to e^+$ decay occurs at an early time ($0 \sim 100$ ns), which makes the first and second pulses, and an accidental activity makes the third pulse (see the upper middle figure in Figure 3.23).

- Muon time accidental: The two-pulse $\mu^+ \to e^+$ decay makes the first and third pulses, and an accidental activity makes the second pulse (see the lower middle figure in Figure 3.23).

- Tail fluctuation: The muon makes the first pulse, and a tail fluctuation of the first pulse recorded in TD is identified as the second pulse. The positron from the muon decay makes the third pulse (see the bottom figure in Figure 3.23).

Five cuts are prepared to remove these fake $\pi^+ \to \mu^+ \to e^+$ backgrounds (see Table 3.3).

π^+ *Time Consistency Cut*

This cut targets the pion time accidental background. When an accidental activity makes the first pulse and a charged track makes the second pulse in the stopping counter, the timing of the first pulse obtained by the TD (referred to as TD pion time) is not coincident with the track time. Events are rejected if the TD pion time ($t_{\pi,TD}$) and the track time (t_{RS}) do not satisfy

$$|t_{\pi,TD} - t_{RS}| \leq 2.5 \text{ ns}. \tag{3.3}$$

$\mu^+ \to e^+$ *Decay Requirement*

This cut requires that the third pulse in the stopping counter should be due to the positron originating from the $\mu^+ \to e^+$ decay. The positron from the $\mu^+ \to e^+$ decay is emitted from the stopping counter, and it deposits energy in other counters (see left figure in Figure 3.24). The positron finding starts from examining the RS hit counters (referred to as a cluster) in the region ± 1 sectors and ± 2 layers of the stopping counter. The cluster is required to be adjacent to the stopping counter and to have hits in the same sector as the stopping counter. Candidates for the positron are found by requiring that the average time of the hits in the cluster is coincident (within ± 2.4 ns) with the time of the third pulse in the stopping counter and the z positions of the hits in the cluster, obtained from the end-to-end time differences of the hits, are consistent with that of the third pulse in the stopping counter. In the case that an accidental track that passes through the stopping counter makes a third pulse, the track deposits energy in the counters on

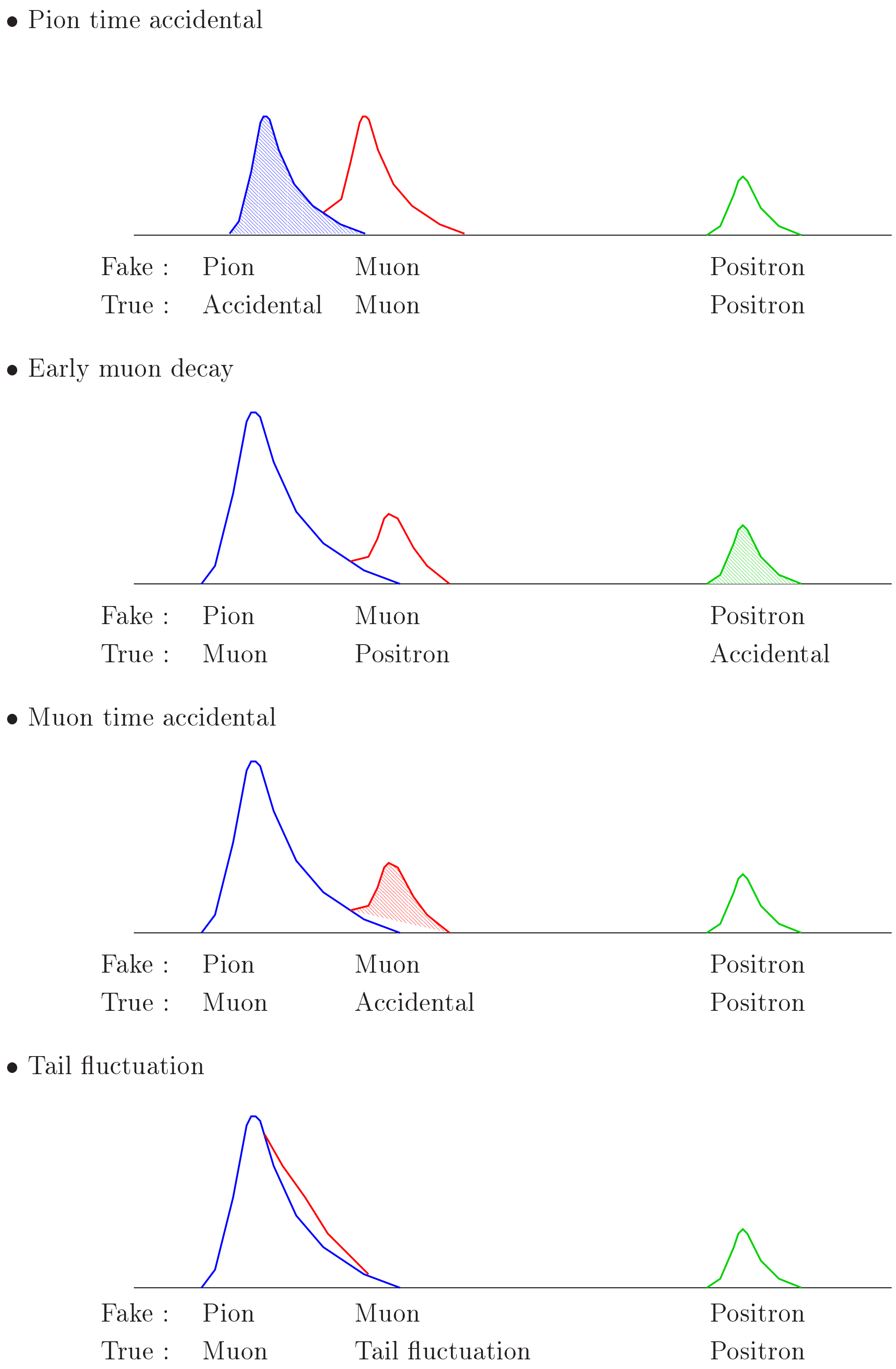

Figure 3.23: Cases where the two-pulse $\mu^+ \rightarrow e^+$ decay fakes the three-pulse $\pi^+ \rightarrow \mu^+ \rightarrow e^+$ decay sequence.

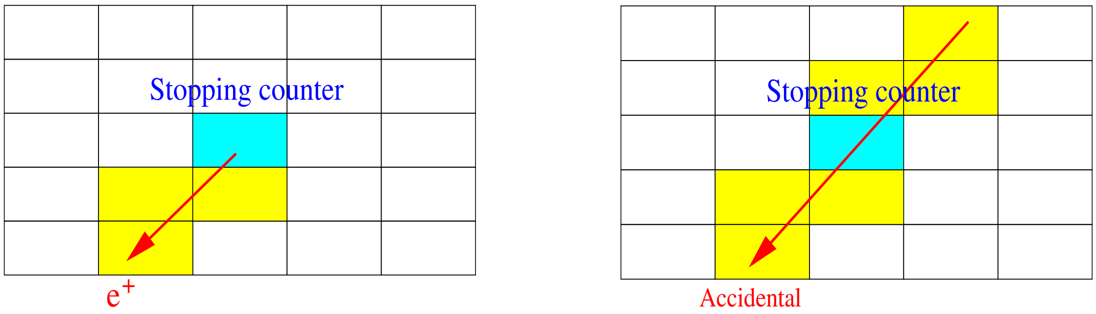

Figure 3.24: Schematic downstream views of signals (left) and backgrounds (right) of the $\mu^+ \to e^+$ decay. Each rectangle shows an RS scintillator. The counter in the center shows the stopping counter and the counters on the arrow show the hit counters.

both sides of the stopping counter (see right figure in Figure 3.24). The positron from the stopping counter can be determined by distinguishing between one-side and both-side tracks. The early muon decay background is removed by requiring that the third pulse, not the second pulse, is due to the positron from the $\mu^+ \to e^+$ decay.

Cut on Muon Time Accidental

This cut targets the muon time accidental background. It is probable that accidental activities that deposit energy in the stopping counter also make hits in other RS counters around the stopping counter. Any accidental activities coincident with the muon time are searched for in the neighboring RS counters of the stopping counter and the counters in BV, BVL and EC. The time windows and energy thresholds for the various subsystems in RS, BV, BVL and EC are optimized in order to have the highest rejection power at a given acceptance value of 94%. Events are rejected if the energy sum of hits within a time window in any subsystem is greater than the energy threshold. The time windows and energy thresholds for the various subsystems are summarized in Table B.3.

Cut on Muon Time Accidental in the Track Counters

This cut rejects the muon time accidental background by performing double-pulse fitting in the two RS track counters prior to the stopping counter. The purpose of the double-pulse fitting in the track counter is to eliminate accidental activities that overlap the charged track, and make a second pulse in the stopping counter. If the qualities of fits with the double-pulse assumption are better than those with the single-pulse assumption, and if the time of the fitted second pulse is coincident (within ± 5 ns) with the muon time in the stopping counter, the events are rejected.

Neural Net $\pi^+ \to \mu^+$ Decay Cut

This cut targets the tail fluctuation background. Tail fluctuations can be observed when there is a discrepancy between the measured pulse shape and the template pulse shape, which is calibrated with pion pulses. The qualities of fits to the fluctuated pulses are worse than those to the well-separated first and second pulses. Tail fluctuations of pulses originate from noises in the transportation of signals from PMTs to TDs. The pulse fluctuations at both ends should not be correlated. The pulse area and time of the fitted second pulse tend to be small in the fluctuated pulse. The separations between pion (which have clear double pulses) and muon (which have fluctuated pulse) tracks are good in the distributions of the following variables:

- Energy of the second pulse (E_μ).
- Time of the second pulse (T_μ).
- Log of the product of the χ^2 ratios of single- to double-pulse fits for both ends ($\log_{10}(R(1) \cdot R(2))$ where $R(i)$ is the χ^2 ratio for end i [4]).
- Log of the product of the single-pulse fit χ^2's for both ends ($\log_{10}(\chi_1^2(1) \cdot \chi_1^2(2))$ where $\chi_1^2(i)$ is the single-pulse fit χ^2 for end i).
- Difference between the z positions of the first (z_π) and second (z_μ) pulses obtained by the energy ratio of both ends ($z_\pi - z_\mu$).
- Time difference between both ends (dt).

The definition of each variable is described in Table A.1. The distributions of the variables for pions and muons are shown in Figure 3.25. Applying a fixed cut to each variable causes a non-negligible acceptance loss. In order to achieve a higher acceptance at the same rejection as the fixed cuts, a Neural Network (NN) technique is adopted.

NN functions are derived via a Multi-Layer Perception (MLP) program incorporated in the library of Physics Analysis Workstation (PAW) [44]. The NN functions give their output from several input variables (sometimes referred to as neuron). The NN functions peak their output values for a signal sample around 1 and those for a background sample around 0. In order to achieve a good separation between signal and background events, the MLP program performs a number of trials for training the NN functions. Half of a sample is used for training the NN functions, and the other half is used for confirming that the trained function has the same performance on both samples.

To create a NN function, the Pion Scattering and $K_{\mu 2}$ Range Tail events in the $\pi\nu\bar{\nu}(1)$ trigger, which pass all other $\pi^+ \to \mu^+ \to e^+$ Decay Sequence Cuts, are used as signal and background samples, respectively. The tail fluctuation background is enhanced in the background sample by imposing all the other $\pi^+ \to \mu^+ \to e^+$ Decay Sequence Cuts and removing the other backgrounds. A 5-variable NN function is obtained using the above six variables as neurons. The z position and time differences are combined to create a χ^2 as a neuron,

$$\chi^2 \equiv \left(\frac{dz}{\sigma_{dz}}\right)^2 + \left(\frac{dt}{\sigma_{dt}}\right)^2, \tag{3.4}$$

where $dz \equiv z_\pi - z_\mu$ and σ_{dz} (σ_{dt}) is the sigma of the dz (dt) distribution. The distributions of the outputs of the NN function for pions and muons are shown in Figure 3.26. Using the pions' and muons' distributions, the rejection of this cut as a function of the acceptance is obtained by changing the cut position (see Figure 3.27). The cut position at 0.76 in the output of the NN function is determined so that the acceptance of this cut is 85%.

[4] End 1 and 2 mean upstream and downstream ends, respectively.

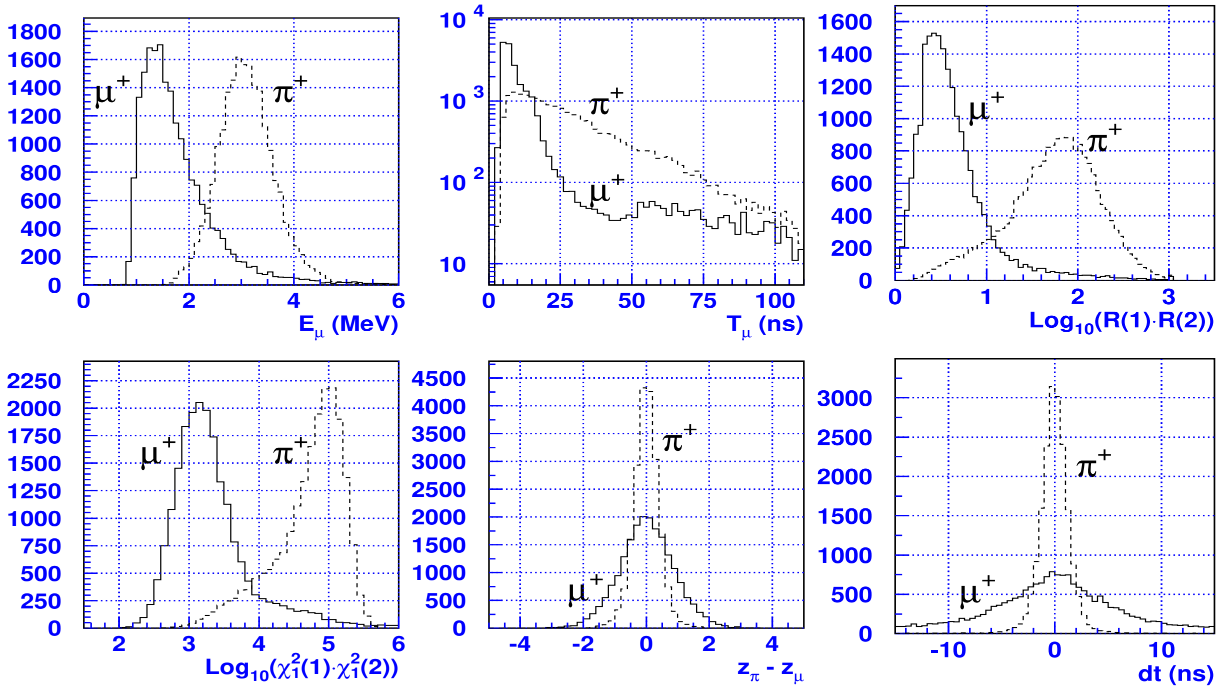

Figure 3.25: Distributions of the input variables for the Neural Net function in pion (dashed) and muon (solid) events. The energy of the second pulse (top left), time of the second pulse (top middle), log of the product of the χ^2 ratios of single- to double-pulse fits for both ends (top right), log of the product of the single-pulse fit χ^2's for both ends (bottom left), z position difference between the first and second pulses obtained from the energy ratio of both ends (bottom middle), and time difference of the second pulses in both ends (bottom right).

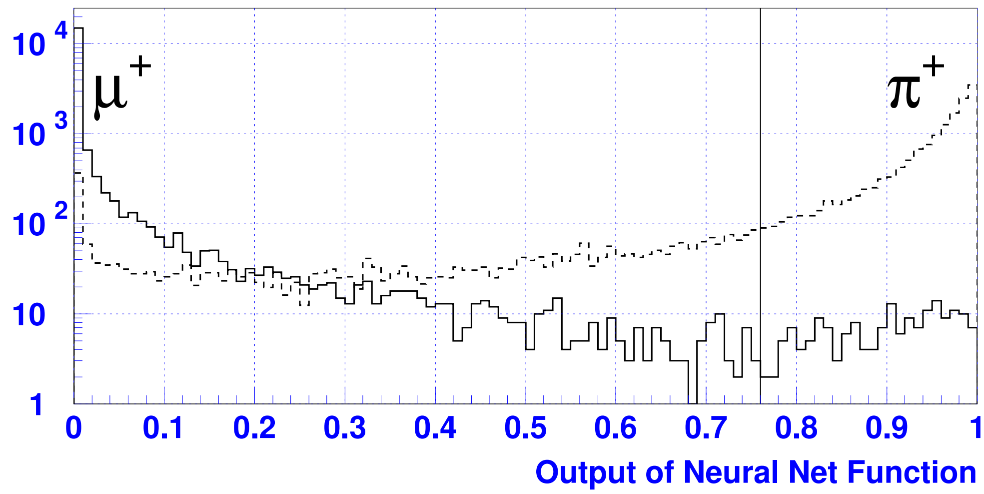

Figure 3.26: Distributions of the outputs of the NN function for pion (dashed) and muon (solid) events. Events with an output of the NN function less than 0.76 are rejected.

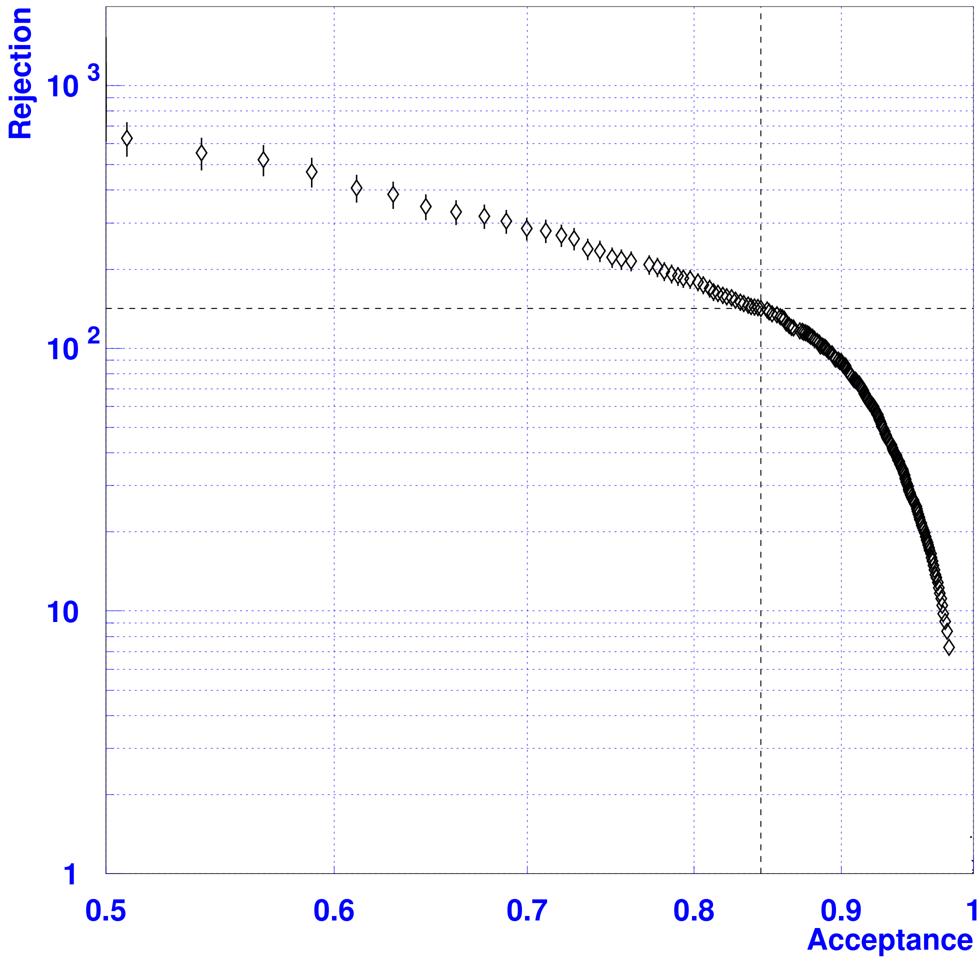

Figure 3.27: Rejection of the Neural Net $\pi^+ \to \mu^+$ Decay Cut as a function of the acceptance. The cross point of the vertical and horizontal lines shows the rejection and acceptance at the cut position.

3.5.4 Rejections against Photons and Accidental Activities

The signature of $K^+ \to \pi^+\nu\bar{\nu}$ is a single π^+ track, and no other particle is observed in the detector. Any activities that originate from a K^+ decay must be detected in the subsystems of the detector. The main backgrounds, including photon activities, are the $K_{\pi 2}$ and $K_{\mu\nu\gamma}$ decays. The energy of photons from $\pi^0 \to \gamma\gamma$ in $K_{\pi 2}$ decays is $20.2 < E_\gamma < 225.3$ MeV in the rest frame of K^+. On the contrary, the energy of a photon from $K_{\mu\nu\gamma}$ decays is in the range $0 < E_\gamma < 236$ MeV, and photons with low energy ($E_\gamma < 50$ MeV) are dominant [45]. The detection of photons whose energy is a few MeV is necessary to eliminate backgrounds related to photons.

The total rejection against backgrounds associated with photons is required to be 10^6. A rejection of 10^4 is already achieved by the online photon veto; further rejection is required to be 10^2 in the offline analysis.

Searches for the photons coincident with the track time are performed in the subsystems of the Barrel Veto (BV), the Barrel Veto Liner (BVL), the Range Stack (RS), the End Caps (EC), the target, the I-Counter (IC), the V-Counter (VC), the Collar (CO) and the Microcollar (MC). Different time windows and energy thresholds are set to the individual subsystems. For the BV, BVL and RS, whose scintillator signals are read out by both-end PMTs, energies and times of photon hits are basically obtained from the geometrical mean and the average time of both ends, respectively. In the case that the energies or times are missed in a single end of the ADCs or TDCs, these single-end hits are categorized separately and different time windows and energy thresholds are applied because the precisions of the time and energy measurements of the single-end hits are worse than those of the both-end hits. The definitions of all the categories are summarized in Appendix B.6.

The time window and energy threshold in each category are optimized by changing their cut positions to achieve better acceptance and rejection. The rejection of the Photon Veto Cuts against the $K_{\pi 2}$ background as a function of acceptance is shown in Figure 3.28. The cut position for each category is determined so that the $K_{\pi 2}$ background is reasonably suppressed in the background estimation. The cut position for each category is summarized in Table B.4. An acceptance of 90.5% and a rejection of 84.3 are achieved using this set of cut positions.

3.6 Background Characterization

The signal region for $K^+ \to \pi^+\nu\bar{\nu}$ is a "box" in multi-dimensional cut space. It is important to understand the distributions of all the backgrounds inside the signal region, because signal-to-background ratios of events observed near the boundary of the signal region are relatively lower than those of events observed deep inside the signal region. In the Bifurcation Method, several variables whose distributions for signals and backgrounds are well-separated are used to achieve large suppressions of backgrounds. These variables are also useful to understand the distributions of both the signals and backgrounds.

Below are the variables used to characterize each background.

- $K_{\pi 2}$ background:

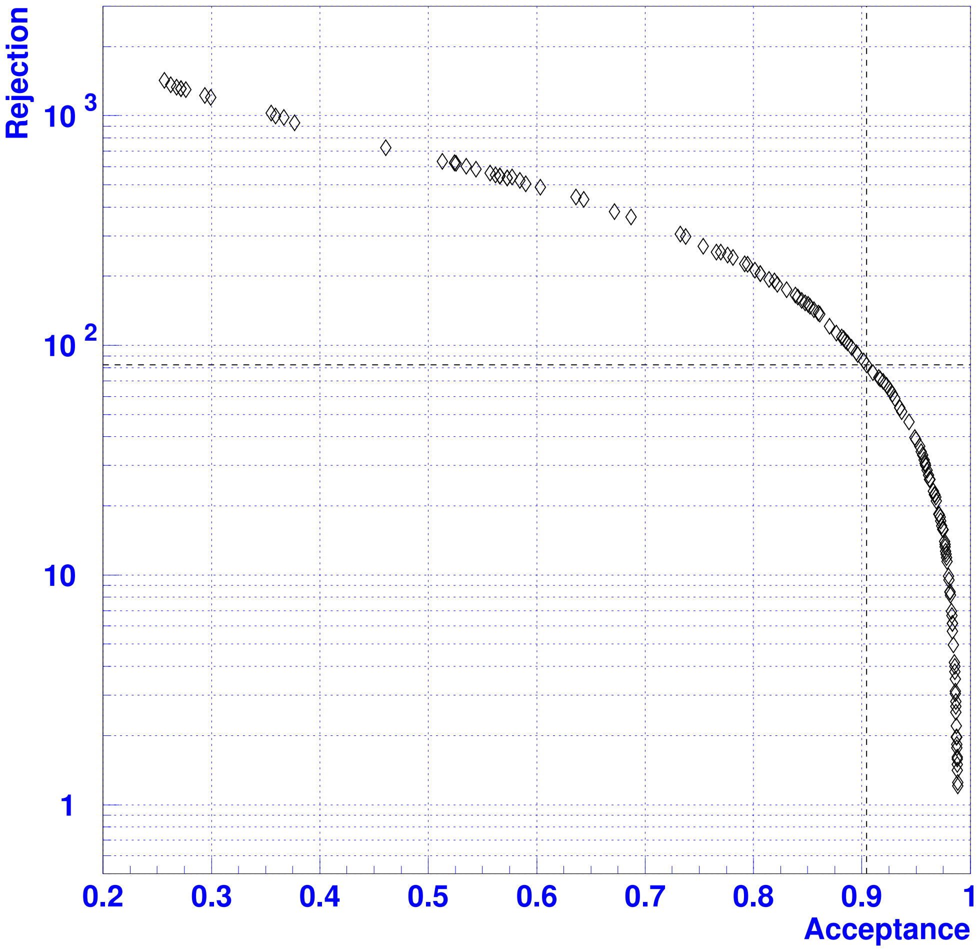

Figure 3.28: Rejection of the Photon Veto Cuts against the $K_{\pi 2}$ background as a function of the acceptance. The cross point of the vertical and horizontal lines shows the rejection and acceptance at the cut position.

– Deviations of the momentum, energy and range from the $K_{\pi 2}$ peaks: P_{dev}, E_{dev} and R_{dev}.
– The severity of the Photon Veto cut.

- Muon background:
  – Momentum (for $K_{\mu 2}$ Range Tail background).
  – Range deviation χ_{R-P} (for Muon Band background).
  – The output of the Neural Net function for $\pi^+ \to \mu^+ \to e^+$.
- Beam background:
  – Delayed coincidence $t_\pi - t_K$ (for Single Beam and CEX backgrounds).
  – Timing of beam particles with respect to the track time (for Double Beam background).

For the $K_{\pi 2}$ background, the background levels and the acceptances are examined by changing the severity of the Phase Space Cuts (i.e., varying P_{dev}, E_{dev}, R_{dev} simultaneously by certain amounts). At each value of P_{dev}, E_{dev}, R_{dev}, the background level compared to that at the standard cut position can be measured based on the distribution of the $K_{\pi 2}$ background in the P_{dev}, E_{dev}, R_{dev} parameter space. The relative acceptance can also be measured in the same way. Functions which represent the relative $K_{\pi 2}$ background level and acceptance at each P_{dev}, E_{dev}, R_{dev} can therefore be obtained. The functions that are associated with the $K_{\pi 2}$ kinematics are called the $K_{\pi 2}$ kinematic functions. The relative background level as a function of the relative acceptance with the same Phase Space Cuts, obtained from the $K_{\pi 2}$ kinematic functions, is shown in Figure 3.29. The background level and the acceptance between the individual cut points are calculated by a linear interpolation.

In addition to the $K_{\pi 2}$ kinematic functions, other functions are derived from the corresponding variables. The functions associated with the Photon Veto Cuts (the Photon Veto functions) represent the relative $K_{\pi 2}$ background level and the relative acceptance at each set of time windows and energy thresholds for the individual subsystems. The relative background level as a function of the relative acceptance obtained from the Photon Veto functions is shown in Figure 3.30.

The functions associated with the kinematics of the $K_{\mu 2}$ Range Tail background (the $K_{\mu 2}$ Range Tail functions) are measured based on the momentum distribution of the $K_{\mu 2}$ Range Tail background. The $K_{\mu 2}$ Range Tail functions represent the relative background level and the relative acceptance at each momentum value; see Figure 3.31. The functions associated with the kinematics of the Muon Band background (the Muon Band functions) are measured based on the range deviation (χ_{R-P}) distribution of the Muon Band background. The Muon Band functions represent the relative Muon Band background level and the relative acceptance at each χ_{R-P} value; see Figure 3.32. The relative background level as a function of the relative acceptance obtained from the $K_{\mu 2}$ Range Tail and Muon Band functions are shown in Figure 3.33.

The functions associated with the $\pi^+ \to \mu^+ \to e^+$ identification (the $\pi^+ \to \mu^+ \to e^+$ functions) are measured based on the distribution of the Muon background in the

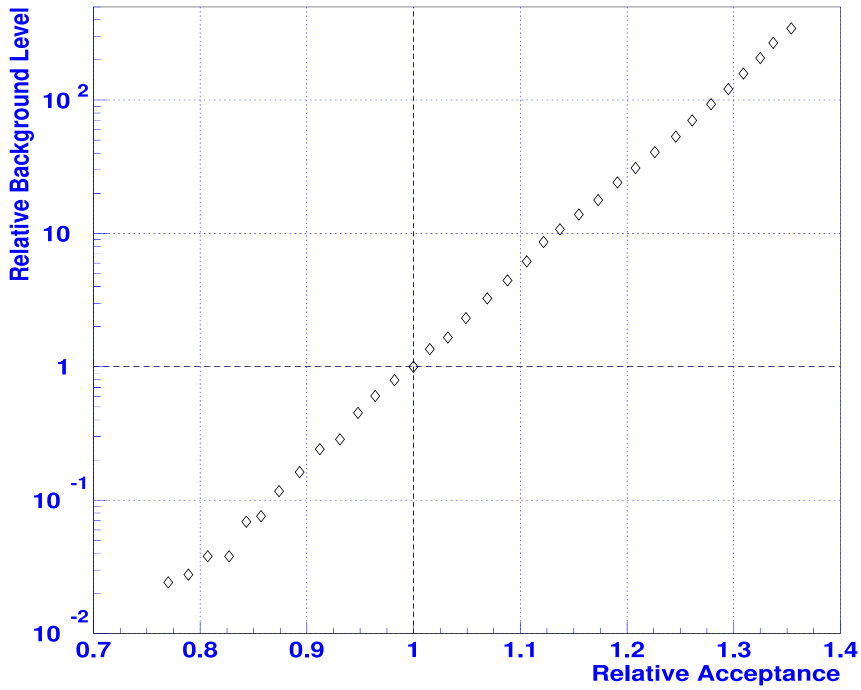

Figure 3.29: Relative background level as a function of the relative acceptance from the $K_{\pi 2}$ kinematic functions. The background level and the acceptance are normalized by those at the standard cut position.

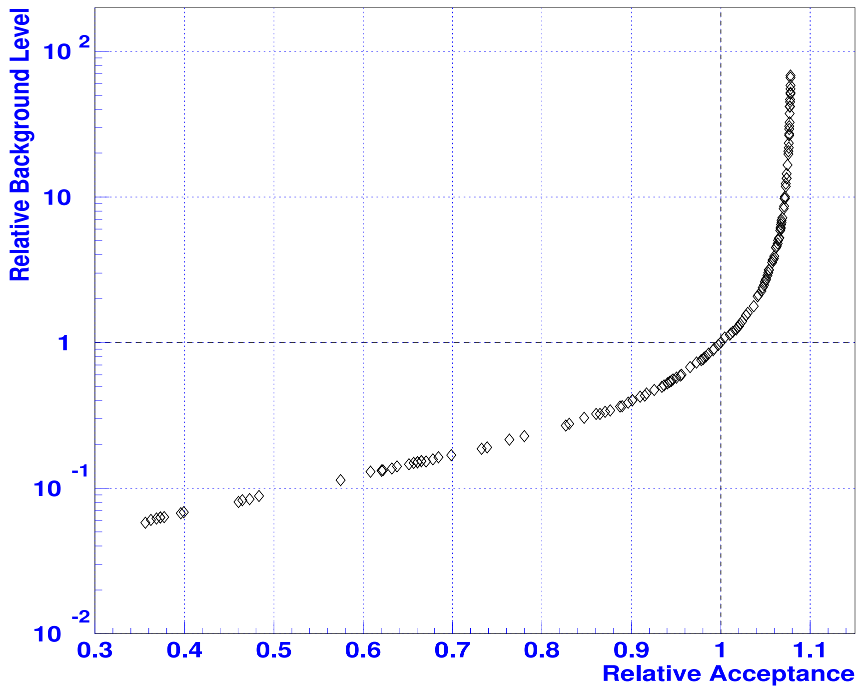

Figure 3.30: Relative background level as a function of the relative acceptance from the Photon Veto functions. The background level and the acceptance are normalized by those at the standard cut position.

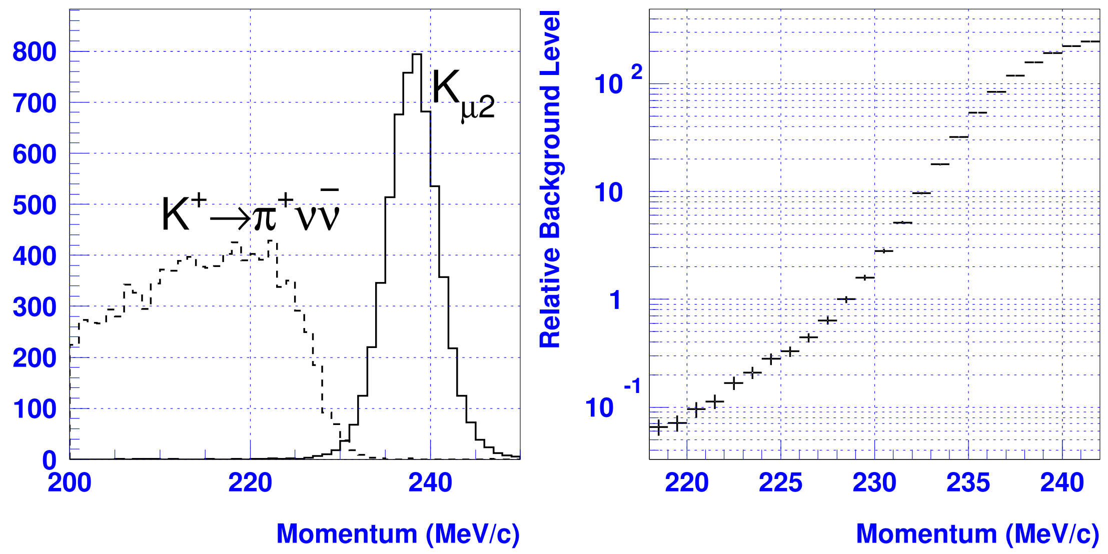

Figure 3.31: Momentum distributions for the signal (dashed) and background (solid) events (left). The signal sample is obtained from the Monte Carlo $K^+ \to \pi^+\nu\bar{\nu}$ events and the background sample from the $K_{\mu 2}$ Range Tail events in the $\pi\nu\bar{\nu}(1)$ trigger. Relative muon background level as a function of momentum (right). Each background level is normalized by that at the standard cut position ($P = 229$ MeV/c).

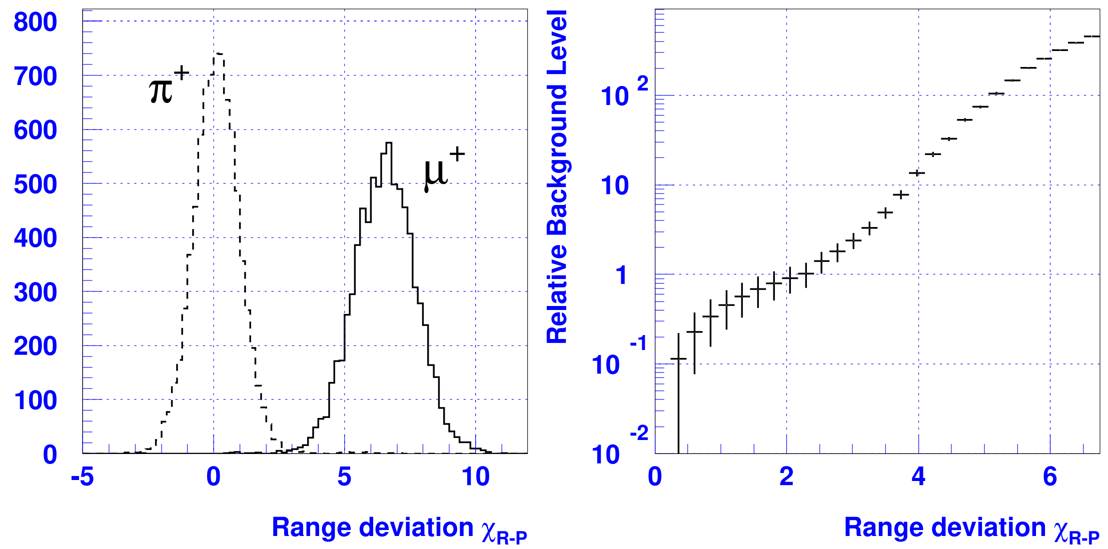

Figure 3.32: Distributions of the range deviation χ_{R-P} for the signal (dashed) and background (solid) events (left). The signal and background samples are obtained from the Pion Scattering and Muon Band events in the $\pi\nu\bar{\nu}(1)$ trigger. Relative Muon Band background level as a function of the range deviation (right). Each background level is normalized by that at the standard cut position ($\chi_{R-P} = 2.2$).

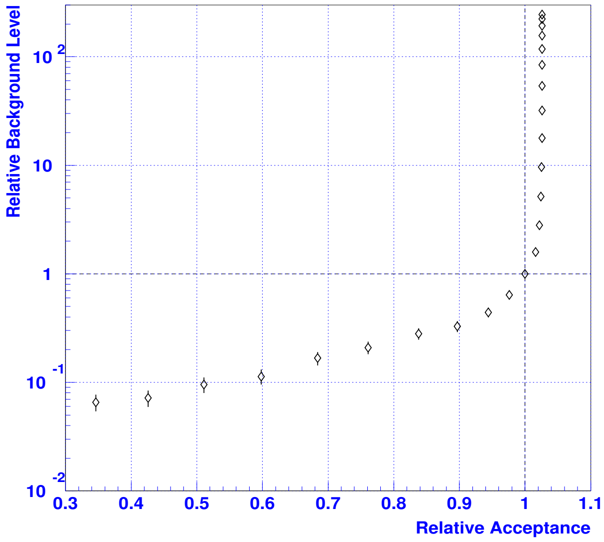

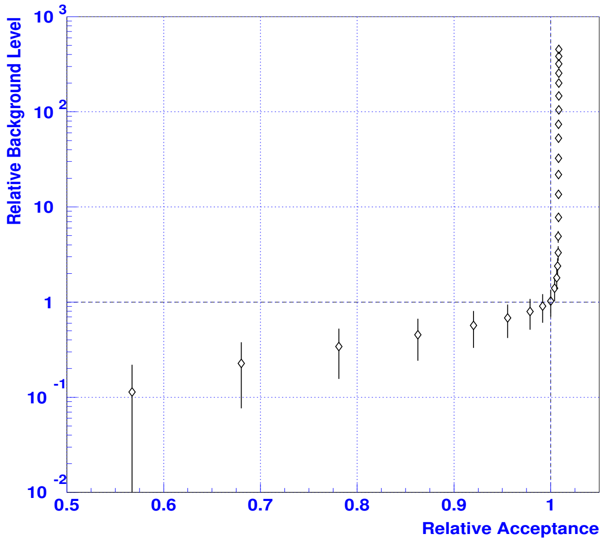

Figure 3.33: Relative $K_{\mu 2}$ Range Tail background level as a function of the relative acceptance (left). Relative Muon Band background level as a function of the relative acceptance (right).

parameter space of the Neural Net function (i.e., the output of the NN function). The $\pi^+ \rightarrow \mu^+ \rightarrow e^+$ functions represent the relative Muon background level and the relative acceptance at each output value of the NN function. The relative Muon background level as a function of the relative acceptance obtained from the $\pi^+ \rightarrow \mu^+ \rightarrow e^+$ functions is shown in Figure 3.34.

Finally, a set of functions associated with the Single Beam (including CEX) and Double Beam backgrounds (the 1-Beam and 2-Beam functions) are measured based on the Delayed Coincidence $t_\pi - t_K$ and the timings of hits in the BWPCs (t_{BWPC}) with respect to the track time (t_{RS}). The 1-Beam functions represent the relative background level and the relative acceptance at each value of $t_\pi - t_K$. The 2-Beam function represents the relative background level and relative acceptance at each value of $t_{BWPC} - t_{RS}$. The relative background levels as functions of the relative acceptances obtained from the 1-Beam and 2-Beam functions are shown in Figure 3.35. The relative background level and the relative acceptance at each parameter of the function are summarized in Appendix C.

3.7 Likelihood Analysis for Branching Ratio Calculation

All of these functions provide the relative background levels and the relative acceptances inside (and even outside) the signal region. The distributions of all backgrounds in the multi-dimensional cut space can be understood with these functions. Signal-to-background ratios, anywhere inside the signal region, can therefore be obtained by using the information of these functions. In order to investigate how a signal likelihood or a signal-to-background ratio varies inside the signal region, the signal region is divided into many small sub-regions ("cells"), and the signal likelihood or the signal-to-background

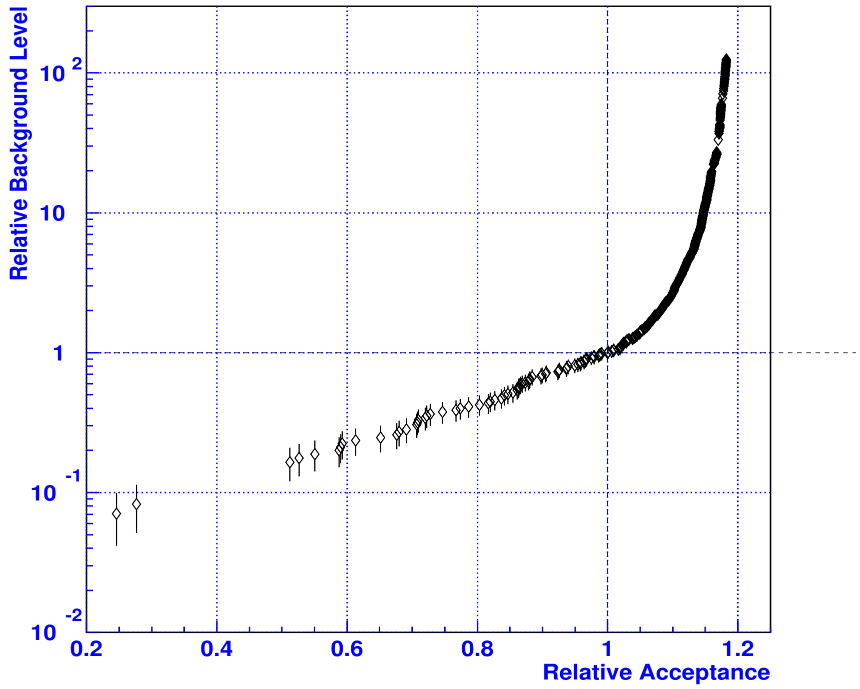

Figure 3.34: Relative Muon background level as a function of the relative acceptance from the $\pi^+ \rightarrow \mu^+ \rightarrow e^+$ function.

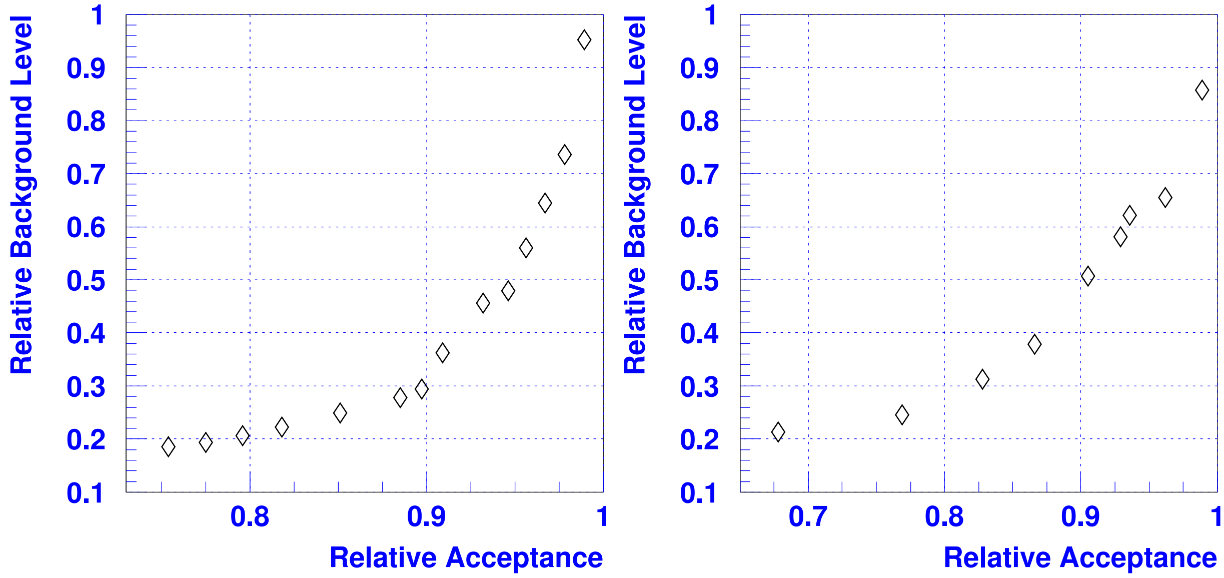

Figure 3.35: Relative background levels as functions of the relative acceptance for the Single Beam (left) and Double Beam (right) backgrounds. These functions show the relative background levels and relative acceptances inside the signal region.

ratio in each cell is determined.

The parameter space of each function is divided into bins, and cells are constructed by combining all of the binned parameter spaces. In each cell (the cell index is referred to as i), the signal acceptance, A_i, and the background level of all background sources, b_i, are obtained from the functions. The expected number of signal events in each cell, s_i, is assumed to be $s_i = \mathcal{B} N_K A_i$, where $\mathcal{B}$ is the branching ratio for $K^+ \to \pi^+ \nu\bar{\nu}$ [5] and N_K is the number of kaon decays in the target. Both the signal s_i and background b_i are estimated throughout the cells and the signal-to-background ratio in each cell, s_i/b_i, is obtained. If an event is observed in a cell that has a large signal-to-background ratio, the signal likelihood for the event is high.

Since both the signal s_i and background b_i are expected to be small in rare-decay searches, a careful statistical treatment is required to calculate the signal likelihood and the confidence levels. The branching ratio is obtained in E949 via a likelihood analysis. Following the method by T. Junk [46], a likelihood is constructed from the ratio of two joint Poisson probabilities: one is the probability with the signal-plus-background hypothesis; the other with the background hypothesis. That is, a likelihood estimator X, for n cells, is defined as

$$X \equiv \prod_{i=1}^{n} X_i, \quad \text{with} \quad X_i = \frac{\mathrm{e}^{-(s_i+b_i)}(s_i+b_i)^{d_i}}{d_i!} \Big/ \frac{\mathrm{e}^{-b_i}(b_i)^{d_i}}{d_i!} = \mathrm{e}^{-s_i}\left(1+\frac{s_i}{b_i}\right)^{d_i}, \tag{3.5}$$

where d_i is the number of observed candidate events in cell i. Once the signal region is examined and a set of observed candidates, d_i, is determined, the likelihood estimator, X, is calculated based on the given configuration of $\{s_i\}$, $\{b_i\}$ and $\{d_i\}$. The branching ratio is determined so that the likelihood X should be maximized by varying $\mathcal{B}$ as a parameter.

3.8 Determination of Signal Region

In cut developments using uniformly sampled 1/3 data in the $\pi\nu\bar{\nu}(1)$ trigger, all of the cut positions have been determined. Although the signal region should basically be a region inside the cut positions of all the selection criteria, the definition of the signal region is modified, before looking into the potential signal regions, in order to enlarge the signal acceptance. The modification is motivated as follows:

- The distributions of both signals and backgrounds in the cut space are understood well by the functions.
- The background levels can also be controlled well in the enlarged signal regions.
- In the likelihood ratio technique, the signal-to-background ratios of the cells that contain candidate events, not the total background level in the whole signal region, contribute to the branching-ratio measurement.

[5] The results obtained with the likelihood technique in this section do not depend on the value of $\mathcal{B}$ used in calculating s_i.

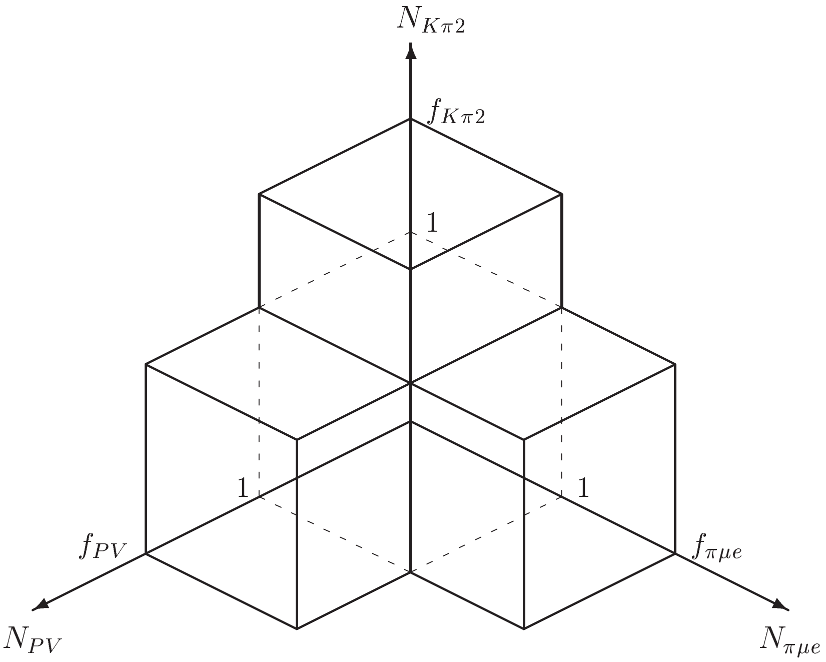

Figure 3.36: Schematic figure of the Signal Region in the 3-dimensional parameter space of the $\pi^+ \to \mu^+ \to e^+$, $K_{\pi 2}$ kinematic and Photon Veto functions (in the unit of relative background level).

The cuts to be loosened are those related to the $K_{\pi 2}$ kinematic, Photon Veto and $\pi^+ \to \mu^+ \to e^+$ functions. The cuts for the Muon and Beam backgrounds are not loosened, because the cut positions for the $K_{\mu 2}$ Range Tail and Muon Band backgrounds are at the knee in the background level v.s. acceptance curve (see Figure 3.33); loosening them does not provide much acceptance gain. Loosening the cut positions of the $K_{\pi 2}$ kinematic, Photon Veto and $\pi^+ \to \mu^+ \to e^+$ functions provides a relatively large acceptance gain. However, loosening three cuts simultaneously increases the background levels. The signal region is the combination of the following three cases:

- the cuts for the $K_{\pi 2}$ kinematics are loosened,
- the Photon Veto Cuts are loosened,
- the $\pi^+ \to \mu^+ \to e^+$ Decay Sequence Cuts are loosened.

When one of the three is loosened, the cut positions of the other two are kept unchanged. The schematic figure of the signal region in 3-dimensional space is shown in Figure 3.36. The revised (enlarged) signal region consists of the standard signal region, which is created without loosening any cuts, plus three extensions. Hereafter, the revised and standard signal regions are referred to as the Signal Region and the 1×1 Region, respectively. The regions created by loosening the Photon Veto Cuts, $\pi^+ \to \mu^+ \to e^+$ Decay Sequence Cuts and $K_{\pi 2}$ kinematic cuts are referred to as PV Extended, $\pi^+ \to \mu^+ \to e^+$ Extended and $K_{\pi 2}$ Kinematics Extended Regions, respectively [6]. The loosening factors for the cuts

[6] Each Extended Region includes the 1×1 Region.

Cuts	Loosening factor	Acceptance gain
$\pi^+ \to \mu^+ \to e^+$	4.2	$\times 1.12$
$K_{\pi 2}$ kinematic	9.5	$\times 1.12$
Photon Veto	4.0	$\times 1.07$
Total acceptance gain		$\times 1.31$

Table 3.4: Loosening factors for the $\pi^+ \to \mu^+ \to e^+$ Decay Sequence Cuts, the $K_{\pi 2}$ Kinematic Cuts and the Photon Veto Cuts (second column) with their acceptance gains (third column).

($f_{\pi\mu e}$, $f_{K\pi 2}$ and f_{PV}) are developed so that the background levels after loosening them are acceptable. The loosening factors and acceptance gains are summarized in Table 3.4. The loosening factors for these three cuts are $f_{\pi\mu e} = 4.2$, $f_{K\pi 2} = 9.5$ and $f_{PV} = 4.0$, which means 4.2-times more background related to the $\pi^+ \to \mu^+ \to e^+$ identification, 9.5-times more $K_{\pi 2}$ background and 4.0-times more background related to Photon Veto. The total acceptance gain by enlarging the signal region is 31%, which is the sum of the individual acceptance gains (12% from $K_{\pi 2}$, 12% from $\pi^+ \to \mu^+ \to e^+$ identification, and 7% from Photon Veto).

Chapter 4

Background Estimation

In this chapter, estimations of the background levels in the Signal Region are described. The backgrounds for $K^+ \to \pi^+ \nu\bar{\nu}$ are categorized into three groups:

- $K_{\pi 2}$ background,
- Muon background ($K_{\mu 2}$ Range Tail and Muon Band backgrounds), and
- Beam background (Single Beam, Double Beam, and Charge Exchange (CEX) backgrounds).

All of the backgrounds, except for the CEX background, are estimated with real data via a technique called the "Bifurcation Method". Estimations of the $K_{\pi 2}$ and Beam backgrounds are performed with a uniformly-sampled 2/3 portion of the $\pi\nu\bar{\nu}(1)$ trigger data (referred to as a 2/3 sample). The background estimation with a 2/3 sample is expected to have less bias than that with a 1/3 sample, which is used for designing the cuts. An estimation of the Muon background is performed with the full $\pi\nu\bar{\nu}(1)$ trigger data, because larger statistics are needed for the estimations [1].

4.1 Method of Background Estimation

In this analysis, the number of expected signal events is small. Background levels in the Signal Region have to be smaller than the expected signal events. Background measurements based on small samples have large statistical uncertainties. Estimations of background levels by the Bifurcation Method help to enhance the statistics and to make reliable measurements of background levels having less than one event. The estimation is performed with two uncorrelated cuts or groups of cuts, which are independently "inverted" to enhance the statistics. In other words, background samples are created by selecting events that fail at least one of the selection criteria used in this analysis.

A pictorial explanation for the Bifurcation Method is shown in Figure 4.1. First of all, a sample targeting one specific background source is selected by removing the other background sources. The number of events remaining after applying the setup cuts is

[1] Muon background estimation with a 2/3 sample was also performed, and it was confirmed that the estimations obtained from 2/3 and full samples are consistent.

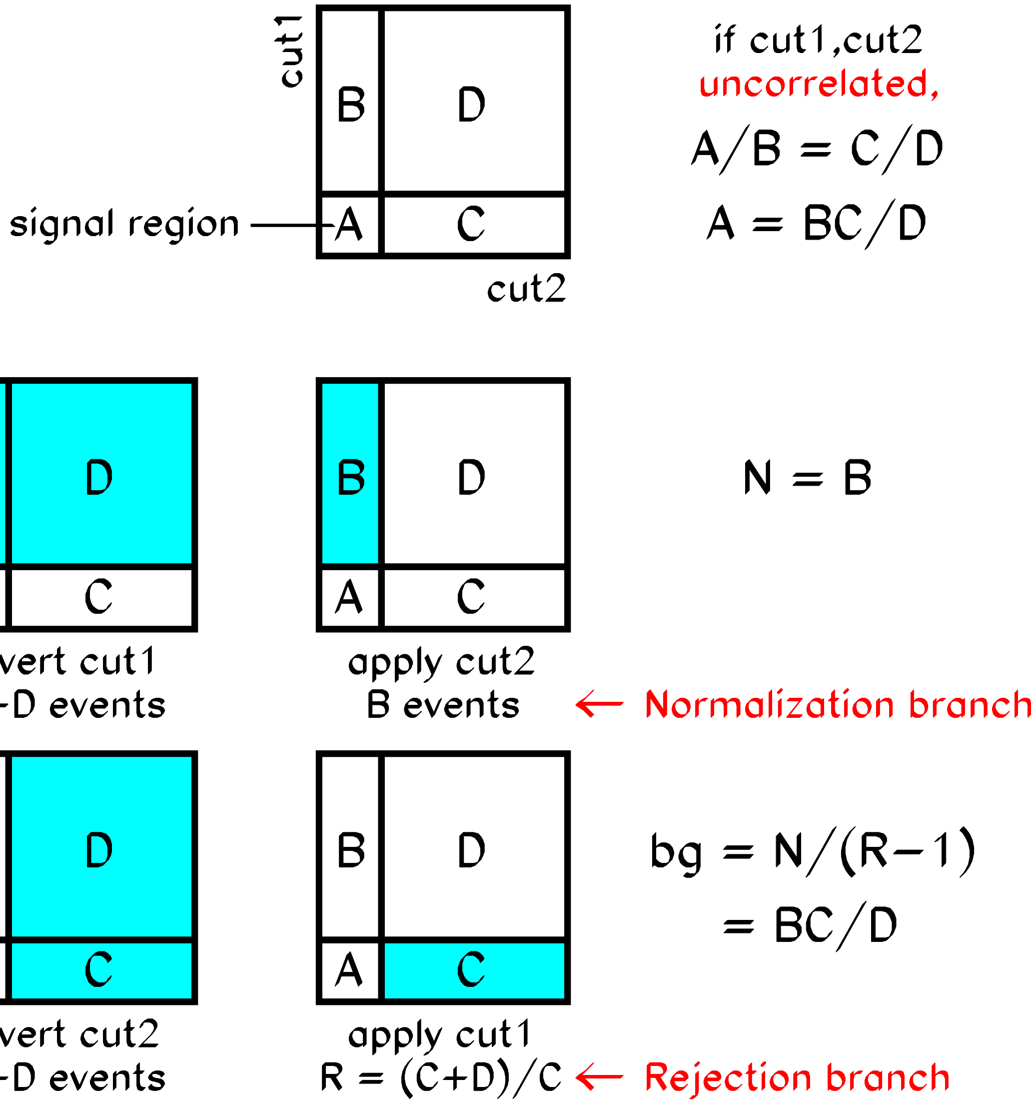

Figure 4.1: Pictorial explanation of the Bifurcation Method.

$A + B + C + D$ events. Each figure in Figure 4.1 shows the parameter space of two cuts, namely "cut1" and "cut2". The number of background events in the Signal Region (i.e., region "A") is A events. If the two cuts are uncorrelated, that is, if the rejection of a cut does not depend on the rejection of the other cut, the ratio of the number of background events in region "A" to region "B" must be equal to the ratio in region "C" to region "D", i.e., $A/B = C/D$. Background events in the Signal Region are therefore obtained from the relation $A = BC/D$. This is how background levels in the Signal Region are estimated using events outside the Signal Region.

The way to proceed with the Bifurcation Method is as follows:

- A specific background sample is prepared by inverting "cut1" ($B + D$ events remain); "cut2" is applied to the sample and B events remain (see the second row in Figure 4.1). This stream is called a "Normalization Branch".

- On the other hand, another background sample is also prepared by inverting "cut2" ($C + D$ events remain). By imposing "cut1", the ratio D/C is obtained (see the third row in Figure 4.1). The rejection factor of this "cut1", R, is calculated from the ratio $(C + D)/C$. This stream is called a "Rejection Branch".

- The number of background events in the Signal Region is estimated by the number of events remaining in the Normalization Branch, N $(= B)$, divided by the rejection factor, $R - 1$ $(= D/C)$, i.e., $N_{Bkg} = N/(R - 1)$.

As an example, a brief explanation for the $K_{\pi 2}$ background estimation via the Bifurcation Method is presented in Figure 4.2. The $K_{\pi 2}$ background sample in the $K^+ \rightarrow \pi^+ \nu \bar{\nu}$ trigger data is selected by removing the Muon and Beam backgrounds (corresponding to the first row in Figure 4.1). In the Normalization Branch, $K_{\pi 2}$ events are selected by requiring photon activities (i.e., the Photon Veto Cuts ("cut1") are inverted). The Phase Space Cuts (i.e., cuts on momentum, energy and range, "cut2") are applied to the $K_{\pi 2}$ sample and N events remain in the Normalization Branch (corresponding to the second row in Figure 4.1). In the Rejection Branch, $K_{\pi 2}$ events with momentum, energy and range in the $K_{\pi 2}$ peak are selected (i.e., the Phase Space Cuts, "cut2", are inverted). the Photon Veto Cuts ("cut1") are applied to the $K_{\pi 2}$ events in the kinematic peak (corresponding to the third row in Figure 4.1) and the rejection factor of the Photon Veto Cuts, $R - 1$, is measured. Finally, the $K_{\pi 2}$ background level is estimated based on the number of remaining events in the Normalization Branch (N) and the rejection factor ($R - 1$).

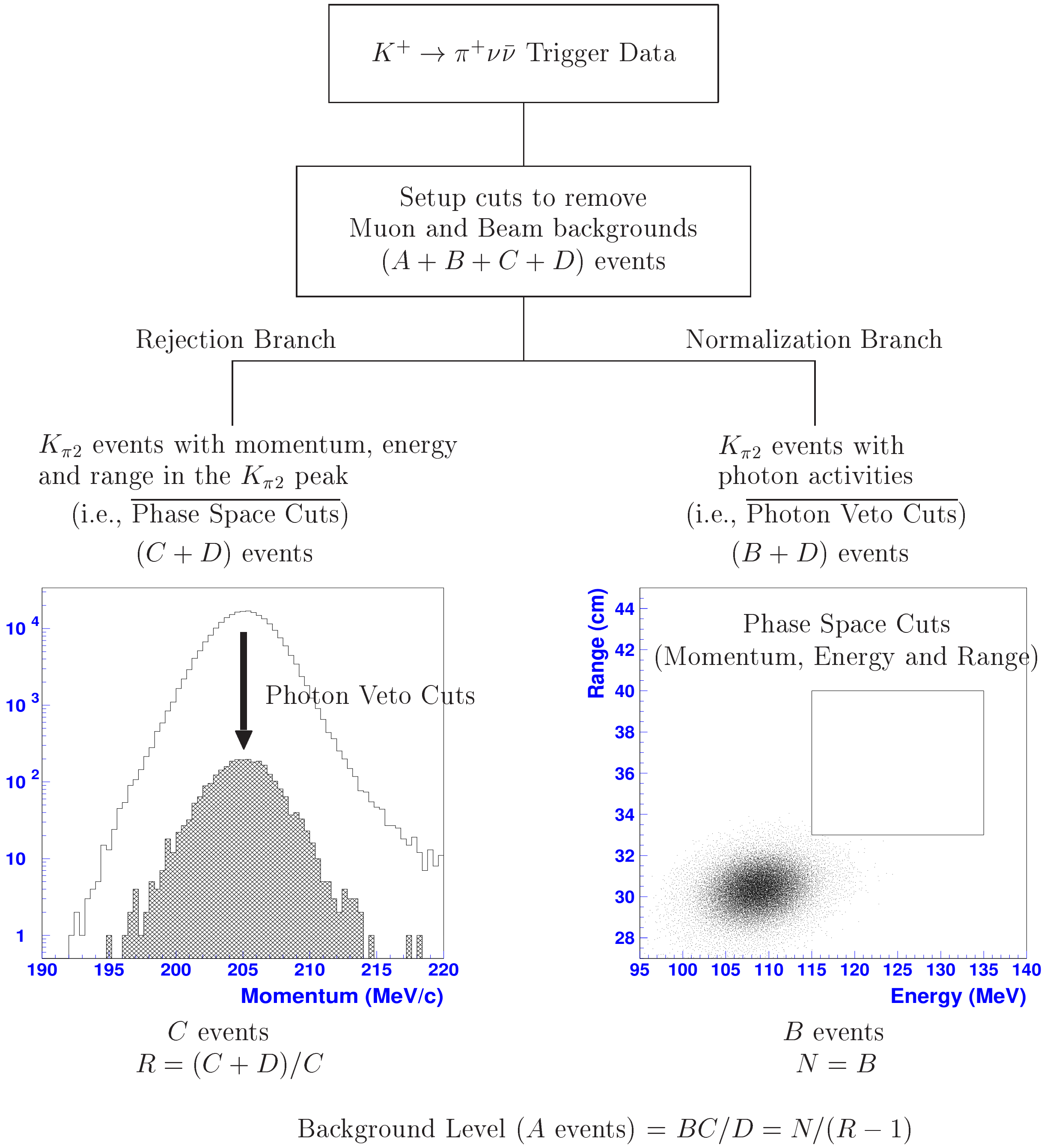

Figure 4.2: Example of the Bifurcation Method.

4.2 $K_{\pi 2}$ Background Estimation

The $K_{\pi 2}$ decay has a charged track with monochromatic momentum, range and energy, and has two photons at the track time. Two cuts for the Bifurcation are therefore the Phase Space Cuts to the π^+ track and the Photon Veto Cuts.

The $K_{\pi 2}$ background level is estimated in the following way. Setup cuts are applied to the $\pi\nu\bar{\nu}(1)$ trigger sample in order to remove other backgrounds, and to select events with well-reconstructed π^+ tracks. In the Rejection Branch, $K_{\pi 2}$ events with the momentum, energy, and range in the $K_{\pi 2}$ peak are selected (i.e., inverse of the Phase Space Cuts). Photon Veto Cuts are imposed on this $K_{\pi 2}$-rich sample. The Photon Veto rejection is measured to be

$$R_{PV} = \frac{481362}{5710} = 84.3 \pm 1.2(stat.). \tag{4.1}$$

In the Normalization Branch, $K_{\pi 2}$ events are selected by requiring photon activities (i.e., inverse of the Photon Veto Cuts). The Phase Space Cuts ($P_{dev} \geq 2.5$, $E_{dev} \geq 2.5$ and $R_{dev} \geq 2.75$) are imposed on this sample to count the number of the $K_{\pi 2}$ events remaining in the Normalization Branch. The suppression of the Phase Space Cuts is so large; the statistics of the events remaining in the Normalization Branch are very small. In order to perform a more precise estimation, so-called Second Bifurcation Method is performed.

Second Bifurcation means the Normalization Branch is further bifurcated. The Phase Space Cut for Energy ($E_{dev} \geq 2.5$) and the Cuts for Range and Momentum ($R_{dev} \geq 2.75$ and $P_{dev} \geq 2.5$) are separated as two independent cuts. The expected number of events in the Normalization Branch (N_{NB}) can be estimated by $N_{NB} = N_{RP}/(R_E - 1)$, where N_{RP} is the number of events that remain after the Phase Space Cuts for Range and Momentum are imposed, and R_E is the rejection of the Phase Space Cut for Energy. Details concerning the $K_{\pi 2}$ background estimation with the Second Bifurcation Method are given in Appendix D.1.

The estimation by the Second Bifurcation Method results in 1.04±0.20 events of the $K_{\pi 2}$ background (inside the 1×1 Region [2]) in the Normalization Branch. The estimations for the PV Extended, $\pi^+ \to \mu^+ \to e^+$ Extended and $K_{\pi 2}$ Kinematics Extended Regions are performed in the same way as the 1×1 Region, except that the corresponding cuts are loosened. The expected numbers of events in the Normalization Branch are summarized in Table 4.1.

Region	N_{NB} (events)
1×1	1.04±0.20
PV Extended	0.97±0.24
$\pi^+ \to \mu^+ \to e^+$ Extended	1.15±0.20
$K_{\pi 2}$ Kinematics Extended	9.01±1.00

Table 4.1: Expected numbers of events remaining in the Normalization Branch. The errors are statistical.

The background level in the Signal Region is evaluated by the sum of the background levels in the individual Extended Regions. Since each Extended Region contains the 1×1

[2] The 1×1 Region and the Signal Region are defined in Section 3.8

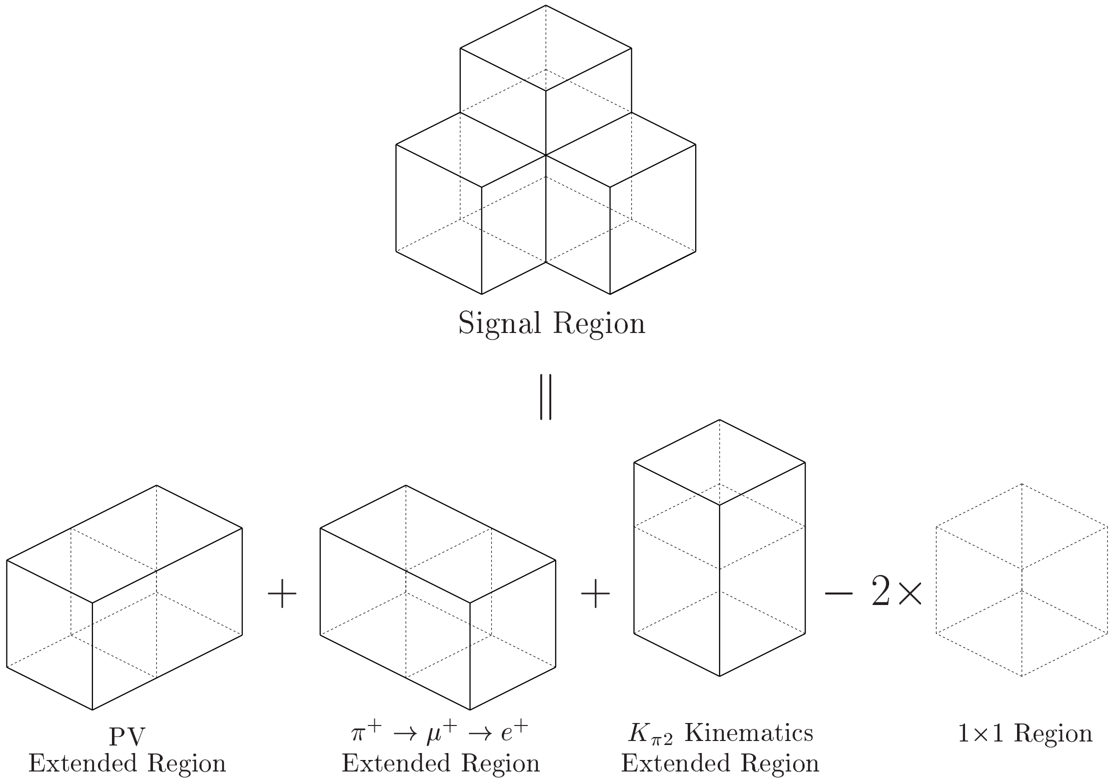

Figure 4.3: Method of the background level calculation in the Signal Region.

Region, the background levels that are over-counted should be subtracted (see Figure 4.3). The $K_{\pi 2}$ background level in the Signal Region is therefore obtained in the following way:

$$N_{K_{\pi 2}} = 1.5 \times \left[\frac{N_{NB}(PV)}{R'_{PV} - 1} + \frac{N_{NB}(\pi\mu e)}{R_{PV} - 1} + \frac{N_{NB}(K_{\pi 2})}{R_{PV} - 1} - 2\frac{N_{NB}(1 \times 1)}{R_{PV} - 1} \right], \tag{4.2}$$

where R'_{PV} represents the Photon Veto rejection at the loose cut position and is by a factor of 4 smaller than the standard Photon Veto rejection [3]. The coefficient 1.5 is the normalization factor from a 2/3 sample to the full sample. The $K_{\pi 2}$ background level is estimated to be

$$N_{K_{\pi 2}} = 0.216 \pm 0.023(stat.) \quad \text{in the Signal Region,} \tag{4.3}$$
$$N_{K_{\pi 2}} = 0.019 \pm 0.005(stat.) \quad \text{in the } 1 \times 1 \text{ Region.} \tag{4.4}$$

[3]The Photon Veto rejection at the loose cut position should be used for the estimation in the PV Extended Region.

4.3 Muon Background Estimation

The Muon background consists of $K_{\mu 2}$ Range Tail events, which originate from $K_{\mu 2}$ muons with elastic (or inelastic) scattering in the Range Stack, and the Muon Band events, which originate from $K_{\mu\nu\gamma}$ and $K_{\mu 3}$ decays, or π^+'s decaying in flight to μ^+. In all of these events, the muon track comes to rest, or interacts in the Range Stack. The $\pi^+ \rightarrow \mu^+ \rightarrow e^+$ Decay Sequence Cuts suppress these events. On the other hand, the $K_{\mu 2}$ Range Tail events have momenta consistent with $K_{\mu 2}$ ($P = 236$ MeV/c), measured correctly in the UTC; however, their ranges (and also energies) are smaller than those from $K_{\mu 2}$, and could satisfy the Phase Space Cuts for Range and Energy ($E \leq 135$ MeV and $R \leq 40$ cm). Only the Phase Space Cut for Momentum ($P \leq 229$ MeV/c) can work to suppress this background. The Kinematic Cut targeting the Muon Band background is different from that for the $K_{\mu 2}$ Range Tail background. Muons from the Muon Band events can be in the signal phase space due to their original momenta being lower than $K_{\mu 2}$, but their ranges are longer than those expected for pions with the same momenta. The Range-Momentum Consistency Cut, Equation (3.2), suppresses this background. Estimations for these backgrounds are performed separately.

The Muon background level is estimated in the following way. Setup cuts are applied to the $\pi\nu\bar{\nu}(1)$ trigger sample in order to remove the $K_{\pi 2}$ and Beam backgrounds. The $\pi^+ \rightarrow \mu^+$ Double Pulse Fitting Cut is applied to select events with the $\pi^+ \rightarrow \mu^+$ decay signature. In the Rejection Branch, $K_{\mu 2}$ Range Tail events whose momenta are consistent with $K_{\mu 2}$ are selected while Muon Band events in the range deviation (χ_{R-P}) peak are selected (i.e., inverse of the Kinematic Cuts for Muon background). Phase Space Cuts for Range and Energy are imposed on both backgrounds. The rejection of the $\pi^+ \rightarrow \mu^+ \rightarrow e^+$ Decay Sequence Cuts is measured together with both backgrounds. The rejection is measured to be

$$R_{\pi\mu e} = \frac{38268}{85} = 450.2 \pm 48.8(stat.). \tag{4.5}$$

In the Normalization Branch, Muon events that fail the $\pi^+ \rightarrow \mu^+ \rightarrow e^+$ Decay Sequence Cuts are selected (i.e., inverse of the $\pi^+ \rightarrow \mu^+ \rightarrow e^+$ Decay Sequence Cuts). The number of Muon events remaining in the Normalization Branch is obtained by applying the Phase Space Cuts and all other Kinematic Cuts. Since only a few events remain in the Normalization Branch, the Second Bifurcation Method is performed. In the Second Bifurcation, the $K_{\mu 2}$ Range Tail and Muon Band events are separately estimated. Contaminations of the $K_{\mu 2}$ Range Tail and Muon Band backgrounds into the Signal Region are estimated by using the template momentum and range deviation distributions (referred to as the Line Shape Method). Details of the Muon Background estimation are described in Appendix E.

The estimation by the Line Shape Method results in 4.65±0.14 and 2.19±0.14 events of the $K_{\mu 2}$ Range Tail and Muon Band backgrounds (inside the 1×1 Region) in the Normalization Branch, respectively. The numbers of events left in the Normalization Branch (N_{NB}) are summarized in Table 4.2. The $K_{\mu 2}$ Range Tail and Muon Band background levels in the Signal Region are obtained in the same way as the $K_{\pi 2}$ background estima-

Region	N_{NB} (events)	
	Muon Band	$K_{\mu 2}$ Range Tail
1×1	2.19±0.14	4.65±0.14
PV Extended	3.85±0.24	5.07±0.14
$\pi^+ \to \mu^+ \to e^+$ Extended	2.18±0.14	4.56±0.13
$K_{\pi 2}$ Kinematics Extended	2.27±0.14	4.65±0.14

Table 4.2: Numbers of events remaining in the Normalization Branch for the estimations of the Muon Band and $K_{\mu 2}$ Range Tail background levels. The errors are statistical.

tion,

$$N_{\text{Muon}} = \frac{N_{NB}(PV)}{R_{\pi\mu e} - 1} + \frac{N_{NB}(\pi\mu e)}{R'_{\pi\mu e} - 1} + \frac{N_{NB}(K_{\pi 2})}{R_{\pi\mu e} - 1} - 2\frac{N_{NB}(1 \times 1)}{R_{\pi\mu e} - 1}, \tag{4.6}$$

where $R'_{\pi\mu e}$ represents a rejection of the $\pi^+ \to \mu^+ \to e^+$ Decay Sequence Cuts at the loose cut position and is by a factor of 4.2 smaller than the standard one [4]. The background levels in the Signal Region (and the 1×1 Region) for the $K_{\mu 2}$ Range Tail and Muon Band backgrounds are summarized in Table 4.3.

Background	Signal Region	1×1 Region
$K_{\mu 2}$ Range Tail	0.0439±0.0050	0.0103±0.0011
Muon Band	0.0244±0.0030	0.0049±0.0006
Total	0.0683±0.0058	0.0152±0.0013

Table 4.3: Summary of the Muon background levels. The errors are statistical.

The Muon background level is therefore estimated to be

$$N_{\text{Muon}} = 0.0683 \pm 0.0058(stat.) \quad \text{in the Signal Region,} \tag{4.7}$$

$$N_{\text{Muon}} = 0.0152 \pm 0.0013(stat.) \quad \text{in the } 1 \times 1 \text{ Region.} \tag{4.8}$$

[4]The rejection of the $\pi^+ \to \mu^+ \to e^+$ Decay Sequence Cuts at the loose cut position should be used for estimations in the $\pi^+ \to \mu^+ \to e^+$ Extended Region.

4.4 Beam Background Estimation

4.4.1 Single Beam Background

The Single Beam background includes events in which beam pions scatter in the target, and events in which beam kaons decay in flight in the target [5]. In both cases the incoming particles scatter or decay immediately after they enter the target. The Delayed Coincidence Cuts can therefore suppress the Single Beam background. Moreover, the Timing Cuts in the beam instrumentation suppress the Single Beam background, since the times are expected to be close to the track time [6] due to the prompt scattering or decaying. The two cuts for the Bifurcation are the Delayed Coincidence Cuts and the Timing Cuts in the beam instrumentation.

The Single Beam background level is estimated in the following way. Setup cuts are applied to the $\pi\nu\bar{\nu}(1)$ trigger sample in order to remove other backgrounds. In the Rejection Branch, the Photon Veto Cuts except for the target are applied to remove $K_{\pi 2}$, $K_{\mu\nu\gamma}$, and $K_{\mu 3}$ decay-in-flight events. The Delayed Coincidence rejection is measured with the Pion Scattering events, which are tagged by requiring a small dE/dx in the B4 Hodoscope. The Delayed Coincidence rejection for K^+ decay-in-flight events is assumed to be the same as that for Pion Scattering events, since it is difficult to isolate K^+ decay-in-flight events without ambiguity [7]. The Delayed Coincidence rejection is summarized in Table 4.4.

Region	Rejection
Signal Region	$56178/16 = 3511.1 \pm 877.7$
1×1 Region	$51471/16 = 3216.9 \pm 804.1$

Table 4.4: Rejection of the Delayed Coincidence Cuts for the Single Beam background.

In the Normalization Branch, some additional setup cuts are applied for cleanup. Prompt events are tagged by inverting the Delayed Coincidence Cuts. The Pion Scattering and K^+ decay-in-flight events are estimated together. The Timing Cut in the Kaon Čerenkov Counter, the Photon Veto Cuts and the $\pi^+ \to \mu^+ \to e^+$ Decay Sequence Cuts are applied to suppress the $K_{\pi 2}$, $K_{\mu\nu\gamma}$ and $K_{\mu 3}$ decay-in-flight events; the Timing Cut in the Pion Čerenkov Counter and the dE/dx Cut in the B4 Hodoscope are also applied to suppress the Pion Scattering events; 14 events remain in the Signal Region and 9 events remain in the 1×1 Region, respectively. With the measured Delayed Coincidence rejection, the Single Beam background level is estimated to be

$$N_{1BM} = \frac{1.5 \times 14}{3511.1 - 1} = 0.00598 \pm 0.00219(stat.) \quad \text{in the Signal Region,} \quad (4.9)$$

$$N_{1BM} = \frac{1.5 \times 9}{3216.9 - 1} = 0.00420 \pm 0.00175(stat.) \quad \text{in the } 1 \times 1 \text{ Region.} \quad (4.10)$$

The coefficient 1.5 is the normalization factor from the 2/3 sample to the full sample.

[5] Events in which K^+ decay-in-flights occur between the Čerenkov counter and target are also included.
[6] Time of a charged track measured in the RS.
[7] In the Single Beam background sample, the contribution of the K^+ decay-in-flight events is negligibly small compared to that of the Pion Scattering events.

4.4.2 Double Beam Background

The Double Beam background consists of events with extra K^+'s or π^+'s in addition to the K^+'s that come at first. The extra K^+ events ($K-K$ events) are those in which the first K^+'s enter the target and then the second K^+'s decay in flight and produce π^+'s. The extra π^+ events ($K-\pi$ events) are the same as the $K-K$ events, except that the π^+'s instead of K^+'s scatter in the target. The Delayed Coincidence Cuts do not work on these events because the Kaon Fiber time (t_K) produced by the first K^+ and the Pion Fiber time (t_π) produced by the second K^+ or π^+ are unrelated. The Timing Cuts in the beam instrumentation (Kaon and Pion Čerenkov Counters, Beam Wire Chambers (BWPCs) and B4 Hodoscope) can reject the Double Beam background, since their timings, if recorded, are correlated to the track time produced by the extra K^+ or π^+. The Target Pattern Recognition Cuts are also able to find extra particles other than the initial K^+ hit when the kaon cluster is apart from the second particle hits.

The Double Beam background level is estimated in the following way. Setup cuts are applied to the $\pi\nu\bar{\nu}(1)$ trigger sample in order to remove $K_{\pi 2}$, Muon and Single Beam backgrounds. In the Rejection Branch, some additional setup cuts are applied to select pion tracks. Double Beam events are selected by requiring hits in the B4 Hodoscope at the track time. The rejection of the Timing Cuts in the Kaon (Pion) Čerenkov Counter and BWPCs is measured with the $K-K$ ($K-\pi$) events tagged by requiring that the second particle has a large (small) dE/dx in the B4 Hodoscope. The rejections are summarized in Table 4.5.

Region	$K-K$ event	$K-\pi$ event
Signal Region	2454/28 = 87.6±16.5	43876/14 = 3134.0±837.5
1×1 Region	2323/27 = 86.0±16.5	42661/14 = 3047.2±814.3

Table 4.5: Rejection of the Timing Cuts in the beam instrumentation for the Double Beam background.

In the Normalization Branch, some additional setup cuts are applied. The estimations for the $K-K$ and $K-\pi$ events are separately performed with the Second Bifurcation Method. Details of the Double Beam background estimation with the Second Bifurcation are described in Appendix D.2.

The predicted numbers of the $K-K$ and $K-\pi$ events remaining in the Normalization Branch are $\mathrm{N}_K = 0.16$ and $\mathrm{N}_\pi = 0.30$ ($\mathrm{N}_K = 0.15$ and $\mathrm{N}_\pi = 0.29$ in the 1×1 Region), respectively. With the measured rejection of the Timing Cuts in the beam instrumentation, the Double Beam background level is estimated to be

$$N_{2beam} = 1.5 \cdot \left(\frac{0.156}{87.6-1} + \frac{0.298}{3134.0-1} \right) = 0.00284 \pm 0.00207(stat.) \tag{4.11}$$

in the Signal Region and

$$N_{2beam} = 1.5 \cdot \left(\frac{0.152}{86.0-1} + \frac{0.293}{3047.2-1} \right) = 0.00283 \pm 0.00207(stat.) \tag{4.12}$$

in the 1×1 Region.

4.4.3 Charge Exchange Background

A Charge Exchange (CEX) reaction of K^+ in the target creates a K_L^0. The semi-leptonic decay of $K_L^0 \to \pi^+ l^- \bar{\nu}_l$ could produce a π^+ track with the kinematic values in the signal phase space. As described in Section 3.1, the CEX events are expected in the target to have a gap between the fibers of the incoming K^+ and the outgoing π^+, and to have an extra l^- track; these events can be suppressed by the Target Pattern Recognition Cuts. The Delayed Coincidence Cuts also suppress them because K_L^0 should not have traveled so far away after imposing cuts on the large gap. The CEX background is therefore expected to be suppressed by the same cuts that are used for the other Beam backgrounds. The CEX background sample is difficult to be isolated from the real data. Instead of using the real data, Monte Carlo data is generated and all cuts are applied to the sample in order to estimate the remaining CEX background events.

For the Monte Carlo simulation, information on the cross section for the CEX reaction, the production points and the momentum vector of K_L^0 is necessary. Since that concerning K_S^0 and K_L^0 from the CEX reaction is the same, and the $K_S^0 \to \pi^+\pi^-$ decay (unlike $K_L^0 \to \pi^+ l^- \bar{\nu}_l$ decay) can be reconstructed easily in the E949 detector, information concerning the K_L^0 production points and momentum vector at the points is obtained from the K_S^0 measurements with real data. The values used to calculate the K_L^0 production rate [8] are summarized in Table 4.6, and the rate is calculated to be $R_{K_L^0} = 2.73 \times 10^{-5}$. Details of the K_S^0 event selection and the measurement of the K_L^0 production rate are described in Appendix F.

Description	Parameter	Values
# of selected K_S^0 events	$N_{K_S^0}$	8086
K_S^0 selection efficiency	$\epsilon_{K_S^0}$	0.138
Photon Veto efficiency	A_{PV}	0.680
$K_S^0 \to \pi^+\pi^-$ Branching Ratio	$\mathcal{B}(K_S^0 \to \pi^+\pi^-)$	0.686
# of K^+ Triggers (10^{12})	KB_{live}	1.77
Prescale Factor	PS	384
K_L^0 Production Rate	$R_{K_L^0}$	2.73×10^{-5}

Table 4.6: K_L^0 production rate and the quantities that are used to estimate it.

Using the quantities measured with K_S^0 data, Monte Carlo events of both $K_L^0 \to \pi^+\mu^-\bar{\nu}_\mu$ ($K_{\mu3}^0$) and $K_L^0 \to \pi^+ e^- \bar{\nu}_e$ (K_{e3}^0) decays are generated in order to estimate the CEX background level; 2.076×10^{11} Monte Carlo events are generated for each decay. These numbers of K_L^0 decays correspond to the number of K^+ entering the target, as

$$\begin{aligned} KB_{live}^{MC} &= 2.076 \times 10^{11} / R_{K_L^0} \\ &= 7.604 \times 10^{15}. \end{aligned} \tag{4.13}$$

All of the signal selection cuts, except for the $\pi^+ \to \mu^+ \to e^+$ Decay Sequence Cuts and the Beam Cuts that are not related to the target quantities, are applied to the Monte

[8] The K_L^0 production rate is defined as $R_{K_L^0} \equiv \frac{N_{K_S^0}}{\epsilon_{K_S^0} \cdot A_{PV} \cdot \mathcal{B}(K_S^0 \to \pi^+\pi^-) \cdot KB_{live}/PS}$.

Carlo events [9]. 77 K_L^0 events in the Signal Region (67 in the 1×1 Region) survive, among which 56 events are due to K_{e3}^0 decay and 21 due to $K_{\mu 3}^0$ decay. The expected CEX events are estimated to be

$$\begin{aligned} N_{CEX} &= \left(N_{pass}^{K_{e3}^0} \times \frac{KB_{live}^{real}}{KB_{live}^{MC}} + N_{pass}^{K_{\mu 3}^0} \times \frac{KB_{live}^{real}}{KB_{live}^{MC}} \right) \times A \\ &= \left(56 \times \frac{1.77 \times 10^{12}}{7.604 \times 10^{15}} + 21 \times \frac{1.77 \times 10^{12}}{7.604 \times 10^{15}} \right) \times 0.250 \\ &= 0.00448 \pm 0.00051(stat.), \end{aligned} \tag{4.14}$$

where $N_{pass}^{K_{e3}^0}$ and $N_{pass}^{K_{\mu 3}^0}$ are the numbers of K_{e3}^0 and $K_{\mu 3}^0$ events passing all cuts, KB_{live}^{real} is the KB_{live} for the real data and A is the acceptance of the cuts that are not used for the Monte Carlo CEX events, and estimated to be 0.250. The error is taken from the statistical error of the surviving Monte Carlo events.

4.4.4 Total Beam Background

The final Beam background levels are summarized in Table 4.7. The total Beam background level in the Signal Region is estimated to be

$$N_{\text{beam}} = 0.0133 \pm 0.0031(stat.). \tag{4.15}$$

Background	Background Level (events)	
	Signal Region	1×1 Region
1 Beam	0.0060±0.0022	0.0042±0.0018
2 Beam	0.0028±0.0021	0.0028±0.0021
CEX	0.0045±0.0005	0.0039±0.0005
Total	0.0133±0.0031	0.0109±0.0028

Table 4.7: Total Beam background level and the contribution from each Beam background. The errors are statistical.

4.5 The "Outside-the-Box" Correlation Study

In the Bifurcation Method, it is assumed that the two Bifurcation cuts used are not correlated; if there are correlations, the estimation becomes screwed up. In order to ensure that the estimations are correct and reliable, it has to be tested whether there could be such a correlation between the two cuts or not.

The test of the correlation is performed with the events outside the Signal Region. If two Bifurcation cuts are not correlated, the background levels inside the Signal Region

[9] The Monte Carlo in E949 does not simulate the beam instrumentation nor the pulse shape information of the TDs and CCDs.

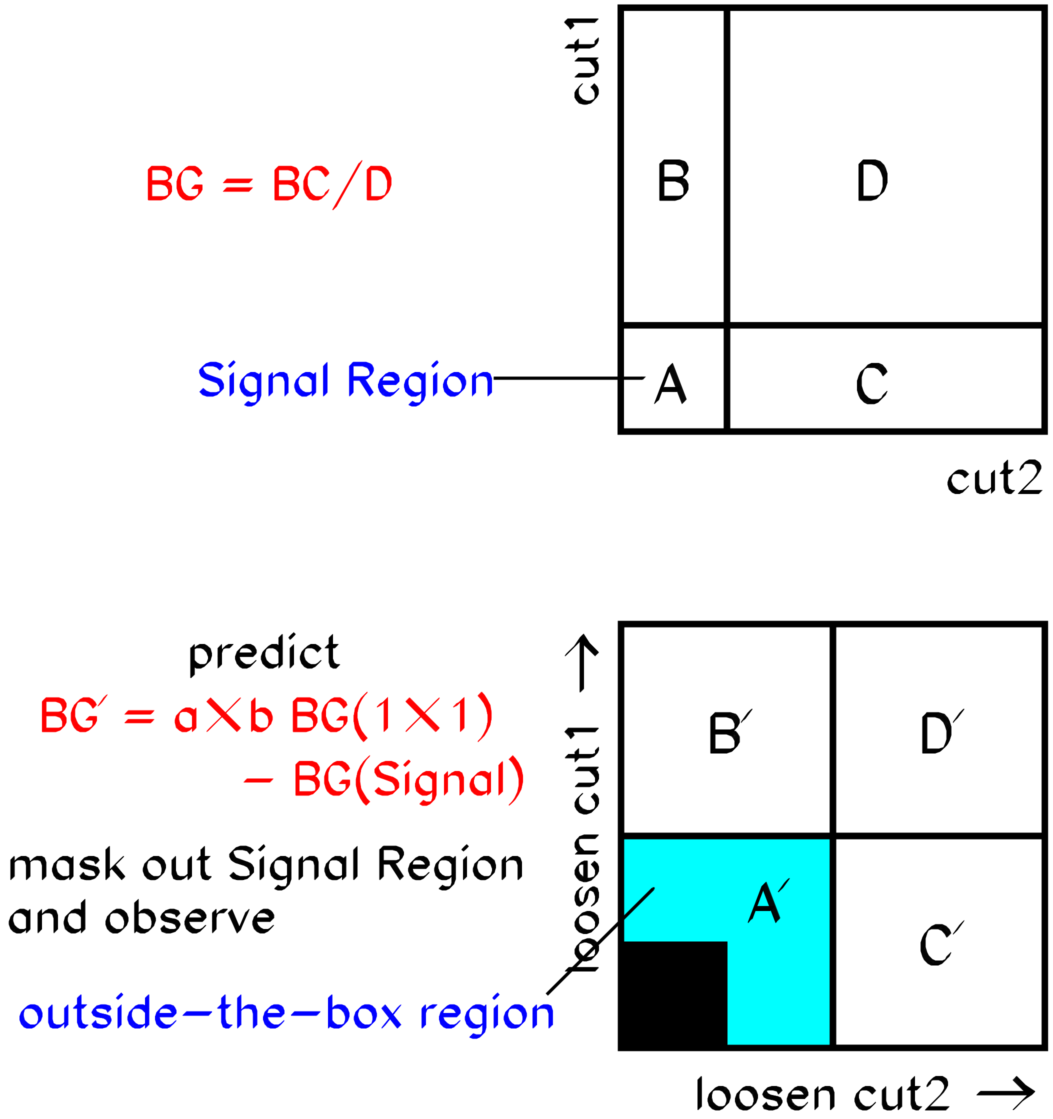

Figure 4.4: Pictorial explanation of the correlation study using the events outside the Signal Region.

are correct. In other words, if the distribution of each background source both inside and outside the Signal Region is understood well by the two functions associated with the Bifurcation cuts, the amount of the background even outside the Signal Region should be estimated correctly.

Figure 4.4 shows a pictorial explanation of the correlation study. A region outside the Signal Region (A' in Figure 4.4) is defined by loosening two Bifurcation cuts (cut1 and cut2) simultaneously by certain amounts (e.g., loosening factors for the cut1 and cut2 are a and b, respectively). It should be noted that the Signal Region is still masked out. This region A' is referred to as the "outside-the-box" region. If the background functions associated with the cut1 and cut2 are correct, the expected number of background events in the outside-the-box region is estimated to be

$$BG(\text{predicted}) = a \times b \times BG(1 \times 1 \text{ Region}) - BG(\text{Signal Region}), \tag{4.16}$$

	(Photon Veto) $\times$ ($K_{\pi 2}$ kinematics)				
$K_{\pi 2}$	10×10 1.11±0.18 3	20×20 4.86±0.61 4	20×50 12.36±1.26 9	50×50 31.11±3.14 22	50×100 62.36±5.59 53
	$(\pi^+ \to \mu^+ \to e^+)$ $\times$ ($K_{\mu 2}$ kinematics)				
$K_{\mu 2}$ Range Tail	10×10 0.35±0.03 0	20×20 1.44±0.10 1	50×50 9.07±0.62 12	80×50 14.52±0.99 16	120×50 21.78±1.48 25
	$(\pi^+ \to \mu^+ \to e^+)$ $\times$ ($K_{\mu 2}$ kinematics)				
Muon Band	10×10 0.31±0.03 1	20×20 1.28±0.11 1	50×20 3.22±0.27 4	80×20 5.17±0.44 5	80×40 10.35±1.07 11

Table 4.8: Results of a correlation study for the $K_{\pi 2}$ (top), $K_{\mu 2}$ Range Tail (middle) and Muon Band (bottom) backgrounds. The first row in each background represents the loosening factors of the Bifurcation cuts; the second represents the predicted number of events in each outside-the-box region, which is obtained from Equation (4.16); and the third represents the number of observed events in each region. The errors in the predictions are statistical uncertainties.

where $BG(1\times 1 \text{ Region})$ and $BG(\text{Signal Region})$ are the background levels in the 1×1 and Signal Regions, respectively, which are measured in the background estimation. The number of observed events in the outside-the-box region should be compared to this predicted number of background events. If the observation does not agree with the prediction, a correlation between the Bifurcation cuts could be indicated. The observation is performed in the same way as the Bifurcation Method used in the background estimation in the Signal Region, except that two Bifurcation cuts are loosened by factors of a and b [10].

The results of the correlation study for the $K_{\pi 2}$, $K_{\mu 2}$ Range Tail and Muon Band backgrounds are summarized in Table 4.8. In this table, the first row in each background represents the loosening factors of the Bifurcation cuts; the second represents the predicted number of events in each outside-the-box region obtained from Equation (4.16); and the third represents the observed number of events in each region. Both the predicted and observed numbers of events are in good agreement. Figure 4.5 visualizes the results of the correlation study. To verify these results numerically, the observations and predictions are fitted with the form

$$N_{\text{obs}} = c \times N_{\text{pred}}, \tag{4.17}$$

where the values of N_{obs} and N_{pred} are arranged so as to be independent bin-to-bin. For example, the value of N_{pred} for the $K_{\pi 2}$ background for the 20×20 bin is taken as

$$\text{Prediction for } 20 \times 20 \text{ bin} = \text{Predicted}(20 \times 20) - \text{Predicted}(10 \times 10), \tag{4.18}$$

where Predicted(20×20) is the value in Table 4.8 for (Photon Veto) $\times$ ($K_{\pi 2}$ Kinematics) of 20×20. A similar procedure is used for N_{obs}. The error on N_{pred} for the 20×20 bin is

[10] The corresponding cut positions can be known by the functions.

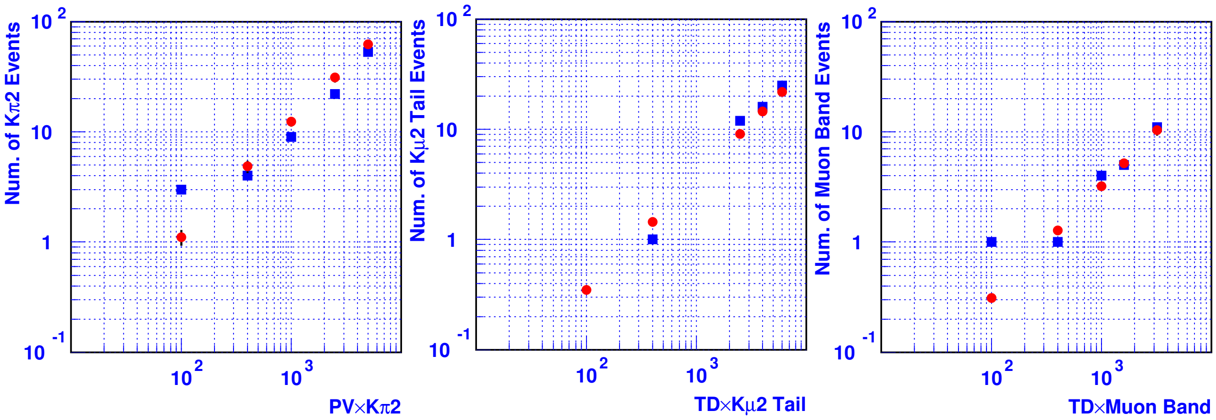

Figure 4.5: Visualization of the results of the correlation test for $K_{\pi 2}$ (left), $K_{\mu 2}$ Range Tail (middle), and Muon Band (right) backgrounds. The vertical axis is the number of predicted or observed events; the horizontal axis is the loosening factor. The dots represent the prediction, and square dots represent the observation.

taken as the difference in quadrature of the corresponding uncertainties in the table. The quantities of the fit are estimated with [5]

$$\chi^2 \equiv -2\ln\mathcal{L} = \sum_{i=1}^{5}\left[2(N^i_{th} - N^i_{obs}) + 2N^i_{obs}\ln(N^i_{obs}/N^i_{th})\right], \tag{4.19}$$

where N^i_{obs} and $N^i_{th}(\equiv c \times N^i_{pred})$ are the observed and theoretical contents of bin i, respectively. The results of the fit are summarized in Table 4.9.

Background	c	χ^2	χ^2 Probability
$K_{\pi 2}$	$0.850^{+0.122+0.150}_{-0.112-0.111}$	6.486	0.166
$K_{\mu 2}$ Range Tail	$1.148^{+0.245+0.156}_{-0.214-0.123}$	2.374	0.667
Muon Band	$1.063^{+0.353+0.210}_{-0.289-0.151}$	4.046	0.400

Table 4.9: Results of fits for the $K_{\pi 2}$, $K_{\mu 2}$ Range Tail and Muon Band backgrounds. The first and second uncertainties on c are the statistical uncertainty in N_{obs} and the uncertainty in N_{pred}, respectively.

The fit takes into account the statistical uncertainty in N_{obs} by using the above equation. To study the uncertainty in c due to the uncertainty in N_{pred}, N_{pred} is varied to be larger and smaller by the amount of uncertainty in N_{pred}, and the change in the fitted value of c is taken as an estimate of the uncertainty. The value of c for each background is close to unity within the uncertainty. This means that the observations and predictions are consistent with each other. These results of the correlation study give us confidence that the background estimations via the Bifurcation Method are correct.

4.6 Summary of Background Estimations

The final background levels are summarized in Table 4.10. The total background level in the Signal Region is estimated to be 0.297±0.024 events, in which the $K_{\pi 2}$ background contribution is the largest (0.216 events). This total background level appears to be non-negligible in the expectation of a few candidate events. However, with the likelihood ratio technique explained in Section 3.7, the branching ratio in this analysis is evaluated from the signal-to-background ratios of the cells where signal candidate events are observed, not from a simple counting of the number of events in the whole Signal Region and comparison with the total background level. The measured total background level is no longer a standard to judge whether the search is background-limited or not.

Background	Background Level (event)	
	Signal Region	1×1 Region
$K_{\pi 2}$	0.216±0.023	0.019±0.005
Muon	0.068±0.006	0.015±0.001
Beam	0.013±0.003	0.011±0.003
Total	0.297±0.024	0.045±0.006

Table 4.10: Total background level and the contribution from each background source. The errors are statistical.

Chapter 5

Examination of the Signal Region

All of the signal selection criteria have been prepared as discussed in Chapter 3, and the background levels for all of the background sources have been estimated as explained in Chapter 4. The Signal Region is therefore examined with all of the $\pi\nu\bar{\nu}(1)$ trigger data.

One candidate event is observed near the upper kinematic limit for $K^+ \to \pi^+\nu\bar{\nu}$ decay. Figure 5.1 shows the range and kinetic energy of the events that pass all of the selection criteria, except for the Phase Space Cuts for Range and Energy. Figure 5.2 shows that the reconstruction of the candidate event is made correctly in the target, UTC and Range Stack. No other beam particle coincident with the track time is detected in the beam instrumentation. No activity is detected at the track time in the photon detectors. The properties of the candidate event are tabulated in Table 5.1.

The charged track of the candidate event has a momentum of $P = 227.3 \pm 2.7$ MeV/c, a kinetic energy of $E = 128.9 \pm 3.6$ MeV and a range of $R = 39.2 \pm 1.2$ cm. Figure 5.3 shows the range vs kinetic energy of Monte Carlo $K^+ \to \pi^+\nu\bar{\nu}$ events that satisfy all of the cuts, except for the Phase Space Cuts for Range and Energy. Figure 5.4 shows the momentum, kinetic energy and range distributions of Monte Carlo $K^+ \to \pi^+\nu\bar{\nu}$ events. All of the cuts, except for the Phase Space Cut for each variable, are applied in the plots. These kinematic values of the candidate event are near the kinematic limit of the $K^+ \to \pi^+\nu\bar{\nu}$ decay. Comparisons with the signal distributions indicate that the candidate event has the proper kinematic quantities as a signal, although it exists in a relatively small acceptance region. Figure 5.5 shows the momentum, kinetic energy and range distributions for the $K_{\pi 2}$ events in the run that contains the candidate event. The fitted mean values of these distributions are consistent with the true kinematic values of $K_{\pi 2}$ decay ($P = 205.1$ MeV/c, $E = 108.6$ MeV and $R = 30.4$ cm). This indicates that the kinematic measurements for this candidate event are correct within the errors of the measurements. Figure 5.6, which shows the range vs momentum distribution of the Muon background, indicates that the candidate event is observed in the region where the Muon background level is relatively higher in the Signal Region. Figure 5.7 shows the momentum distribution of the $K_{\mu 2}$ Range Tail background and the range deviation distribution of the Muon Band background. The range deviation of the candidate event is far away from those of the Muon Band events; however, the momentum is 2.4σ away from the $K_{\mu 2}$ momentum peak. Figure 5.8 shows the signal and background distributions of the three quantities in the Range Stack dE/dx Cuts. All of the distributions show that

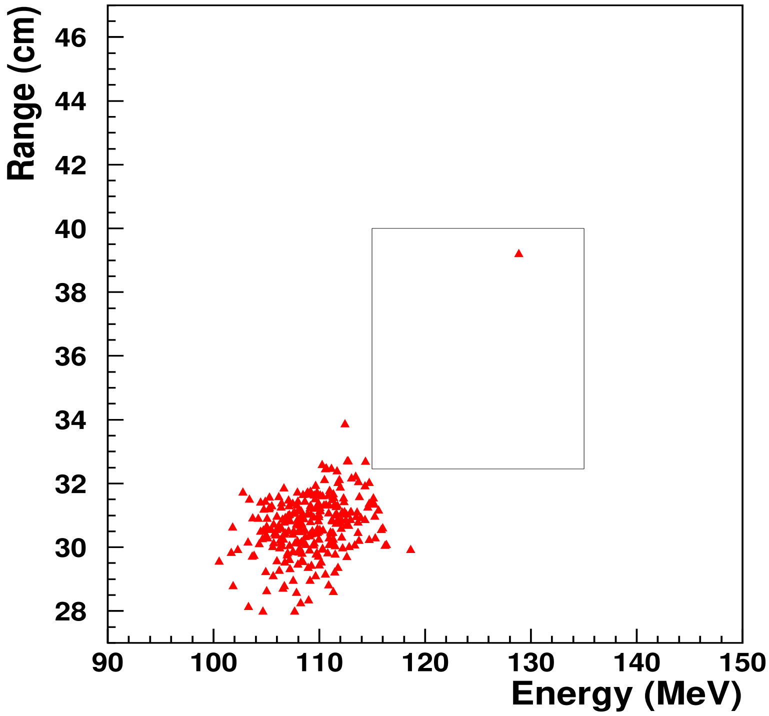

Figure 5.1: Range vs kinetic energy of the events satisfying all of the cuts, except for the Phase Space Cuts for Range and Energy. The rectangle represents the Signal Region in the range vs energy plane. Events around $E = 110$ MeV/c are due to $K_{\pi 2}$, which are not removed by the Photon Veto Cuts.

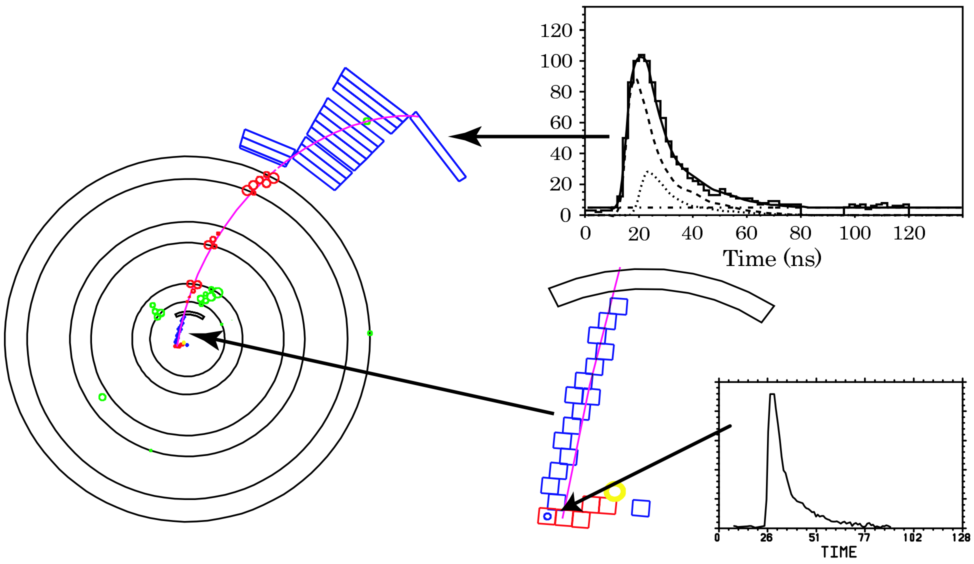

Figure 5.2: Reconstruction of the candidate event (end view). The TD data in the π^+ stopping counter and the reconstruction in the target are also displayed.

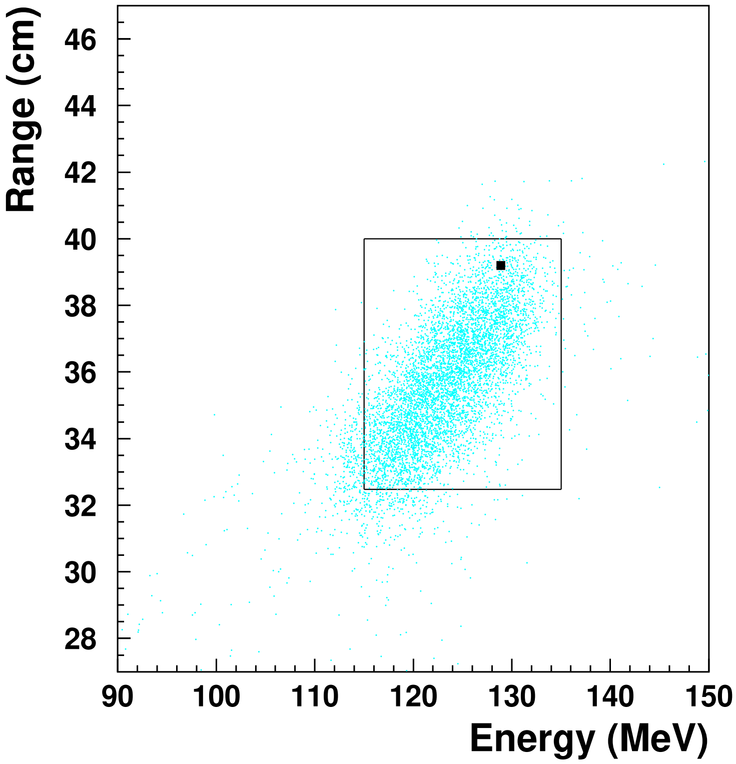

Figure 5.3: Range vs kinetic energy of Monte Carlo $K^+ \to \pi^+\nu\bar{\nu}$ events that pass all of the cuts, except for the Phase Space Cuts for Range and Energy. The rectangle represents the Signal Region in the range vs energy plane. The squared dot indicates the candidate event.

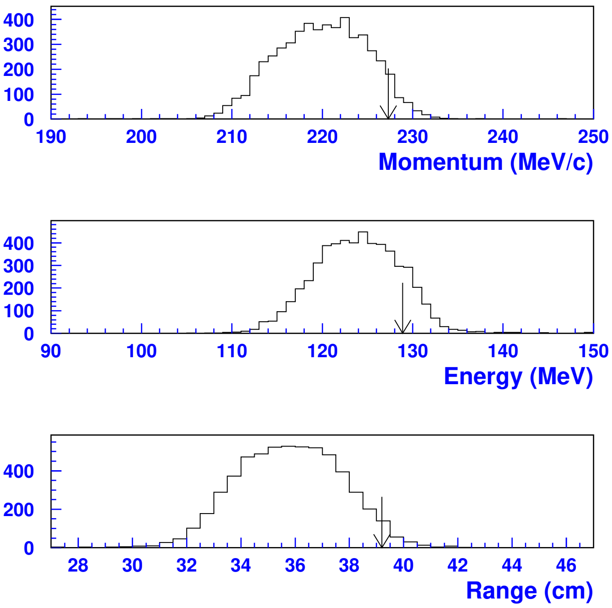

Figure 5.4: Momentum (top), kinetic energy (middle) and range (bottom) distributions of Monte Carlo $K^+ \to \pi^+\nu\bar{\nu}$ events. All of the cuts, except for the cut on each variable, are applied to create these plots. The values for the candidate event are indicated by the arrows.

Quantity	*Value*
Momentum	227.3 MeV/c
Range	39.2 cm
Kinetic Energy	128.9 MeV
Range Deviation in RS (χ_{R-P})	0.63
Cosine of Polar Angle	-0.24
$K^+ \to \pi^+$ Decay Time	4.3 ns
$\pi^+ \to \mu^+$ Decay Time	6.2 ns
$\mu^+ \to e^+$ Decay Time	1370.5 ns
Hit in the Beam Wire Chamber 1	No hit
Hit in the Beam Wire Chamber 2	No hit
Hit in the B4 Hodoscope	No hit
Hit in the Kaon Čerenkov Counter	No hit
Hit in the Pion Čerenkov Counter	No hit
Hit in the Photon Detectors	No hit

Table 5.1: Information on the candidate event.

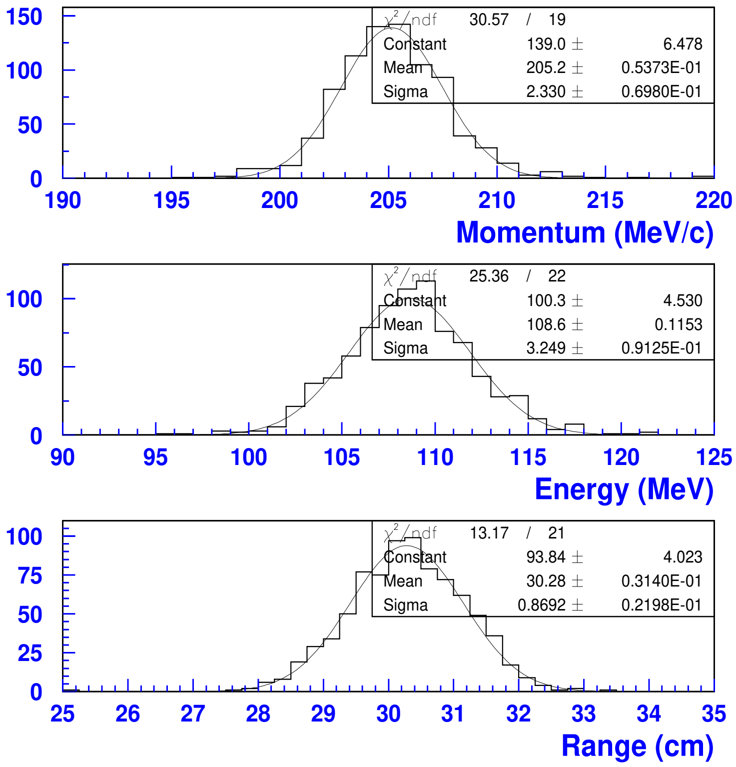

Figure 5.5: Momentum, kinetic energy and range distributions for $K_{\pi 2}$ events in the run that contains the candidate event.

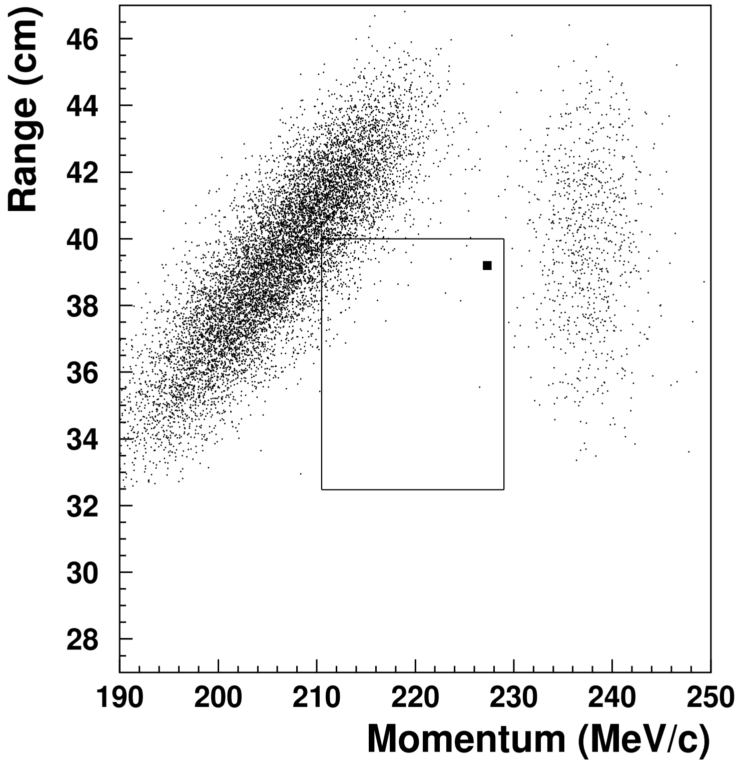

Figure 5.6: Range vs momentum distribution of the Muon background. The square dot shows the candidate event.

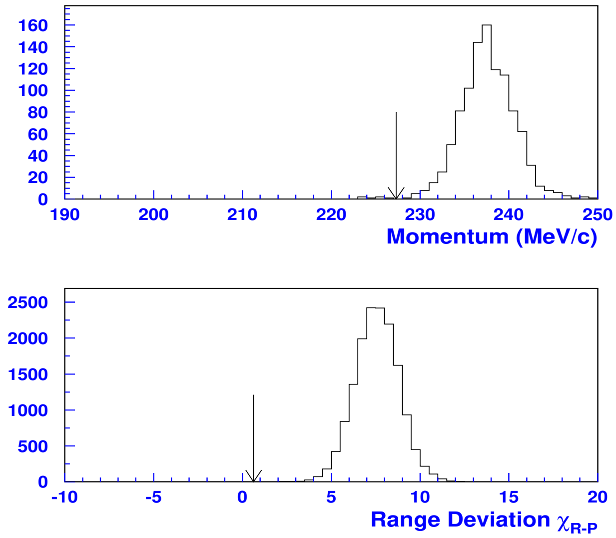

Figure 5.7: Momentum distribution of the $K_{\mu 2}$ Range Tail background (top) and range deviation distribution of the Muon Band background (bottom). The values for the candidate event are indicated by arrows. The range deviation (χ_{R-P}) is defined by Equation 3.2.

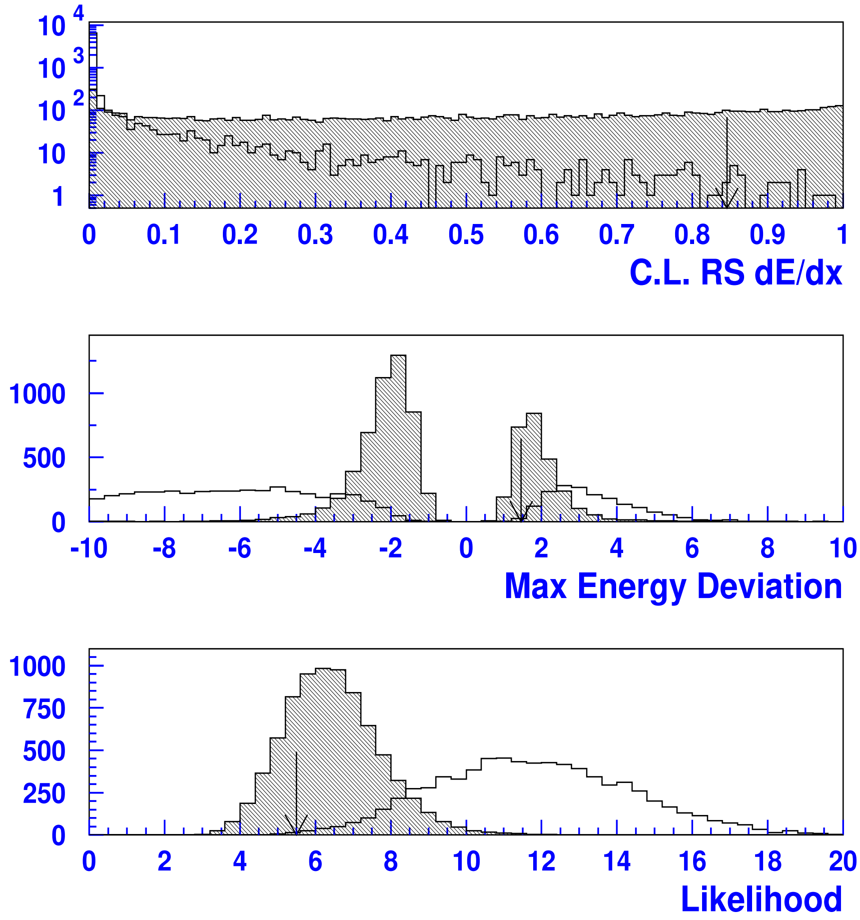

Figure 5.8: Distributions of the three quantities in the Range Stack dE/dx Cuts for signal (hatched) and background (opened) samples. Top, confidence level in the RS energy measurements; Middle, maximum energy deviation in the RS energy measurements; Bottom, likelihood for the RS energy measurements. The signal and background samples are obtained from the Pion Scattering and $K_{\mu 2}$ Range Tail events in the $\pi\nu\bar{\nu}(1)$ trigger, respectively. The values for the candidate event are indicated by the arrows.

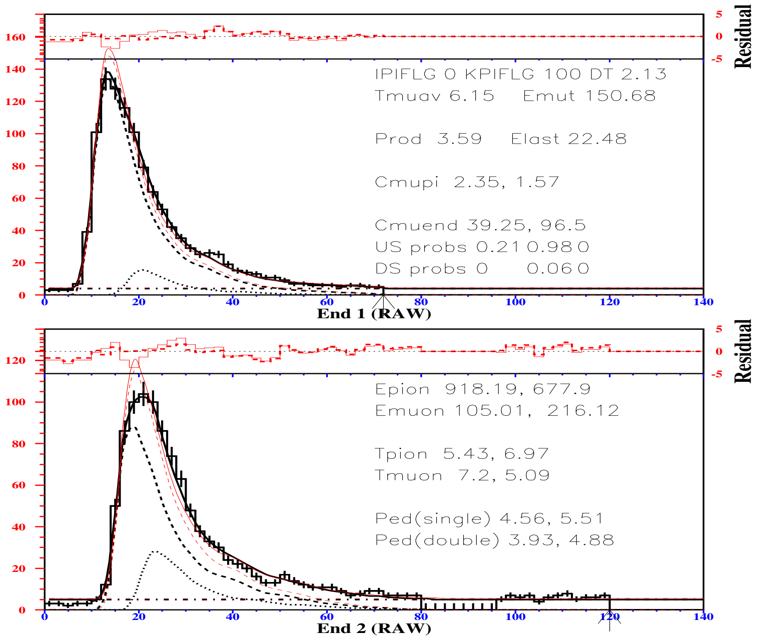

Figure 5.9: TD pulse-shape information on each end of the stopping counter for the candidate event. The solid lines represent the fitted pulse shapes based on the double-pulse assumption. The dotted lines are the fitted first and second pulses. The red solid lines represent the fitted pulse shapes based on the single-pulse assumption.

this event is signal-like, not background-like, and that it has a signature of neither a hard scattering nor a nuclear interaction. The possibility that this event originates from the $K_{\mu2}$ Range Tail background is small.

The candidate event is investigated from the view point of π^+ identification with TDs. TD information in the π^+ stopping counter is shown in Figure 5.9. The $\pi^+ \to \mu^+$ decay time is 6.15 ns. One may doubt that the fitted double pulses are due to a tail fluctuation of a single pulse. However, π^+'s, whose lifetime is 26 ns, could decay at early times (see Figure 5.10). If the first and second pulses are very close in time, the discrimination between the attached pulses becomes worse than that of detached pulses. Events with an early $\pi^+ \to \mu^+$ decay time would therefore have an ambiguity of the π^+ identification. Figure 5.11 shows the signal and background distributions of quantities (neurons) for the Neural Net $\pi^+ \to \mu^+$ Decay Cut in events with an early second pulse time ($T_\mu < 10$ ns). The π^+ signal events are obtained from the Pion Scattering events in the $\pi\nu\bar{\nu}(1)$ trigger by applying tight Kinematic Cuts to ensure that well-reconstructed π^+ tracks are selected. In μ^+ background events, tail fluctuation events are enhanced by imposing all of the $\pi^+ \to \mu^+ \to e^+$ Decay Sequence Cuts, except for the NN $\pi^+ \to \mu^+$ Decay Cut. With reference to the signal and background distributions in the case that the second pulse time is early, the candidate event seems to be more pion-like than muon-like with the exception of $\mathrm{Log}_{10}(R(1) \cdot R(2))$.

In summary, this candidate event has all of the characteristics of the $K^+ \to \pi^+\nu\bar{\nu}$ signal, although the fact that its momentum is near the kinematic limit for the $K^+ \to \pi^+\nu\bar{\nu}$ decay and it has an early π^+ decay time of 6.15 ns gives an ambiguity concerning pion identification.

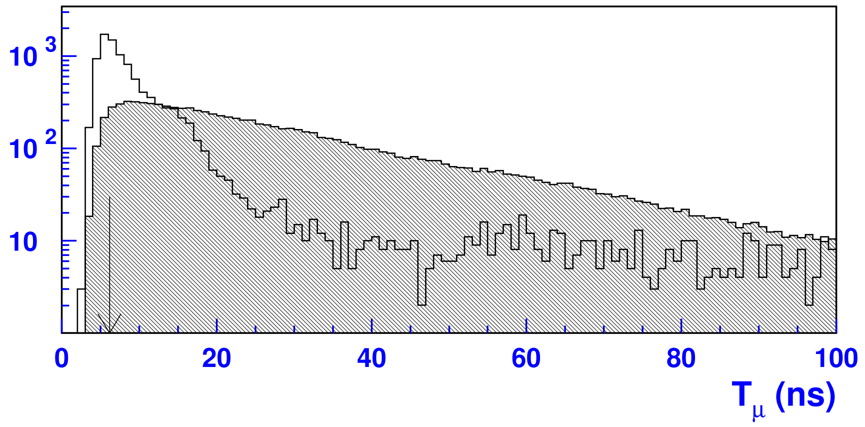

Figure 5.10: Distributions of the fitted second pulse time (T_μ) for π^+ signal (hatched) and μ^+ background (opened) events. Tail fluctuation events are enhanced in the μ^+ background sample. The arrow indicates the candidate event.

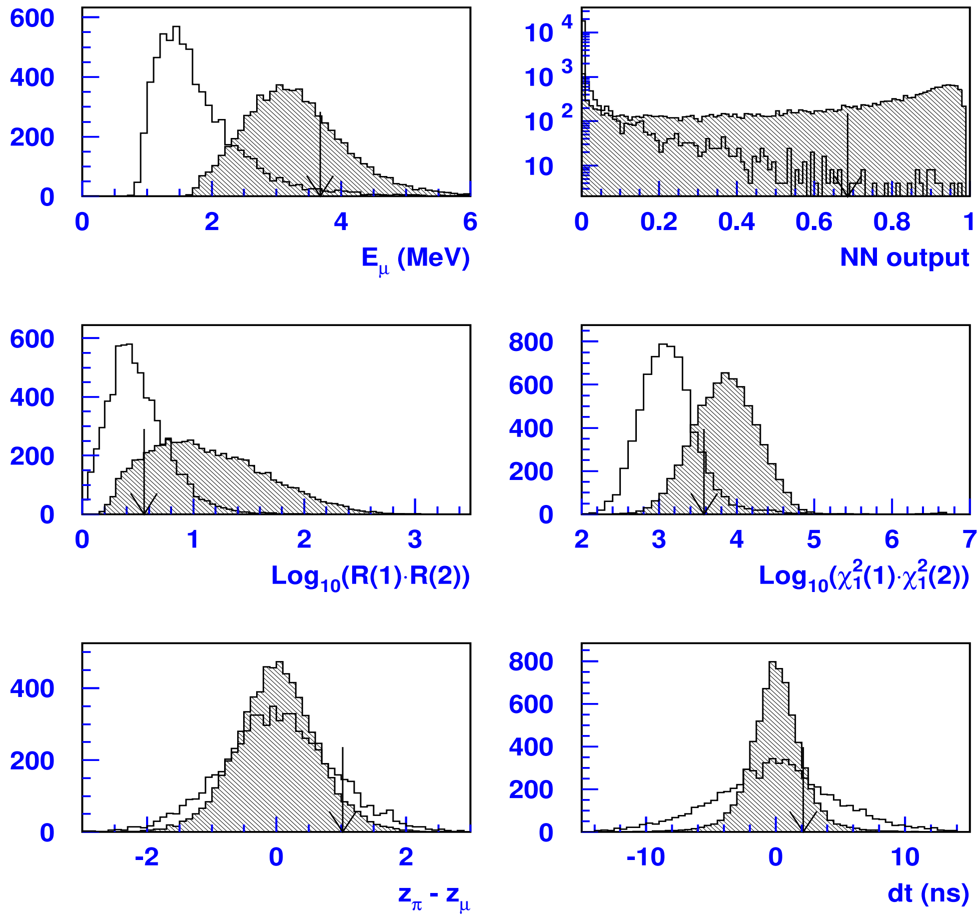

Figure 5.11: Quantities for the Neural Net $\pi^+ \to \mu^+$ Decay Cut in events with an early second pulse time ($T_\mu < 10$ ns). The hatched histograms are for the π^+ signal and the opened ones are for the μ^+ background. The arrows indicate the candidate event. The definition for each variable is explained in Section 3.5.3.

Chapter 6

Acceptance Measurement and Sensitivity

6.1 Acceptance Measurements

The acceptances of both online and offline signal-selection cuts are estimated in order to measure the branching ratio of the $K^+ \to \pi^+\nu\bar{\nu}$ decay. Most of the acceptance factors are measured by using monitor trigger data. The acceptance factors that are related to the $K^+ \to \pi^+\nu\bar{\nu}$ kinematics are derived from Monte Carlo simulations. The monitor trigger data used for the acceptance measurements are tabulated in Table 6.1.

Data	Acceptance Factor
$K_{\mu 2}$	Reconstruction efficiency Beam and target analysis Accidental loss (Photon Veto, accidental muon veto) K^+ stop efficiency
$K_{\pi 2}$	Target reconstruction related to pion tracks
$\pi_{scatter}$	Kinematics related to pion tracks $\pi^+ \to \mu^+ \to e^+$ decay acceptance
$K^+ \to \pi^+\nu\bar{\nu}$ (MC)	Trigger acceptance Phase space and Solid angle π^+ nuclear interactions and decay-in-flight

Table 6.1: Monitor triggers and the acceptance factors.

The signature of the $K_{\mu 2}$ decay (a single charged track and no other activities from the kaon decay) is the same as that of the $K^+ \to \pi^+\nu\bar{\nu}$ signals. $K_{\mu 2}$ events are therefore suitable to measure the charged-track reconstruction efficiency, the beam and target analysis acceptances, and the accidental loss due to both online and offline Photon Veto Cuts. Details of the acceptance measurements with $K_{\mu 2}$ events are described in Appendix G.1.

$K_{\pi 2}$ decay is suitable for calculating the acceptances of the Target Reconstruction Cuts, which involve energy loss of pion tracks. Details concerning the acceptance measurements with $K_{\pi 2}$ events are given in Appendix G.2.

Pion Scattering events provide pion tracks whose stopping layer spreads throughout the Range Stack. They are useful to measure the acceptances of the kinematic constraints on pion tracks (RS dE/dx Cuts, track reconstruction in the UTC and RS, etc). They are also used to measure the $\pi^+ \to \mu^+ \to e^+$ decay acceptance. Details concerning the acceptance measurements with Pion Scattering events are given in Appendices G.3 and G.4.

The trigger acceptance, the phase-space and solid-angle acceptances, and the acceptance loss due to pion nuclear interactions and decay-in-flights are obtained by using Monte Carlo simulations of the $K^+ \to \pi^+\nu\bar{\nu}$ decay, because they are related to the $K^+ \to \pi^+\nu\bar{\nu}$ kinematics and can not be measured by using any monitor trigger data. Details concerning the acceptance measurements with Monte Carlo events are given in Appendix G.5.

There are other acceptance factors: one is the T•2 efficiency [1], and another is the K^+ stop efficiency. The T•2 efficiency accounts for the efficiency of the trigger counter in the Range Stack (i.e., T-Counter). The acceptance loss due to the counter inefficiency and the geometrical inefficiency (which is due to azimuthal gaps between sectors) is estimated with both $K_{\pi 2}$ and $K_{\mu 2}$ events. Details concerning this measurement are given in Appendix G.6.

The K^+ stop efficiency is the fraction of kaons stopping in the target to those entering the target and satisfying the KB requirement. $K_{\mu 2}$ decay is used for this measurement because the signature of $K_{\mu 2}$ events is similar to that of $K^+ \to \pi^+\nu\bar{\nu}$. This acceptance is calculated by taking the ratio of the number of stopped $K_{\mu 2}$ decays to the number of K^+ triggers times the $K_{\mu 2}$ branching ratio. Some selection cuts are required to select the stopped $K_{\mu 2}$ decays. The K^+ stop efficiency is therefore given as

$$\begin{aligned} K^+\ Stop\ Eff. &= \frac{Num.\ of\ Stopped\ K_{\mu 2}\ Decays}{K^+\ Trigger(K_{\mu 2}) \cdot A_{selection\ cuts} \cdot \mathcal{B}(K_{\mu 2})}, \qquad (6.1) \\ \text{where}\quad A_{selection\ cuts} &\equiv A_{bad\ run} \cdot A_{trigger} \cdot A_{polar\ angle} \cdot A_{range} \cdot A_{recon} \cdot \\ &\quad A_{beam\&target} \cdot A_{photon\ veto} \cdot A_{T\bullet 2}. \end{aligned}$$

Here, $A_{T\bullet 2}$ is the T•2 efficiency for $K_{\mu 2}$. The $K_{\mu 2}$ branching ratio is taken from the Particle Data Group (PDG) value. Stopped $K_{\mu 2}$ events are selected by applying the cuts given in Table 6.2. The acceptances of the selection cuts are measured as shown in Table 6.3. The acceptances of the trigger ($A_{trigger}$), the polar angle cut ($A_{polar\ angle}$) and the range requirement (A_{range}) are obtained from the Monte Carlo $K_{\mu 2}$ events. The other acceptances are obtained from the $K_{\mu 2}$ monitor trigger data. Details concerning the acceptance measurements are given in Appendix H. The K^+ stop efficiency is measured to be

$$K^+\ Stop\ Eff. = 0.7740 \pm 0.0011(stat.). \qquad (6.2)$$

The acceptances of the $K^+ \to \pi^+\nu\bar{\nu}$ signal selection cuts are summarized in Table 6.4. Each factor (written in bold) is composed of several components (in parentheses), whose acceptances are estimated using the monitor trigger data and Monte Carlo simulations. Measurements of the phase-space and solid-angle acceptance, the $\pi^+ \to \mu^+ \to e^+$ decay acceptance, and the accidental loss for the Signal Region are performed by loosening the corresponding cut without the other two cuts loosened. The total acceptance for the Signal Region is obtained by summing the total acceptance in the 1×1 Region and the

[1] T•2 is the trigger bit that requires a coincident hit in the first two layers of the RS counters. The definition is explained in Section 2.4.

Cut	# of remaining events
Sample	1010924
Bad Run	1010318
Reconstruction Cuts	806196
Polar Angle	795506
Beam and Target Cuts	393245
Photon Veto Cuts	359031
Range Requirement	355119
Stopped $K_{\mu 2}$ Decays	355119

Table 6.2: Numbers of events passing the $K_{\mu 2}$ selection cuts and the number of stopped $K_{\mu 2}$ decays used in the K^+ stop efficiency measurement.

Stopped $K_{\mu 2}$ Decays	355119
K^+ Trigger ($K_{\mu 2}$)	4.1475×10^6
$A_{bad\ run}$	0.9994
$A_{trigger}$	0.4415
$A_{polar\ angle}$	0.9866
A_{range}	0.9877
A_{recon}	0.8388
$A_{beam\&target}$	0.5585
$A_{photon\ veto}$	0.9295
$A_{T\bullet 2}$	0.9303
$\mathcal{B}(K_{\mu 2})$	0.6351
K^+ Stop Efficiency	0.7740 ± 0.0011

Table 6.3: Summary of the K^+ stop efficiency measurement.

Factor	Acceptance: Signal Region	Acceptance: 1×1 Region	Data	Ref.
Trigger acceptance (A_{trig})	**0.1796±0.0010±0.0090**		MC	G.5
K^+ **stop efficiency** (A_{K+stop})	**0.7740±0.0011**		$K_{\mu 2}$	G.1
Beam and target analysis (A_{beam} w/o RTDIF,PIGAP,TGB4)	**0.5483±0.0007**		$K_{\mu 2}$	G.1
Phase space and solid angle	**0.4020±0.0030**	**0.3662±0.0030**		
(Phase Space)	0.4458 ± 0.0032	0.4061 ± 0.0032	MC	G.5
(COS3D)	0.9687 ± 0.0011		MC	G.5
(ZFRF)	0.9312 ± 0.0016		MC	G.5
(ZUTOUT)	0.9998 ± 0.0001		MC	G.5
π^+ **nucl. int. and decay-in-flight** (A_{NIDIF})	**0.4953±0.0077±0.0248**		MC	G.5
Reconstruction efficiency (A_{recon})	**0.9956±0.0001**		$K_{\mu 2}$	G.1
Other kinematics constraints	**0.5013±0.0071±0.0154**			
($A_{K\pi 2}$)	0.8785 ± 0.0029		$K_{\pi 2}$	G.2
(RTDIF)	0.9893 ± 0.0002		$K_{\mu 2}$	G.1
(PIGAP)	0.9917 ± 0.0002		$K_{\mu 2}$	G.1
(TGB4)	0.9440 ± 0.0004		$K_{\mu 2}$	G.1
($A_{\pi scatter}$)	0.6161 ± 0.0085 ± 0.0189		$\pi_{scatter}$	G.3
$\pi^+ \to \mu^+ \to e^+$ **decay acceptance**	**0.3914±0.0085±0.0074**	**0.3495±0.0076±0.0067**		
(UFATE)	1.0000		MC	G.5
(USTMED)	0.9948 ± 0.0004		MC	G.5
(USTOP_HEX)	0.9971 ± 0.0003		MC	G.5
($A_{\pi\to\mu\to e}$)	0.3946 ± 0.0086 ± 0.0075	0.3523 ± 0.0077 ± 0.0067	$\pi_{scatter}$	G.4
Accidental loss	**0.8204±0.0019**	**0.7509±0.0022**		
(A_{PV})	0.8389 ± 0.0019	0.7678 ± 0.0022	$K_{\mu 2}$	G.1
($A_{LAYER14}$)	0.9820 ± 0.0002		$K_{\mu 2}$	G.1
(A_{acc})	0.9959 ± 0.0006		$K_{\mu 2}$	G.1
T•2 efficiency ($A_{T\bullet 2}$)	**0.9357±0.0011±0.0168**		$K_{\mu 2}$, $K_{\pi 2}$	G.6
Total acceptance	**(2.22±0.07±0.18) × 10^{-3}**	**(1.69±0.05±0.16)×10^{-3}**		

Table 6.4: Acceptances for the $K^+ \to \pi^+\nu\bar{\nu}$ analysis. Each factor (written in bold) consists of several components (in parentheses). The first and second uncertainties represent the statistical and systematic uncertainties, respectively. The 3rd and 4th columns represent the data and the reference for each component.

acceptance gains from the three Extended Regions. The total acceptance in the Signal Region is therefore measured to be

$$A_{total} = 0.00222 \pm 0.00007(stat.) \pm 0.00018(sys.). \tag{6.3}$$

This value is greater by a factor of 1.31 than the total acceptance in the 1×1 Region.

6.2 $K_{\pi 2}$ Branching Ratio Measurement

The $K_{\pi 2}$ branching ratio is measured in order to confirm that the way to measure the acceptances of the $K^+ \to \pi^+ \nu\bar{\nu}$ selection cuts is correct. Stopped $K_{\pi 2}$ events are selected from the $K_{\pi 2}$ monitor trigger data by imposing the cuts given in Table 6.5. The Phase Space Cuts in this selection are defined to be in the $\pm 3\sigma$ region of the $K_{\pi 2}$ peaks in the momentum, range and energy. The $K_{\pi 2}$ branching ratio is calculated as

$$\begin{aligned} \mathcal{B}(K_{\pi 2}) &= \frac{Num.\ of\ Stopped\ K_{\pi 2}\ Decays}{K^+\ Trigger(K_{\pi 2}) \cdot A_{selection\ cuts} \cdot A_{K^+\ stop}}, \qquad (6.4) \\ \text{where} \quad A_{selection\ cuts} &\equiv A_{bad\ run} \cdot A_{trigger} \cdot A_{recon} \cdot A_{polar\ angle} \cdot A_{phase\ space} \cdot \\ & \quad A_{\pi \to \mu \to e} \cdot A_{beam\&target} \cdot A_{T\bullet 2}. \end{aligned}$$

Here, $A_{K^+\ stop}$ is the K^+ stop efficiency obtained from Equation (6.2), $A_{\pi \to \mu \to e}$ is the acceptance of the $\pi^+ \to \mu^+ \to e^+$ decay requirement, and $A_{T\bullet 2}$ is the T•2 efficiency for $K_{\pi 2}$. The acceptances of the selection cuts are measured as shown in Table 6.6. The acceptances of the trigger ($A_{trigger}$), the polar angle cut ($A_{polar\ angle}$) and the Phase Space Cuts ($A_{phase\ space}$) are obtained from the Monte Carlo $K_{\pi 2}$ events, while the other acceptances are obtained from the $K_{\pi 2}$ monitor trigger data. The acceptance of the $\pi^+ \to \mu^+ \to e^+$ decay requirement is obtained from the $\pi_{scatter}$ monitor trigger data by applying the Phase Space Cuts for $K_{\pi 2}$ as the setup, instead of those for $K^+ \to \pi^+ \nu\bar{\nu}$. Details concerning the acceptance measurements are given in Appendix I. The $K_{\pi 2}$ branching ratio is measured to be

$$\mathcal{B}(K_{\pi 2}) = 0.2190 \pm 0.0050(stat.). \tag{6.5}$$

This value agrees with the PDG value 0.212±0.001 within 3.3%, which give us confidence that the acceptance measurements are correct.

6.3 Summary of Acceptance and Sensitivity

Once the acceptances of the $K^+ \to \pi^+ \nu\bar{\nu}$ selection cuts are measured, the sensitivity for the $K^+ \to \pi^+ \nu\bar{\nu}$ analysis in E949 is calculated. In the physics run of the E949 the number of the K^+ triggers for $K^+ \to \pi^+ \nu\bar{\nu}$ was 1.77×10^{12}. By using the measured total acceptance of 0.00222±0.00007($stat.$)±0.00015($sys.$), the sensitivity of the E949 2002 run is calculated to be

$$Sensitivity\ (K^+ \to \pi^+ \nu\bar{\nu}) = (2.55 \pm 0.08 \pm 0.18) \times 10^{-10}, \tag{6.6}$$

where the first and second uncertainties represent the statistical and systematic uncertainties, respectively. The total acceptance and the sensitivity for the $K^+ \to \pi^+ \nu\bar{\nu}$ analysis are summarized in Table 6.7.

Cut	# of remaining events
Sample	84844
Bad Run	84388
Reconstruction Cuts	65495
Polar Angle	64425
Beam and Target Cuts	26523
$\pi^+ \to \mu^+ \to e^+$ Decay Requirement	18688
Stopping Layer Cut	16469
Phase Space Cuts	16405
Stopped $K_{\pi 2}$ Decays	16405

Table 6.5: Numbers of events passing the $K_{\pi 2}$ selection cuts and the number of stopped $K_{\pi 2}$ decays used in the $K_{\pi 2}$ branching ratio measurement.

Stopped $K_{\pi 2}$ Decays	16405
K^+ Trigger ($K_{\pi 2}$)	1.3233×10^6
$A_{bad\ run}$	0.9946
$A_{trigger}$	0.2782
A_{recon}	0.8439
$A_{polar\ angle}$	0.9839
$A_{phase\ space}$	0.9126
$A_{stopping\ layer}$	0.9633
$A_{\pi\to\mu\to e}$	0.8350
$A_{beam\&target}$	0.4622
$A_{T\bullet 2}$	0.9383
$A_{K^+\ stop}$	0.7740
$\mathcal{B}(K_{\pi 2})$	0.2190±0.0050

Table 6.6: Summary of the $K_{\pi 2}$ branching ratio measurement.

	Signal Region	1×1 Region
K^+ Trigger ($K^+ \to \pi^+\nu\bar{\nu}$)	1.77×10^{12}	1.77×10^{12}
Total Acceptance	$(2.22\pm0.07\pm0.15)\times10^{-3}$	$(1.69\pm0.05\pm0.14)\times10^{-3}$
Sensitivity	$(2.55\pm0.08\pm0.18)\times10^{-10}$	$(3.34\pm0.11\pm0.27)\times10^{-10}$

Table 6.7: Acceptance and sensitivity for the $K^+ \to \pi^+\nu\bar{\nu}$ analysis. The first and second uncertainties represent the statistical and systematic uncertainties, respectively.

Chapter 7

Results

7.1 $K^+ \to \pi^+\nu\bar{\nu}$ Branching Ratio

The $K^+ \to \pi^+\nu\bar{\nu}$ branching ratio is measured via a likelihood analysis. All of the cells inside the Signal Region are pre-determined before the examination of the Signal Region. The cell for the candidate event is defined by the bins in the functions, as shown in Table 7.1. The background levels of all the background sources in this cell are summarized in Table 7.2. The largest contribution to the total background level in this cell (5.745×10^{-5} events) is the $K_{\mu 2}$ Range Tail background (4.917×10^{-5} events). The ratio of the acceptance in this cell to the total acceptance in the 1×1 Region ($A^{1\times1}_{total} = 0.001694$) is estimated to be 1.21×10^{-4}. The expected number of signal events in this cell is therefore calculated as

$$\begin{aligned} s_i &= N_K \cdot \mathcal{B} \cdot A^{1\times1}_{total} \cdot A_i \\ &= 1.770 \times 10^{12} \cdot \mathcal{B} \cdot 0.001694 \cdot 1.21 \times 10^{-4} \\ &= 3.628 \times 10^5 \cdot \mathcal{B}, \end{aligned} \tag{7.1}$$

where $\mathcal{B}$ represents the $K^+ \to \pi^+\nu\bar{\nu}$ branching ratio and N_K is the number of K^+ triggers for $K^+ \to \pi^+\nu\bar{\nu}$. With these expected number and background level in the candidate

Function	Bin	$N(BG)$	Reference
$K_{\pi 2}$ kinematics	$0.0 \leq N_{K\pi 2} < 0.2$	0.00	App. C.3
PV	$0.1 < N_{PV} < 0.2$	0.11	-
Muon Band	$0.0 < N_{Band} < 0.5$	0.29	App. C.2
$K_{\mu 2}$ Range Tail	$0.4 < N_{Tail} < 0.6$	0.51	App. C.1
$\pi^+ \to \mu^+ \to e^+$	$1.0 < N_{\pi\to\mu\to e} < 1.5$	1.23	-
1-Beam	$0.0 \leq N_{1beam} < 0.2$	0.00	App. C.4
2-Beam	$0.0 \leq N_{2beam} < 0.2$	0.00	App. C.5

Table 7.1: Bin in each background function (2nd column) and relative background level (3rd column) for the candidate event. The correspondences of the relative background levels to the parameters of the functions are described in references (4th column).

Source	Background Level (event)
$K_{\pi 2}$	0.029×10^{-5}
Muon	5.632×10^{-5}
(Muon Band)	(0.715×10^{-5})
($K_{\mu 2}$ Range Tail)	(4.917×10^{-5})
1 Beam (including CEX)	0.058×10^{-5}
2 Beam	0.026×10^{-5}
Total Background b_i	5.745×10^{-5}
Relative Cell Acceptance A_i	1.210×10^{-4}

Table 7.2: Contribution of each background source to the background level in the cell for the candidate event. Each background level is represented as the number of events. The ratio of the acceptance in the cell to the total acceptance in the 1×1 Region is also tabulated in this table.

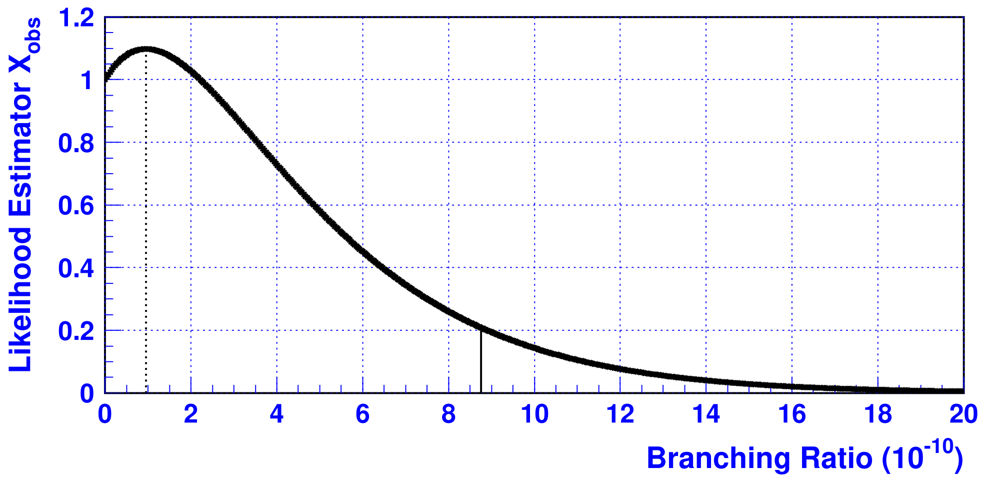

Figure 7.1: Likelihood estimator X_{obs} for the E949 2002 data set as a function of the $K^+ \to \pi^+\nu\bar{\nu}$ branching ratio, $\mathcal{B}$.

event cell, the likelihood estimator, X,

$$X \equiv \prod_{i=1}^{n} X_i, \quad \text{with} \quad X_i = \frac{e^{-(s_i+b_i)}(s_i+b_i)^{d_i}}{d_i!} \Big/ \frac{e^{-b_i}(b_i)^{d_i}}{d_i!} = e^{-s_i}\left(1+\frac{s_i}{b_i}\right)^{d_i} \tag{7.2}$$

gives the central value of the $K^+ \to \pi^+\nu\bar{\nu}$ branching ratio when the likelihood estimator with the given configuration of $\{s_i\}$, $\{b_i\}$ and $\{d_i\}$ (referred to as X_{obs}) gives the maximum value. Figure 7.1 shows the likelihood estimator, X_{obs}, as a function of the $K^+ \to \pi^+\nu\bar{\nu}$ branching ratio, $\mathcal{B}$. This plot indicates that, even though X_{obs} has the maximum value at $\mathcal{B} = 0.96 \times 10^{-10}$, the case that $\mathcal{B} = 0$ is not necessarily ruled out because the candidate event observed in the E949 data has a small signal-to-background ratio. An upper limit for $\mathcal{B}(K^+ \to \pi^+\nu\bar{\nu})$ is calculated with a Bayesian approach. The

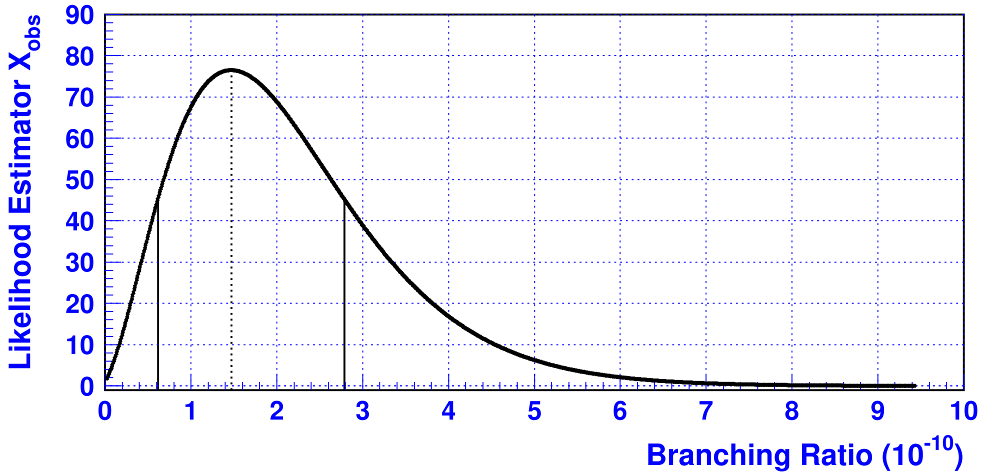

Figure 7.2: Likelihood estimator, X_{obs}, for the combined E787 and E949 results as a function of the $K^+ \to \pi^+\nu\bar{\nu}$ branching ratio, $\mathcal{B}$.

probability to obtain a branching ratio, $\mathcal{B}$, with a given X_{obs} is expressed as [1]

$$P(\mathcal{B}|X_{obs}) = \frac{X_{obs}(\mathcal{B})S(\mathcal{B})}{\int_{-\infty}^{+\infty} X_{obs}(\mathcal{B})S(\mathcal{B})d\mathcal{B}}, \tag{7.3}$$

where $S(\mathcal{B}) = 1$ when $\mathcal{B} \geq 0$ and $S(\mathcal{B}) = 0$ when $\mathcal{B} < 0$. The confidence level $(1-\alpha)$ is calculated as

$$1 - \alpha = \int_{-\infty}^{\mathcal{B}_0} P(\mathcal{B}|X_{obs})d\mathcal{B} = \frac{\int_0^{\mathcal{B}_0} X_{obs}(\mathcal{B})d\mathcal{B}}{\int_0^{+\infty} X_{obs}(\mathcal{B})d\mathcal{B}}. \tag{7.4}$$

With Equations (7.3) and (7.4), an upper limit for $\mathcal{B}(K^+ \to \pi^+\nu\bar{\nu})$ at the 90% confidence level (CL) is obtained as

$$\mathcal{B}(K^+ \to \pi^+\nu\bar{\nu}) < 8.76 \times 10^{-10} \quad (90\% \text{ CL}) \tag{7.5}$$

based on the single candidate event. This limit is consistent with the previous results from E787.

The results from both E787 and E949 are combined to calculate the branching ratio for $K^+ \to \pi^+\nu\bar{\nu}$. In the E787 $K^+ \to \pi^+\nu\bar{\nu}$ analysis, two $K^+ \to \pi^+\nu\bar{\nu}$ candidate events were observed in the signal region [22, 23]. Since all of the measurements (background and acceptance functions, background levels, sensitivity, etc.) of E787 and E949 were performed independently, what should be done for combining both results is to evaluate the likelihood estimator, X_{obs}, from all of the sets of $\{s_i\}$, $\{b_i\}$, and $\{d_i\}$ for both results. For the E949 data set, the Signal Region is divided into 3781 cells, while the E787 signal region has 488 cells. Figure 7.2 shows the likelihood estimator, X_{obs}, for the combined E787 and E949 results as a function of the $K^+ \to \pi^+\nu\bar{\nu}$ branching ratio, $\mathcal{B}$. X_{obs} has the maximum value at $\mathcal{B} = 1.47 \times 10^{-10}$, and the case that $\mathcal{B} = 0$ is unlikely. By using Equation (7.3), a confidence level interval $(1-\alpha)$ is calculated so that the probability

[1] It is assumed that $X_{obs}(\mathcal{B})$ represents the probability density function for the branching ratio.

CL interval	Branching Ratio
68%	$[0.61,2.79]\times10^{-10}$
80%	$[0.45,3.25]\times10^{-10}$
90%	$[0.29,3.90]\times10^{-10}$
95%	$[0.17,4.53]\times10^{-10}$

Table 7.3: $K^+ \to \pi^+\nu\bar{\nu}$ branching ratios at the 68%, 80%, 90%, 95% confidence level intervals.

	E787		E949
Candidate	1995A	1998C	2002A
s_i/b_i	50	7	0.9
$W_i \equiv s_i/(s_i+b_i)$	0.98	0.88	0.48
Background Prob.	0.006	0.02	0.07

Table 7.4: Signal to background ratio (s_i/b_i), signal weight ($W_i \equiv s_i/(s_i+b_i)$), and probability that the background alone gives rise to the candidate event ($1-CL_b$) for each candidate event. The first and second candidate events in E787 and the E949 candidate event are called 1995A, 1998C and 2002A, respectively.

that the true value of the branching ratio is included between $\mathcal{B}_1$ and $\mathcal{B}_2$ ($0 < \mathcal{B}_1 < \mathcal{B}_2$) is $1-\alpha$:

$$1-\alpha = \int_{\mathcal{B}_1}^{\mathcal{B}_2} P(\mathcal{B}|X_{obs})d\mathcal{B} = \frac{\int_{\mathcal{B}_1}^{\mathcal{B}_2} X_{obs}(\mathcal{B})d\mathcal{B}}{\int_0^{+\infty} X_{obs}(\mathcal{B})d\mathcal{B}}, \tag{7.6}$$

where $X_{obs}(\mathcal{B}_1) = X_{obs}(\mathcal{B}_2)$. The $K^+ \to \pi^+\nu\bar{\nu}$ branching ratio at the 68% CL interval is obtained as

$$\mathcal{B}(K^+ \to \pi^+\nu\bar{\nu}) = (1.47^{+1.32}_{-0.86}) \times 10^{-10} \quad \text{(68\% CL interval)} \tag{7.7}$$

based on three candidate events. This measured branching ratio takes only the statistical uncertainty into account. This value is consistent with the SM prediction, although the central value is twice as large as the SM prediction. The $K^+ \to \pi^+\nu\bar{\nu}$ branching ratios at several confidence level intervals are summarized in Table 7.3.

The signal-to-background ratio (s_i/b_i) and the signal weight ($W_i \equiv s_i/(s_i+b_i)$) for each candidate event are summarized in Table 7.4. The value of s_i for each candidate event is calculated based on the central value of the measured branching ratio, 1.47×10^{-10}. The signal-to-background ratio for the E949 candidate event is 0.9. The probability that the background alone gives rise to the E949 candidate event, or a more signal-like configuration, is 0.074; this value is not small, because the candidate event is observed in a region with a relatively small acceptance and a large background. On the other hand, the probability that the background alone gives rise to the three candidate events, or a more signal-like configuration, is 0.001.

Source	68% CL interval (10^{-10})		
	$+1\sigma$	-1σ	relative error
No systematic	[0.615,2.786]		
$K_{\pi 2}$	[0.614,2.785]	[0.616,2.787]	$^{+0.043\%}_{-0.163\%}$
$K_{\mu 2}$ Range Tail	[0.595,2.749]	[0.639,2.829]	$^{+1.533\%}_{-3.270\%}$
Muon Band	[0.611,2.780]	[0.619,2.792]	$^{+0.226\%}_{-0.602\%}$
1 Beam	[0.599,2.768]	[0.631,2.804]	$^{+0.646\%}_{-2.587\%}$
2 Beam	[0.614,2.785]	[0.615,2.786]	$^{+0.007\%}_{-0.098\%}$
Sensitivity	[0.676,3.065]	[0.553,2.507]	$^{+10.00\%}_{-10.00\%}$
Total			$^{+10.14\%}_{-10.85\%}$

Table 7.5: 68% CL intervals with $\pm 1\sigma$ variations of the background levels and the sensitivity. The 2nd and 3rd columns represent the 68% CL intervals with $+1\sigma$ and -1σ variations of each source, respectively. The top and bottom values in the 4th column represent the relative uncertainties with respect to the upper (2.786) and lower (0.615) bounds of the 68% CL interval, respectively.

7.2 Estimation of Systematic Uncertainty

Since the branching-ratio calculation depends on the magnitudes of the expected signal events and the background levels in the candidate event cells, the uncertainties concerning the sensitivity and background levels would affect the branching ratio. In Section 4.5, the correlation between the two Bifurcation cuts in each background source is considered, and the quantity that represents the consistency between the predicted and observed backgrounds outside the Signal Region (the value c) is estimated. The magnitudes for the assumed systematic uncertainties are based on the uncertainties concerning the value c in Table 4.9; from the table, the uncertainty on each background source was estimated to be 20%. From the sensitivity calculation explained in Chapter 6, the uncertainty on the sensitivity was estimated to be 10%. These magnitudes concerning the uncertainties are regarded as being one standard-deviation (1σ) of their systematic uncertainties. The differences in the lower and upper boundaries of the 68% CL interval when the background levels and the sensitivity are varied by $\pm 1\sigma$ are treated as a systematic uncertainty. Table 7.5 summarizes the 68% CL intervals at $\pm 1\sigma$ variations of the background levels and the sensitivity; the main contribution to the systematic uncertainty on the 68% CL intervals is the uncertainty concerning the sensitivity. The systematic uncertainty on the branching ratio is obtained by summing the quadrature of the relative uncertainties, assuming that the uncertainties are not correlated. The systematic uncertainties on the upper and lower bounds (2.786 and 0.615) of the 68% CL interval are estimated to be $+10.14\%$ and -10.85%, respectively. The branching ratio at the 68% CL interval is therefore estimated to be

$$\begin{aligned} \mathcal{B}(K^+ \to \pi^+ \nu \bar{\nu}) &= (1.47^{+1.32}_{-0.86}(stat)^{+0.28}_{-0.07}(sys)) \times 10^{-10} && (7.8) \\ &= (1.47^{+1.60}_{-0.93}) \times 10^{-10}, && (7.9) \end{aligned}$$

where the first and second uncertainties in (7.8) represent the statistical and systematic uncertainties, respectively, and the uncertainty in (7.9) represents the sum of the statistical and systematic uncertainties [2].

7.3 Impact of $K^+ \to \pi^+\nu\bar{\nu}$ Branching Ratio on Unitarity Triangle

The $K^+ \to \pi^+\nu\bar{\nu}$ branching ratio constrains the CKM matrix element, $|V_{td}|$. The quantity that is directly extracted from $\mathcal{B}(K^+ \to \pi^+\nu\bar{\nu})$ is $|\lambda_t| \equiv |V_{ts}^* V_{td}|$. To extract $|V_{td}|$, $|\lambda_t|$ should be divided by $|V_{cb}| \simeq |V_{ts}|$. Since $|V_{cb}|$ should be measured from B decays, the quantity $|\lambda_t|$ is extracted in order to perform an independent measurement from B decays. $|V_{td}|$ is extracted by dividing $|\lambda_t|$ by $|V_{cb}|$.

Equation (1.13) can be written as

$$\mathcal{B}_{\pi^+\nu\bar{\nu}} = \xi \left[(\mathrm{Im}\lambda_t X_t)^2 + \left(\lambda_c \bar{X} + \mathrm{Re}\lambda_t X_t \right)^2 \right], \tag{7.10}$$

where

$$\xi \equiv \frac{3\alpha^2 \mathcal{B}(K^+ \to \pi^0 e^+ \nu)}{|V_{us}|^2 2\pi^2 \sin\Theta_W^4}, \quad \bar{X} \equiv \lambda^4 P_c(X) = \frac{1}{3}(2X_{\mathrm{NL}}^e + X_{\mathrm{NL}}^\tau), \quad \text{and} \quad X_t \equiv X(x_t). \tag{7.11}$$

From the upper limit of $\mathcal{B}(K^+ \to \pi^+\nu\bar{\nu})$ the above equation has the relation

$$\mathcal{B}_{\pi^+\nu\bar{\nu}}^{MAX} \geq \xi \left[(\mathrm{Im}\lambda_t X_t)^2 + \left(\lambda_c \bar{X} + \mathrm{Re}\lambda_t X_t \right)^2 \right]. \tag{7.12}$$

Assuming the extreme case that the second term equals zero (i.e., real parts of the charm and top contributions cancel each other exactly), one obtains the following relations:

$$\begin{aligned} \mathcal{B}_{\pi^+\nu\bar{\nu}}^{MAX} &> \xi \left(\mathrm{Im}\lambda_t X_t \right)^2, \\ |\mathrm{Im}\lambda_t X_t| &< \sqrt{\mathcal{B}_{\pi^+\nu\bar{\nu}}^{MAX} / \xi}. \end{aligned} \tag{7.13}$$

Using $\xi = 1.5226 \times 10^{-4}$ and the measured branching ratio at the 68% CL interval, $\mathcal{B}_{\pi^+\nu\bar{\nu}}^{MAX} = 3.07 \times 10^{-10}$ [3]; taking $m_t = 168.1$ GeV, which gives $X_t = 1.529$, Equation (7.13) yields $|\mathrm{Im}\lambda_t| < 0.928 \times 10^{-3}$.

The limits on the real part of λ_t can be set by assuming the extreme case that the imaginary part of λ_t is equal to zero.

$$\begin{aligned} \mathcal{B}_{\pi^+\nu\bar{\nu}}^{MAX} &> \xi \left(\lambda_c \bar{X} + \mathrm{Re}\lambda_t X_t \right)^2 \\ |\lambda_c \bar{X} + \mathrm{Re}\lambda_t X_t| &< \sqrt{\mathcal{B}_{\pi^+\nu\bar{\nu}}^{MAX} / \xi}. \end{aligned} \tag{7.14}$$

[2]Using a statistical technique developed by T. Junk [46], the branching ratio at the 68% confidence level interval is estimated to be $(1.47^{+1.30}_{-0.89}) \times 10^{-10}$ [47]. The details are described in Appendix J.

[3]All of the values of the branching ratio used in this calculation include the systematic uncertainty.

Since λ_c is negative,

$$\mathrm{Re}\lambda_t X_t \;<\; \sqrt{\mathcal{B}^{MAX}_{\pi^+\nu\bar{\nu}}/\xi} + |\lambda_c \bar{X}|, \tag{7.15}$$

$$\mathrm{Re}\lambda_t X_t \;>\; -\sqrt{\mathcal{B}^{MAX}_{\pi^+\nu\bar{\nu}}/\xi} + |\lambda_c \bar{X}|. \tag{7.16}$$

$\bar{X}$ has a large uncertainty and depends on the charm quark mass, m_c, the scale factor, $\mu_c = \mathcal{O}(m_c)$, and the coupling constant, $\alpha_s(M_Z^2)$. Maximizing $\bar{X}$ ($= 1.098 \times 10^{-3}$) in Equation (7.15) gives $\mathrm{Re}\lambda_t < 1.085 \times 10^{-3}$. Minimizing $\bar{X}$ ($= 0.761 \times 10^{-3}$) in Equation (7.16) gives $\mathrm{Re}\lambda_t > -0.8197 \times 10^{-3}$. Note that the limit given in Equation (7.15) is also a limit on $|\lambda_t X_t|$, because, for a given $\mathcal{B}_{\pi^+\nu\bar{\nu}}$, $|\lambda_t|$ is maximum when it is real and directed opposite to $\lambda_c \bar{X}$.

From the lower limit of $\mathcal{B}(K^+ \to \pi^+\nu\bar{\nu})$ we obtain

$$\begin{aligned}
\mathcal{B}^{MIN}_{\pi^+\nu\bar{\nu}} &< \xi|\lambda_c\bar{X} + \lambda_t X_t|^2, \\
\sqrt{\mathcal{B}^{MIN}_{\pi^+\nu\bar{\nu}}/\xi} &< |\lambda_c\bar{X} + \lambda_t X_t| \\
&< |\lambda_c\bar{X}| + |\lambda_t X_t|, \\
\sqrt{\mathcal{B}^{MIN}_{\pi^+\nu\bar{\nu}}/\xi} - |\lambda_c\bar{X}| &< |\lambda_t X_t|.
\end{aligned} \tag{7.17}$$

By maximizing $\bar{X}$, we obtain $|\lambda_t| > 2.355 \times 10^{-4}$.

In summary, from $\mathcal{B}(K^+ \to \pi^+\nu\bar{\nu})$=$(1.47^{+1.60}_{-0.93}) \times 10^{-10}$ (68% CL) the limits on λ_t are

$$\begin{aligned}
0.236 \times 10^{-3} < &\quad |\lambda_t| \quad < 1.085 \times 10^{-3}, \\
-0.820 \times 10^{-3} < &\quad \mathrm{Re}\lambda_t < 1.085 \times 10^{-3}, \\
&\quad \mathrm{Im}\lambda_t < 0.928 \times 10^{-3}.
\end{aligned} \tag{7.18}$$

From $\mathcal{B}(K^+ \to \pi^+\nu\bar{\nu})$= $(1.47^{+2.83}_{-1.22}) \times 10^{-10}$ (90% CL) the limits on λ_t are

$$\begin{aligned}
0.107 \times 10^{-3} < &\quad |\lambda_t| \quad < 1.256 \times 10^{-3}, \\
-0.990 \times 10^{-3} < &\quad \mathrm{Re}\lambda_t < 1.256 \times 10^{-3}, \\
&\quad \mathrm{Im}\lambda_t < 1.099 \times 10^{-3}.
\end{aligned} \tag{7.19}$$

The limits on $|V_{td}|$ are extracted from Equations (7.18) and (7.19) by using the measured limits $|V_{cb}| \simeq [0.039, 0.044]$ in Equation (1.5);

$$0.0054 < \; |V_{td}| \; < 0.0278 \quad (68\%\ \mathrm{CL}), \tag{7.20}$$

$$0.0024 < \; |V_{td}| \; < 0.0322 \quad (90\%\ \mathrm{CL}). \tag{7.21}$$

The latter is compared with the current experimental range of $|V_{td}|$, $0.0048 < |V_{td}| < 0.014$, as shown in Equation (1.5). The limits on $|V_{td}|$ obtained from our results are a bit wider than those from other measurements. Figure 7.3 shows the impact of the $K^+ \to \pi^+\nu\bar{\nu}$ branching ratio on the unitarity triangle. The central value of the measured $K^+ \to \pi^+\nu\bar{\nu}$ branching ratio does not intersect with the area of (ρ,η) constrained by $|V_{ub}|$, ϵ_K, $\sin 2\beta$, and Δm_d in other measurements, all of which support the SM prediction. This

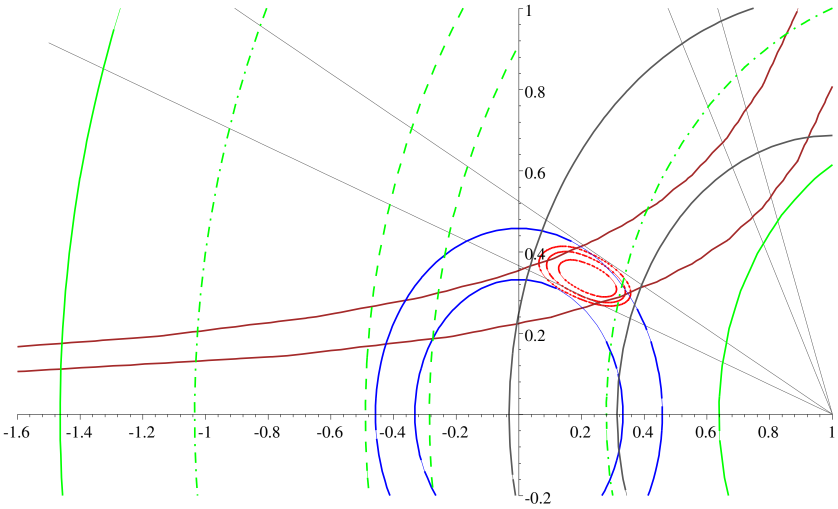

Figure 7.3: Impact of the $K^+ \to \pi^+ \nu\bar{\nu}$ branching ratio on the unitarity triangle [48]. The green lines indicate the constraints from the $K^+ \to \pi^+ \nu\bar{\nu}$ branching ratio (with theoretical uncertainty): central value (dashed), 68% CL interval (dot-dashed), 90% CL interval (solid). The red ovals show the 68%, 90%, 95% CL areas from other measurements ($|V_{ub}|$, ϵ_K, $\sin 2\beta$, Δm_d).

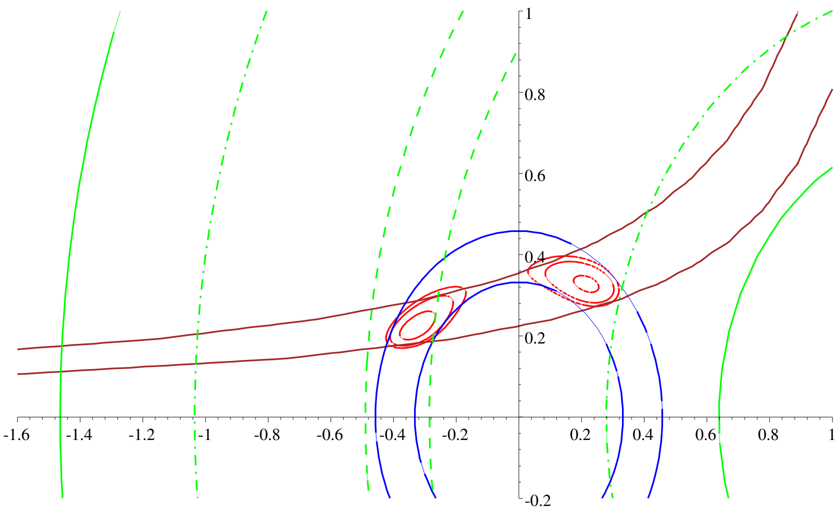

Figure 7.4: Impact of the $K^+ \to \pi^+ \nu\bar{\nu}$ branching ratio on the unitarity triangle excluding the constraints from the $\sin 2\beta$ and Δm_d measurements [48]. The green lines indicate the $K^+ \to \pi^+ \nu\bar{\nu}$ branching ratio (with theoretical uncertainty): central value (dashed), 68% CL interval (dot-dashed), 90% CL interval (solid). The red ovals show 68%, 90%, 95% CL areas from other measurements ($|V_{ub}|$ and ϵ_K).

result is very interesting in that the discrepancy may indicate new physics. For example, once the constraints from the measurements of $\sin 2\beta$ and Δm_d, both of which are obtained from the $\Delta F = 2$ weak processes, are removed, the central value intersects with the area constrained by the other K and B decays in the region $\gamma > 90^{\circ}$ (Figure 7.4) [49]. The $K^+ \to \pi^+ \nu\bar{\nu}$ branching ratio should be measured precisely with more statistics and, with the measurement of the $K_L^0 \to \pi^0 \nu\bar{\nu}$ branching ratio, independent measurements of ρ and η from K and B decays are necessary to see whether there is a discrepancy or not.

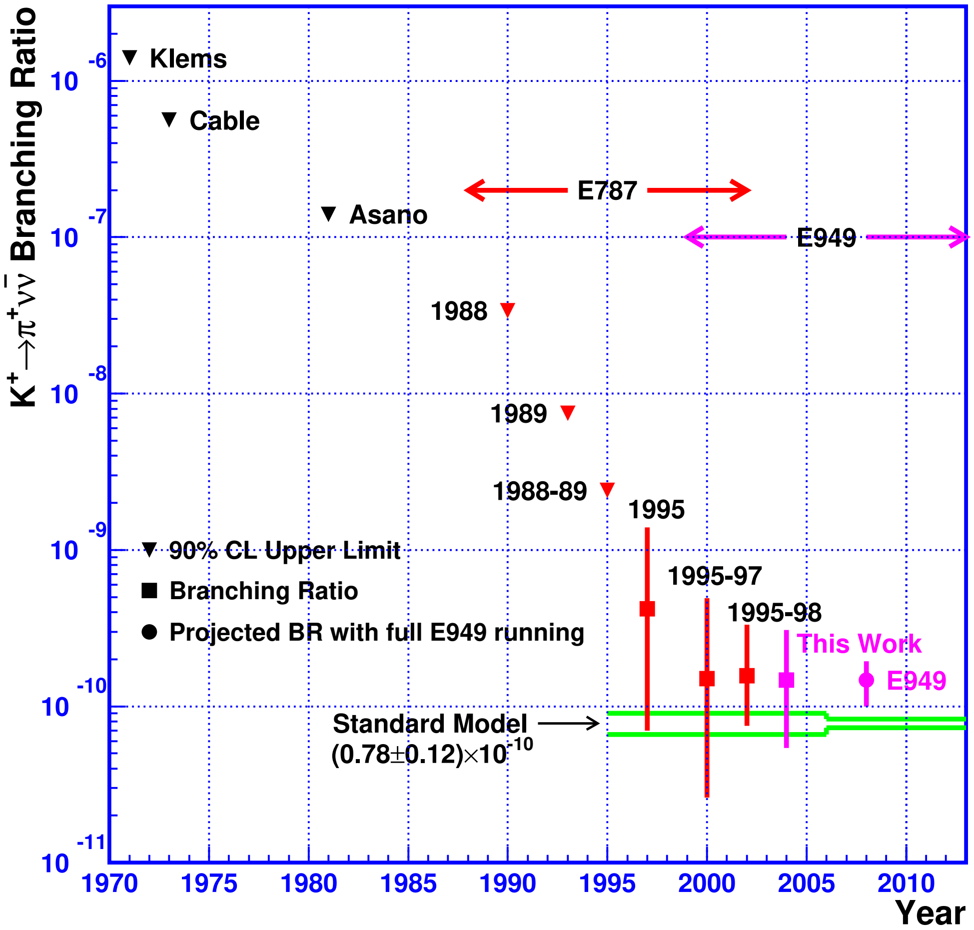

Figure 7.5: History of the search for the $K^+ \to \pi^+\nu\bar{\nu}$ decay. The vertical and horizontal axes show the $K^+ \to \pi^+\nu\bar{\nu}$ branching ratio and the publication year, respectively. The dot represents the projected branching ratio with the full E949 running period, assuming that the central value of the branching ratio is the same as the measured value of 1.47×10^{-10}. The error bars represent the 68% CL intervals. The 68% CL interval only for the combined E787 and E949 result includes the systematic uncertainty.

7.4 Progress in the Study of $K^+ \to \pi^+\nu\bar{\nu}$

Figure 7.5 summarizes the history of the search for $K^+ \to \pi^+\nu\bar{\nu}$ decay. Figure 7.6 shows the recent progress since 1995. The result from this study is consistent with the SM prediction; however, the central value remains twice as much as the SM prediction. It should be confirmed whether or not the measured value remains unchanged with more statistics. As shown in Figures 7.5 and 7.6, we would be able to collect 10-20 $K^+ \to \pi^+\nu\bar{\nu}$ candidate events with the full running period of E949. With such an amount of $K^+ \to \pi^+\nu\bar{\nu}$ signals, a possible discrepancy can be seen.

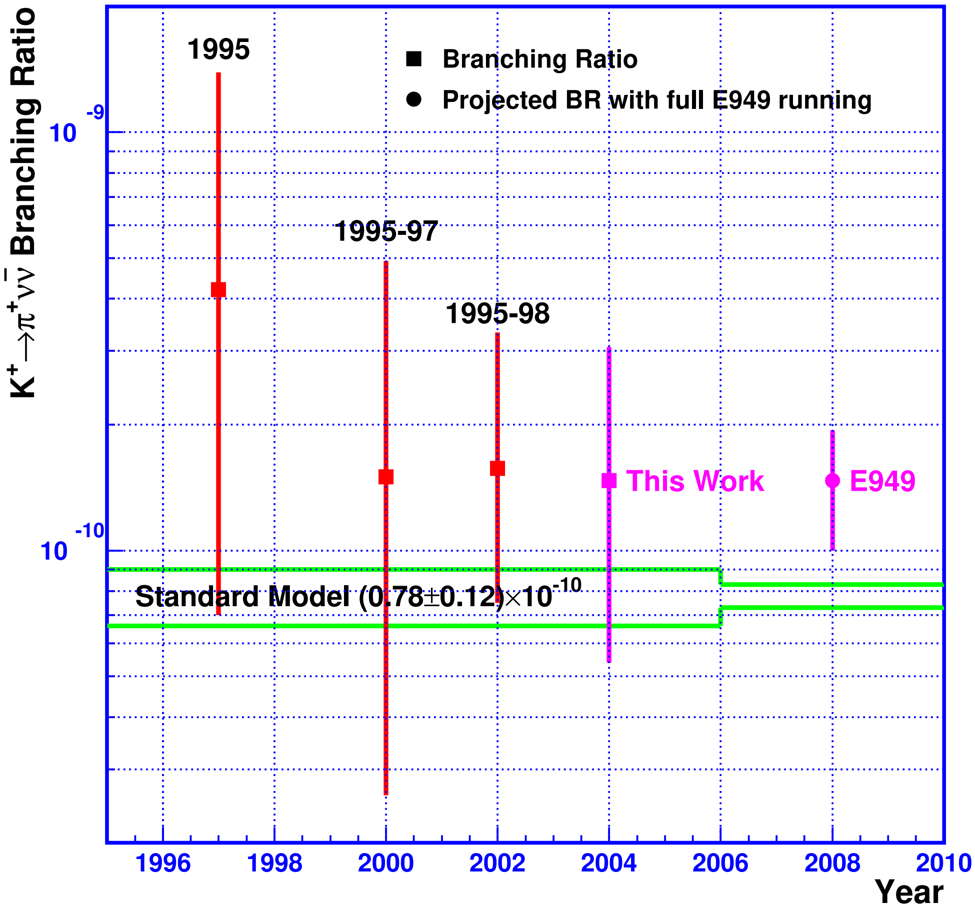

Figure 7.6: Zoom up of the recent results in Figure 7.5. The 68% CL interval only for the combined E787 and E949 result includes the systematic uncertainty.

Chapter 8

Conclusion

The rare decay $K^+ \to \pi^+ \nu\bar{\nu}$ is a flavor-changing-neutral-current process and proceeds via 1-loop diagrams that mediate the top quark. This decay involves the coupling of top to down quarks. The branching ratio of $K^+ \to \pi^+ \nu\bar{\nu}$ is expressed by the magnitude of the CKM matrix element, $|V_{td}|$. Measuring $\mathcal{B}(K^+ \to \pi^+ \nu\bar{\nu})$ is one of the cleanest ways to extract $|V_{td}|$.

BNL-E949 is a successor to BNL-E787. The E949 detector was upgraded to achieve better measurements in the beam rate, twice that of E787. E949 examined stopped K^+ decays. A high-intensity K^+ beam was produced at the Alternating Gradient Synchrotron (AGS) by exposing 65 trillion protons per spill to a platinum target. Kaons with 710 MeV/c were transported to the E949 detector, and came to rest in a scintillating fiber target. 3.9×10^6 K^+'s decayed at rest in the target per spill. The data were collected in 2002, which corresponded to 1.77×10^{12} K^+ decays.

The data were analyzed by a blind analysis. The Signal Region was masked out until the selection criteria were determined and the background levels were estimated. The development of the cuts and the estimation of the background levels were performed by using the Bifurcation Method. The Signal Region was enlarged compared to that in E787 with an increased confidence in the likelihood analysis. The enlargement of the Signal Region increased the acceptance by 30%. The total background level in the Signal Region was estimated to be 0.30 ± 0.02 events.

An examination of the Signal Region yielded one event near the upper kinematic limit of the $K^+ \to \pi^+ \nu\bar{\nu}$ decay. Based on the candidate event, an upper limit was set to be $\mathcal{B}(K^+ \to \pi^+ \nu\bar{\nu}) < 8.76 \times 10^{-10}$ at the 90% CL. E787 and E949 results were combined and the branching ratio was measured to be 1.47×10^{-10}, at which the likelihood estimator based on three events observed in the momentum region $211 \leq P \leq 229$ MeV/c has the maximum value. The 68% CL interval, including both the statistical and systematic uncertainties, was set to be $[0.54, 3.07] \times 10^{-10}$ with the statistical method described in Sections 7.1 and 7.2, and to be $[0.58, 2.77] \times 10^{-10}$ [47] with the T. Junk's method described in Appendix J. The measured branching ratio was twice as large as the SM prediction of $(0.78 \pm 0.12) \times 10^{-10}$, but was consistent within the error. At the measured central value of the branching ratio, the additional candidate event had a signal-to-background ratio of 0.9.

From the measured branching ratio, we set the limits on both $|\lambda_t|$ and $|V_{td}|$ to be

$$0.107 \times 10^{-3} < |\lambda_t| < 1.256 \times 10^{-3} \quad \text{and} \quad 0.0024 < |V_{td}| < 0.0322,$$

at the 90% CL interval, which was consistent with the current experimental range of $0.0048 < |V_{td}| < 0.014$ at the 90% CL interval.

Acknowledgments

First of all, I would like to express my great appreciation to my supervisor, Prof. S. Sugimoto, who gave me opportunities to join the BNL-E949 collaboration and to stay for a long time at BNL and TRIUMF for my research work.

I would like to express my thankfulness to Prof. T.K. Komatsubara. He gave me much useful advice for my study. I would not have been able to work on this experiment without his help.

I would like to express my gratitudes to Prof. D.A. Bryman, Dr. S. Chen, Dr. J. Hu, Prof. P. Kitching, Dr. A. Konaka, Dr. J. Mildenberger, Dr. T. Numao, and Dr. R. Poutissou of TRIUMF, Dr. I-H. Chaing, Dr. M.V. Diwan, Dr. J.S. Frank, Dr. D.E. Jaffe, Dr. S.H. Kettell, Dr. K.K. Li, Dr. L.S. Littenberg and Dr. G. Redlinger of BNL, Dr. D.V. Vavilov of IHEP, Mr. K. Mizouchi of Kyoto University and Mr. T. Yoshioka of KEK. They gave me a great deal of valuable advice in analyzing the $\pi\nu\bar{\nu}(1)$ data. I was very glad to have many discussions with them, which helped my study and encouraged me. They have had a great influence on my attitude as a scientist.

I would like to thank Prof. M. Kobayashi, Prof. T. Nakano, Prof. M. Nomachi, Dr. T. Nomura, Dr. K. Omata, Prof. T. Sato, Prof. T. Shinkawa, Prof. Y. Tamagawa and Prof. Y. Yoshimura, who helped me many times during my stays in BNL; their help really encouraged me when I was staying there for a long period. I would like to express my thanks to Mr. T. Fujiwara and Mr. T. Tsunemi for their useful advice in weekly meetings. I would also like to express my acknowledgments to other E949 collaborators in Japan, Canada, Russia, and the United States.

Finally, I would like to express my deepest gratitudes to my parents. They helped me whenever I had difficulties in my life and gave me a talent that led me to be a scientist. Thanks to them, I have had a lot of wonderful opportunities in my life.

This research was supported by the Japan-U.S. Cooperative Research Program in High Energy Physics and the Grant-in-Aid for Scientific Research on Priority Areas "Origin of Mass".

Appendix A

Offline Event Reconstruction

Event reconstruction consists of (1) reconstruction of a charged track in the target, UTC and Range Stack, (2) reconstruction of the kaon path and the decay vertex in the target, (3) reconstruction of beam particle hits in the beam instrumentation, and (4) reconstruction of photon hits in the photon detectors. The event reconstruction in the x-y view is shown in Figure A.1.

Charged-track reconstruction is performed twice for the target, UTC and RS. The first step is to search for the Range Stack counters that have hits due to the track (called the track counters). At first, a sector that has coincident TDC hits in the first two layers of the RS counters around the *online* T•2 timing is determined to be the *offline* T•2 sector. If the sector is not found, the *online* T•2 sector is used. The track counters are determined to be the counters that have TDC hits coincident with the T•2 timing. The average time of the track counters is defined as the track time, "t_{RS}". The outermost and most clockwise track counter is defined as the *offline* stopping counter.

In UTC track reconstruction, the track is reconstructed by two separated fits in the x-y plane (perpendicular to the beam axis) and the r-z plane (formed by the radial and beam axes). In the x-y plane, a circle is fitted to the hit positions derived from the sense-wire locations and drift distances. In the r-z plane, a straight line is fitted to the cathode strip hits. The polar angle of the charged track is evaluated from this r-z fitting.

In the first step of the target reconstruction, the reconstruction code examines the times, energies and positions of the target fibers having CCD hits, and categorizes them into "kaon", "pion", "opposite-side pion" and "gamma" fibers. The "kaon" fibers are determined by picking up the fibers that have energies of typically larger than 4 MeV, times coincident with that of the B4 Hodoscope, and positions located beside the extrapolated UTC track. The average time of the kaon fibers is defined as the target kaon time, "t_K", and the energy sum of the kaon fibers represents the target kaon energy. The kaon decay vertex is determined by picking up the kaon fiber that is closest to the extrapolated UTC track and farthest from the x-y position of the B4 Hodoscope hit. The z position of the kaon decay vertex is obtained by extrapolating the UTC track to the kaon decay vertex fiber. The "pion" and "opposite-side pion" fibers are selected by taking the fibers which have energies typically less than 1 MeV, times coincident with the track time, and positions located along the UTC track extrapolation. The fibers on the side of the UTC track relative to the decay vertex are assigned to "pion" fibers. The fibers on the other side

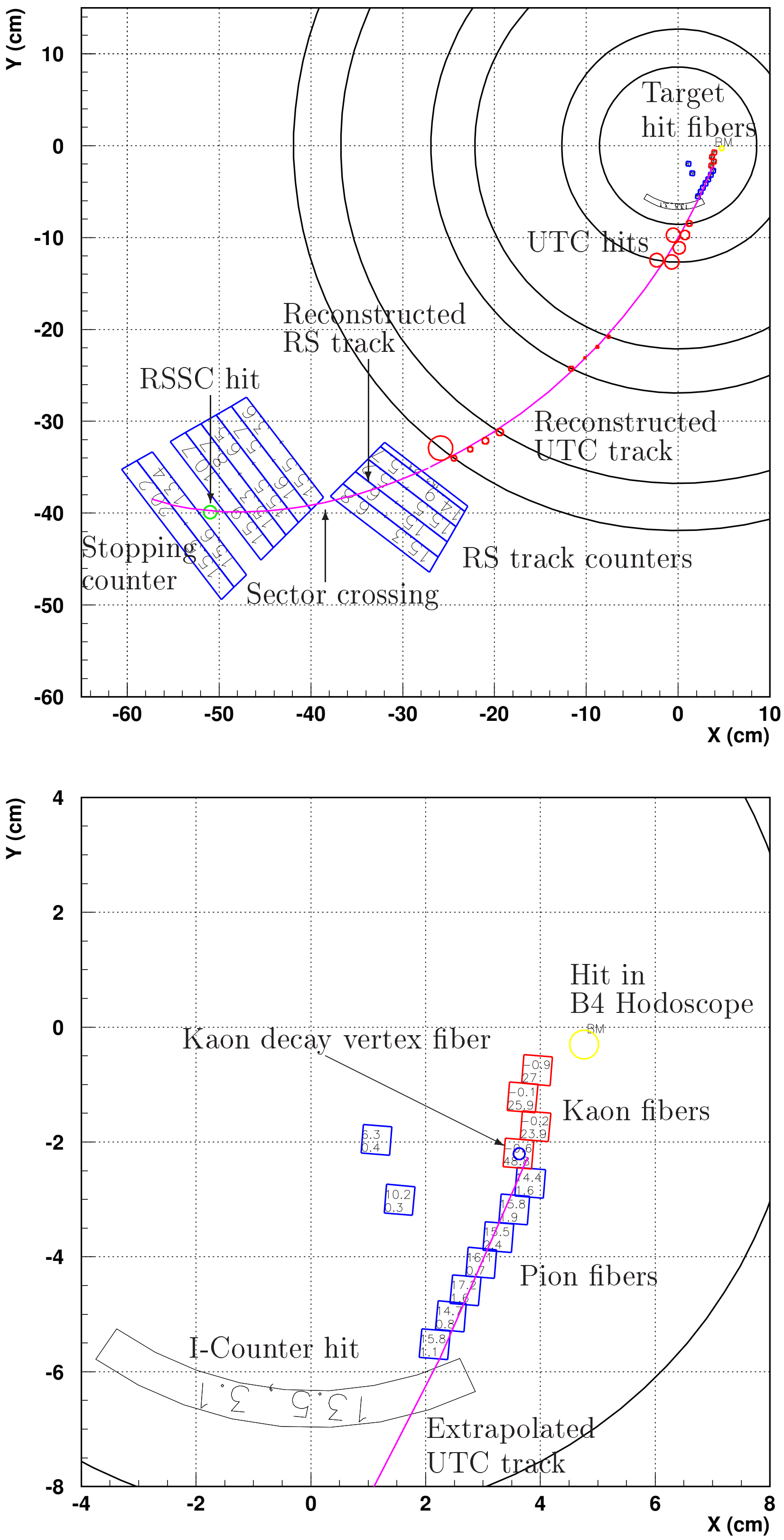

Figure A.1: Reconstruction of an event in the x-y view: the reconstruction in the target, UTC and Range Stack (top), and the reconstruction in the target (bottom).

are assigned to "opposite-side pion" fibers, and could potentially be indicating additional charged particles. The average time of hits in the pion fibers is defined as the target pion time, "t_π". The fibers which have times consistent with the track time and which are not categorized as the kaon, pion or opposite-side pion fibers are assigned to "gamma" fibers. Hits in the gamma fibers potentially originate from photons or secondary beam particles.

In the stopping counter, the $\pi^+ \to \mu^+$ decay signature is searched for via a pulse-fitting method. Details concerning the pion identification with the pulse fitting are given in the next section.

After the pulse fitting is made, a second iteration of the track reconstruction is performed. The second iteration of the UTC track fitting is performed by including the positions of the target pion fibers into the x-y fit. The momentum in the UTC is calculated from the radius of the circle in the x-y fit and the polar angle in the r-z fit. Finally, the total momentum of the charged track is obtained by correcting the momentum in the UTC by the target range, the I-Counter range and the amount of dead materials due to the inner wall of the UTC and the drift gas. After the UTC track determination is finished, a second iteration of the target reconstruction is made. In this iteration, a double-pulse fitting is performed with the CCD pulses of the kaon decay vertex fiber to look for the $K^+ \to \pi^+$ decay pattern. The energy loss of the pion in the kaon decay vertex fiber, obtained from the second pulse found by the fitting, is subtracted from the target kaon energy and is added to the target pion energy.

The energy deposit of the charged track in the Range Stack is calculated at this moment. There are three ways to measure the energy loss in the RS counters: (1) the energy obtained from the ADC, (2) the energy from the TD pulse height, and (3) the energy from the TD pulse area. The energy deposit in each track counter is primarily obtained from the ADC energy, which is the area of a pulse within an ADC gate of 100 ns. In the case that an accidental hit deposits energy in one of the track counters within the ADC gate, the track energy could be overestimated, and would result in a contamination of the $K_{\pi 2}$ background to the Signal Region. To avoid this, the energy obtained from the TD pulse height information is used instead of the ADC energy if the ADC energy is much greater than the energy expected from the TD pulse height, because the pulse height of the track hit is less disturbed by the existence of an accidental pulse. The total energy deposit of the track in the RS is obtained by summing up the energies from the ADCs (or TD pulse heights) in the track counters, and by subtracting the muon energy in the stopping counter measured by the TD pulse fitting [1]. This visible energy in each track counter is corrected to the true energy deposit by Birk's formula [43],

$$\frac{dL}{dx} = \frac{dE/dx}{1 + k_B \cdot dE/dx}, \tag{A.1}$$

where L is the luminescence in a plastic scintillator and $k_B = 0.01$ is called Birk's constant.

The range of the charged track in the RS is calculated via a track-fitting method. The path of the charged track is calculated separately in the x-y and r-z planes. The

[1] In the stopping counter, the energy of the μ^+ from the $\pi^+ \to \mu^+$ decay would have been recorded in the ADC, in addition to the energy of the π^+ track coming to rest, if the π^+ decays at rest within the ADC gate. In this case, the muon energy should be subtracted from the ADC energy in order to avoid an overestimation of the π^+ kinetic energy.

fitting is performed only in the x-y plane. In the track-fitting code, the propagation of a track in the RS is performed by losing kinetic energy with the Bethe-Bloch formula with the pion assumption, and by being bent in a 1 Tesla magnetic field. By varying the incident momentum and angle (in the x-y plane) at the entrance of the RS, which are treated as input parameters, the track propagation is repeated until the track matches the measured positions of the sector crossing and RSSC hits and the measure energy in the stopping counter. In the r-z plane, the path of the track is obtained by extrapolating the UTC track to the stopping position of the track. The χ^2's are calculated by examining the residuals between the extrapolated UTC track and the z measurements based on the end-to-end time differences in the individual RSSCs and RS counters. The range in the RS is calculated from the path length of the fitted track, and is then corrected to the total range by adding the target range, the range in the I-Counter, and the ranges in the dead materials using the extrapolated UTC track.

In the Kaon and Pion Čerenkov Counters, coincident TDC or CCD hits are clustered from 14 PMTs in each. The average time and the multiplicity of those hits are calculated for each cluster. In the two sets of Beam Wire Chambers, beam particle hits are reconstructed when two or three planes have coincident TDC hits. In the case to reconstruct three-plane hits, it is required that the hit wires cross at a point. The TDC values of the wire hits are averaged to obtain the time of the incoming particle. In the B4 Hodoscope, two perpendicular counters in different layers are clustered when they have coincident TDC or CCD hits. The time and x-y position of the cluster are obtained from the energy-weighted average of the TDC or CCD hits. The measured energy deposits are used to separate kaons and pions, which leave different energies to the B4 Hodoscope. The times of hits in any of the above beam detectors are used to remove Double Beam events by checking extra activities at the track time.

In the photon detectors, the time and energy of each module in the detector subsystems are calculated. The hits that are coincident with the track time are searched for to veto the backgrounds that include photons.

A.1 Observation of $\pi^+ \to \mu^+$ Double Pulses

In the π^+ stopping counter, the $\pi^+ \to \mu^+$ decay signature is identified via a pulse-fitting method. When a π^+ comes to rest in the Range Stack, the stopping counter has the signature of double pulses due to the π^+ and the secondary μ^+. The pulse-fitting algorithm performs χ^2 fitting twice (and sometimes three times) with a single-pulse assumption and a double-pulse assumption by varying the leading edges, heights and pedestals of the template pulses that were prepared for the individual counters at both ends, and calibrated by the $\pi_{scatter}$ monitor trigger data. A triple-pulse fitting is performed when more than two pulses are found, or one of the quantities for the double-pulse fitting is worse than a certain threshold value, that is, the fitted second pulse does not look to be due to a μ^+, but an accidental. The algorithm returns the fitting qualities for both the single- and double-pulse assumptions (and triple-pulse assumption) and the time and energy information of the pulses obtained by the fitting. These outputs are tabulated in Tables A.1 and A.2. The TD pulse shapes in the examples of the double-pulse and triple-pulse fittings are shown in Figures A.2 and A.3.

A.1.1 Assignment of Triple Pulses

In the case of the triple-pulse fitting, the assignment of the triple pulses to the pion, muon and accidental is important because the $\pi^+ \to \mu^+ \to e^+$ Decay Sequence Cuts (in particular, the Neural Net $\pi^+ \to \mu^+$ Decay Cut) depend on the pulse assigned as a muon (and also pion). Any incorrect assignment of the accidental as a muon causes an acceptance loss of the pion identification.

The pulse assignment is performed as follows: at first, a pulse whose timing is closest to the track time is assigned as a pion. Then, there are three cases for assigning the other two pulses: (1) the accidental is detected before the pion pulse (top figure in Figure A.4), (2) two pulses are detected after the pion pulse (the earlier is a muon and the later is an accidental (middle in Figure A.4)), and (3) two pulses are detected after the pion pulse (the earlier is an accidental and the later is a muon (bottom in Figure A.4)). In case (1) above, the pulse detected after the pion is assigned as a muon. When there are two pulses after the pion (cases (2) and (3) above), the muon is determined in the following algorithm:

1. A pulse whose energy in each end is > 0.8 MeV (single-end energy cut) is assigned as a muon if the other pulse fails the single-end energy cut.

2. If both pulses satisfy the single-end energy cut, the end-to-end time differences of both pulses are examined, and

3. the pulse that gives the minimum time difference is assigned as a muon when the time difference in the other pulse is more than 6 ns (time difference cut).

4. A pulse whose area ratio of one end to the other is consistent with that of the pion pulse is assigned as a muon when both pulses pass the time-difference cut and satisfy the condition that the geometrical mean of the both-end energies is $0.8 < E < 11$ MeV (mean energy cut).

5. A pulse which passes the mean energy cut is assigned as a muon when both pulses satisfy the time-difference cut and the remaining pulse fails the mean-energy cut.

6. Case 4 is further classified: an earlier pulse whose energy is within $\pm 3\sigma$ of the muon energy peak (~ 3.04 MeV, $\sigma \sim 0.5$ MeV) is assigned as a muon.

Because of this triple-pulse fitting, we recovered the 10% acceptance loss of the $\pi^+ \to \mu^+$ Double-Pulse Fitting Cut, whose performance became worse for a high beam rate.

Variables	Descriptions
ipiflg	integer that represents the fitting results. ipiflg=0 means a good double-pulse is found.
cmuend(i)	single-pulse fit χ^2 for end i.
cpiend(i)	double-pulse fit χ^2 for end i.
cmupi(i)	χ^2 ratio of the single-pulse fit to double-pulse fit for end i ($\equiv$ cmuend(i)/cpiend(i)).
prod	Product of cmupi(1) and cmupi(2) ($\equiv$ cmupi(1)·cmupi(2))
emuon(i)	Pulse area of the second pulse for end i in TD counts.
emuonc(i)	Calibrated second-pulse energy for end i in MeV.
emut	Geometrical mean of emuon(1) and emuon(2) ($\equiv \sqrt{\text{emuon(1)} \cdot \text{emuon(2)}}$)
emutc	Geometrical mean of emuonc(1) and emuonc(2) ($\equiv \sqrt{\text{emuonc(1)} \cdot \text{emuonc(2)}}$)
tmuon(i)	Time of the second pulse with respect to first-pulse time for end i in ns.
tmuav	Average time of the second pulses in both ends in ns ($\equiv$ 0.5·(tmuon(1) + tmuon(2)))
dt	Time difference of the second pulses in both ends in ns ($\equiv$ tmuon(1)−tmuon(2))
epion(i)	Pulse area of the first pulse for end i in TD counters.
tpion(i)	Time of the first pulse for end i in ns.
ped(single)	pedestal with single-pulse assumption.
ped(double)	pedestal with double-pulse assumption.

Table A.1: Output of the pulse-fitting algorithm for the single- and double-pulse assumptions. The end i means $i = 1$ for the upstream end and $i = 2$ for the downstream end.

Variables	Descriptions
kpiflg	3-digit integer that represents the reason why the triple pulse fitting is performed.
c3pend(i)	triple-pulse fit χ^2 for end i.
cmu3p(i)	χ^2 ratio of the single-pulse fit to triple-pulse fit for end i ($\equiv$ cmuend(i)/c3pend(i)).
cpi3p(i)	χ^2 ratio of the double-pulse fit to triple-pulse fit for end i ($\equiv$ cpiend(i)/c3pend(i)).
prod3	Product of cmu3p(1) and cmu3p(2) ($\equiv$ cmu3p(1)·cmu3p(2))
e3p(i)	Pulse area of the third pulse for end i in TD counts.
e3pc(i)	Calibrated third-pulse energy for end i in MeV.
e3pt	Geometrical mean of e3p(1) and e3p(2) ($\equiv \sqrt{\text{e3p(1)} \cdot \text{e3p(2)}}$)
e3ptc	Geometrical mean of e3pc(1) and e3pc(2) ($\equiv \sqrt{\text{e3pc(1)} \cdot \text{e3pc(2)}}$)
t3p(i)	Time of the third pulse with respect to first-pulse time for end i in ns.
t3pav	Average time of the third pulses in both ends in ns ($\equiv$ 0.5·(t3p(1) + t3p(2)))
dt3	Time difference of the third pulses in both ends in ns ($\equiv$ t3p(1)−t3p(2))
ped(triple)	pedestal with triple-pulse assumption.

Table A.2: Output of the pulse-fitting algorithm for the triple-pulse assumption.

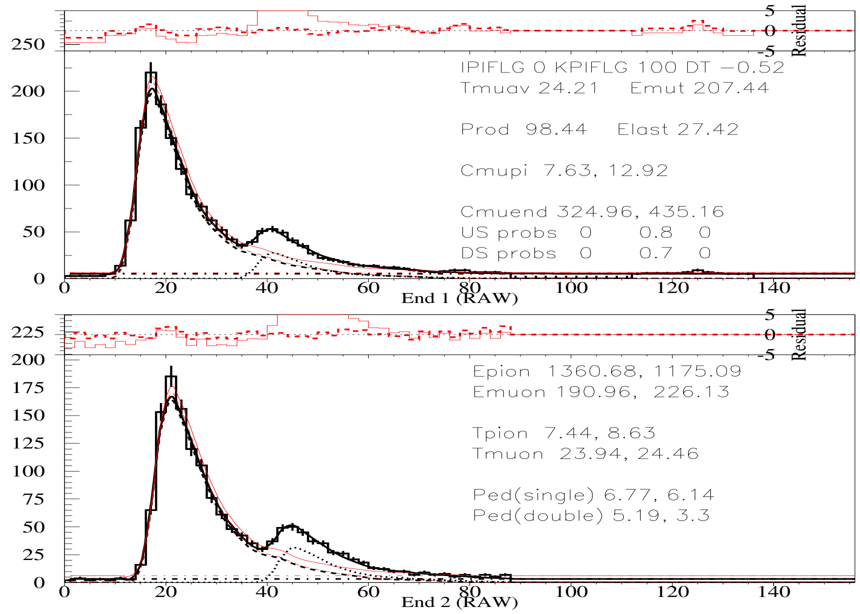

Figure A.2: Double-pulse fitting to the TD pulse shape in the stopping counter for the upstream (top) and downstream (bottom) ends.

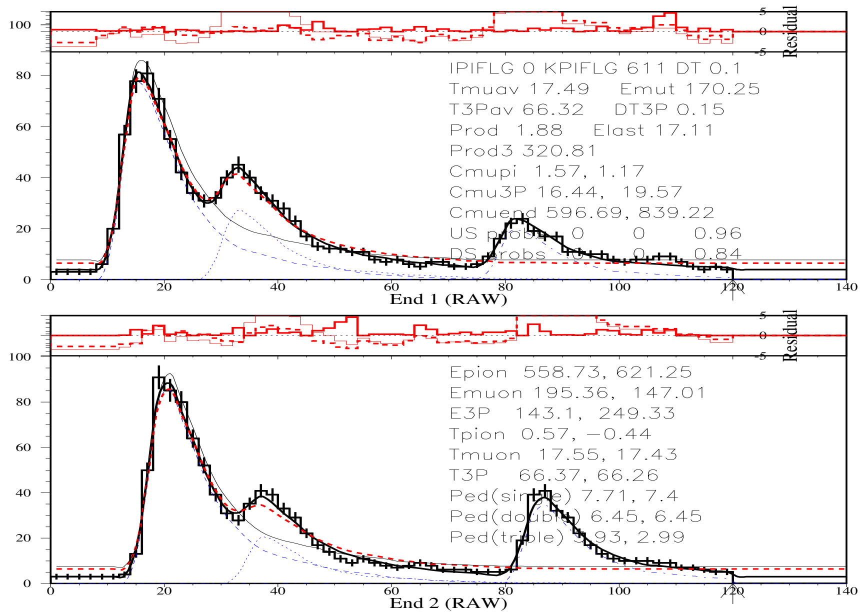

Figure A.3: Triple-pulse fitting to the TD pulse shape in the stopping counter for the upstream (top) and downstream (bottom) ends.

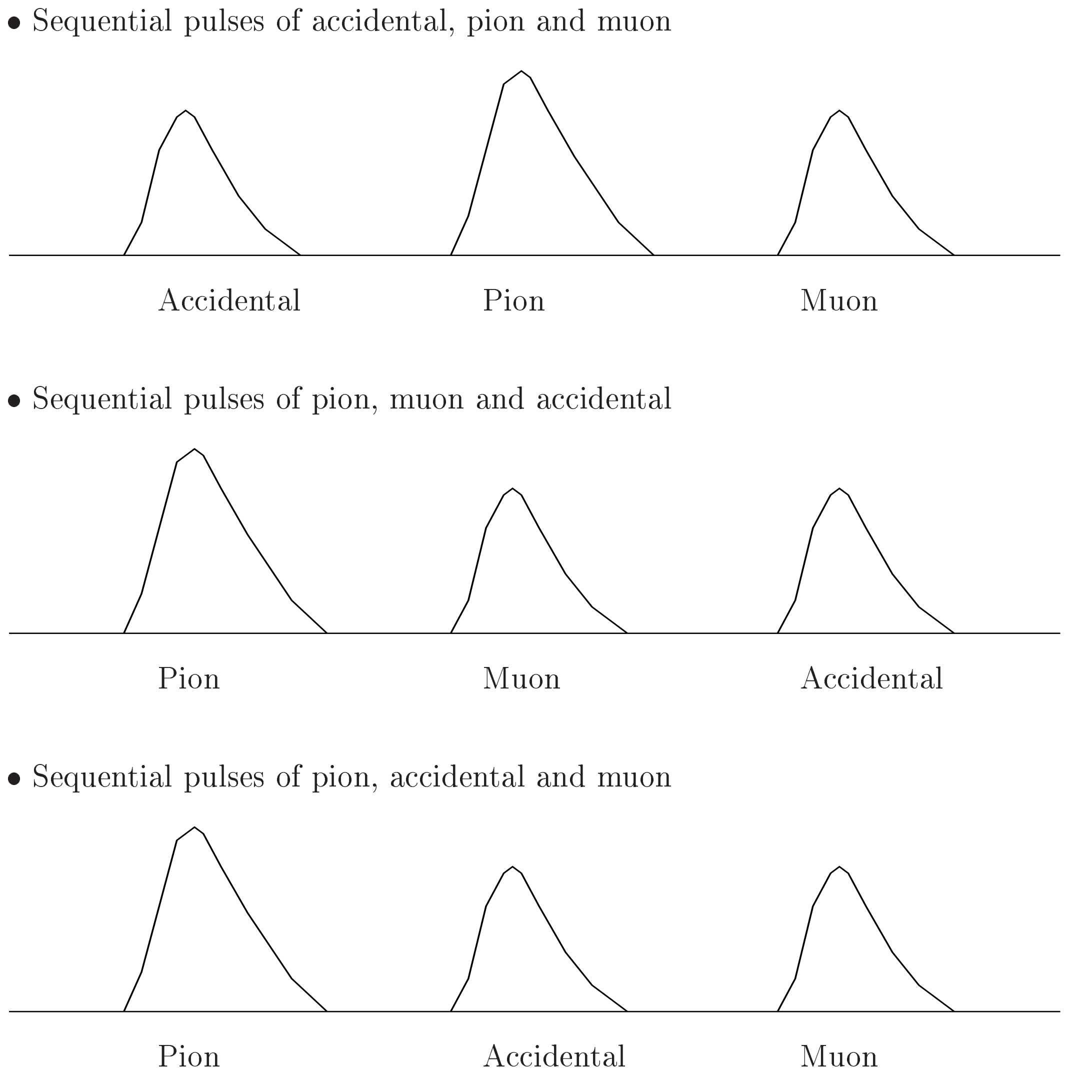

Figure A.4: Assignment of the triple pulses to the pion, muon and accidental: the sequential pulses of the accidental, pion and muon (top), the sequential pulses of the pion, muon and accidental (middle), and the sequential pulses of the pion, accidental and muon (bottom).

Appendix B

List of Cuts

B.1 Pass 1 Cuts

B.1.1 Event Reconstruction Quality Cuts

- Trigger Bit (TRBIT)
  The event passes the online trigger bit of $\pi\nu\bar{\nu}(1)$.

- Data Taking Quality (BAD_RUN)
  The runs when some problems on the beam, detector, and electronics happened were assigned as "bad run" during the detector calibration. Events in the bad runs are removed.

- Charged Track Reconstruction (RD_TRK)
  The track is reconstructed in the Range Stack.

- Track Time Reconstruction (TRKTIM)
  The average time of the track hits in the Range Stack is obtained.

- Consistency between Online and Offline Stopping Counters (STLAY)
  The stopping counter that is found by online Stopping Counter Finder (SCF) should be the same as that found by offline track finding routine.

- Stopping Counter Performance (BAD_STC)
  Some TD channels had problems on recording input signals in specific period of data taking. These "bad TD channels" were listed during the detector calibration. The charged track should not stop in the counters where the corresponding TD were unable to record signals properly.

- Track Fitting in UTC (UTC)
  The track is successfully reconstructed in the UTC.

- Matching Between UTC and RS Tracks (UTC/RANGE)
  The track reconstructed in the UTC should point the T•2 sector in the RS.

- Target Reconstruction (TARGET)
  Target reconstruction is successfully done.

- Momentum in UTC (PDC)
  Momentum measured by the UTC should be less than 280 MeV/c. This requirement removes the failure of UTC pattern recognition.

B.1.2 Muon Background Rejection Cuts

- $\pi^+ \to \mu^+$ Double-Pulse Fitting (FITPI)
  $\pi^+ \to \mu^+$ double pulses were found by fitting TD pulses in the stopping counter.

- Photon Veto around Stopping Counter (RSHEX)
  No extra hit is allowed in the stopping counter and the hextants that do not have track hits.

- Sector Crossing Cut (RSHEX2)
  No sector crossing is allowed in the stopping layer.

- π^+ Stop Fiducial Requirement (LAY14)
  The charged track should not come to rest in the support materials for the RSSC second layer, which is embedded between the RS layers 14 and 15.

B.2 Pass 2 Cuts

- Crude Photon Veto Cut (PVCUT)
  Perform photon veto in the Barrel Veto (BV), End Cap (EC) and Range Stack (RS). Photon hits that are coincident with the charged track time (in-time hits) are selected. Events are rejected if the energy sum of the in-time hits in each subsystem is above the threshold. The time windows and energy thresholds are summarized in Table B.1.

Subsystem	Time Window	Energy Threshold
Barrel Veto	± 2.0 ns	1.5 MeV
End Cap	± 1.5 ns	3.5 MeV
Range Stack	± 1.5 ns	3.0 MeV

Table B.1: The time windows and energy thresholds for Barrel Veto, End Cap and Range Stack.

- Target Reconstruction Cut (TGCUT)
  This cut consists of the following requirements:
  - Kaon decay vertex is inside the target.
  - The time consistency between the average time of the kaon fiber hits in the target (target kaon time) and the B4 Hodoscope hit time is within 4 ns.

- The time consistency between the average time of the pion fiber hits in the target (target pion time) and the I-Counter hit time is within 5 ns.
- The energy deposit in the I-Counter should be consistent with those of pions.

- Accidentals at Muon Time (TDCUT)
Search for accidental activities in the RS that are coincident with the second pulse time (muon time) in the stopping counter. Events are rejected if the energy sum of the coincident hits exceeds a threshold.

- Beam dE/dx & Double Beam Cut (PSCUT)
Require that the energy deposit in the B4 Hodoscope is greater than a specific value and no extra beam particle coincident with the track time is recorded.

- Target Photon Veto Cut (TGPVCUT)
Require no extra activities other than kaon and pion hits in the target. This cut rejects events with photon activities in the target and events with an extra beam particle in the target.

- Delayed Coincidence Cut (DELCO2)
Require that kaons should decay at least 2 ns after entering the target.

- $\pi_{scatter}$ Selection Cut (TGPVTR)
Require that the time difference between the incoming and outgoing particles is less than 2 ns. Also required is that there are some extra activities in the target.

B.3 Beam Cuts

B.3.1 Particle Identification

- dE/dx in B4 Hodoscope (B4DEDX)
Kaon identification is performed by examining a dE/dx in the B4 Hodoscope. The dE/dx in the B4 Hodoscope is required to be greater than or equal to 1.85 MeV.

B.3.2 Kaon Stop Requirement

- Delayed Coincidence Cuts (DELC)
The target pion time, t_π, is at least 2 ns later than the target kaon time, t_K (i.e., $t_\pi - t_K \geq 2$ ns). The cut position is tightened if either target kaon or pion times have a large uncertainty.
  - $t_\pi - t_K \geq 5$ ns if the discrepancy between the target kaon time and B4 hit time is greater than 1 ns.
  - $t_\pi - t_K \geq 6$ ns if the discrepancy between the target pion time and track time is greater than 1.5 ns.
  - $t_\pi - t_K \geq 5$ ns if t_π is obtained from the time of the I-Counter hit, not from the target pion fiber hits.

- $t_\pi - t_K \geq 4$ ns if the energy deposit of a kaon in the target is less than or equal to 50 MeV.
- $t_\pi - t_K \geq 3$ ns if there are less than 4 target pion fibers found.
- $t_\pi - t_K \geq 3$ ns if a beam likelihood value is less than 200.
- $t_\pi - t_K \geq 4$ ns if the discrepancy between any of the individual kaon fiber times and the average kaon time is greater than 2 ns.
- $t_\pi - t_K \geq 4$ ns if the discrepancy between any of the individual pion fiber times and the average pion time is greater than 3.5 ns.

B.3.3 Double-Beam Cuts

- Double-Pulse Fitting in B4 Hodoscope (B4CCD)
  Pulses recorded in the B4 CCD are fitted with a double-pulse assumption. Reject events if hit modules have a signature of double pulses, and the average time of the fitted second pulses is within ±3.5 ns of the track time. The signature of double pulses means the ratio of a single-pulse fit χ^2 to a double-pulse fit χ^2 is greater than a certain value, and the energy of the fitted second pulse exceeds a threshold.

- Timing in B4 Hodoscope (B4TRS)
  Events are rejected if the average TDC time of hit modules in B4 Hodoscope is within ±2.5 ns of the track time, or the average CCD time of hit modules is within ±1.5 ns of the track time when the energy sum is above a threshold.

- Timing in BWPCs (BWTRS)
  Events are rejected if a time of a hit cluster in any Beam Wire Chambers is within ±4.5 ns of the track time.

- Timing in Kaon Čerenkov Counter (CKTRS)
  Events are rejected if the average TDC or CCD time of hits in the Kaon Čerenkov Counter is within ±2 ns of the track time.

- Extra Timing Cut in Kaon Čerenkov Counter (CKTAIL)
  The average time of hits in the Kaon Čerenkov Counter, obtained from the trailing edge of the pulses (minus the TDC width), should not be coincident with the track time. The time windows for this cut is dependent on the value of $t_\pi - t_K$.

  1. $t_\pi - t_K < 15$ ns: events are rejected if there are any hits within ±3 ns of the track time.
  2. $15 \leq t_\pi - t_K < 25$ ns: events are rejected if there are any hits within ±3.5 ns of the track time.
  3. $t_\pi - t_K \geq 25$ ns: events are rejected if there are any hits within ±2 ns of the track time.

- Timing in Pion Čerenkov Counter (CPITRS)
  Events are rejected if the average TDC or CCD time of hits in the Pion Čerenkov Counter is within ±2 ns of the track time.

- Extra Timing Cut in Pion Čerenkov Counter (CPITAIL)
  The average time of hits in the Pion Čerenkov Counter, obtained from the trailing edge of the pulses (minus the TDC width), should not be coincident with the track time. Event are rejected if there are any hits within ± 2 ns of the track time.

B.3.4 Pathology Cuts

- Beam Likelihood Cut (B4EKZ)
  A likelihood is constructed from the energy deposit in B4 Hodoscope, the energy sum of the kaon fibers and the K^+ stopping z position. The likelihood value is required to be greater than 2.
- Tight Beam Likelihood Cut (B4EKZ_IC)
  The beam likelihood cut is tightened if no pion fiber is found in the target. The likelihood value is required to be greater than 12.5.
- Consistency Cut between B4 Hodoscope Analyses (B4ETCON)
  Requires a consistency between different analyses in B4 Hodoscope.
- Target Kink (DRP)
  Charged tracks with a kink in the target should be removed. The maximum (minimum) distance from the hit position of target pion fibers to the center of the circle that is fitted to the track path are examined. Reject events if the distribution of the pion fibers is broad, namely

  $$\frac{d_{max} - d_{min}}{R_{tg}} > 0.35$$

  where d_{max} and d_{min} are the maximum and minimum distances, respectively, and R_{tg} is the range of the track in the target.
- Matching between Target and UTC (DTGTTP)
  Require that the target and UTC tracks are well matched to each other at the target radius.
- Energy Cut on Target Pion Fiber near Decay Vertex (EPIMAXK)
  Require that any target pion fiber close to the decay vertex should have an energy of less than 3 MeV.
- Energy Cut on Target Pion Fiber (EPITG)
  Require any target pion fiber should have an energy of less than or equal to 5 MeV.
- Kaon Time in I-Counter (KIC)
  Events are rejected if target kaon fibers are found near the I-Counter and a hit time in the I-Counter is coincident with the target kaon time.
- Opposite-side Pion Fibers (OPSVETO)
  Energy sum of the target fibers, which are on the opposite side of the pion fibers relative to the decay vertex and are coincident with the target pion time (within ± 3.0 ns), should be less than 2 MeV.

- Extra Cut on Opposite-side Pion Fibers (OPSVETO_LKB)
  The above cut is tightened to 0.5 MeV when a beam likelihood value is less than 200.

- Back-to-back Track Cut in Target (PHIVTX)
  Reject events with back-to-back tracks in the target.

- Quality on Target Path Length Calculation (RTDIF)
  Require the small uncertainty in the calculation of the pion path length in the target.

- Target Gap Cut between Kaon and Pion Fibers (TARGF)
  Reject events with the gap between kaon cluster and nearest pion fiber in the target.

- Energy in Target Edge Fibers (TGEDGE)
  Reject events with more than 4 MeV energy in any of target edge fibers within ± 5 ns of the track time.

- Energy-Range Consistency in Target (TGER)
  Reject events with a small energy ($E_{tg} < 1$ MeV) and a non-negligible range ($R_{tg} > 2$ cm) in the target.

- Double-beam Cut in Target (TGGEO)
  Timing information in the I-Counter is used to reject Double Beam background with the following signatures: (1) both particles enter the target from a target edge or an I-Counter, (2) the first particle or its decay product deposits a large energy pulse in the I-Counter, and (3) the first particle enters the target, decaying downstream or decaying very late (i.e., the decay product is not detected). The second particle is scattered upstream of the beam line and misses in some beam counters; later, by multiple scattering it enters the target and intersects the hit fibers of the first beam particle. These signatures fool the target reconstruction.

- Target Reconstruction (TGQUALT)
  The kaon vertex is reconstructed inside the target.

- Timing Consistency between Range Stack and I-Counter (TIC)
  Require timing consistency between the track time (t_{RS}) and I-Counter hit time (t_{IC}).
  $$|t_{RS} - t_{IC}| \leq 5.0 \text{ ns}$$

- Timing Consistency between Target and B4 Hodoscope (TIMCON)
  Require the consistency between the target kaon time (t_K) and the time of hit in the B4 Hodoscope (t_{B4}), and between the target pion time (t_π) and the track time (t_{RS}).
  $$|t_K - t_{B4}| \leq 3.0 \text{ ns} \quad \text{and} \quad -4.5 < t_\pi - t_{RS} < 4.0 \text{ ns}$$

- Target Fiducial Cut (TGZFOOL)
  Require z position of the kaon decay vertex obtained from the UTC extrapolation should be within the target fiducial volume. This cut ensure that the kaon decays in the target.

- Timing Consistency among Target Kaon Fibers (TGTCON)
  Require the consistency between the average time of the kaon fiber hits and the times of the individual kaon fiber hits in the target.

- Photon Veto in Upstream Photon Veto and Ring Veto (UPV/RVTRS)
  Reject events with any activities at the track time in the Upstream Photon Veto or in the Ring Veto.

B.4 Kinematic Cuts

B.4.1 Fiducial Cuts

- Stopping Layer Requirement (LAYV4)
  Require that the π^+ stopping layer is between 11 and 18, which ensures the π^+ stops in the Range Stack as requested in the trigger.

- Layer 14 Cut (LAYER14)
  No charged track is allowed to come to rest in the RSSC second layer embedded between RS layers 14 and 15. Events are rejected if the stopping layer is 14 and a prompt RSSC hit is found in the same sector or one sector clockwise of the stopping counter.

- Polar Angle Cut (COS3D)
  Require that cosine of the polar angle of a charged track ($\cos\theta$) is within ± 0.5 ($|\cos\theta| \leq 0.5$).

- Stopping Z Position Cut (ZFRF)
  Require that π^+ stopping z position in the Range Stack ($Z_{\pi stop}$) is within the fiducial volume. Cut position depends on the stopping layer of the event.

Stopping Layer	Cut Condition
11,12	$-35 \leq Z_{\pi stop} \leq 35$ cm
13	$-40 \leq Z_{\pi stop} \leq 40$ cm
14	$-30 \leq Z_{\pi stop} \leq 30$ cm
15,16,17,18	$-50 \leq Z_{\pi stop} \leq 50$ cm

Table B.2: Cut conditions of π^+ stopping z position for various stopping layers.

- Fiducial Cut in UTC (ZUTOUT)
  Charged track should pass the UTC fiducial volume. The z position at the UTC outer layer should be within the active region ($|z| \leq 25$ cm).

B.4.2 Track Reconstruction Cuts

- Track Reconstruction in UTC (UTCQUAL)
  Reject events with poor UTC fits in either x-y or z. Events with overlapping tracks are also rejected.

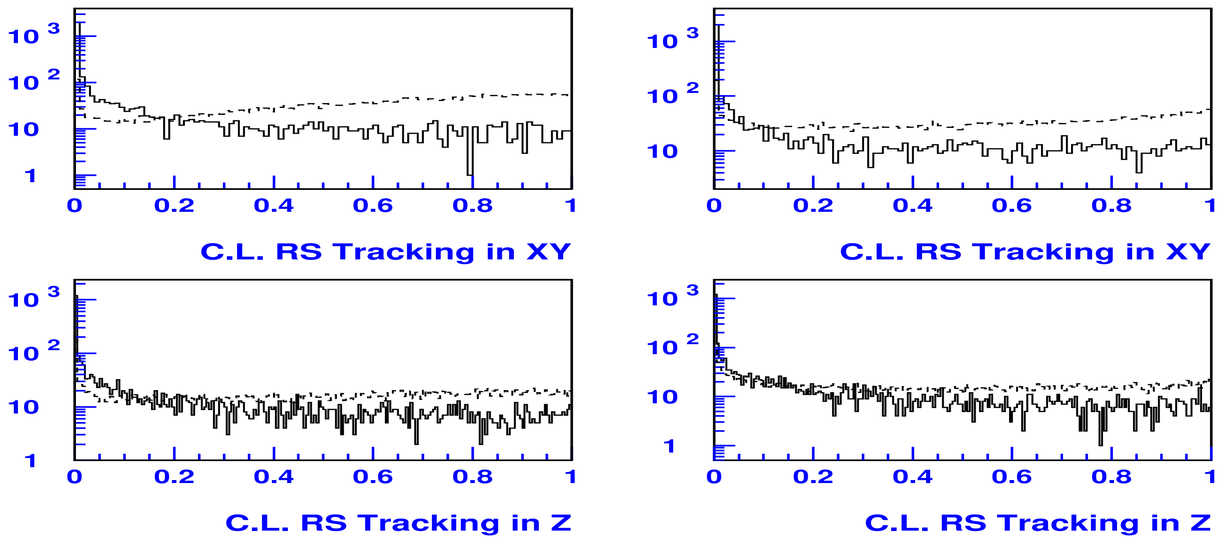

Figure B.1: Confidence levels in the Range Stack track reconstruction for π^+ (dashed) and μ^+ (solid) tracks. Top left: the confidence level for the χ^2 Probability Cut for RS Track Reconstruction. Top right: the confidence level for the Track Matching in RS X-Y Measurements. Bottom left: the confidence level for the Track Matching in RSSC Z Measurements. Bottom right: the confidence level for the Track Matching in RS Z Measurements. The π^+ and μ^+ tracks are obtained from the $\pi_{scatter}$ and $K_{\mu 2}$ monitor trigger data, respectively.

- χ^2 Probability Cut for RS Track Reconstruction (PRRF)
  Reject events if the quality of the Range Stack track fitting in x-y plane is poor. The RS track fitting is performed using sector crossing positions, RSSC hit positions, and energy deposit in the π^+ stopping counter. The cut position is at the confidence level of 0.05 (upper left in Figure B.1).

- Track Matching in RS X-Y Measurements (PRRFXY)
  Reject events if the matching in the x-y plane between the UTC extrapolation and the positions of the sector crossing and the RSSC hits is poor. The confidence level obtained from the residuals should be 0.05 or more (upper right in Figure B.1).

- Track Matching in RSSC Z Measurements (PRRFZ1)
  This cut rejects events with the charged track scattering in the Range Stack. Reject events if the matching in the r-z plane between the UTC extrapolation and the RSSC hit positions is poor. The confidence level should be 0.005 or more (lower left in Figure B.1).

- Track Matching in RS Z Measurements (PRRFZ2)
  This cut rejects events with the charged track scattering in the Range Stack. Reject events if the matching in the r-z plane between the UTC extrapolation and the track hit positions in the RS counters is poor. The confidence level should be 0.005 or more (lower right in Figure B.1).

B.4.3 dE/dx Cuts in Target and Range Stack

- Maximum Energy Deviation in RS (CHIMAX)
  Deviations of energy deposits in the individual track counters are examined.

$$\chi_i \equiv \frac{\log E^i_{exp} - \log E^i_{meas}}{\sigma^i}$$

  where E^i_{meas} is the measured energy deposit in the ith track counter and E^i_{exp} is the energy in the ith track counter expected from the measured range. Reject events with the absolute value of the largest χ_i greater than or equal to 4.

- Confidence Level in RS Energy Measurements (CLRSDEDX)
  The confidence level is calculated from the energy deviations in the individual track counters. The cut position is at 0.04. The cut position is tightened to 0.2 when the largest energy deviation is negative.

- Likelihood Cut for RS Energy Measurements (RSLIKE)
  A likelihood is constructed from the energy deposits in the track counters. The likelihood value is required to be between 0 and 10.

- I-Counter Energy Cut (EIC)
  Require the consistency between the measured (E_{meas}) and estimated (E_{est}) energy deposits in the I-Counter.

$$|E_{meas} - E_{est}| \leq 5 \text{ MeV and } (E_{meas} - E_{est}) \leq 1.75 \text{ MeV}$$

- Target dE/dx Cut (TGDEDX)
  Reject events if the target range is too long ($R_{tg} > 12$ cm), the target pion energy is too large ($E_{tg} > 28$ MeV), or they do not satisfy the relation ($E_{tg} \times 9.5 > R_{tg} \times 28.0$ or $E_{tg} \times 10.0 < (R_{tg} - 2.0) \times 21.5$) as shown in Figure B.2.

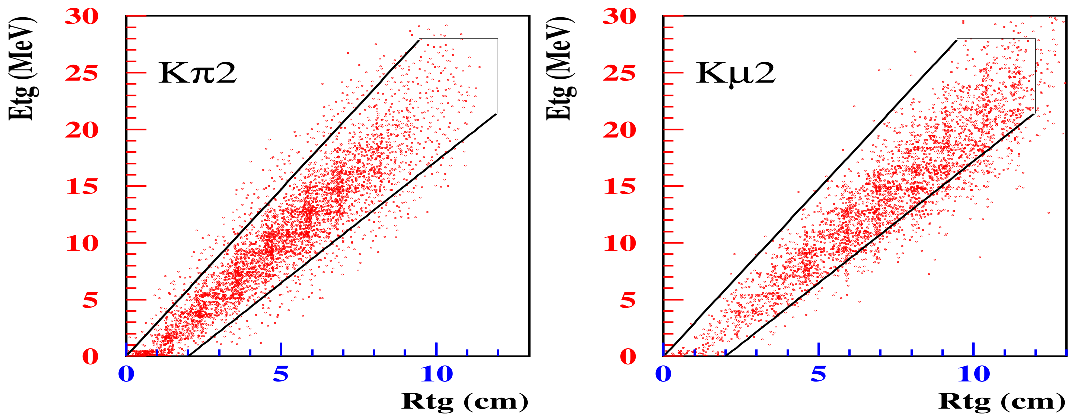

Figure B.2: Scatter plots of the target energy (E_{tg}) vs target range (R_{tg}) for pion (left) and muon (right) tracks.

B.4.4 Target Reconstruction Cuts

- Target Likelihood Cut (LIKE)
  Events with photon hits that are hidden in the pion fibers should be removed. A likelihood is constructed by times of the target pion fibers and distances between the UTC extrapolation path and the target pion fiber hit positions. The likelihood should be 3.2 or less (Figure B.3).

- Extra Target Likelihood Cut (LIKE2)
  Another likelihood is constructed only by the distances between the UTC extrapolated track and the target pion fiber hit positions. The likelihood should be 2.3 or less (Figure B.3).

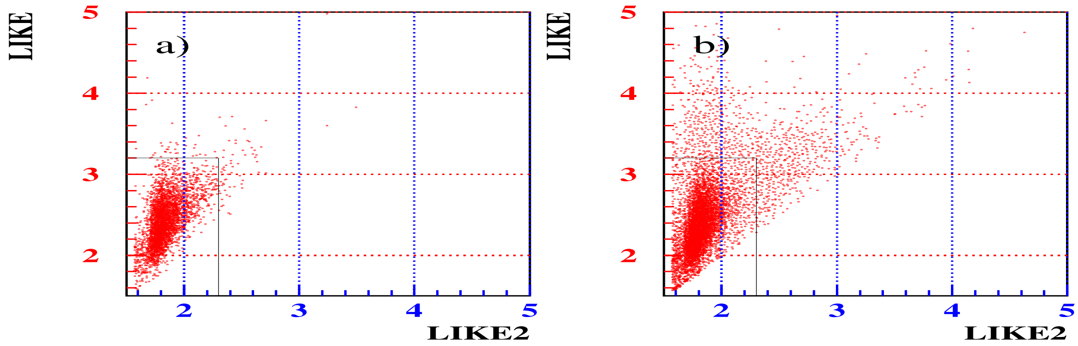

Figure B.3: Scatter plots of the two likelihood values ("LIKE" and "LIKE2") for the events without (left) and with (right) extra photon activities in the target other than a charged track.

- Consistency between B4 Hodoscope and Target Hit Positions (DB4)
  Reject events with the distance from the xy hit position in B4 Hodoscope to the nearest target kaon fiber of more than 2 cm.

- Extra Consistency Cut between B4 Hodoscope and Target Hit Positions (DB4TIP)
  Reject events with the distance from the xy hit position in B4 Hodoscope to the nearest extreme tip of a kaon cluster of more than 2 cm.

- Target Gap Cut among Kaon Fibers (DVXTIP)
  Reject events with the distance between the kaon decay vertex and the nearest extreme tip of the kaon cluster of more than 0.7 cm.

- Target Gap between Kaon and Pion Fibers (DVXPI)
  Reject events with the distance between the kaon decay vertex and the closest pion fiber of more than 1.5 cm.

- Target Gap between Pion Fibers (PIGAP)
  Reject events with a gap of target pion track of greater than 1.6 cm. This cut is tightened to 1.0 cm when the cosine of the polar angle is negative and the z position of the track in the I-Counter is less than -7 cm.

B.4.5 π/μ Separation in Range Stack

- Range-Momentum Consistency (RNGMOM)
  The deviation of range in the Range Stack (χ_{R-P}) is required to be

$$\chi_{R-P} \equiv \frac{R_{meas} - R_{exp}}{\sigma_R} \leq 2.2$$

  where R_{exp} is the range expected from momentum with the assumption that the charged track is a pion.

B.4.6 Phase Space Cuts

- Phase Space Cuts in the $K_{\pi 2}$ Side
  Cut on the momentum, energy and range using the deviations from the $K_{\pi 2}$ peak ($P_{peak} = 205.1$ MeV/c, $E_{peak} = 108.6$ MeV, $R_{peak} = 30.4$ cm).

$$\begin{aligned} P_{dev} &\equiv \frac{P_{meas} - P_{peak}}{\sigma_P} \geq 2.5 \\ E_{dev} &\equiv \frac{E_{meas} - E_{peak}}{\sigma_E} \geq 2.5 \\ R_{dev} &\equiv \frac{R_{meas} - R_{peak}}{\sigma_R} \geq 2.75 \end{aligned}$$

  where P_{meas}, E_{meas} and R_{meas} are the measured values of the momentum, energy and range, respectively, and σ_P, σ_E and σ_R are the sigmas for the $K_{\pi 2}$ peak values.

- Phase Space Cuts in the $K_{\mu 2}$ Side
  Cut on the momentum, energy and range.

Momentum	:	$P \leq 229$ MeV/c
Energy	:	$E \leq 115$ MeV
Range	:	$R \leq 40$ cm

- Loosened Phase Space Cuts in the $K_{\pi 2}$ Side
  Phase Space Cuts in the lower side are loosened to allow 9.5-times more $K_{\pi 2}$ background in comparison with that at the standard cut position.

$$N_{K\pi 2} \leq 9.5$$

B.5 $\pi^+ \to \mu^+ \to e^+$ Decay Sequence Cuts

- Pion Time Consistency (TDTCON)
  Events in which an accidental hit plus a sequential hit of a muon track fake the $\pi^+ \to \mu^+$ double pulses in the stopping counter should be removed. The first pulse time in the stopping counter, obtained from the TD Double-Pulse Fitting ($t_{\pi,TD}$), is required to be within ± 2.5 ns of the track time (t_{RS}).

$$|t_{\pi,TD} - t_{RS}| \leq 2.5 \text{ ns}$$

- $\mu^+ \to e^+$ Decay Requirement (EV5)
  A signature consistent with the $\mu^+ \to e^+$ decay is required in and around the stopping counter. A cluster of hits coincident with the third pulse time of the stopping counter is searched for around the stopping counter. Reject events if the cluster has hits counters on both side of the stopping counter.

- Cut on Muon Time Accidental (ELVETO)
  Events with accidental activities coincident with the second pulse time in the stopping counter should be removed. The accidental hits are searched for in the Range Stack, Barrel Veto, Barrel Veto Liner, and End Cap. Reject events if the energy sum of the coincident hits in any subsystem is above a threshold. The time window and energy threshold for each category are tabulated in Table B.3.

Category	Time Window (ns)	Energy Threshold (MeV)
Both-end hit category		
Range Stack (RS)	± 3.00	0.20
RS (TD)	± 0.25	5.20
Barrel Veto (BV)	± 1.25	0.20
Barrel Veto Liner (BVL)	± 2.75	0.20
Single-end hit category		
RS single energy, both timing	± 7.00	0.20
RS both energy, single timing	± 4.50	9.40
RS single energy, single timing	± 8.75	6.60
RS no energy, both timing	± 5.00	-
RS (TD) single energy, single timing	± 3.00	3.20
BV single energy, both timing	± 3.00	1.60
BV both energy, single timing	± 0.25	0.40
BV single energy, single timing	± 3.00	1.80
BV no energy, both timing	± 5.75	-
BVL both energy, single timing	± 0.75	0.10
BVL single energy, single timing	± 5.00	1.00
BVL no energy, both timing	± 5.50	-
Other category		
End Cap (EC)	± 0.25	22.00

Table B.3: Time window and energy threshold for each category of the muon time accidental cut.

- Cut on Muon Time Accidental in the Track Counters (TDFOOL)
  Events with accidental activities overlaping the track counters and creating the second pulse in the stopping counter should be removed. TD pulses in the two layers prior to the stopping counter are fitted with a double-pulse assumption. Reject events if the fitted pulses are consistent with double pulses and the fitted time of the second pulse is coincident with the second-pulse time in the stopping counter.

- Neural Net $\pi^+ \to \mu^+$ Decay Cut (TDVARNN)
  Tail fluctuation background as well as muon time background should be removed. The Neural Net function with five variables is constructed from the single-pulse fit χ^2's, the ratios of a single-pulse fit χ^2 to that of a double-pulse fit, the energy and time of the fitted second pulse, and the difference of the second pulse times between both ends. The cut position on the NN function is set to 0.76.

B.6 Photon Veto Cuts

Any activity, whose timing is coincident with the track time, is searched for in the Barrel Veto, Barrel Veto Liner, Range Stack, End Cap, Target, I-Counters, V-Counters, Collar, and Microcollar to remove events with photons. The time window and energy threshold for each category are tabulated in Table B.4. Hits in the BV, BVL, and RS are further categorized into subcategories, depending on whether the counter has hits in both ends or only in single end. Time windows for the "single-end hit categories" are widened.

Category	Time window (ns)	Energy threshold (MeV)	Rejection
Both-end hit category			
Barrel Veto (BV)	± 4.5	0.20	14.56 ± 0.21
Barrel Veto Liner (BVL)	± 2.0	0.00	1.25 ± 0.01
Range Stack (RS)	± 1.50	3.80	3.33 ± 0.04
Single-end hit category			
BV single energy, single timing	± 9.50	4.80	1.
BV single energy, both timing	± 1.00	2.80	1.
BV both energy, single timing	± 11.00	8.80	1.
BVL both energy, single timing	± 2.50	17.60	1.01 ± 0.01
RS no energy, both timing	± 2.00	-	1.
Other category			
End Cap (EC)	± 2.25	3.80	2.30 ± 0.03
EC inner ring	± 1.75	1.00	1.19 ± 0.01
Target	± 1.30	4.79	1.49 ± 0.01
I-Counter	± 2.25	0.40	1.32 ± 0.01
V-Counter	± 2.00	1.60	1.05 ± 0.01
Collar (CO)	± 1.25	0.80	1.05 ± 0.01
Microcollar (MC)	± 1.50	2.80	1.
Total			84.3 ± 1.17

Table B.4: Time window and energy threshold for each category of the Photon Veto Cuts.

Appendix C

Tables for Functions

C.1 $K_{\mu 2}$ Range Tail Function

Momentum (MeV/c)	Rel. N_{BG}	Rel. Acc.
242	244.6	1.026
241	223.2	1.026
240	192.6	1.026
239	156.5	1.026
238	117.8	1.026
237	83.99	1.026
236	53.75	1.026
235	32.05	1.026
234	17.83	1.026
233	9.646	1.025
232	5.158	1.024
231	2.804	1.022
230	1.591	1.016
229	**1.000**	**1.000**
228	0.638	0.976
227	0.442	0.944
226	0.328	0.897
225	0.281	0.838
224	0.209	0.761
223	0.167	0.684
222	0.113	0.598
221	0.095	0.511
220	0.072	0.426
219	0.066	0.346

Table C.1: Background and acceptance functions related to the kinematics of the $K_{\mu 2}$ Range Tail background.

Table C.1 shows the values of the $K_{\mu 2}$ Range Tail functions at the different cut positions of the momentum (1st column). The background levels (2nd column) and acceptances (3rd column) are normalized to those at the standard cut position (momentum at 229 MeV/c). The background levels are measured with the $K_{\mu 2}$ Range Tail events in the $\pi\nu\bar{\nu}(1)$ trigger and the acceptances are measured with the Monte Carlo $K^+ \to \pi^+\nu\bar{\nu}$ events.

C.2 Muon Band Function

χ_{R-P}	Rel. N_{BG}	Rel. Acc.
6.75	453.5	1.0084
6.50	383.1	1.0084
6.25	319.9	1.0084
6.00	255.6	1.0084
5.75	201.0	1.0084
5.50	146.7	1.0083
5.25	105.0	1.0083
5.00	74.00	1.0082
4.75	52.90	1.0081
4.50	32.60	1.0081
4.25	21.90	1.0081
4.00	13.60	1.0080
3.75	7.800	1.0079
3.50	4.900	1.0078
3.25	3.300	1.0077
3.00	2.400	1.0071
2.75	1.800	1.0061
2.50	1.400	1.0040
2.20	**1.000**	**1.0000**
2.00	0.909	0.9915
1.75	0.795	0.9786
1.50	0.682	0.9553
1.25	0.568	0.9201
1.00	0.455	0.8626
0.75	0.341	0.7810
0.50	0.227	0.6801
0.25	0.114	0.5672
0.00	0.000	0.4493

Table C.2: Background and acceptance functions related to the kinematics of the Muon Band background.

Table C.2 shows the values of the Muon Band functions at the different cut positions of the range deviation (1st column). The background levels (2nd column) and acceptances (3rd column) are normalized to those at the standard cut position (range deviation = 2.20). The background levels are measured with the Muon Band events in the $\pi\nu\bar{\nu}(1)$ trigger and the acceptances are measured with the Pion Scattering events in the $\pi\nu\bar{\nu}(1)$ trigger.

C.3 $K_{\pi 2}$ Kinematic Function

P_{dev}	E_{dev}	R_{dev}	Rel. N_{BG}	Rel. Acc.
1.45	1.45	1.70	344.8	1.354
1.50	1.50	1.75	267.7	1.337
1.55	1.55	1.80	206.5	1.325
1.60	1.60	1.85	158.6	1.309
1.65	1.65	1.90	120.9	1.295
1.70	1.70	1.95	93.05	1.279
1.75	1.75	2.00	70.42	1.261
1.80	1.80	2.05	53.25	1.246
1.85	1.85	2.10	40.78	1.226
1.90	1.90	2.15	31.02	1.208
1.95	1.95	2.20	24.20	1.191
2.00	2.00	2.25	17.79	1.173
2.05	2.05	2.30	13.88	1.155
2.10	2.10	2.35	10.73	1.137
2.15	2.15	2.40	8.631	1.122
2.20	2.20	2.45	6.166	1.106
2.25	2.25	2.50	4.441	1.088
2.30	2.30	2.55	3.252	1.069
2.35	2.35	2.60	2.317	1.049
2.40	2.40	2.65	1.655	1.032
2.45	2.45	2.70	1.352	1.015
2.50	**2.50**	**2.75**	**1.000**	**1.000**
2.55	2.55	2.80	0.797	0.982
2.60	2.60	2.85	0.603	0.964
2.65	2.65	2.90	0.452	0.948
2.70	2.70	2.95	0.286	0.931
2.75	2.75	3.00	0.241	0.912
2.80	2.80	3.05	0.162	0.893
2.85	2.85	3.10	0.117	0.874
2.90	2.90	3.15	0.076	0.857
2.95	2.95	3.20	0.069	0.843
3.00	3.00	3.25	0.038	0.827
3.05	3.05	3.30	0.038	0.807
3.10	3.10	3.35	0.028	0.789
3.15	3.15	3.40	0.024	0.770

Table C.3: Background and acceptance functions related to the $K_{\pi 2}$ kinematics.

Table C.3 shows the values of the $K_{\pi 2}$ kinematic functions at the different cut positions of momentum, energy and range deviations (1st, 2nd, 3rd column). The background levels (4th column) and acceptances (5th column) are normalized to those at the standard cut position ($P_{dev} = 2.50$, $E_{dev} = 2.50$, $R_{dev} = 2.75$). The background levels are measured with the $K_{\pi 2}$ events in the $\pi\nu\bar{\nu}(1)$ trigger and the acceptances are measured with the Monte Carlo $K^+ \to \pi^+\nu\bar{\nu}$ events.

C.4 1-Beam Function

$(t_\pi - t_K)/idc$	$\times 10^{-3}$ (events)			Rel. N_{BG}	Rel. Acc.
	$N_\pi + N_K$	N_{CEX}	N_{total}		
1.00	**3.850**	**3.891**	**7.741**	**1.000**	**1.000**
1.05	3.850	3.521	7.371	0.952	0.989
1.10	2.566	3.129	5.695	0.736	0.978
1.15	2.139	2.857	4.996	0.645	0.967
1.20	1.284	2.626	4.337	0.560	0.956
1.24	1.284	2.428	3.712	0.479	0.946
1.30	0.855	2.249	3.533	0.456	0.932
1.40	0.428	1.950	2.806	0.362	0.909
1.45	0.428	1.851	2.279	0.294	0.897
1.50	0.428	1.722	2.150	0.278	0.885
1.65	0.428	1.500	1.927	0.249	0.851
1.80	0.428	1.299	1.727	0.223	0.818
1.90	0.428	1.169	1.597	0.206	0.796
2.00	0.428	1.074	1.502	0.194	0.775
2.10	0.428	1.012	1.440	0.186	0.754

Table C.4: Background and acceptance functions related to the Single Beam background. The 1st column represents "normalized delayed coincidence", which is $t_\pi - t_K$ divided by the cut positions for the various Delayed Coincidence conditions (i.e., idc =2,3,4,5,6 ns).

Table C.4 shows the values of the 1-Beam functions at the different cut positions of Delayed Coincidence (1st column). The background levels (5th column) and acceptances (6th column) are normalized to those at the standard cut position ($(t_\pi - t_K)/idc = 1.00$). The 2nd and 3rd column represent the background levels (in unit of event) for Single Beam background and CEX background, and the 4th column represents the total background level (in unit of event). The background levels for Single Beam (CEX) background are measured with the Single Beam background sample in the $\pi\nu\bar{\nu}(1)$ trigger (Monte Carlo CEX events), and the acceptances are measured with the stopped kaon events in the $K_{\mu 2}$ monitor trigger.

C.5 2-Beam Function

BWHRS	$\times 10^{-3}$ (events)			Rel. N_{BG}	Rel. Acc.
	N_{K-K}	$N_{K-\pi}$	N_{total}		
0.00	**2.560**	**0.267**	**2.836**	**1.000**	**1.000**
0.50	2.177	0.256	2.434	0.858	0.989
2.00	1.701	0.158	1.858	0.655	0.962
3.25	1.605	0.158	1.763	0.622	0.936
3.50	1.510	0.158	1.648	0.581	0.929
4.50	1.321	0.039	1.439	0.507	0.905
6.00	1.036	0.039	1.076	0.379	0.866
7.50	0.847	0.039	0.887	0.313	0.828
10.00	0.658	0.039	0.697	0.246	0.769
14.50	0.564	0.039	0.604	0.213	0.678

Table C.5: Background and acceptance functions related to the Double Beam background.

Table C.5 shows the values of the 2-Beam functions at the different cut positions of the timing in the BWPCs (1st column). The background levels (5th column) and acceptances (6th column) are normalized to those at the standard cut position (BWPC timing = 0.00). The 2nd and 3rd column represent the background levels (in unit of event) for $K-K$ and $K-\pi$ Double Beam backgrounds, respectively, and the 4th column represents the total background level (in unit of event). The background levels are measured with the Double Beam events in the $\pi\nu\bar{\nu}(1)$ trigger and the acceptances are measured with the single kaon beam events in the $K_{\mu2}$ monitor trigger.

Appendix D

Details of the Background Estimations

D.1 $K_{\pi 2}$ Background Estimation with Second Bifurcation Method

The $K_{\pi 2}$ background level from the Second Bifurcation Method is measured by following the Normalization Branch in Figure D.1. Figure D.2 shows the Normalization Branch of the $K_{\pi 2}$ background estimation with the Second Bifurcation Method. Two cuts for the Second Bifurcation are the Phase Space Cuts for Range and Momentum ($R_{dev} \geq 2.75$ and $P_{dev} \geq 2.5$) and the Cut for Energy ($E_{dev} \geq 2.5$). The loose Phase Space Cuts ($R_{dev} > 1$ and $P_{dev} > 1$) are imposed for the setup of the Second Bifurcation. In the Normalization Branch of the Second Bifurcation (right branch in Figure D.2), the number of events surviving the Cuts for Range and Momentum (N_{RP}) is counted. In the Rejection Branch, the rejection of the Cut for Energy (R_E) is measured. The estimated number of $K_{\pi 2}$ events in the Normalization Branch from the Second Bifurcation Method is expressed as $N_{NB} = N_{RP}/(R_E - 1)$.

To study the validity of the result from the Second Bifurcation and the consistency with the results from the Normalization Branch without the Second Bifurcation, the number of remaining events in the Normalization Branch and the estimated number of events from the Second Bifurcation Method are compared by changing the cut positions of the momentum, energy, range deviations. Table D.1 summarizes the values of N_{RP}, R_E, and the expected $K_{\pi 2}$ events (N_{NB}) at each R_{dev}, E_{dev}, and P_{dev} cut position. Since the energy and range are partly correlated [1], the expected $K_{\pi 2}$ background obtained from N_{RP} and R_E is smaller than the number of events remaining after imposing all the Phase Space Cuts. With the loose cut positions at $R_{dev} = 1.70$, $E_{dev} = 1.45$ and $R_{dev} = 1.45$, 360 events passed the Phase Space Cuts; however, the estimated number of events obtained from the Second Bifurcation is

$$N_{NB} = N_{RP}/(R_E - 1) = 1930/(8.270 - 1) = 265.5.$$

[1] Because the range in the π^+ stopping counter is calculated from the energy deposit in the stopping counter.

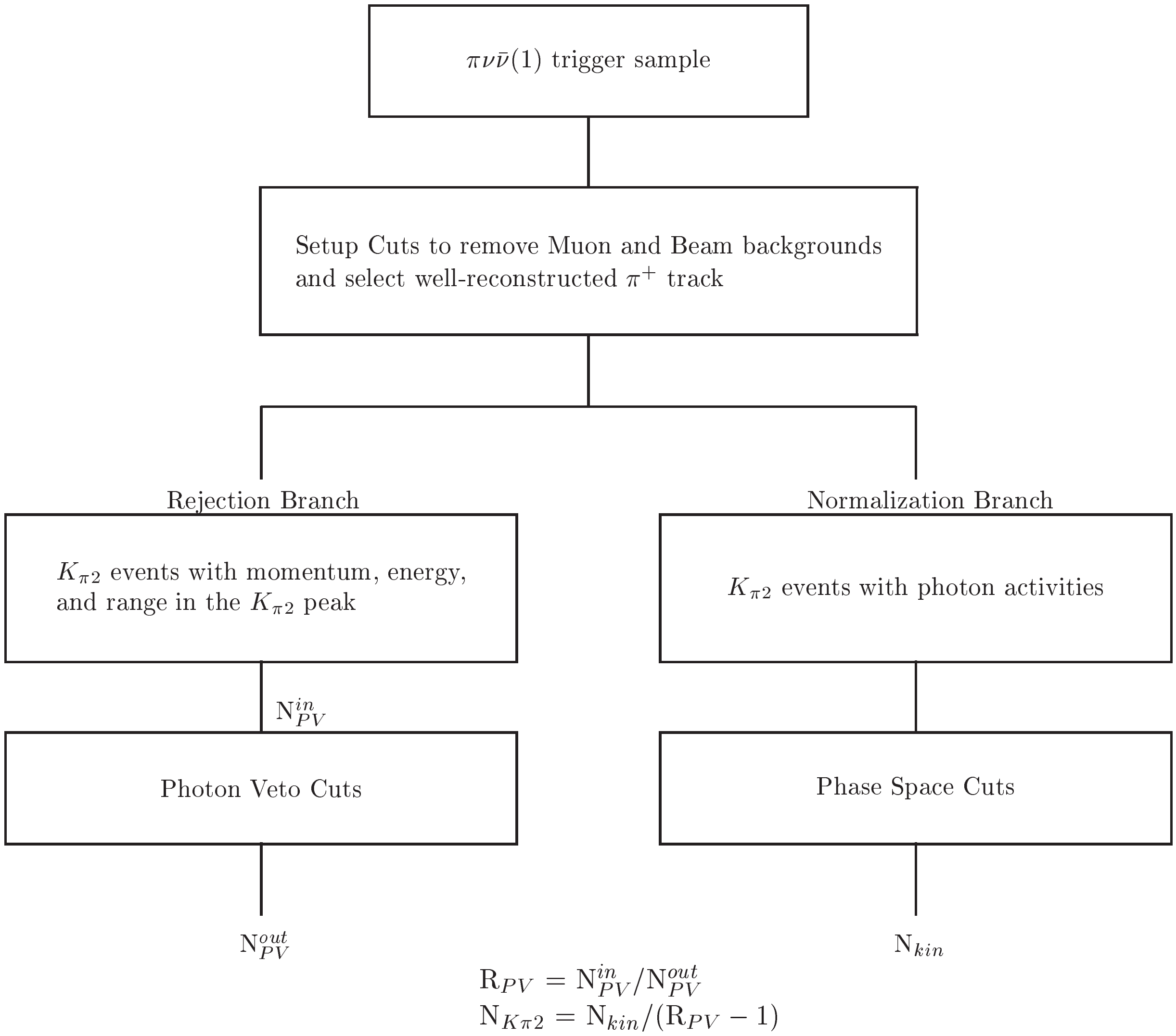

Figure D.1: Method of the $K_{\pi 2}$ background estimation.

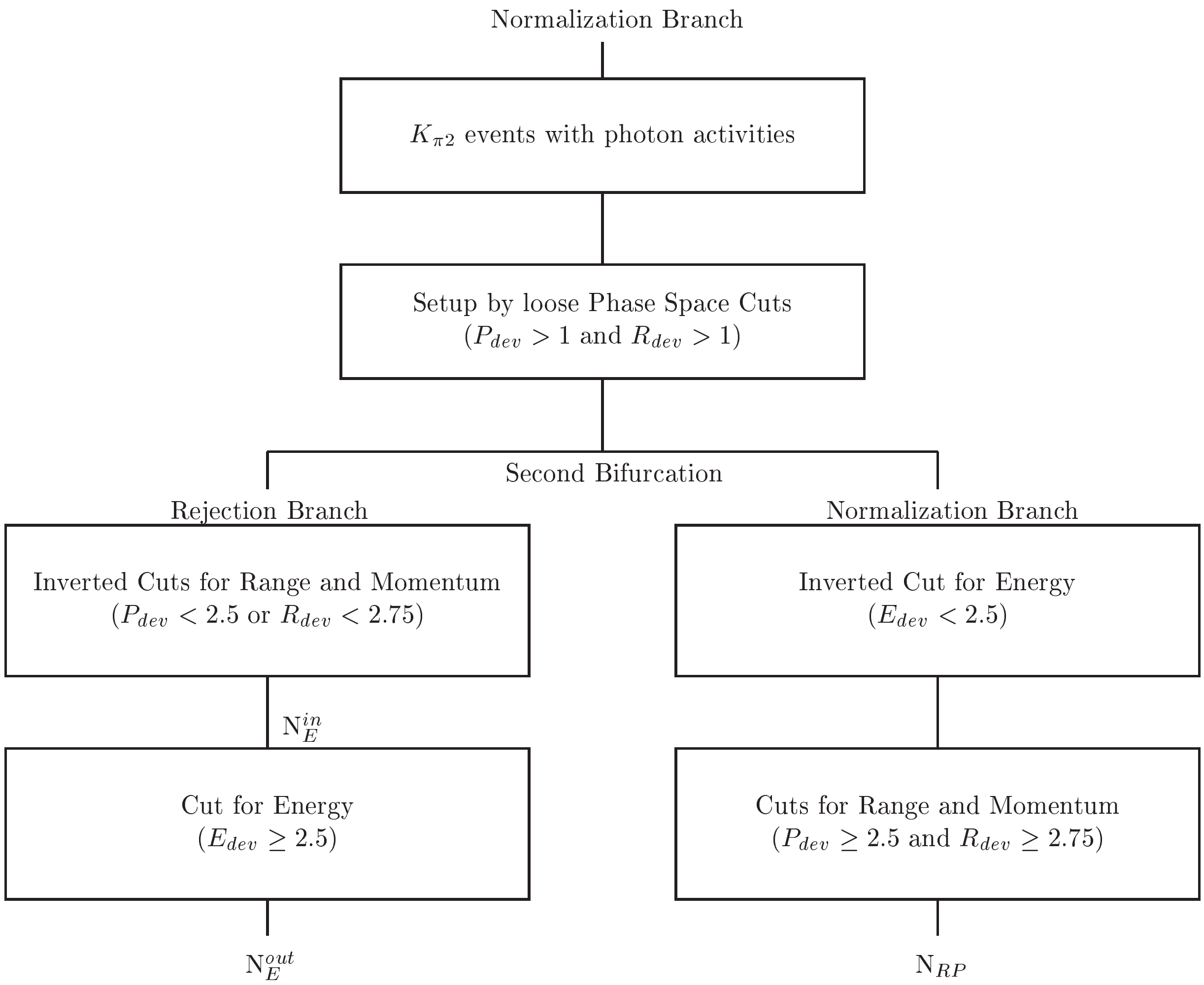

$$\mathrm{R}_E = \mathrm{N}_E^{in}/\mathrm{N}_E^{out}$$
$$\mathrm{N}_{NB} = \mathrm{N}_{RP}/(\mathrm{R}_E - 1)$$

$$\mathrm{N}_{K\pi 2} = \mathrm{N}_{NB}/(\mathrm{R}_{PV} - 1)$$

Figure D.2: Normalization Branch of the $K_{\pi 2}$ background estimation with the Second Bifurcation.

R_{dev}	E_{dev}	P_{dev}	N_{RP}	$R_E - 1$	N_{NB}
1.70	1.45	1.45	1930	7.270	360.000±18.683
1.75	1.50	1.50	1651	8.010	279.478±15.177
1.80	1.55	1.55	1404	8.830	215.618±12.278
1.85	1.60	1.60	1188	9.732	165.618±9.901
1.90	1.65	1.65	998	10.721	126.228±7.948
1.95	1.70	1.70	837	11.683	97.144±6.428
2.00	1.75	1.75	695	12.818	73.523±5.138
2.05	1.80	1.80	579	14.122	55.594±4.112
2.10	1.85	1.85	483	15.383	42.577±3.327
2.15	1.90	1.90	403	16.872	32.389±2.682
2.20	1.95	1.95	346	18.570	25.265±2.211
2.25	2.00	2.00	284	20.734	18.574±1.741
2.30	2.05	2.05	249	23.298	14.492±1.440
2.35	2.10	2.10	207	25.054	11.203±1.180
2.40	2.15	2.15	180	27.084	9.012±0.999
2.45	2.20	2.20	144	30.341	6.436±0.773
2.50	2.25	2.25	114	33.325	4.639±0.604
2.55	2.30	2.30	90	35.966	3.393±0.479
2.60	2.35	2.35	71	39.802	2.419±0.373
2.65	2.40	2.40	58	45.505	1.728±0.290
2.70	2.45	2.45	52	49.882	1.414±0.250
2.75	**2.50**	**2.50**	**43**	**55.908**	**1.043±0.200**
2.80	2.55	2.55	39	63.552	0.832±0.168
2.85	2.60	2.60	33	71.083	0.630±0.137
2.90	2.65	2.65	28	80.604	0.471±0.110
2.95	2.70	2.70	20	91.021	0.298±0.080
3.00	2.75	2.75	18	97.295	0.251±0.070
3.05	2.80	2.80	13	104.488	0.169±0.054
3.10	2.85	2.85	10	109.897	0.123±0.044
3.15	2.90	2.90	7	122.571	0.077±0.032
3.20	2.95	2.95	7	130.061	0.073±0.030
3.25	3.00	3.00	5	165.346	0.041±0.020
3.30	3.05	3.05	5	172.000	0.039±0.019
3.35	3.10	3.10	4	195.591	0.028±0.015
3.40	3.15	3.15	4	215.250	0.025±0.014

Table D.1: Number of events surviving the Phase Space Cuts for Range and Momentum N_{RP}, the rejection of the Phase Space Cut for Energy R_E and the number of events remaining in the Normalization Branch predicted from the Second Bifurcation N_{NB} at different R_{dev}, E_{dev}, P_{dev} cut positions. N_{NB} is calculated as $N_{RP}/(R_E - 1) \times 1.356$. The errors are statistical.

The ratio of these two numbers $360/265.5 = 1.356$ is treated as the correction factor. In Table D.1, the factor 1.356 is already applied. The factor is assumed to be the same at any positions of R_{dev}, E_{dev}, P_{dev}, since there is no event inside the Signal Region and no way to confirm the consistency. The magnitude of the correction factor is almost unrelated with the positions of R_{dev}, E_{dev}, P_{dev} outside the Signal Region, which indicates that the correction factor, measured outside the Signal Region, is extended to the region inside the Signal Region. By multiplying the factor 1.356, the predicted number of events matches, at each cut position, the number of events observed in the Normalization Branch without the Second Bifurcation.

The expected number of $K_{\pi 2}$ events at the standard cut position ($P_{dev} \geq 2.5$, $E_{dev} \geq 2.5$, $R_{dev} \geq 2.75$) is therefore estimated to be 1.043±0.200 events.

D.2 Double Beam Background Estimation with Second Bifurcation Method

Figure D.3 explains the method of the Double Beam background estimation. The Second Bifurcation Method is adopted to the Normalization Branch. The two cuts for the Second Bifurcation are the Target Pattern Recognition Cuts [2] and the Timing Cuts in the B4 Hodoscope. The Second Bifurcation Method for the $K-K$ events is shown in Figure D.4. The Timing Cuts in the Pion Čerenkov Counter are applied as the setup to remove the $K-\pi$ events. The $K-K$ events are tagged by inverting the Timing Cuts in the Kaon Čerenkov Counter and BWPCs. After applying all other Kinematic Cuts and the $\pi^+ \to \mu^+ \to e^+$ Decay Sequence Cuts to select π^+ track events, the $K-K$ events in the Normalization Branch (N_K) are estimated with the number of events passing the Timing Cuts in the B4 Hodoscope, divided by the rejection of the Target Pattern Recognition Cuts and Photon Veto Cut for Target. The $K-\pi$ events in the Normalization Branch (N_π) is also estimated in the same manner. The Second Bifurcation Method for the $K-\pi$ events is shown in Figure D.5.

Table D.2 summarizes the number of events remaining after the Timing Cuts in the B4 Hodoscope are imposed and the rejection of the Target Pattern Recognition Cuts and Photon Veto Cut for Target. The estimation by the Second Bifurcation Method results in 0.156 $K-K$ events and 0.298 $K-\pi$ events in the Normalization Branch (inside the Signal Region).

Region	$K-K$ event		$K-\pi$ event	
	Rejection	Normalization	Rejection	Normalization
Signal Region	$272/2 = 136.0 \pm 95.8$	21	$6584/7 = 940.6 \pm 355.3$	278
	$N_K = 21/(136.0-1) = 0.156 \pm 0.115$		$N_\pi = 278/(940.6-1) = 0.298 \pm 0.114$	
1×1 Region	$212/2 = 106.0 \pm 74.6$	16	$5834/7 = 833.4 \pm 314.8$	244
	$N_K = 16/(106.0-1) = 0.152 \pm 0.114$		$N_K = 244/(833.4-1) = 0.293 \pm 0.112$	

Table D.2: Observed number of events and the rejection factors in the Second Bifurcation for the Double Beam background estimation.

[2]The Target Pattern Recognition Cuts consists of the beam and target likelihood cuts, the cuts associated with gaps among the target hit fibers, the cuts on the extra activities, the consistency between the target and B4 Hodoscope hit positions.

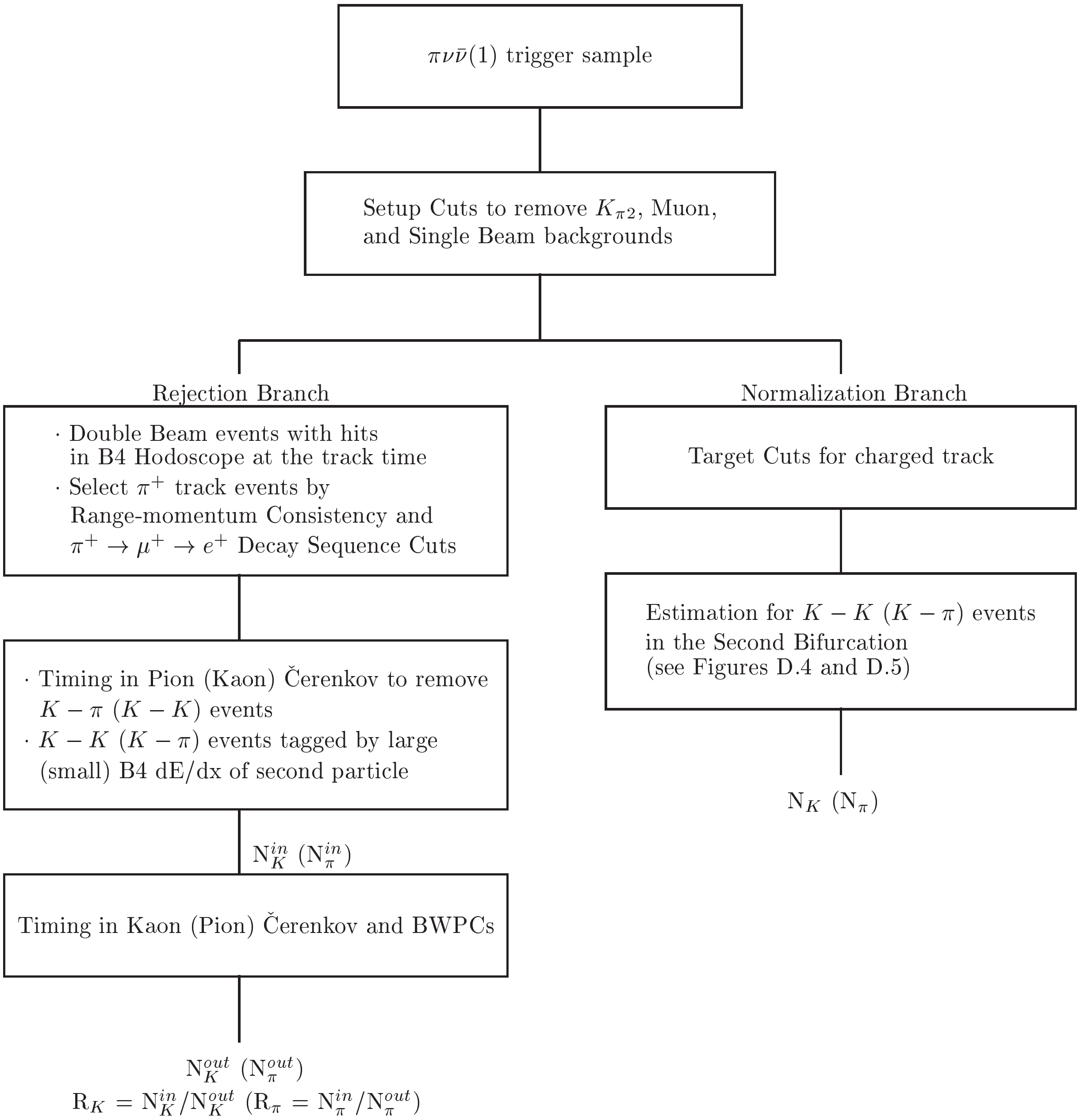

$$\mathrm{N}_{\mathrm{2beam}} = \mathrm{N}_K/(\mathrm{R}_K - 1) + \mathrm{N}_\pi/(\mathrm{R}_\pi - 1)$$

Figure D.3: Method of the Double Beam background estimation.

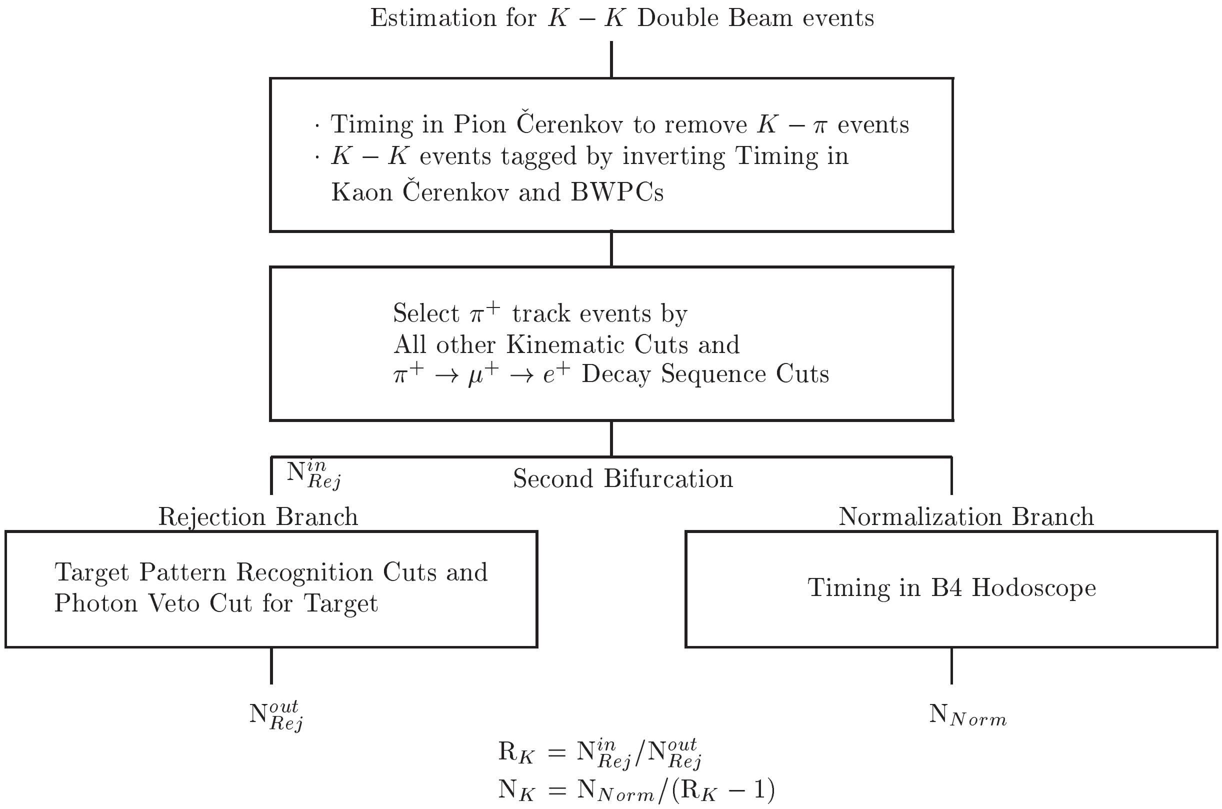

Figure D.4: Second Bifurcation of the $K-K$ Double Beam background estimation.

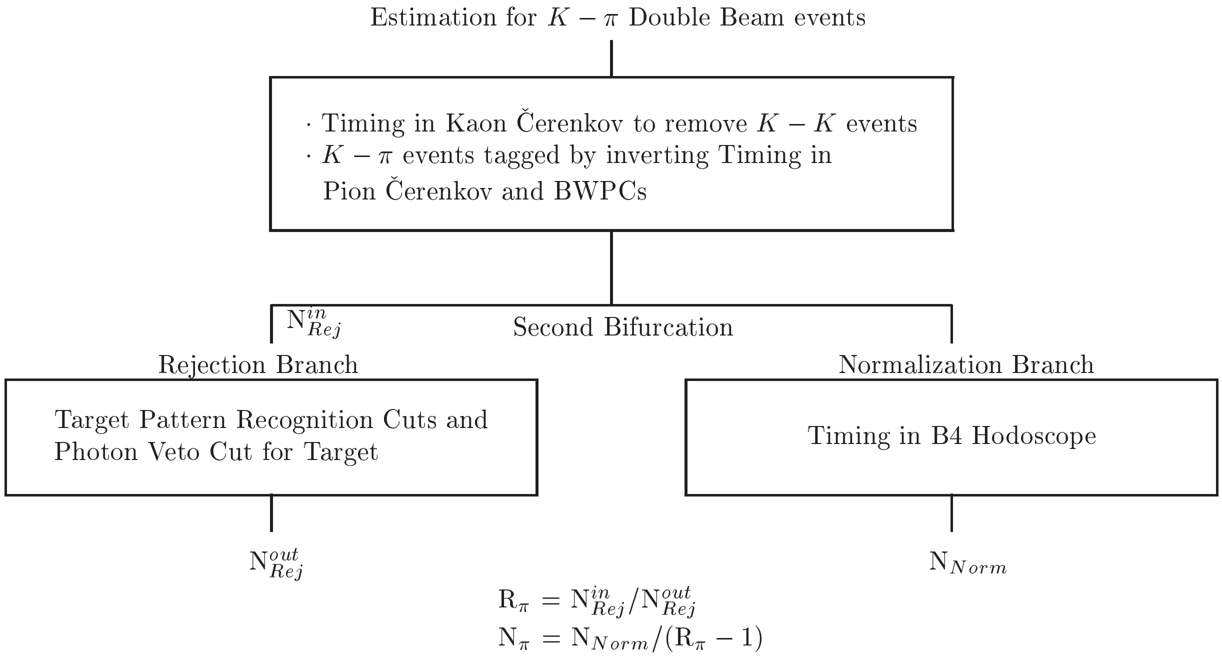

Figure D.5: Second Bifurcation of the $K-\pi$ Double Beam background estimation.

Appendix E

Trigger Effects on Muon Background

Some of the requirements in the $\pi\nu\bar{\nu}(1)$ trigger have rejection against $K_{\mu 2}$ decay. One of the requirements is "layer-19 veto", $\overline{19_{ct}}$, which means that events are rejected if the charged track reaches layer 19, which is the outermost Range Stack layer. Another one is the refined range requirement, L0_rr(1), which suppresses events with a small polar angle. Most of the muon tracks from $K_{\mu 2}$ decay reach the 19th RS layer and are rejected by the $\overline{19_{ct}}$ requirement. The $K_{\mu 2}$ events survive the layer-19 veto when the polar angle of the charged track is small and the charged track comes to rest near the edge of the RS scintillators. The refined range requirement is targeting these events. The $K_{\mu 2}$ events are therefore suppressed by these two trigger requirements. Figure E.1 shows scatter plots of the range vs momentum and the range deviation χ_{R-P} vs momentum of the Muon background sample in the $\pi\nu\bar{\nu}(1)$ trigger. Figure E.2 shows the correlation between the range deviation and the momentum in both Muon Band and $K_{\mu 2}$ Range Tail events. The correlation is supposed to be due to the effects of the trigger requirements.

Since the requirements $\overline{19_{ct}}$ and L0_rr(1) are included in the $\pi\nu\bar{\nu}(1)$ trigger, their effect should be estimated by using some monitor trigger data that do not include these two requirements. However, no monitor trigger data has a sufficient number of Muon Band and $K_{\mu 2}$ Range Tail events after these two requirements are imposed because the rejection of the trigger requirements is quite large. Monte Carlo simulations that generate the Muon Band and $K_{\mu 2}$ Range Tail events are used to estimate the trigger effects.

E.1 Effect on Muon Band Background

The Muon Band background originates from three-body $K^+ \to \mu^+$ decays (e.g., $K_{\mu\nu\gamma}$ and $K_{\mu 3}$) and π^+ decay-in-flight to μ^+. Since $K_{\mu 3}$ decay has a charged track with momentum $P < 215$ MeV/c, and two photons from π^0 in the decay are suppressed by the Photon Veto requirement in the $\pi\nu\bar{\nu}(1)$ trigger, $K_{\mu 3}$ decay does not have much contribution to the Muon Band background. A Monte Carlo simulation that generates $K^+ \to \mu^+\nu\gamma$ decay is used to estimate the trigger effects on the Muon Band background. A million $K_{\mu\nu\gamma}$ decays are generated by the Monte Carlo simulation, and the effects of the layer-19 veto and refined range requirements are estimated (Figure E.3). With the application of the refined range requirement, the decrease of the χ_{R-P} mean value is large because it rejects events with a longer range ($R >\sim 45$ cm) and events with a larger range

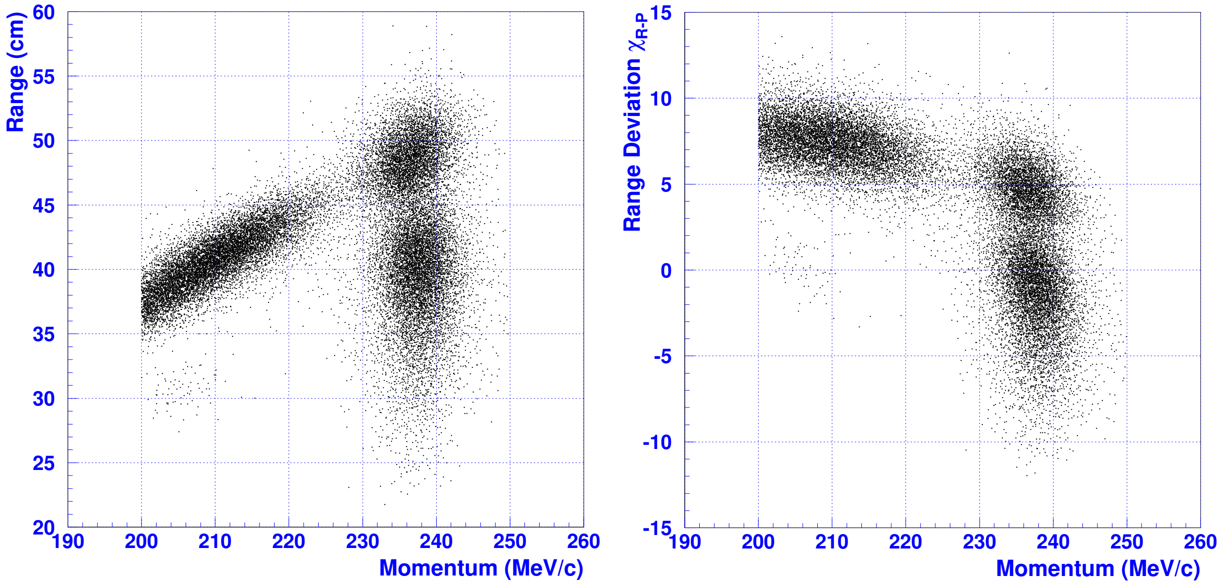

Figure E.1: Scatter plots of the range vs momentum (left) and the range deviation (χ_{R-P}) vs momentum (right) for the Muon background.

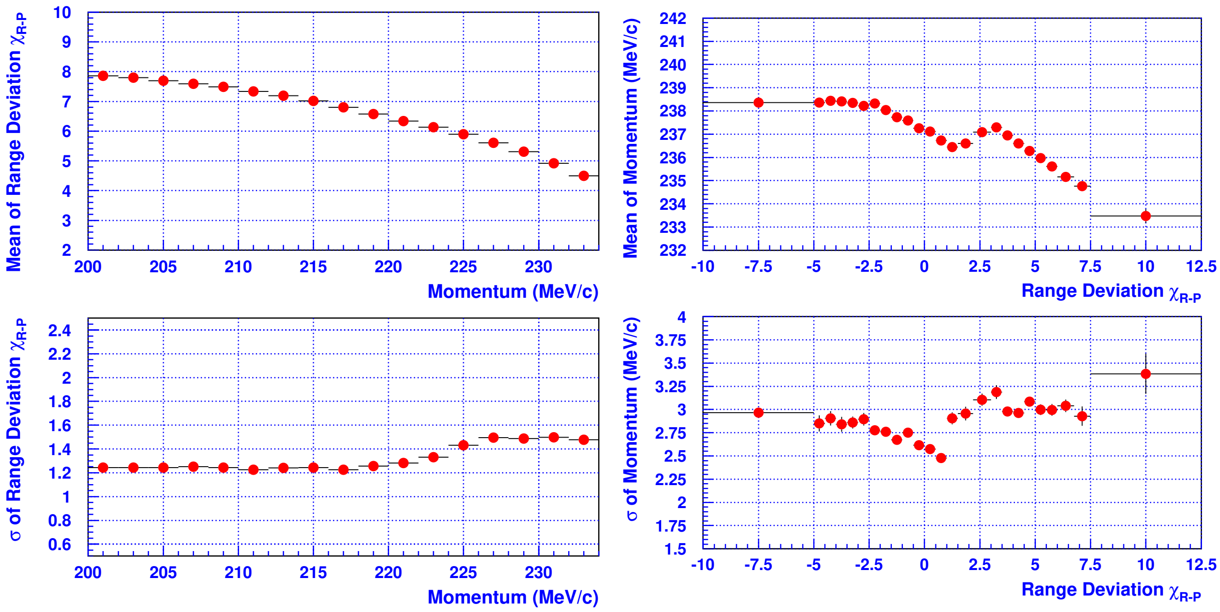

Figure E.2: Left: Mean (top) and sigma (bottom) of the range deviation χ_{R-P} as a function of the momentum for the Muon Band events. Right: Mean (top) and sigma (bottom) of the momentum as a function of the range deviation, χ_{R-P}, for the $K_{\mu 2}$ Range Tail events.

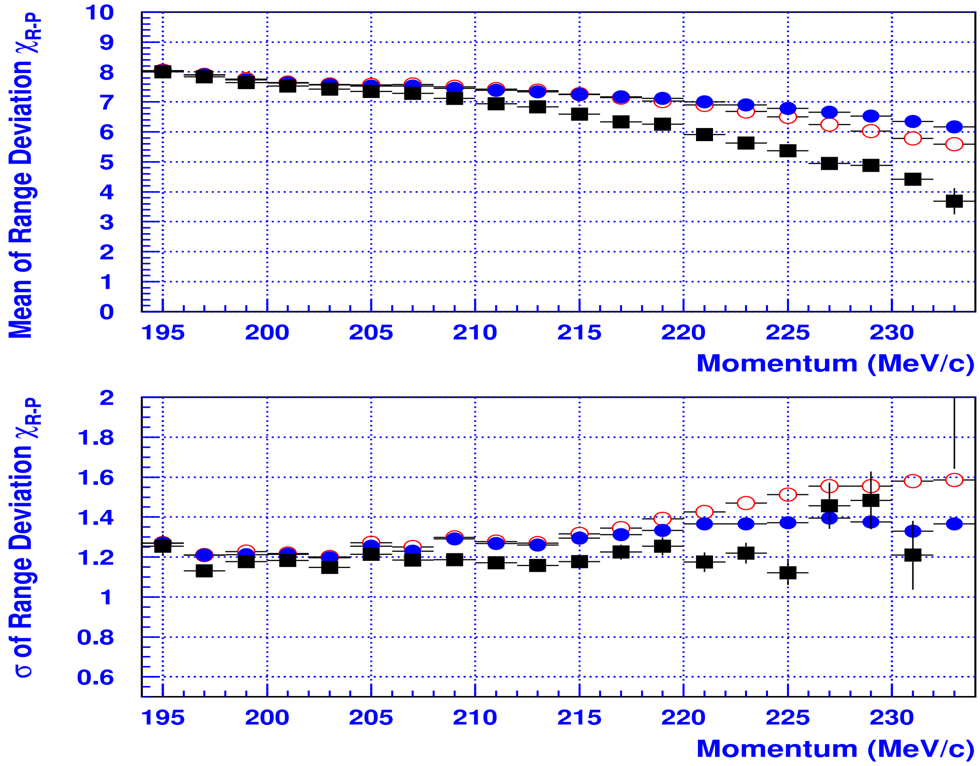

Figure E.3: Mean (top) and sigma (bottom) of the range deviation χ_{R-P} as a function of the momentum. Dot: neither a layer-19 veto nor a refined range requirement is applied. Circle: layer-19 veto is applied. Square Dot: both a layer-19 veto and a refined range requirement is applied.

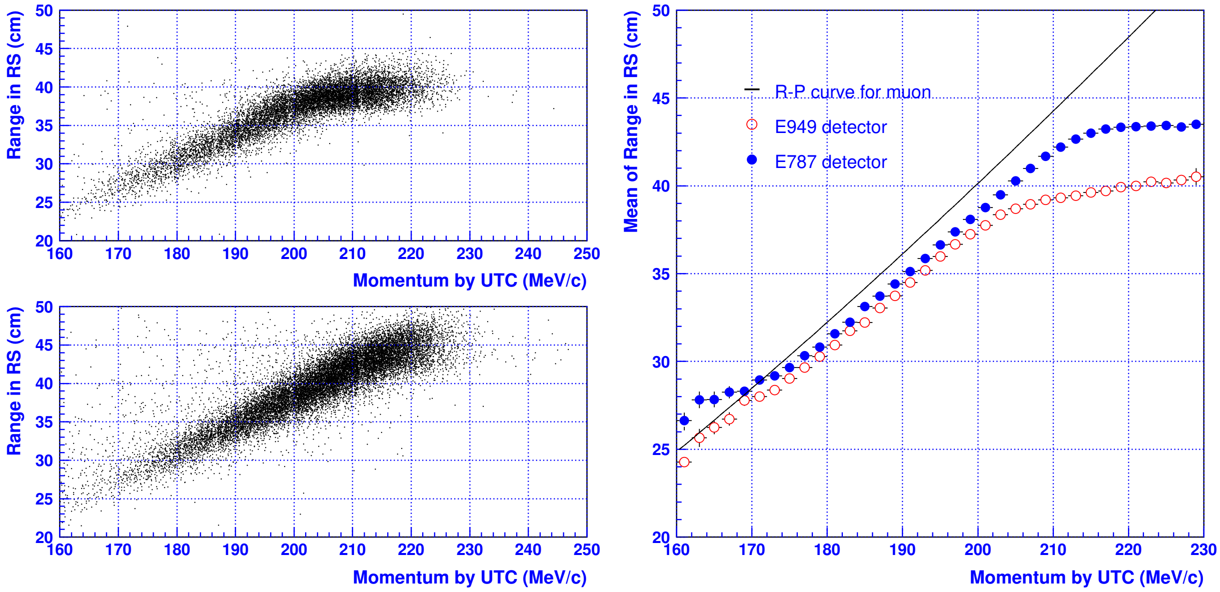

Figure E.4: Left plots: scatter plots of the range in the Range Stack vs momentum measured by the UTC for the Monte Carlo $K_{\mu\nu\gamma}$ events generated with the E949 (top) and E787 (bottom) detectors. Right plot: mean of the range in the Range Stack as a function of the momentum measured by the UTC for E787 (dots) and E949 (circles) detector simulations. The line represents the range-momentum correlation curve for muons.

deviation are cut off at a higher momentum region. Even without application of the two requirements, the decrease can still be seen. This is because the track reconstruction code can calculate a range only inside the Range Stack and target. When a charged track passes through the Range Stack and reaches the Barrel Veto Liner, the range in the BVL can not be calculated by the reconstruction code, resulting in the measured range being smaller than expected. If the radius of the Range Stack would be large, so that all of the muon tracks from $K_{\mu 2}$ could come to rest in the Range Stack, the range of the whole path length could be calculated for the longer range muon tracks from $K_{\mu 2}$. The E949 detector has 19 RS layers that correspond to a total thickness of 39 cm, whereas the E787 detector had the RS layers up to 21 [1] corresponding to a total thickness of 44 cm. The fraction of events in which the range is miscalculated is larger in E949 than E787. A Monte Carlo simulation with the E787 detector does allow a range calculation of a longer path length than the E949 detector, as shown in Figure E.4.

In summary, the decrease of range deviation in the Muon Band events originates for the above reasons, and the original χ_{R-P} distribution does not change as the momentum changes.

[1]The 20th and 21st layers were replaced with the Barrel Veto Liner in the upgrade to the E949 detector.

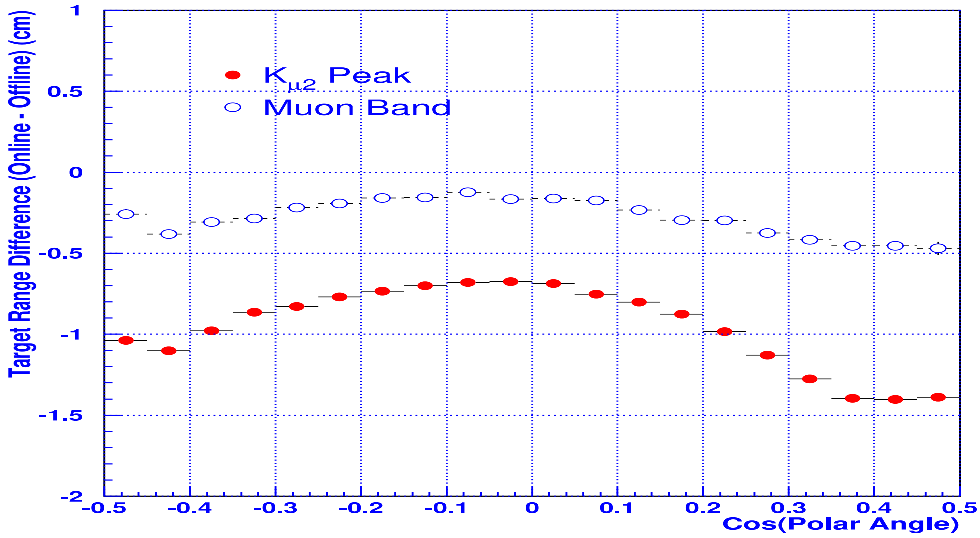

Figure E.5: Difference between the online and offline target ranges as a function of the cosine polar angle for the $K_{\mu2}$ peak (dot) and the Muon Band (circle) events.

E.2 Effect on the $K_{\mu2}$ Range Tail Background

The trigger requirement of the layer-19 veto largely suppresses the $K_{\mu2}$ peak events. The $K_{\mu2}$ events can still survive the layer-19 veto if their path length in the target is long; their polar angle is small ($|\cos\theta| \simeq 0.5$); or they come to rest at the edge of the Range Stack scintillators. The refined range requirement can suppress these events that survive the layer-19 veto. The refined range requirement can reject those events with $R >\sim 45$ cm, and all of the $K_{\mu2}$ peak events should be removed by it. However, as shown in Figure E.1, some $K_{\mu2}$ peak events still survive the refined range requirement because of a discrepancy between the range calculated at the online trigger and the actual range. The online target range is calculated based on the number of target hit fibers, and is the path length projected to the x-y plane in the real case. The discrepancy between the real and online target ranges becomes larger, since the polar angle is smaller and the target range is longer (Figure E.5).

The refined range requirement also suppresses the $K_{\mu2}$ Range Tail events, resulting in a gap between the $K_{\mu2}$ peak events that survive the refined range requirement and the $K_{\mu2}$ Range Tail events in the region $\chi_{R-P} < 2$. The refined range requirement creates a diagonal gap in the range deviation and momentum plane; the $K_{\mu2}$ Range Tail events on the higher momentum side are cut off in the region $0 < \chi_{R-P} < 2$, which results in the momentum peak shift shown in the right-hand plots of Figure E.2. The momentum distribution for the $K_{\mu2}$ Range Tail events originally does not change as the range deviation, χ_{R-P}, varies.

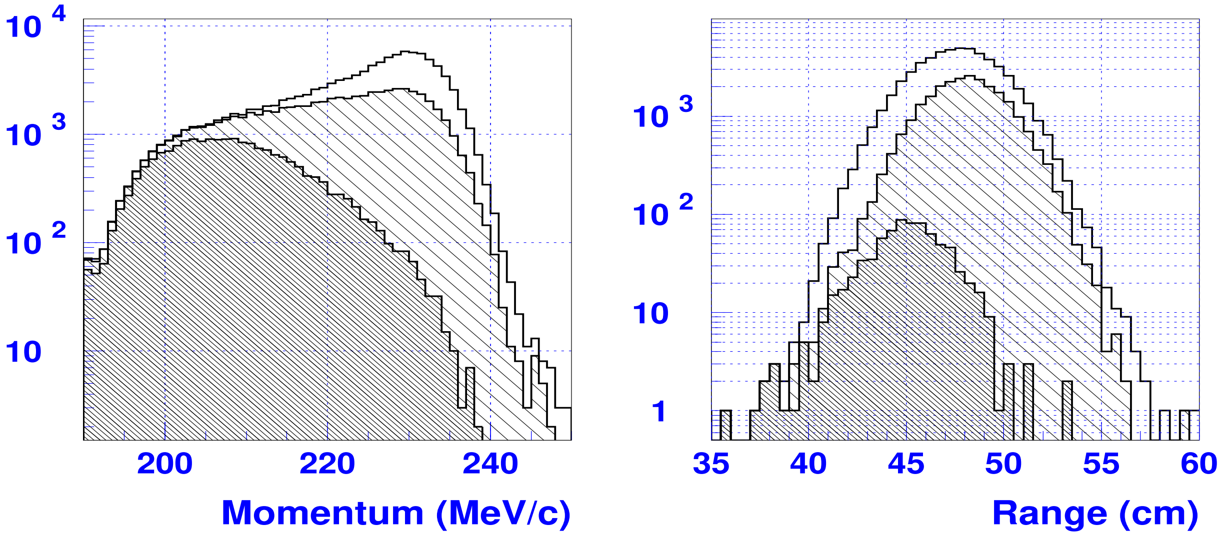

Figure E.6: Effects of the trigger requirements on the Muon Band events. Momentum distributions (left) and range distributions (right). The Monte Carlo $K_{\mu\nu\gamma}$ events are simulated for the Muon Band events.

E.3 Measurement of the Trigger Rejection Factors

Figure E.6 shows the effect of the trigger requirements on the Muon Band events, which is estimated by the Monte Carlo $K_{\mu\nu\gamma}$ events. The left-hand plot shows the momentum distributions of the Monte Carlo $K_{\mu\nu\gamma}$ events without any trigger requirements (opened), with the layer-19 veto (hatched), and with both the layer-19 veto and refined range requirement (narrowly hatched). The right-hand plot shows the range distributions of the Monte Carlo $K_{\mu\nu\gamma}$ events in the momentum region $P > 225$ MeV/c without any trigger requirements (opened), with the layer-19 veto (hatched), and with both the layer-19 veto and the refined range requirement (narrowly hatched). The rejection becomes larger as the momentum increases; however, even for events with higher momenta > 225 MeV/c, the rejection of events in the Signal Region ($R \leq 40$ cm) is small.

In the Muon background estimation, explained later, template distributions of the range deviation and the momentum are used to estimate the fractions of the Muon Band and $K_{\mu 2}$ Range Tail events inside the cut positions; the fractions are normalized based on the original momentum and range deviation spectra. The momentum and range deviation distributions in the $\pi\nu\bar{\nu}(1)$ trigger sample should be corrected to the original distributions, which would be seen if the trigger requirements had not been imposed, since the Muon background events in the high-momentum region have been reduced. The trigger rejection factors must be measured and multiplied as the normalization factors.

The trigger rejection factor to the Muon Band events is measured with the Monte Carlo $K_{\mu\nu\gamma}$ events. Figure E.7 shows the trigger rejection factors to the Muon Band events as a function of the momentum. The number of Muon Band events in the original momentum distribution can be estimated by multiplying the number of events in the $\pi\nu\bar{\nu}(1)$ trigger sample by the trigger rejection factors. In the $\pi\nu\bar{\nu}(1)$ trigger sample, however, the Muon Band events can not be discriminated from the $K_{\mu 2}$ Range Tail events in the momentum

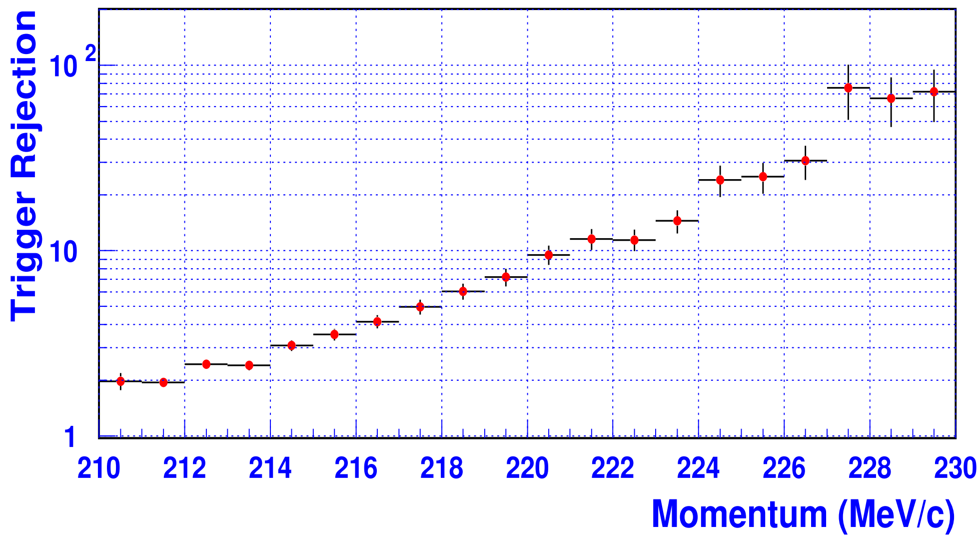

Figure E.7: Trigger rejection factors to the Muon Band events as a function of the momentum.

region > 225 MeV/c (see Figure E.8). Since, in the momentum region < 225 MeV/c, the momentum distribution of the Monte Carlo events is consistent with that of the Muon Band events in the $\pi\nu\bar{\nu}(1)$ trigger sample when the trigger requirements are imposed, it is assumed that the Monte Carlo events could also reproduce the momentum distribution of the Muon Band events in the momentum region > 225 MeV/c. Thus, the number of Muon Band events in the original momentum distribution is estimated by the Monte Carlo events. Table E.1 summarizes the trigger rejection factors and the expected number of Muon Band events in the original momentum distribution.

In the same way as for the Muon Band events, the trigger rejection factors to the $K_{\mu 2}$ Range Tail events are estimated. Figure E.9 shows the trigger rejection factors to the $K_{\mu 2}$ Range Tail events as a function of the range deviation, χ_{R-P}. The circles represent the rejection factors obtained from the Monte Carlo simulation and the squares represent those from the $K_{\mu 2}$ Range Tail events in one of the monitor trigger data that does not include the refined range requirement. The trigger rejection factors from the Monte Carlo simulation and real data are consistent with each other. The Monte Carlo simulation can therefore be used to estimate the trigger rejection factors. Table E.2 summarizes the trigger rejection factors to the $K_{\mu 2}$ Range Tail events and the expected numbers of $K_{\mu 2}$ Range Tail events in the original χ_{R-P} distribution.

E.4 Background Estimation with Line Shape Method

Figure E.10 explains the method of the Muon background estimation. In the Normalization Branch, the Muon background events that fail the $\pi^+ \to \mu^+ \to e^+$ Decay Sequence Cuts are selected. The estimations for the number of Muon Band and $K_{\mu 2}$ Range Tail events remaining in the Normalization Branch are separately performed.

The Muon background is concentrated at a higher momentum (also higher range)

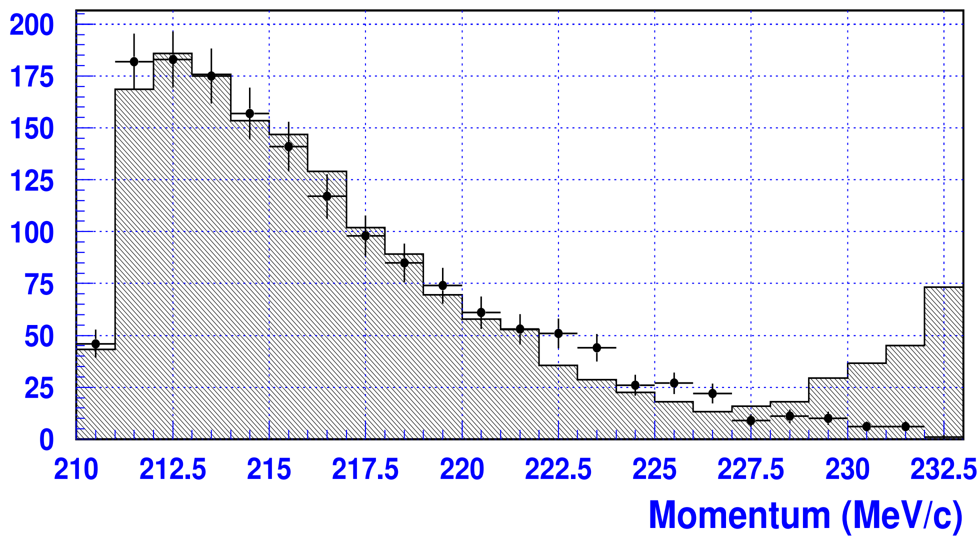

Figure E.8: Comparison of the momentum distributions between the Muon Band events in the $\pi\nu\bar{\nu}(1)$ trigger (histogram) and the Monte Carlo $K_{\mu\nu\gamma}$ events satisfying both trigger requirements (dots).

Momentum (MeV/c)	Trigger Rejection	Expected # of Events
$211 < P < 212$	1.951±0.101	2070.8
$212 < P < 213$	2.448±0.139	2080.1
$213 < P < 214$	2.406±0.139	1954.7
$214 < P < 215$	3.083±0.202	2247.2
$215 < P < 216$	3.539±0.252	2316.9
$216 < P < 217$	4.145±0.334	2251.9
$217 < P < 218$	4.980±0.450	2265.8
$218 < P < 219$	6.035±0.598	2381.9
$219 < P < 220$	7.216±0.779	2479.4
$220 < P < 221$	9.508±1.152	2692.9
$221 < P < 222$	11.604±1.524	2855.4
$222 < P < 223$	11.451±1.532	2711.5
$223 < P < 224$	14.477±2.106	2957.6
$224 < P < 225$	24.154±4.638	2915.8
$225 < P < 226$	25.037±4.721	3138.7
$226 < P < 227$	30.546±6.405	3120.1
$227 < P < 228$	75.889±25.129	3171.2
$228 < P < 229$	66.546±19.912	3398.7
Total		47010.4

Table E.1: Trigger rejection factor to the Muon Band events (second column) and the expected number of Muon Band events in the original momentum distribution (third column) in each momentum bin.

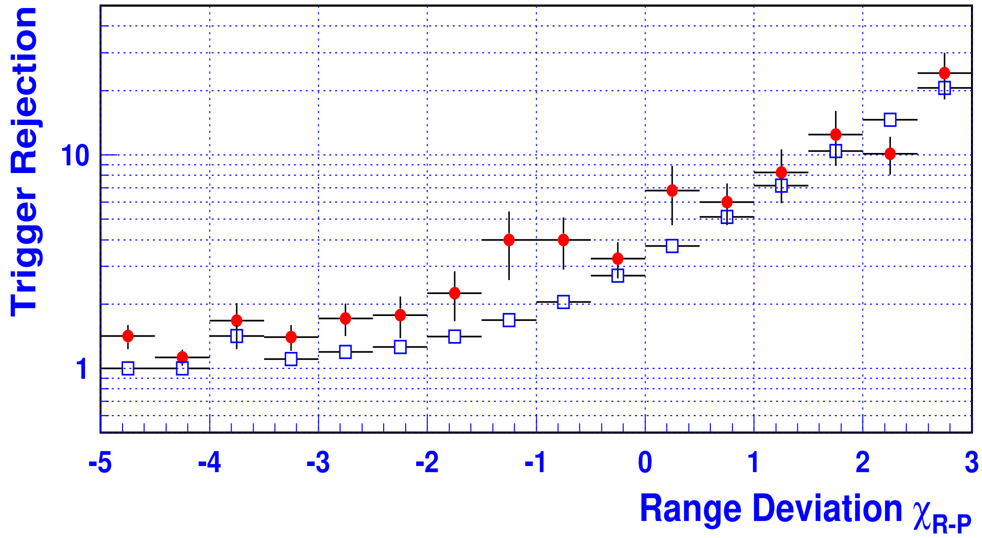

Figure E.9: Trigger rejection factors to the $K_{\mu 2}$ Range Tail events as a function of the range deviation, χ_{R-P}. The rejections indicated by the circles are obtained from the Monte Carlo simulation, which generates the $K_{\mu 2}$ Range Tail events, and those indicated by the squares from one of the monitor trigger data that contains the $K_{\mu 2}$ Range Tail events.

Range Deviation	Trigger Rejection	Expected # of Events
$\chi < -2.5$	1.196±0.032	77
$-2.5 < \chi < -2.0$	1.260±0.023	125
$-2.0 < \chi < -1.5$	1.406±0.019	148
$-1.5 < \chi < -1.0$	1.678±0.019	235
$-1.0 < \chi < -0.5$	2.048±0.021	289
$-0.5 < \chi < 0.0$	2.712±0.027	445
$0.0 < \chi < 0.5$	3.737±0.040	602
$0.5 < \chi < 1.0$	5.111±0.065	649
$1.0 < \chi < 1.5$	7.176±0.124	797
$1.5 < \chi < 2.2$	12.710±0.464	1703
Total		5070

Table E.2: Trigger rejection factor to the $K_{\mu 2}$ Range Tail events (second column) and the expected number of $K_{\mu 2}$ Range Tail events in the original χ_{R-P} distribution (third column) in each χ_{R-P} bin.

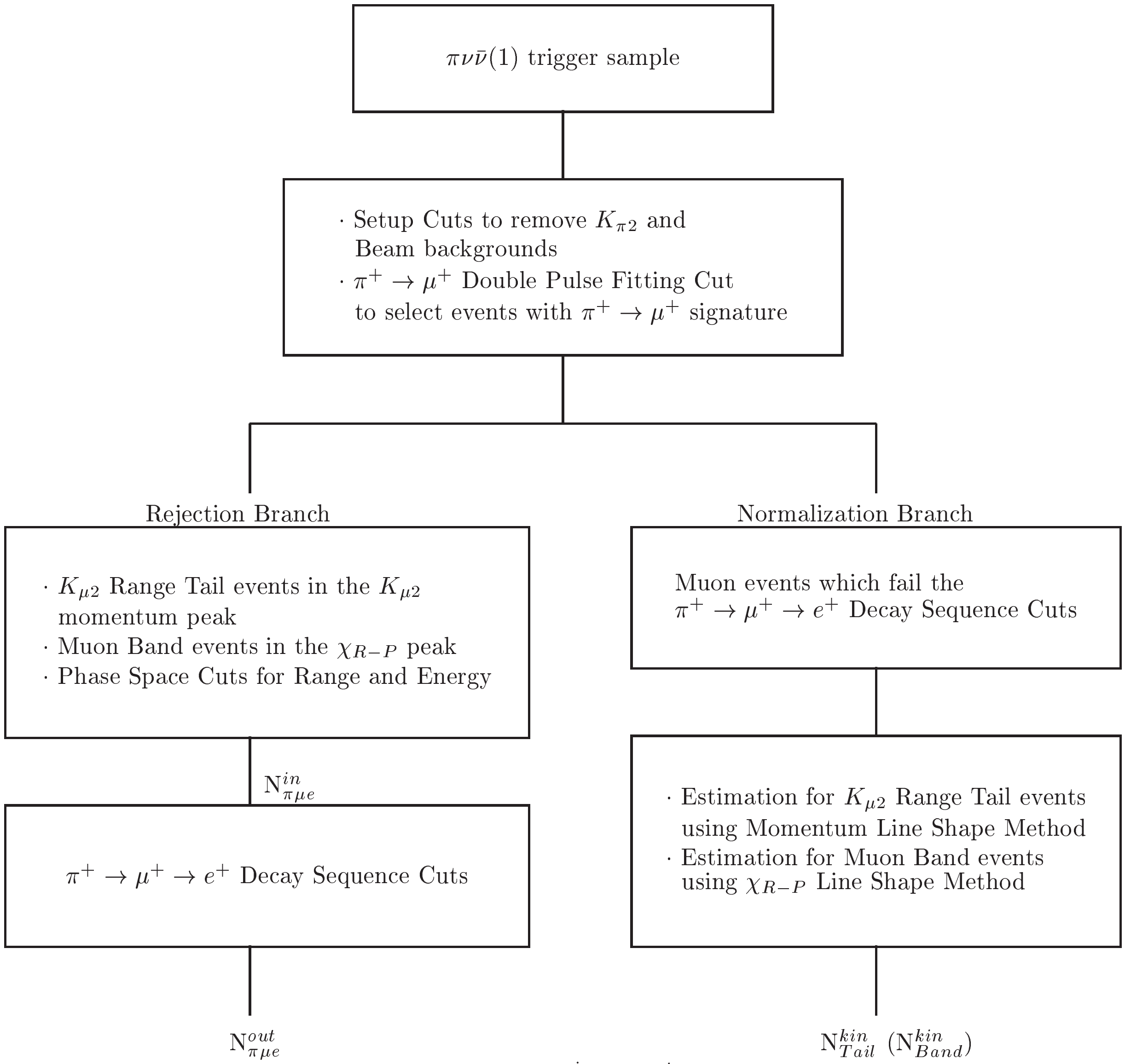

$$R_{\pi\mu e} = N^{in}_{\pi\mu e}/N^{out}_{\pi\mu e}$$
$$N_{Tail} = N^{kin}_{Tail}/(R_{\pi\mu e} - 1)$$
$$N_{Band} = N^{kin}_{Band}/(R_{\pi\mu e} - 1)$$
$$N_{Muon} = N_{Tail} + N_{Band}$$

Figure E.10: Method for estimating the Muon background.

region of the Signal Region (see left plot of Figure E.1). In the higher momentum region, there is a contamination of the $K_{\mu 2}$ Range Tail events to the tail of the χ_{R-P} distribution in the Muon Band background sample. In order to estimate the Muon Band background correctly, the χ_{R-P} distribution of events in the lower momentum region ($218 < P < 225$ MeV/c) are used as a template for an χ_{R-P} line-shape study (see Figure E.11). This region is chosen because the $K_{\mu 2}$ Range Tail contamination is expected to be small after applying the RS dE/dx Cuts (defined in Section 3.5.2). The fraction of events with $\chi_{R-P} \leq 2.2$ in this template is estimated to be

$$F_T(\chi_{R-P} \leq 2.2) = \frac{10}{94131} = 1.062 \times 10^{-4}, \tag{E.1}$$

where 10 events satisfy $\chi_{R-P} \leq 2.2$ in the template sample, and the total number of events in the template sample has been corrected by the trigger rejection factor (94131 in the denominator). The expected Muon Band events with $\chi_{R-P} \leq 2.2$ are estimated by normalizing the fraction 1.062×10^{-4} to the number of events in the original momentum distribution as

$$N_{\text{Band}} = \sum_i N_{\text{Band}}(i; \chi_{R-P} \leq 2.2) = 1.062 \times 10^{-4} \sum_i N_{\text{Band}}(P_i), \tag{E.2}$$

where $N_{\text{Band}}(P_i)$ is the number of Muon Band events in momentum bin P_i of the original momentum distribution. As shown in Table E.1, the term $\sum_i N_{\text{Band}}(P_i)$ gives 47010 events in the momentum region $211 \leq P \leq 229$ MeV/c. The expected number of the Muon Band events, N_{Band}, is therefore 4.992. The number N_{Band} should be corrected by the rejection factor of the Phase Space Cuts for Range and Energy (R_{ER}), which depends on both the momentum and χ_{R-P}, since they are not applied in this estimation. The net rejection factor for the Muon Band events is estimated to be 2.283 [2]. The expected number of Muon Band events that remain in the Normalization Branch is therefore estimated to be $4.992/2.283 = 2.187 \pm 0.138$ events (inside the 1×1 Region).

For estimating the $K_{\mu 2}$ Range Tail background level, the momentum distribution of events with $-2.5 < \chi_{R-P} < -1$ is used as a template for the momentum line shape study (see Figure E.12). The Muon Band contamination is expected to be small in this region. The fraction of events with $P \leq 229$ MeV/c in this template is estimated to be

$$F_T(P \leq 229 \text{ MeV/c}) = \frac{157}{48139} = 3.261 \times 10^{-3}, \tag{E.3}$$

where 157 events satisfy $P \leq 229$ MeV/c in the template sample, and the total number of events in the template sample has been corrected by the trigger rejection factor (48139 in the denominator). The number of events in the $P \leq 229$ MeV/c region is estimated by normalizing the fraction 3.261×10^{-3} to the amount of events in the original χ_{R-P} distribution. The expected $K_{\mu 2}$ Range Tail events with $P \leq 229$ MeV/c is therefore formulated as

$$N_{\text{Tail}} = \sum_i N_{\text{Tail}}(\chi_i; P \leq 229 \text{ MeV/c}) = 3.261 \times 10^{-3} \sum_i N_{\text{Tail}}(\chi_i), \tag{E.4}$$

[2]In reality, the Signal Region in the two dimensional space of momentum and χ_{R-P} is divided into cells and the rejection factor is measured cell by cell. This measurement needs larger statistics of the Muon background sample.

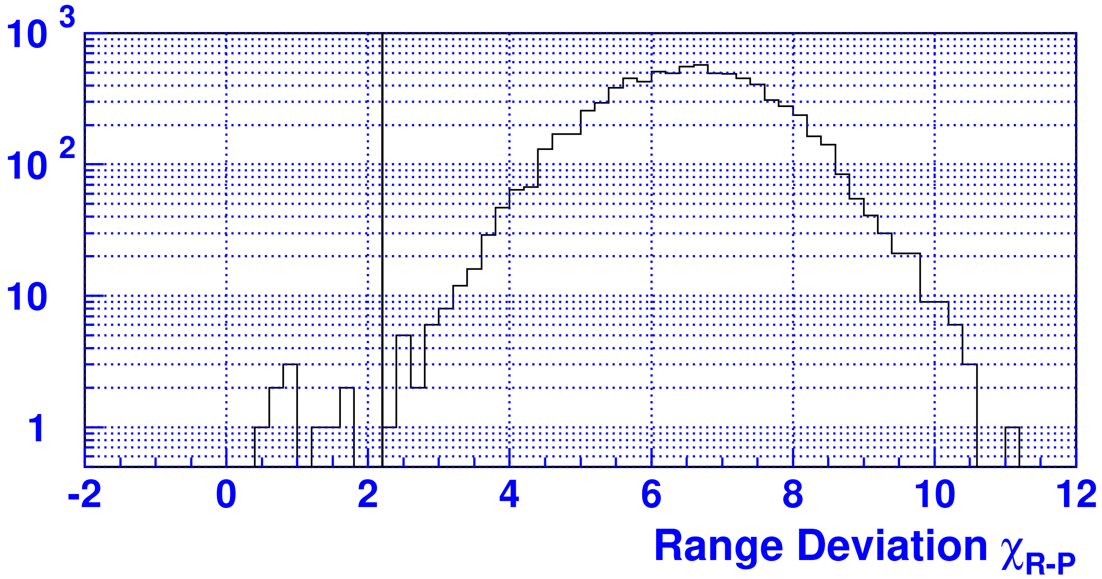

Figure E.11: Template range deviation distribution obtained from the Muon Band events in the $\pi\nu\bar{\nu}(1)$ trigger sample. The vertical line at 2.2 shows the cut position.

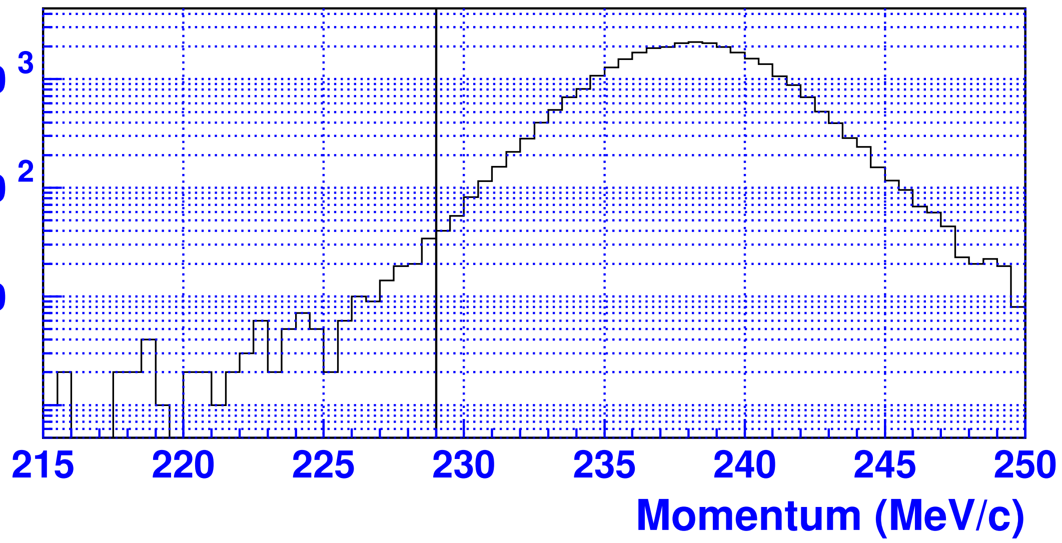

Figure E.12: Template momentum distribution obtained from the $K_{\mu2}$ Range Tail events in the $\pi\nu\bar{\nu}(1)$ trigger sample. The vertical line at $P = 229$ MeV/c shows the cut position.

where $N_{\mathrm{Tail}}(\chi_i)$ is the number of the $K_{\mu2}$ Range Tail events in the χ_{R-P} bin χ_i of the original χ_{R-P} distribution. The term $\sum_i N_{\mathrm{Tail}}(\chi_i)$ gives 5070 events in the region $\chi_{R-P} \leq$ 2.2, as shown in Table E.2. The N_{Tail} is estimated to be 16.53. The net rejection factor (R_{ER}) for the $K_{\mu2}$ Range Tail events is estimated to be 3.559. The expected number of $K_{\mu2}$ Range Tail events remaining in the Normalization Branch is therefore estimated to be $16.53/3.559 = 4.645 \pm 0.141$ (inside the 1×1 Region).

Appendix F

K_S^0 Selection for Producing CEX Spectrum

For the CEX Monte Carlo simulation, the production point and momentum vector of K_L^0 are necessary. The information on these can not be obtained theoretically. Since the production point and momentum vector of K_S^0 are the same as those of K_L^0, the $K_S^0 \to \pi^+\pi^-$ decay, which is easily reconstructed in the E949 detector, is studied. The K_S^0 data were collected by the CEX trigger defined as

$$CEX\ trigger = \mathrm{KB} \cdot \overline{\mathrm{DC}} \cdot 2(\mathrm{T} \bullet 2) \cdot (6_{ct} + 7_{ct}) \cdot \overline{(\mathrm{EC} + \pi\mathrm{B})}. \tag{F.1}$$

This trigger requires a kaon entering the target (KB), a prompt particle from K_S^0 ($\overline{\mathrm{DC}}$), more than two charged tracks entering the RS ($2(\mathrm{T}\bullet 2)$), no hit in the End Caps ($\overline{\mathrm{EC}}$) and no extra beam π^+ entering the target ($\overline{\pi\mathrm{B}}$). The background from K_L^0 with momentum less than 100 MeV/c is expected to be significant. The production rate for these K_L^0's is obtained by

$$R_{K_L^0} = \frac{N_{K_S^0}(P < 100\ \mathrm{MeV/c})}{\epsilon_{K_S^0} \cdot A_{PV} \cdot \mathcal{B}(K_S^0 \to \pi^+\pi^-) \cdot KB_{live}/PS}, \tag{F.2}$$

where $\epsilon_{K_S^0}$ is the $K_S^0 \to \pi^+\pi^-$ reconstruction efficiency for K_S^0's produced with $P <$ 100 MeV/c, A_{PV} is the acceptance of the online Photon Veto, $\mathcal{B}(K_S^0 \to \pi^+\pi^-)$ is the $K_S^0 \to \pi^+\pi^-$ branching ratio, $N_{K_S^0}(P < 100\ \mathrm{MeV/c})$ is the number of reconstructed $K_S^0 \to \pi^+\pi^-$ decays passing the CEX trigger with $P < 100$ MeV/c, KB_{live} is the number of K^+ triggers after correcting for the online trigger dead time, and PS is the online prescale factor for CEX trigger. The K_S^0 events are selected by the following requirements:

- prompt decay,
- at least two charged tracks with opposite charges,
- pion mass cut on each track, and
- invariant mass of two tracks consistent with K_S^0 mass.

The invariant mass distribution of K_S^0 is shown in Figure F.1. After applying the K_S^0 selection cuts, 8086 events were observed. The information of these events were used to generate the beam file for the K_L^0 Monte Carlo simulation.

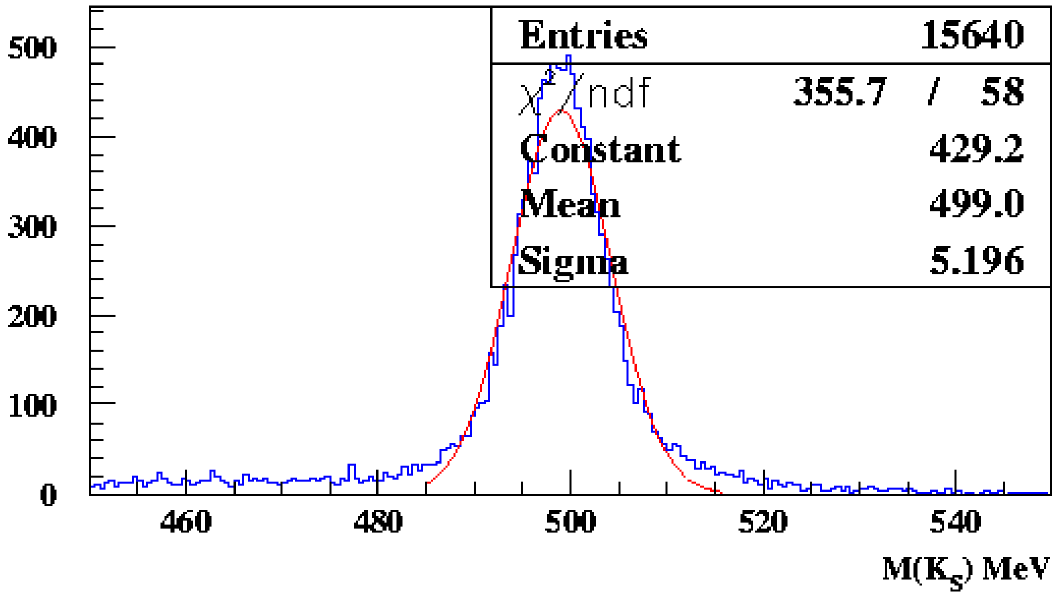

Figure F.1: Invariant mass distribution of K_S^0 in $K_S^0 \to \pi^+\pi^-$ events.

Appendix G

Acceptance Measurements

G.1 Acceptance Factors from $K_{\mu 2}$ Events

The acceptance factors measured by using $K_{\mu 2}$ monitor trigger data are for the reconstruction cuts, the cuts for the beam and target analysis, and the accidental loss due to Photon Veto Cuts. $K_{\mu 2}$ events are selected by requiring momentum, energy, range in the $K_{\mu 2}$ peaks ($\pm 2\sigma$). For the photon veto acceptance measurements, it is required that the track does not reach the 19th RS layer in order to remove the events in which the track leaves the energy in the Barrel Veto and Barrel Veto Liner. The acceptance loss due to the Layer 14 Cut ($1 - A_{LAYER14}$) is measured by looking into accidental hits in the RSSC at the sector opposite to the stopping counter. The measured acceptances are summarized in Table G.1.

In addition, the acceptance loss due to accidental hits in the RS layer-19 counters is also measured by the $K_{\mu 2}$ monitor trigger data. The online trigger requirement $\overline{19_{ct}}$ removes events with hits in the layer-19 counters of the charged track sectors [1], even in the case that the hit is not due to the charged track. $K_{\mu 2}$ events with the charged tracks stopping in layer 17 are selected, and the online trigger bit for $\overline{19_{ct}}$ of these events is checked. The acceptance associate with accidental hits in the layer 19 (A_{acc}) is measured to be

$$A_{acc} = 0.9959 \pm 0.0006(stat.). \tag{G.1}$$

The acceptance from $K_{\mu 2}$ monitor trigger data ($A_{K_{\mu 2}}$) is therefore measured to be

$$A_{K_{\mu 2}} = 0.3812 \pm 0.0012(stat.). \tag{G.2}$$

[1] The charged track sector is defined in Section 2.4.

Cut	# Events	Acceptance
Setup for A_{RD}	541883	-
RD_TRK	541883	1.00000
TRKTIM	541863	0.99996
A_{RD}	0.99996±0.00001	
Setup for A_{UTCTG}	410990	-
UTC/RANGE	410990	1.00000
UTC_QUAL	410990	1.00000
TARGET	409213	0.99568
A_{UTCTG}	0.99568±0.00010	
A_{recon}	0.99564±0.00010	
Setup for A_{beam}	462513	-
ICBIT	462513	1.00000
TIC	461687	0.99821
TIMCON	460181	0.99674
DCBIT	406131	0.88255
DELCO2	389333	0.95864
TGTCON	386416	0.99262
DELCO	348611	0.90206
CKTRS	342844	0.98346
CKTAIL	334196	0.97478
B4DEDX	329063	0.98464
CPITRS	327540	0.99537
CPITAIL	327348	0.99941
PSCUT	318362	0.97255
TARGF	305027	0.95811
DTGTTP	304971	0.99982
RTDIF	301720	0.98934
TGQUALT	301720	1.00000
PIGAP	299219	0.99171
TGB4	282449	0.94395
KIC	278304	0.98532
TGGEO	275098	0.98848
EIC	267568	0.97263
EICKIN	265327	0.99162
B4EKZ	258234	0.97327
B4ETCON	256842	0.99461
TGZFOOL	256842	1.00000
TGCUT	256841	1.00000
BWTRS	247876	0.96510
UPV/RVTRS	243736	0.98330
B4TRS	237925	0.97616
B4CCD	234860	0.98712
A_{beam}	0.50779±0.00074	
Setup for A_{PV}	37383	-
HEX	34884	0.93315
Online PV	33000	0.94599
$\overline{20_{ct}+21_{ct}}$	32716	0.99139
STLAY	32248	0.98570
Offline PV	28704	0.92195
A_{PV}	0.76784±0.00218	
Setup	816980	-
LAYER14	802237	0.98195
$A_{LAYER14}$	0.98195±0.00015	
A_{acc}	0.9959±0.0006	
$A_{K_{\mu2}}$	0.3812±0.0012	

Table G.1: Acceptances of the $K^+ \to \pi^+\nu\bar{\nu}$ selection cuts from $K_{\mu2}$. The symbolic names of the cuts in the table are described in Appendix B. The errors are statistical.

G.2 Acceptance Factors from $K_{\pi 2}$ Events

Cut	# Events	Acceptance
Setup for A_{ops}	12952	-
OPSVETO	12753	0.98464
OPSVETO_LKB	12753	1.00000
A_{ops}	0.98464±0.00108	
Setup for A_{tgkin}	12695	-
TGDEDX	12231	0.96345
TGER	12229	0.99984
TGLIKE	12006	0.98176
EPITG	11997	0.99925
EPIMAXK	11845	0.98733
TGEDGE	11783	0.99477
PHIVTX	11433	0.97030
UTC_QUAL2	11371	0.99458
DRP	11327	0.99613
A_{tgkin}	0.89224±0.00275	
$A_{K_{\pi 2}}$	0.87853±0.00288	

Table G.2: Acceptances of the $K^+ \to \pi^+ \nu\bar{\nu}$ selection cuts from $K_{\pi 2}$. The symbolic names of the cuts in the table are described in Appendix B. The errors are statistical.

The acceptance measurements using $K_{\pi 2}$ monitor trigger data are for the acceptances of the target cuts which involve the energy loss in the target. $K_{\pi 2}$ events are selected by requiring photon activities in the photon detectors and momentum, energy, range in the $K_{\pi 2}$ peaks ($\pm 2\sigma$). The measured acceptances using $K_{\pi 2}$ monitor trigger data are summarized in Table G.2. The acceptance from $K_{\pi 2}$ monitor trigger data is measured to be

$$A_{K_{\pi 2}} = 0.8785 \pm 0.0029(stat.). \tag{G.3}$$

G.3 Kinematic Acceptance Factors from Pion Scattering Events

Cut	Loose Phase Space		Standard Phase Space		Tight Phase Space	
	# Events	Acceptance	# Events	Acceptance	# Events	Acceptance
Setup	5002	-	3248	-	1862	-
UTC_QUAL1	4640	0.92763	3033	0.93381	1742	0.93555
RNGMOM	4591	0.98944	3002	0.98978	1724	0.98967
RSDEDX	3926	0.85515	2604	0.86742	1507	0.89117
PRRF	3403	0.86679	2293	0.88057	1343	0.89117
PRRFZ	3001	0.88187	2022	0.88181	1189	0.88533
LAY14	2970	0.98967	2001	0.98961	1176	0.98907
Acceptance	0.59376±0.00694		0.61607±0.00853		0.63158±0.01118	
$A_{\pi scatter}$	0.6161±0.0085					

Table G.3: Kinematic cut acceptances using Pion Scattering events. The symbolic names of the cuts in the table are described in Appendix B. The errors are statistical.

The acceptance measurements from $\pi_{scatter}$ monitor trigger data are for the acceptance of the Kinematic Cuts, which depend on the particle type of the charged track. Pion Scattering events are selected by requiring prompt timing and small dE/dx in the B4 Hodoscope. The Phase Space Cuts are additionally applied to select the events in the signal phase space.

The Pion Scattering events arise from scatterings in the target, not from kaon decays at rest. Assignments of the hits in the target to the kaon fibers and pion fibers could be screwed up because their timings are close to each other, and energy deposits of the incoming and outgoing particles at around the vertex point are somehow different between scatterings and decays at rest; both of these features would result in more uncertainties in the momentum, energy and range measurements in the Pion Scattering events.

Acceptances are therefore measured by loosening or tightening the Phase Space Cuts by ± 1 standard deviation, and any systematic uncertainties are estimated by taking their difference. The measured acceptances for the different setup cuts are summarized in Table G.3. The acceptance from the $\pi_{scatter}$ monitor trigger data is measured to be

$$A_{\pi scatter} = 0.6161 \pm 0.0085(stat.) \pm 0.0189(sys.), \tag{G.4}$$

where the systematic uncertainty is due to the acceptance difference between the loose and tight phase spaces.

G.4 $\pi^+ \to \mu^+ \to e^+$ Decay Acceptance from Pion Scattering Events

Cut	Loose Setup Cuts		Tight Setup Cuts	
	# Events	Acceptance	# Events	Acceptance
Setup	4966	-	3203	-
FITPI (bad data)	4962	0.99919	3199	0.99875
FITPI (counting)	4117	0.82971	2701	0.84433
RSHEX2	4045	0.98251	2659	0.98445
L1.1	3090	0.76391	2035	0.76533
L1.2	2674	0.86537	1772	0.87076
TDCUT	2504	0.93642	1657	0.93510
EV5	2138	0.85383	1408	0.84973
ELVETO	2029	0.94902	1339	0.95099
TDFOOL	2028	0.99951	1339	1.00000
TDVARNN	1716	0.84615	1134	0.84690
Acceptance	0.3456±0.0068		0.3590±0.0086	
$A_{\pi\to\mu\to e}$	0.3523±0.0077			

Table G.4: $\pi^+ \to \mu^+ \to e^+$ decay acceptances from $\pi_{scatter}$ monitor trigger data with different setup cuts. The π^+ time consistency cut is included in the "FITPI" cut. The symbolic names of the cuts in the table are described in Appendix B. The errors are statistical.

The $\pi^+ \to \mu^+ \to e^+$ decay acceptance is measured by using the $\pi_{scatter}$ monitor trigger data. This acceptance measurement includes both of online and offline π^+ identification cuts. In this $\pi_{scatter}$ monitor trigger data, events with pion decay-in-flight and pion absorption in the stopping counter might be contaminated and make the acceptance lower. The contamination is estimated by using the Monte Carlo events of the $K^+ \to \pi^+\nu\bar{\nu}$; the contributions of the pion stop, decay-in-flight and absorption can be obtained. From the study, the contamination is estimated to be 1.4%, which is assigned as the upper systematic uncertainty. On the other hand, the $\pi^+ \to \mu^+ \to e^+$ decay acceptance could be measured larger when the Track Reconstruction Quality Cuts are applied in the setup because they remove events with accidentals. Although the contamination of the pion absorption and pion decay-in-flight might be increased, the acceptance is measured without applying the Track Reconstruction Cuts. The acceptances with tight and loose setup cuts are measured to understand the systematic uncertainty. The difference between the tight and loose setup cuts is whether the RS dE/dx Cuts and the Track Reconstruction Cuts are applied or not. The measured acceptances are summarized in Table G.4. The acceptance of 0.3590 in the tight setup case has been corrected by the factor of 1.014 in order to take into account the pion absorption and pion decay-in-flight. The acceptance in the loose setup case is smaller by 0.84% than that in the tight one. The 0.84% acceptance decrease gives the lower systematic uncertainty. The $\pi^+ \to \mu^+ \to e^+$ decay acceptance is measured to be

$$A_{\pi\to\mu\to e} = 0.3523 \pm 0.0077(stat.) \pm 0.0067(sys.), \tag{G.5}$$

where the mean value is derived from the average of the two acceptance values, and the systematic uncertainty is taken from the difference between them.

G.5 Acceptance Factors from Monte Carlo Events

Cut	NIDIF (ON)		NIDIF (OFF)	
	# Events	Acceptance	# Events	Acceptance
Setup	199998	-	150000	-
T•2	77876	0.3894	61713	0.4114
$(6_{ct} + 7_{ct})$	54722	0.7027	50657	0.8208
DC	54722	1.0000	50657	1.0000
$\overline{19_{ct}}$	54567	0.9971	50638	0.9996
$\overline{\mathrm{BV} + \mathrm{BVL} + \mathrm{EC}}$	54453	0.9980	50638	1.0000
HEX	54377	0.9986	50638	1.0000
Refined Range	23490	0.4320	26934	0.5319
$A_{trigger}$	0.1175±0.0007		0.1796±0.0010	
Setup	23387	-	26920	-
UFATE	20945	0.8956	26920	1.0000
USTMED	20785	0.9924	26779	0.9948
USTOP_HEX	20409	0.9819	26702	0.9971
COS3D	19823	0.9713	25865	0.9687
LAYER14	19749	0.9963	25850	0.9994
ZFRF	18473	0.9354	24071	0.9312
ZUTOUT	18470	0.9998	24065	0.9998
Loose Phase Space	7114	0.3852	10727	0.4458
Phase Space	6426	0.3479	9773	0.4061
A_{MC}(Signal Region)	0.3042±0.0030		0.3985±0.0030	
A_{MC}(1×1 Region)	0.2748±0.0029		0.3630±0.0029	

Table G.5: Summary of the acceptances obtained from the Monte Carlo events. The symbolic names of the cuts in the table are described in Appendix B. The errors are statistical.

The acceptance measurements using the Monte Carlo simulation of the $K^+ \to \pi^+ \nu\bar{\nu}$ are for the trigger acceptance, the phase space and solid angle acceptances, and the acceptance loss due to pion decay-in-flight or pion nuclear interaction. The Monte Carlo simulation generates the $K^+ \to \pi^+ \nu\bar{\nu}$ events with the pion decay-in-flight and nuclear interaction (NIDIF) turned on and off separately. The simulation starts from an input file which contains the x, y, z positions of the kaon decay vertex in the target and has the time, energy and position information of real kaon fibers and gamma fibers in the target. $K^+ \to \pi^+ \nu\bar{\nu}$ events are generated at the decay vertex based on the input file, and the trigger acceptance, the phase space and solid angle acceptances, and the π^+ stop efficiency are measured. Since the phase space acceptance exclusively depends on the momentum, range and energy, these kinematic quantities of the Monte Carlo events are adjusted by comparing those of the real data. The Monte Carlo simulation also generates the $K_{\pi 2}$ decay. The momentum, range and energy of the $K_{\pi 2}$ events in both Monte Carlo and real data are compared. The momentum, range and energy of the $K_{\pi 2}$ peaks in the Monte Carlo are adjusted to be consistent with those in the real data. The same correction as the $K_{\pi 2}$ is applied to the $K^+ \to \pi^+ \nu\bar{\nu}$.

The trigger acceptance and the phase space and solid angle acceptances with NIDIF on and off are summarized in Table G.5. Table G.6 shows the comparison of the $K_{\pi 2}$ kinematic quantities between the Monte Carlo data and the real data. The resolution of the

Quantity	Monte Carlo	Real Data
Momentum (MeV/c)	205.1	205.1
Range (cm)	30.4	30.4
Energy (MeV)	108.5	108.7
Momentum Resolution (MeV/c)	2.34	2.29
Range Resolution (cm)	1.02	0.87
Energy Resolution (MeV)	3.02	3.02

Table G.6: Comparison of the $K_{\pi 2}$ kinematic quantities between Monte Carlo and real data.

momentum and energy of the $K_{\pi 2}$ peaks in the Monte Carlo are almost the same as those in the real data. However, the range resolution in the Monte Carlo is worse than that in the real data. It is expected that the discrepancy in the range resolution yields a 5% difference in acceptance. This is assigned to the systematic uncertainty. The trigger acceptance is taken from $A_{trigger}$ with NIDIF off.

$$A_{trigger} = 0.1796 \pm 0.0010(stat.) \pm 0.0090(sys.), \tag{G.6}$$

where the 5% systematic uncertainty is assigned. The phase space and solid angle acceptances (A_{MC}) are also taken from those with NIDIF off and they are measured to be

$$\begin{aligned} A_{MC} &= 0.3985 \pm 0.0030(stat.) \qquad \text{for Signal Region,} \\ &= 0.3630 \pm 0.0029(stat.) \qquad \text{for } 1 \times 1 \text{ Region.} \end{aligned} \tag{G.7}$$

The π^+ stop efficiency (A_{NIDIF}) can be estimated by comparing the trigger acceptance and the phase space and solid angle acceptances with and without NIDIF.

$$\begin{aligned} A_{NIDIF} &= \frac{A_{trigger}(NIDIFon)}{A_{trigger}(NIDIFoff)} \times \frac{A_{MC}(NIDIFon)}{A_{MC}(NIDIFoff)} \\ &= 0.4953 \pm 0.0077(stat.) \pm 0.0248(sys.), \end{aligned} \tag{G.8}$$

where the 5% systematic uncertainty is assigned.

G.6 Measurement of the T•2 Efficiency

Cut	$K_{\mu 2}$	$K_{\pi 2}$
Setup	678726	190552
Bad Run	677206	189474
Reconstruction Cuts	280030	70558
Polar Angle	269194	68235
Beam and Target Cuts	83870	18101
Photon Veto Cuts	73193	-
$\pi^+ \to \mu^+ \to e^+$ Decay Requirement	-	11271
Momentum in the $K_{\mu 2}$ peak	61166	-
Stopping Layer Cut	-	10208
Hit in UTC Outer Layer	54227	9147
Z Fiducial Cut	48247	8089

Table G.7: Numbers of reconstructed $K_{\mu 2}$ and $K_{\pi 2}$ events used in the T•2 efficiency measurement.

T•2 efficiency accounts for the acceptance loss due to the geometrical and counter inefficiencies of the T-Counters. The geometrical inefficiency represents the inefficiency due to the track passing through an azimuthal gap between two adjacent T-Counters. The counter inefficiency occurs if the scintillation light induced by the charged track is not detected by the PMTs.

The T•2 efficiency is measured by using a special monitor trigger data without requiring the T•2. With the monitor trigger data a charged track is reconstructed without using the T•2. $K_{\mu 2}$ and $K_{\pi 2}$ events in the sample are selected and the T•2 efficiency (geometrical and counter inefficiencies) are measured for both $K_{\mu 2}$ and $K_{\pi 2}$. The numbers of reconstructed $K_{\mu 2}$ and $K_{\pi 2}$ events are summarized in Table G.7. "Photon Veto Cuts" means the Photon Veto Cuts except for the Barrel Veto, Barrel Veto Liner and Range Stack. Stopping Layer Cut requires that the stopping layer is between 8 and 16. It is required that the reconstructed charged track should point the T-Counter because the T•2 efficiency is underestimated if the charged particle actually pass outside the edge of the T-Counters. To avoid such a case, hits in the UTC outer layer are required. In order to ensure that the track passes through the T-Counters, the charged track extrapolated by the UTC is required to have z position within ± 20 cm region of the T-Counters (Z Fiducial Cut). This fiducial requirement increases the T•2 efficiency because events with the track pointing the z edge of the T-Counters, whose fraction to the whole events without T•2 is large, are removed. The difference in the T•2 efficiency due to the Z Fiducial Cut is assigned as the systematic uncertainty.

The online T•2 bits of the reconstructed events are checked to measure the T•2 efficiency. The fraction of the events with T•2 bit is tabulated in Table G.8. Since specific two T-Counters have much smaller T•2 efficiency due to a problem on electronics, these

	$K_{\mu 2}$	$K_{\pi 2}$
T•2 Efficiency (total)	0.9303±0.0012	0.9423±0.0026
T•2 Efficiency (good)	0.9345±0.0012	0.9429±0.0027
T•2 Efficiency (bad)	0.8819±0.0052	0.9346±0.0098
Geometrical Inefficiency	0.03214	0.02855
Counter Inefficiency (good)	0.03336	0.02855
Counter Inefficiency (bad)	0.08596	0.03685
k (good)	2.097	1.741
k (bad)	1.514	1.616

Table G.8: T•2 efficiency, geometrical and counter inefficiencies, and photoelectron yield per MeV k for $K_{\mu 2}$ and $K_{\pi 2}$. These values are separately measured for the cases of the good and bad sectors.

Sector	$\epsilon(geometrical)$	k	T•2 efficiency
Good Sectors	0.03035	1.919	0.9380±0.0011
Bad Sectors	0.03035	1.565	0.9099±0.0050

Table G.9: Counter inefficiency, photoelectron yield k, and T•2 efficiency for $K^+ \to \pi^+ \nu\bar{\nu}$.

counters are separately treated. The T•2 efficiency can be expressed as

$$\begin{aligned} A_{T\bullet 2} &= 1 - \epsilon(geometrical) - \epsilon(counter) \\ &= 1 - \epsilon(geometrical) - e^{-kE}, \end{aligned} \tag{G.9}$$

where $\epsilon(geometrical)$ and $\epsilon(counter)$ represent the geometrical and counter inefficiencies, k represents the number of photoelectrons per MeV, and E is the mean energy deposit in the T-Counters. The mean energy deposits in the T-Counters for $K_{\mu 2}$, $K_{\pi 2}$ and $K^+ \to \pi^+ \nu\bar{\nu}$ are measured with the Monte Carlo simulation to be 1.62 MeV, 2.05 MeV, 1.80 MeV, respectively. Using the values in Table G.8 and Equation (G.9), the values of k for $K_{\mu 2}$ and $K_{\pi 2}$ are estimated as shown in Table G.8. The geometrical inefficiency and the photoelectron yield k for $K^+ \to \pi^+ \nu\bar{\nu}$ are obtained from the average of those for $K_{\mu 2}$ and $K_{\pi 2}$ (Table G.9). T•2 efficiencies for $K^+ \to \pi^+ \nu\bar{\nu}$ in both good and bad sectors are calculated by using Equation (G.9). The net T•2 efficiency for $K^+ \to \pi^+ \nu\bar{\nu}$ is obtained from the weighted average of the values in the good and bad sectors and is measured to be

$$A_{T\bullet 2} = 0.9357 \pm 0.0011(stat.) \pm 0.0168(sys.), \tag{G.10}$$

where the systematic uncertainty accounts for the difference due to Z Fiducial Cut.

Appendix H

Acceptance Factors for the K^+ Stop Efficiency Calculation

The acceptances of the $K_{\mu 2}$ selection cuts used in the calculation of the K^+ stop efficiency are measured with $K_{\mu 2}$ events in the real and Monte Carlo data. The acceptances measured using the Monte Carlo $K_{\mu 2}$ events are tabulated in Table H.1. The acceptances of the trigger ($A_{trigger}$), the polar angle cut ($A_{polar\ angle}$), and the range requirement (A_{range}) are taken from the Monte Carlo acceptance measurement.

Cut	# Events	Acceptance
Setup	50000	-
T•2	22721	0.45442
$17_{ct} + 18_{ct} + 19_{ct}$	22077	0.97166
$A_{trigger}$(MC)	0.44154±0.00222	
UTC/RANGE	22064	0.99941
UTC_QUAL	20427	0.92581
TARGET	20389	0.99814
A_{recon}(MC)	0.92354±0.00179	
COS3D	20116	0.98661
$A_{polar\ angle}$(MC)	0.98661±0.00080	
$R > 40$ cm	19869	0.98772
A_{range}(MC)	0.98772±0.00078	
$A_{K_{\mu 2}}$(MC)	0.3974±0.0022	

Table H.1: Acceptance factors for the K^+ stop efficiency calculation, obtained from the Monte Carlo $K_{\mu 2}$ events. The symbolic names of the cuts in the table are described in Appendix B. The errors are statistical.

The other acceptances ($A_{bad\ run}$, A_{recon}, $A_{beam\&target}$ and $A_{photon\ veto}$) are measured with the $K_{\mu 2}$ monitor trigger data, as tabulated in Table H.2. In this measurement, the same cuts as used to measure the acceptance factors from $K_{\mu 2}$ ($A_{K_{\mu 2}}$) are adopted [1]. By using the same cuts, the uncertainty in the $A_{K_{\mu 2}}$ is canceled when the K^+ stop efficiency is multiplied by the $A_{K_{\mu 2}}$ to get the total acceptance.

[1] I.e., the cuts described in Table G.1 are used.

Cut	# Events	Acceptance
Setup for A_{RD}	648394	-
RD_TRK	648394	1.00000
TRKTIM	648347	0.99993
A_{RD}	0.99993±0.00001	
Setup for A_{UTCTG}	487336	-
UTC/RANGE	487336	1.00000
UTC_QUAL	410597	0.84253
TARGET	408821	0.99567
A_{UTCTG}	0.83889±0.00053	
A_{recon}	0.83883±0.00053	
Setup for $A_{beam\&target}$	600807	-
ICBIT	600807	1.00000
TIC	599650	0.99807
TIMCON	597618	0.99661
TGTCON	593163	0.99255
DCBIT	523290	0.88220
DELCO	452473	0.86467
CKTRS	444871	0.98320
CKTAIL	433702	0.99940
B4DEDX	426932	0.98439
CPITRS	424939	0.99533
CPITAIL	424685	0.99940
TARGF	406779	0.95784
DTGTTP	406704	0.99982
RTDIF	402318	0.98922
TGQUALT	402318	1.00000
PIGAP	398978	0.99170
TGB4	376730	0.94424
KIC	371264	0.98549
TGGEO	366882	0.98820
B4EKZ	355998	0.97033
B4ETCON	354089	0.99464
TGZFOOL	354089	1.00000
BWTRS	341320	0.96394
U/RPVTRS	335566	0.98314
$A_{beam\&target}$	0.55853±0.00064	
Setup for $A_{photon\ veto}$	361027	-
PV w/o BV	335566	0.92948
$A_{photon\ veto}$	0.92948±0.00043	
Setup for $A_{bad\ run}$	1010411	-
BAD_RUN	1009954	0.99955
BAD_STC	1009805	0.99985
TRIGGER	1009805	1.00000
$A_{bad\ run}$	0.99940±0.00002	
$A_{K_{\mu 2}}$	0.4352±0.0006	

Table H.2: Acceptance factors for the K^+ stop efficiency calculation, obtained from the $K_{\mu 2}$ monitor trigger data. The errors are statistical.

Appendix I

Acceptance Factors for the $K_{\pi 2}$ Branching Ratio Measurement

The acceptances of the $K_{\pi 2}$ selection cuts used in the calculation of the $K_{\pi 2}$ branching ratio are measured with both the $K_{\pi 2}$ monitor trigger data and the $K_{\pi 2}$ data generated by the Monte Carlo simulation. The acceptances of the trigger ($A_{trigger}$), the phase space cut ($A_{phase\ space}$), the polar angle cut ($A_{polar\ angle}$), and the stopping layer cut ($A_{stopping\ layer}$) are taken from the Monte Carlo acceptance measurement, as tabulated in Table I.1. The other acceptances (A_{recon}, $A_{beam\&target}$, $A_{bad\ run}$ and $A_{\pi\to\mu\to e}$) are obtained from the measurement with the $K_{\pi 2}$ monitor trigger data, as tabulated in Table I.2.

Cut	# Events	Acceptance
Setup	49997	-
T•2	22697	0.45397
$6_{ct} + 7_{ct}$	19090	0.84108
$\overline{19_{ct}}$	18797	0.98465
UFATE	15910	0.84641
USTMED	15568	0.97850
USTOP_HEX	13909	0.89344
$A_{trigger}$(MC)	0.2782±0.0020	
UTC/RANGE	13909	1.00000
UTC_QUAL	12660	0.91020
TARGET	12532	0.98989
A_{recon}(MC)	0.9010±0.0025	
Stopping Layer	12072	0.96329
$A_{stopping\ layer}$(MC)	0.96329±0.00168	
COS3D	11878	0.98393
$A_{polar\ angle}$(MC)	0.98393±0.00114	
Phase Space	10840	0.91261
$A_{phase\ space}$(MC)	0.91261±0.00259	
$A_{K_{\pi 2}}$	0.2168±0.0018	

Table I.1: Acceptance factors for the $K_{\pi 2}$ branching ratio calculation, obtained from the Monte Carlo $K_{\pi 2}$ events. The symbolic names of the cuts in the table are described in Appendix B. The errors are statistical.

Cut	# Events	Acceptance
Setup for A_{RD}	51416	-
RD_TRK	51416	1.00000
TRKTIM	51416	1.00000
A_{RD}	1.00000±0.00000	
Setup for A_{UTCTG}	32980	-
UTC/RANGE	32980	1.00000
UTC_QUAL	28117	0.85255
TARGET	27831	0.98983
A_{UTCTG}	0.84388±0.00200	
A_{recon}	0.84388±0.00200	
Setup for $A_{beam\&target}$	32055	-
ICBIT	32055	1.00000
TIC	32055	1.00000
TIMCON	31970	0.99735
TGTCON	31847	0.99615
DCBIT	31542	0.99042
DELCO	27898	0.88447
CKTRS	24368	0.87347
CKTAIL	23710	0.97300
B4DEDX	23032	0.97140
CPITRS	22657	0.98372
CPITAIL	22442	0.99051
TARGF	22431	0.99951
DTGTTP	21467	0.95702
RTDIF	21462	0.99977
TGQUALT	21277	0.99138
PIGAP	21277	1.00000
TGB4	21098	0.999159
KIC	20002	0.94805
TGGEO	19855	0.99265
B4EKZ	16358	0.82387
B4ETCON	15886	0.97115
TGZFOOL	15806	0.99496
BWTRS	15806	1.00000
U/RPVTRS	15096	0.95508
$A_{beam\&target}$	0.46224±0.00278	
Setup for $A_{bad\ run}$	84793	-
BAD_RUN	84752	0.99952
BAD_STC	84338	0.99512
TRIGGER	84338	1.00000
$A_{bad\ run}$	0.99463±0.00025	
$A_{\pi\to\mu\to e}$	0.83498±0.00542	
$A_{K_{\pi2}}$	0.3240±0.0029	

Table I.2: Acceptance factors for the $K_{\pi2}$ branching ratio calculation, obtained from the $K_{\pi2}$ monitor trigger data. The symbolic names of the cuts in the table are described in Appendix B. The errors are statistical.

Appendix J

Likelihood Analysis in the E949 Publication

J.1 Calculation of the Branching Ratio

In Chapter 7, the branching ratios for the $K^+ \to \pi^+\nu\bar{\nu}$ decay were evaluated from the integrated area of the likelihood estimator X_{obs}. The way to evaluate the branching ratio in the E949 publication [47] is based on the statistical technique developed by T. Junk [46].

As explained in Section 3.7, the likelihood estimator X, Equation (3.5), is used to evaluate the branching ratio with the information on the expected number of signal events $\{s_i\}$, the background level $\{b_i\}$ and the observed number of events $\{d_i\}$ in the cells. Once the set of observed number of events $\{d_i\}_{obs}$ in the Signal Region is obtained, the value of the X for $\{d_i\}_{obs}$, which is referred to as X_{obs}, is determined. All the experimental outcomes (all sets of $\{d_i\}$) which give values of X less than or equal to X_{obs} are selected. Summing the probabilities of these experimental outcomes, assuming the presence of signal and background, gives the confidence level as:

$$CL_{s+b} \equiv P_{s+b}(X \leq X_{obs}) = \sum_{X(\{d_i\}) \leq X_{obs}} \prod \frac{e^{-(s_i+b_i)}(s_i+b_i)^{d_i}}{d_i!}. \tag{J.1}$$

Also, summing the probabilities of these experimental outcomes, assuming the presence of background alone, gives the confidence level:

$$CL_b \equiv P_b(X \leq X_{obs}) = \sum_{X(\{d_i\}) \leq X_{obs}} \prod \frac{e^{-b_i} b_i^{d_i}}{d_i!}. \tag{J.2}$$

The (modified) frequentist confidence level for signal, CL_s, is determined as the ratio

$$CL_s \equiv \frac{CL_{s+b}}{CL_b}. \tag{J.3}$$

By treating the branching ratio $\mathcal{B}$ as a parameter and varying it, the value of $\mathcal{B}$ which give the maximum value of X_{obs} with the given configuration of $\{s_i\}$, $\{b_i\}$ and $\{d_i\}$ is

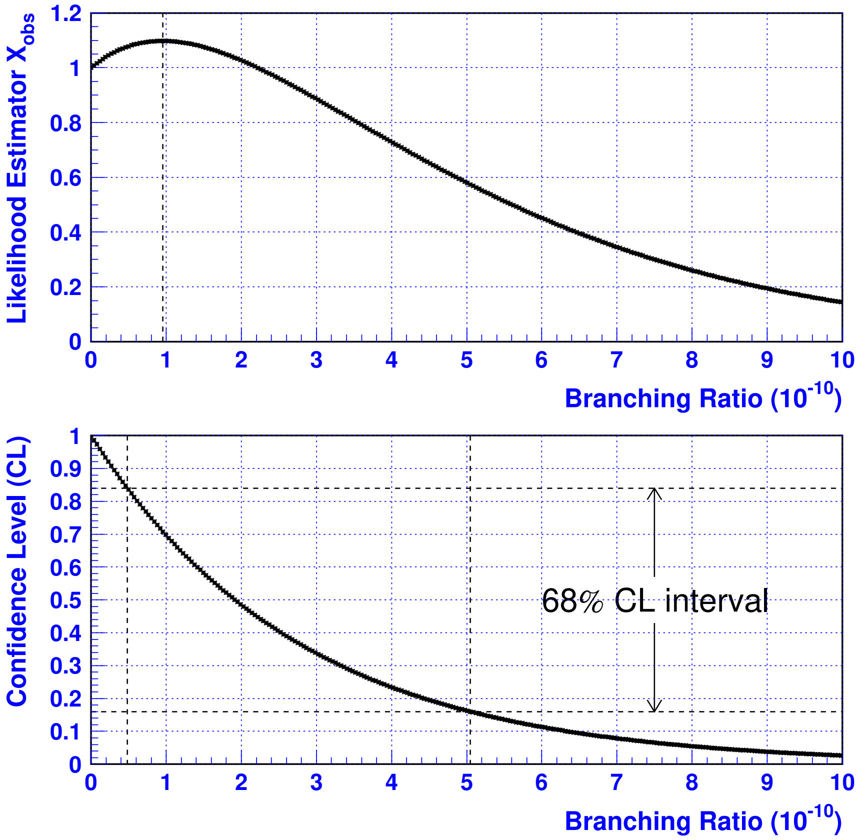

Figure J.1: Likelihood estimator X_{obs} (top) and confidence level CL_s (bottom) for E949 2002 data set as a function of $K^+ \to \pi^+\nu\bar{\nu}$ branching raito $\mathcal{B}$.

regarded as the central value of the branching ratio. Confidence level intervals are also evaluated from Equation (J.3) assuming that it is a function of $\mathcal{B}$.

For the E949 data set, the likelihood estimator X_{obs} and the confidence level CL_s as a function of $\mathcal{B}$ are shown in Figure J.1. In the upper plot of Figure J.1, X_{obs} has the maximum value at $\mathcal{B} = 0.96 \times 10^{-10}$ which gives the central value of the branching ratio. A 68% confidence level interval is obtained from an interval of confidence level between $CL_s = 0.84$ and $CL_s = 0.16$. The branching ratio for $K^+ \to \pi^+\nu\bar{\nu}$ at the 68% confidence level interval is obtained as:

$$\mathcal{B}(K^+ \to \pi^+\nu\bar{\nu}) = (0.96^{+4.09}_{-0.47}) \times 10^{-10} \quad \text{(68\% CL interval)} \tag{J.4}$$

based on the single candidate event.

For the combined E787 and E949 data set, the likelihood estimator X_{obs} and confidence level CL_s as a function of $\mathcal{B}$ are shown in Figure J.2. X_{obs} has the maximum value at $\mathcal{B} = 1.47 \times 10^{-10}$. The branching ratio for $K^+ \to \pi^+\nu\bar{\nu}$ at the 68% confidence level interval is obtained as:

$$\mathcal{B}(K^+ \to \pi^+\nu\bar{\nu}) = (1.47^{+1.30}_{-0.89}) \times 10^{-10} \quad \text{(68\% CL interval)} \tag{J.5}$$

based on the three candidate events.

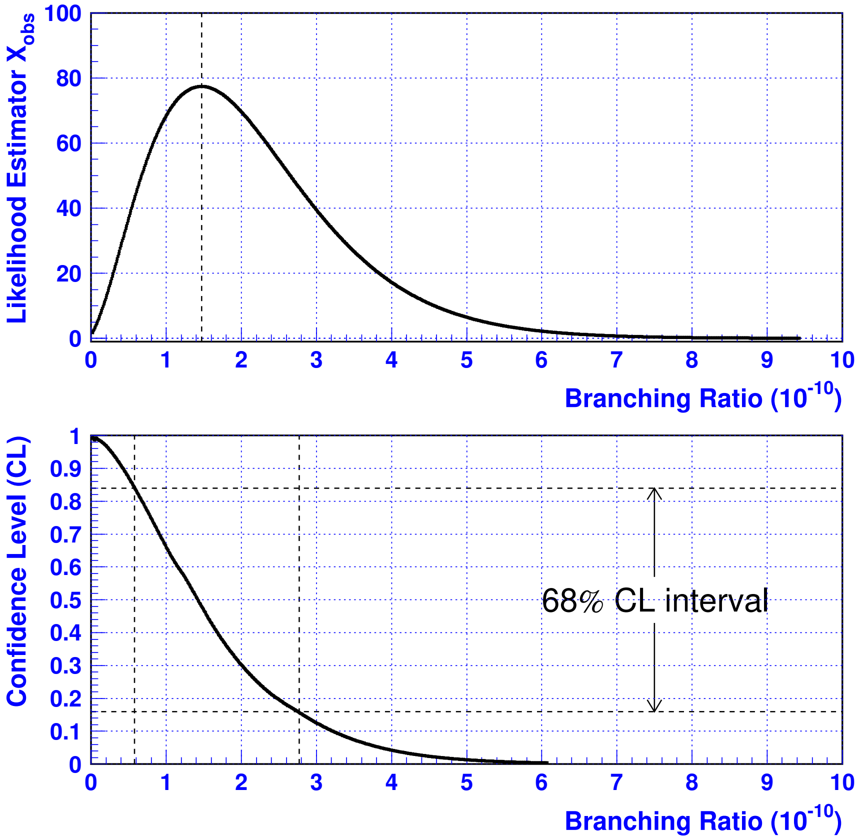

Figure J.2: Likelihood estimator X_{obs} (top) and confidence level CL_s (bottom) for the combined E787 and E949 data set as a function of $K^+ \to \pi^+ \nu\bar{\nu}$ branching ratio $\mathcal{B}$.

J.2 Effects of Systematic Uncertainty on the Branching Ratio

In the method by T. Junk, the effects of systematic uncertainty is taken into account. An inclusion of the effects of systematic uncertainties into the branching-ratio calculation is performed as follows: the likelihood estimator X is replaced with

$$X = \prod_{i=1}^{n} \frac{\int_0^\infty \int_0^\infty \frac{e^{-((s'-s_i)^2/2\sigma_{s_i}^2 + (b'-b_i)^2/2\sigma_{b_i}^2)}}{2\pi\sigma_{s_i}\sigma_{b_i}} X_i ds' db'}{\int_0^\infty \int_0^\infty \frac{e^{-((s'-s_i)^2/2\sigma_{s_i}^2 + (b'-b_i)^2/2\sigma_{b_i}^2)}}{2\pi\sigma_{s_i}\sigma_{b_i}} ds' db'} \tag{J.6}$$

where the X_i is averaged over by the Gaussian functions of signal and background. In Section 7.2, the magnitudes of systematic uncertainties on the sensitivity and the background level for each source were estimated to be 10% and 20%, respectively. The plot of confidence level vs. branching ratio (the lower plot of Figure J.2) has already been derived from Equation (J.6).

Appendix K

Analysis of the $K^+ \to \pi^+ X^0$ Decay

The experimental signature of $K^+ \to \pi^+ X^0$ is the same as $K^+ \to \pi^+ \nu\bar{\nu}$ except that the kinematic values of π^+ are monochromatic (P = 227.1 MeV, E = 127.0 MeV, R = 38.6 cm). The same analysis method as used in the $K^+ \to \pi^+ \nu\bar{\nu}$ analysis is used to search for $K^+ \to \pi^+ X^0$ except for the Phase Space Cuts (and the acceptance factors for it).

The signal region for $K^+ \to \pi^+ X^0$ is the same as $K^+ \to \pi^+ \nu\bar{\nu}$ except that the Phase Space Cuts are $\pm 2\sigma$ regions of momentum, energy, range peaks. The upper edges of the Phase Space Cuts are tightened ($P \leq 229$ MeV/c, $E \leq 135$ MeV, and $R \leq 40$ cm as in $K^+ \to \pi^+ \nu\bar{\nu}$) so that the Muon background can be suppressed. The expected background level is small (0.05 events), because the region is far from the $K_{\pi 2}$ peaks.

The candidate event observed in the Signal Region for $K^+ \to \pi^+ \nu\bar{\nu}$ is also in the $K^+ \to \pi^+ X^0$ signal region; the candidate event is not exactly identified as $K^+ \to \pi^+ X^0$ signal, and only the upper limit is set with the assumption that the background is absent.

The trigger, phase space, and solid angle acceptances are measured with the Monte Carlo simulation which generates the $K^+ \to \pi^+ X^0$ decay (Table K.1). All the acceptance factors for the $K^+ \to \pi^+ X^0$ analysis are summarized in Table K.2. The acceptance factors for the enlarged signal region (Signal Region) are also measured. For the $K^+ \to \pi^+ X^0$ Signal Region, the Phase Space Cuts are not loosened; the acceptance gains from only the PV Extended and $\pi^+ \to \mu^+ \to e^+$ Extended Regions are taken into account, which results in 21% acceptance gain with respect to that for the 1×1 Region. The total acceptance and sensitivity for the $K^+ \to \pi^+ X^0$ analysis are measured to be

$$A_{total} = (6.89 \pm 0.20 \pm 0.52) \times 10^{-3} \quad \text{and} \quad S.E.S = (0.82 \pm 0.02 \pm 0.06) \times 10^{-10}, \quad \text{(K.1)}$$

where the first and second errors are the statistical and systematic uncertainties.

There was no candidate event in the $K^+ \to \pi^+ X^0$ signal region of E787. The combined E787 and E949 sensitivity of 0.196×10^{-10} and the Feldman and Cousins method [50] in the assumption of one signal event and no background give the upper limit for the $K^+ \to \pi^+ X^0$ decay as:

$$\mathcal{B}(K^+ \to \pi^+ X^0) < 3.81 \times 0.196 \times 10^{-10} = 0.747 \times 10^{-10} \quad \text{(K.2)}$$

at 90% confidence level. This limit is larger than the previous limit 0.59×10^{-10} (90% CL) from the E787 result [22, 23] due to one candidate event in E949.

Cut	NIDIF (ON)		NIDIF (OFF)	
	# Events	Acceptance	# Events	Acceptance
Setup	100000	-	60000	-
T•2	43768	0.4377	27354	0.4559
$(6_{ct} + 7_{ct})$	36379	0.8312	27353	1.0000
DC	36379	1.0000	27353	1.0000
$\overline{19_{ct}}$	35814	0.9845	27198	0.9943
$\overline{\mathrm{BV} + \mathrm{BVL} + \mathrm{EC}}$	35643	0.9952	27198	1.0000
HEX	35532	0.9969	27198	1.0000
Refined Range	24219	0.6816	23512	0.8645
$A_{trigger}$	0.2422±0.0014		0.3919±0.0020	
Setup	24066	-	23504	-
UFATE	21105	0.8770	23504	1.0000
USTMED	20911	0.9908	23261	0.9897
USTOP_HEX	20255	0.9686	23187	0.9968
COS3D	19413	0.9584	22168	0.9561
LAYER14	19290	0.9937	22133	0.9984
ZFRF	17538	0.9092	20087	0.9076
ZUTOUT	17533	0.9997	20076	0.9995
Loose Phase Space	10748	0.6130	14174	0.7060
Phase Space	10748	0.6130	14174	0.7060
A_{MC}(Signal Region)	0.4466±0.0032		0.6030±0.0032	
A_{MC}(1×1 Region)	0.4466±0.0032		0.6030±0.0032	

Table K.1: Summary of the trigger, phase space, and solid angle acceptances for $K^+ \to \pi^+ X^0$ with the pion nuclear interaction and decay-in-flight (NIDIF) turned on or off. The symbolic names of the cuts in the table are described in Appendix B. The errors are statistical.

Factor	Acceptance	
	Signal Region	1×1 Region
Trigger acceptance	0.3919±0.0020±0.0196	
K^+ stop efficiency	0.7740±0.0011	
Beam and target analysis	0.5483±0.0007	
Phase space and solid angle	0.6123±0.0032	
π^+ nucl. int. and decay-in-flight	0.4577±0.0054±0.0229	
Reconstruction efficiency	0.9956±0.0001	
Other kinematics constraints	0.5013±0.0071±0.0154	
$\pi^+ \to \mu^+ \to e^+$ decay acceptance	0.3893±0.0085±0.0074	0.3476±0.0076±0.0066
Accidental loss	0.8204±0.0019	0.7509±0.0022
T•2 efficiency	0.9357±0.0011±0.0168	
Total acceptance	$(6.89\pm0.20\pm0.52)\times10^{-3}$	$(5.68\pm0.17\pm0.44)\times10^{-3}$
K^+ Trigger ($K^+ \to \pi^+ X^0$)	1.77×10^{12}	
Sensitivity	$(0.82\pm0.02\pm0.06)\times10^{-10}$	$(0.99\pm0.03\pm0.08)\times10^{-10}$

Table K.2: Acceptances and sensitivity for the $K^+ \to \pi^+ X^0$ analysis. The first and second uncertainties represent the statistical and systematic uncertainties, respectively.

Bibliography

[1] N. Cabibbo, Phys. Rev. Lett. **10**, 531 (1963).

[2] S.L. Glashow, J. Iliopoulos, and L. Maiani, Phys. Rev. **D2**, 1285 (1970).

[3] M. Kobayashi and T. Maskawa, Prog. Theor. Phys. **49**, 652 (1973).

[4] L. Wolfenstein, Phys. Rev. Lett. **51**, 1945 (1983).

[5] Particle Data Group, S. Eidelman *et al.*, Phys. Lett. **B592**, 1 (2004)

[6] C. Jarlskog, Phys. Rev. Lett. **55**, 1039 (1985); C. Jarlskog, Z. Phys. **C29**, 491 (1985); C. Jarlskog and R. Stora, Phys. Lett. **B208**, 268 (1988).

[7] A.J. Buras, F. Schwab, and S. Uhlig, arXiv:hep-ph/0405132 (2004).

[8] T. Inami and C.S. Lim, Prog. Theor. Phys. **65**, 297 (1981).

[9] G. Buchalla and A.J. Buras, Nucl. Phys. **B548**, 309 (1999).

[10] G. Buchalla and A.J. Buras, Nucl. Phys. **B398**, 285 (1993).

[11] M. Musiak and J. Urban, Phys. Lett. **B451**, 161 (1999).

[12] W.J. Marciano and Z. Parsa, Phys. Rev. **D53**, 1 (1996).

[13] Particle Data Group, K. Hagiwara *et al.*, Phys. Rev. **D66**, 010001 (2002).

[14] A.J. Buras, M.E. Lautenbacher, and G. Ostermaier, Phys. Rev. **D50**, 3433 (1994).

[15] D. Rein and L.M. Sehgal, Phys. Rev. **D39**, 3325 (1989); J.S. Hagelin and L.S. Littenberg, Prog. Part. Nucl. Phys. **23**, 1 (1989); M. Lu and M.B. Wise, Phys. Lett. **B324**, 461 (1994); S. Fajfer, arXiv:hep-ph/9602322 (1996); C.Q. Geng, I.J. Hsu, and Y.C. Lin, Phys. Rev. **D54**, 877 (1996).

[16] K. Anikeev *et al.*, Workshop Report "B Physics at the Tevatron: Run II and Beyond", arXiv:hep-ph/0201071 (2002).

[17] A. Belyaev *et al.*, Kaon Physics working Group Report "Kaon Physics with a High-intensity Proton Driver", arXiv:hep-ph/0107046 (2001); G. Isidori, arXiv:hep-ph/0110255 (2001); G. Buchalla, arXiv:hep-ph/0110313 (2001).

[18] A.J. Buras, arXiv:hep-ph/0402191 (2004); G. Isidori, arXiv:hep-ph/0301159 (2003).

[19] A.J. Buras *et al.*, arXiv:hep-ph/0402112 (2004); A.J. Buras *et al.*, arXiv:hep-ph/0408142 (2004).

[20] Y. Grossman and Y. Nir, Phys. Lett. **B398**, 163 (1997).

[21] F. Wilczek, Phys. Rev. Lett. **49**, 1549 (1982); J.L. Feng *et al.*, Phys. Rev. **D57**, 5875 (1998).

[22] S. Adler *et al.*, Phys. Rev. Lett. **79**, 2204 (1997).

[23] S. Adler *et al.*, Phys. Rev. Lett. **88**, 041803 (2002); S. Adler *et al.*, Phys. Rev. Lett. **84**, 3768 (2000);

[24] J.H. Klems *et al.*, Phys. Rev. **D4**, 66 (1971).

[25] G.D. Cable *et al.*, Phys. Rev. **D8**, 3807 (1973).

[26] Y. Asano *et al.*, Phys. Lett. **B107**, 159 (1981).

[27] M.S. Atiya *et al.*, Nucl. Instr. Meth. **A321**, 129 (1992).

[28] S. Adler *et al.*, Phys. Rev. Lett. **76**, 1421 (1996).

[29] B. Bassalleck *et al.*, E949 proposal, BNL-67247, TRI-PP-00-06 (1999), `http://www.phy.bnl.gov/e949/` .

[30] T. Yoshioka *et al.*, IEEE Trans. Nucl. Sci. **51**, 199 (2004).

[31] J. Doornbos *et al.*, Nucl. Instr. Meth. **A444**, 546 (2000).

[32] D.A. Bryman *et al.*, Nucl. Instr. Meth. **A396**, 394 (1997).

[33] M. Atiya *et al.*, Nucl. Instr. Meth. **A279**, 180 (1989).

[34] E.W. Blackmore *et al.*, Nucl. Instr. Meth. **A404**, 295 (1998).

[35] R.A. McPherson, "Chasing the Rare Decay $K^+ \to \pi^+\nu\bar{\nu}$", Princeton University, Ph.D. Thesis, November, 1995.

[36] I.H. Chiang *et al.*, IEEE Trans. Nucl. Sci. **42**, 394 (1995).

[37] T.K. Komatsubara *et al.*, Nucl. Instr. Meth. **A404**, 315 (1998).

[38] C. Caso *et al.*, European Physical Journal **C3**, 1 (1998).

[39] P. Meyers, "A modified Version of the UMC Multiple Scattering Routine MSCAT1", E787 Technical Note No.77 (1985). Unpublished.

[40] A.J. Stevens, "Nuclear Interactions in CH revisited", E787 Technical Note No.140 (1987). Unpublished.

[41] W.R. Nelson *et al.*, "The EGS4 Code Syatem", SLAC 265, SLAC (1985).

[42] T. Sekiguchi, "Development of Silicon Strip Detector for Rare Kaon Decay Experiments", University of Tokyo, Master Thesis, January, 2002.

[43] J.B. Birks, Proc. Phys. Soc. **A64**, 874 (1951).

[44] The reference manual can be found in
`http://paw.web.cern.ch/paw/mlpfit/pawmlp.html`.
The PDF version of the reference manual can also be available in
`http://schwind.home.cern.ch/schwind/MLPfit/doc/pawmlp.pdf`.

[45] S. Adler *et al.*, Phys. Rev. Lett. **85**, 2256 (2000); M.R. Convery, "First Measurement of Structure Dependent $K^+ \to \mu^+ \nu_\mu \gamma$", Princeton University, Ph.D. Thesis, November, 1996.

[46] T. Junk, Nucl. Instr. Meth. **A434**, 435 (1999).

[47] V.V. Anisimovsky *et al.*, Phys. Rev. Lett. **93**, 031801 (2004).

[48] Figures 7.3 and 7.4 are made by G. Isidori.

[49] G. Isidori, arXiv:hep-ph/0307014 (2003); G. Isidori, arXiv:hep-ph/0301159 (2003).

[50] G.J. Feldman and R.D. Cousins, Phys. Rev. **D57**, 3873 (1998).